Title

Measuring Nuclear Lifetimes with Two Gamma-Ray Imaging Techniques

Author

Crabbs, Robert

Publication Date

2016

Measuring Nuclear Lifetimes with Two Gamma-Ray Imaging Techniques

by

Robert David Crabbs

A dissertation submitted in partial satisfaction of the

requirements for the degree of

Doctor of Philosophy

in

Engineering – Nuclear Engineering

in the

Graduate Division

of the

University of California, Berkeley

Committee in charge:

Professor Kai Vetter, Chair
Dr. I-Yang Lee
Professor Per Petersen
Professor William Holzapfel

Summer 2016

Measuring Nuclear Lifetimes with Two Gamma-Ray Imaging Techniques

Abstract

Measuring Nuclear Lifetimes with Two Gamma-Ray Imaging Techniques

by

Robert David Crabbs

Doctor of Philosophy in Engineering – Nuclear Engineering

University of California, Berkeley

Professor Kai Vetter, Chair

The GRETA collaboration has developed a large position-sensitive HPGe detector array for both stable and radioactive beam experiments, called the **G**amma-**R**ay **E**nergy **T**racking **IN**-Beam **A**rray (GRETINA). The array's primary purpose is for high-efficiency, high-precision gamma-ray spectroscopy. Its position sensitivity allows experimenters to sequence photon tracks via Compton kinematics. This tracking is used, among other things, to estimate the emission angle of a gamma ray relative to its parent nucleus's velocity. This is key for spectroscopy because it gives a way to correct for Doppler shifts in photon energy.

Because GRETINA can measure both energy and position of individual photon interactions, it also opens the door for gamma-ray imaging. I sought to use these capabilities to measure the lifetimes of short-lived nuclear states produced by in-beam experiments. The current approach to this problem – called the "Recoil Distance Method" (RDM) – requires large amounts of beamtime, a resource which is in short supply. With gamma-ray imaging, on the other hand, we can theoretically extract these lifetimes "for free", using the same data taken during spectroscopy runs. Where RDM generally requires multiple measurements to find a lifetime, imaging delivers full de-excitation curves from a single run. Lifetimes can be extracted directly by fitting to these curves.

The research presented here provides a feasibility study of two gamma-ray imaging techniques: traditional Compton imaging, and a new method based on Doppler shifts. Where Compton imaging depends on the first two hits in a photon track, "Doppler-Shift imaging" requires only the first. This is extremely promising, as I found that GRETINA's position resolution greatly limits the fidelity of Compton imaging. Doppler-shift imaging is more

sensitive to detector energy-resolution, but largely insensitive to position resolution. In both cases, finite imaging resolution causes an imaged de-excitation curve to deviate from the ideal, purely exponential shape. To improve accuracy, curve fitting must account for the detector imaging response.

Many parameters affect the overall imaging response of GRETINA. I evaluated several of them here through a series of detailed Geant4 simulations, and explored several data cuts to improve imaging quality. In general, Doppler-shift imaging offers 5-6x better imaging resolution and 2-3x better imaging efficiency. With data filters, Compton imaging resolution can deliver comparable resolution at the expense of 85-90% of counts.

The end goal of this imaging work is to understand how imaging response translates to precision in lifetime measurements. Imaging resolution, counting statistics, and the lifetime of the nuclear state in question all have significant effects on this precision. I studied each parameter using detailed simulations built in Geant4, calculating sensitivity ranges for lifetime measurements using gamma-ray imaging. I found that even very poor imaging resolution can be corrected for if the detector response is accurately characterized. For example, with 25.0 mm imaging resolution and 50K samples per lifetime curve, we can achieve $< 5\%$ relative uncertainty on measured lifetimes between 29 ps and 5.2 ns at 0.3c parent velocity.

However, while the simulations are extremely encouraging, an experimental validation with ^{92}Mo was ultimately unsuccessful. At 35 ps, the lifetime of the isotope's 740 keV transition is on the lower edge of our sensitivity range – especially when combined with the very low 0.085c recoil velocity of the parent nucleus. I also ran into complications from Compton background counts in the experimental spectrum, which made it very difficult to characterize the imaging response reliably. Knowing this, however, we now have a better idea of the requirements for using gamma-ray imaging in lifetime experiments.

To Stephanie Yeh

Where would this Slytherin be were it not for the love and support of his Hufflepuff fiancée?

You have always been there to help me up when I'm feeling down. You gave me someone to talk to all those times I needed to vent, and you kept the inner Hulk-Robert in check when Geant4 didn't want to cooperate and the damn printer melted down.

Thank you for all the backrubs, the hours of anime, the awesome surprise paintball and LAN-party birthdays. Thank you for being my Medieval sparring partner on Memorial Glade, and for helping me stay sane through 5 years of grad school (and the 4 years of undergrad before that). Thank you having faith in me all that time.

I never would have made it without you.

Contents

List of Figures

List of Tables

Acknowledgments

To I-Yang Lee, who continued mentoring and encouraging me through his retirement, and who created the very foundation on which this work rests. Thank you for the many, many meetings over the years, and for your sage advice on not just academia but many other aspects of my life. I'll always try to keep in mind that the hard part is choosing what *not* to do.

To Kai Vetter, the professor who introduced me to radiation detection when I was but an undergrad. Thank you for putting up with me while I took my wayward journey through grad school, and for being stern when I needed it. You pushed me to keep growing. I hope one day I can repay you for the investment you've made in me.

To Jasmina Vujic and the NSSC, for making grad school possible. Any entrepreneur would feel blessed to have the same generous support that you give your students.

To Per Petersen, both for sitting on my committee, and for the thoroughly enjoyable and thought-provoking semester in NE 267. You're a truly inspirational teacher.

To Bill Holzapefel, for showing me how to build 100 kV plasma arcs in my kitchen, and for introducing me to a nifty method of isotope separation during my quals. Everything is cooler with lasers!

To Peter Hosemann, who showed us that it's not diamonds, but cubic zirconia, that last forever (at least in high radiation fields).

To Rick Norman, for two wonderful and friendly courses in nuclear science. I feel like you and Richard Feynmann surely must be related.

To Max Fratoni, for showing a newbie nuclear engineer how neutrons and reactors work. The NTE is a lot less intimidating now.

To Joonhong Ahn, who answered all my stupid questions and taught me everything I know about nuclear waste management. NE 124 remains one of my all-time favorite courses. Rest in peace, professor.

To Lisa Zemelman and Kirsten Wimple, who keep the fires burning and the trains running on time in the NE department. We students would be lost without you.

To Geant4, LaTeX, Ubuntu Linux, and other open-source software. Despite the **many** hours of grief these tools caused me – this dissertation simply would not have existed without them. Seriously, though, someone really needs to write better software for physicists.

To Eugene Evans, my best bud from Ridge House. You're the peanut butter to my jelly, the Spock to my Kirk. Here's to all our memories at Haste, from the irresponsible backyard physics experiments to the late nights (early mornings?) playing Smash Brothers!

To my many other supportive friends and family, and all my companions in the SCA. Thanks for all the good times and encouragement while I've been away in school. I'm looking forward to many visits ahead!

To my mom, dad, and brother, for the decades of love and encouragement. I could not have asked for a better family. Thank you for showing me that I'm valued when I most doubt myself, and for giving me the strength to forge ahead. I know there's always a place for me to come back to and recharge. Thank you for everything!

Chapter 1

Introduction

1.1 Problem Statement and Motivation

This project seeks to not only measure nuclear lifetimes, but also expand scientific work in general by reducing the need for beamtime in lifetime measurements. Lifetime is an important test of our models of the strong force, but obtaining data is currently quite laborious and expensive. I propose using gamma-ray imaging for these measurements. Doing so may extend the range of lifetimes that can be studied with in-beam experiments. In addition, if we can cut down on the required beamtime, it will allow us to measure lifetimes for more states, as well as free up time at accelerator facilities for other experiments.

The lifetime of an excited nucleus is critical to our understanding of subatomic forces. Quantum mechanics dictates that all systems have a non-zero probability to transition into another allowed state. (See pages 40-41 in Reference [21].) This law is quantified in Fermi's Golden Rule, which gives the probability per unit time λ_{fi} of observing a transition from an initial nuclear state to some other final state:

$$\lambda_{fi} = \frac{2\pi}{\hbar}|M_{fi}|^2\rho(E_f) \tag{1.1}$$

$$M_{fi} = \int \Psi_f * V\Psi_i dv \tag{1.2}$$

where $\rho(E_f)$ is the density of final states at energy E_f, and M_{fi} is the transition "matrix element" of the transition operator V. The initial state of the system is represented by the wave-function Ψ_i, while the final state is represented by Ψ_f. These wavefunctions are predicted by nuclear models – in other words, the theoretical forms and relative strengths of the forces in the nucleus. For any given theory of the strong, weak, and electromagnetic forces, one can use quantum mechanics to predict everything from excitation energies to nuclear spins to decay pathways.

References [21] and [16] go into more detail about nuclear structure calculations. For our purposes here, the important thing is that Equation 1.2 can be re-arranged to solve for M_{fi} in terms of the nuclear lifetime:

$$|M_{fi}| = \sqrt{\frac{\hbar}{2\pi\rho(E_f)\tau_{fi}}} \tag{1.3}$$

where $\tau_{fi} = 1/\lambda_{fi}$ is the lifetime of transition from the initial to final state. By measuring this lifetime, one obtains a data point to compare against the theoretical predictions of a given nuclear model.

Reference [35] provides an excellent example. The article focuses on low-lying excited states and their transitions in the "halo" nucleus ^{19}C. By measuring the lifetime of the first $3/2^+$ state, they found that the M1 transition is greatly suppressed. This confirmed expectations they had from the shell model for light halo nuclei, and has suggested further lifetime measurements in other mass regions. (Halo nuclei form near the neutron or proton drip-lines, where an overabundance of one type of nucleon produces lower-than-average binding energy. The nucleons form a "halo" orbit around the tightly-grouped nuclear core, which expands the effective radius of the nucleus significantly beyond that predicted by the liquid-drop model. [36])

Reference [18] details another nuclear structure experiment, this time focused on collectivity and deformation in the ^{72}Kr nucleus. As discussed in pp. 134-149 from Reference [21], nucleons can act in groups to produce patterned energy levels, called bands. The specific *type* of collective behavior yields different transition strengths between the states. Here, the experimenters concluded that "The rapid increase of collectivity in the $4^+ \rightarrow 2^+$ transition relative to that for the $2^+ \rightarrow 0^+$ transition suggests that the onset of the oblate-prolate shape transition occurs at low spin in ^{72}Kr, presenting an extreme example of the shape transition in atomic nuclei."

We could also use a measured lifetime to deduce the spin-parities of a nucleus's energy levels. The transition strengths between levels depend on the transitions' energies and angular-momentum transfers. In general, it is very unlikely for a photon to carry more than one unit of angular momentum. This means, for example, that a transition from $J^\pi = 9/2^+$ to $J^\pi = 3/2^+$ is highly-suppressed (with M3 as the lowest permitted multipole mode). On the other hand, a transition from $J^\pi = 9/2^+$ to $J^\pi = 7/2^-$ would be far stronger. Measuring the partial lifetime of a specific transition tells how relatively strong that transition is, and hence sheds light on the final state's spin-parity. [21]

Our models are most reliable near the so-called "Valley of Stability", where nuclei have lifetimes of at least a few seconds. It's near the proton and neutron drip-lines that the models fail. We have a lot less data for these exotic, short-lived nuclei. Studying them is the mission of multiple facilities, such as MSU's **F**acility for **R**are **I**sotope **B**eams (FRIB).

In these facilities, rare nuclei are produced by accelerating a high-energy projectile (like ^{48}Ca or ^{84}Kr) into a thin target (like ^{12}C or ^{9}Be). In some experiments, the reaction products are themselves projectiles in a secondary beam that produces even more exotic isotopes. The products are typically created in an excited state, and will therefore de-excite some time later as they travel downstream. The recoil velocity of the products is dictated by reaction kinematics, and is typically between 0.05-0.45c. (This velocity is limited by the energy per nucleon that can be delivered by the facility's accelerator.)

To measure a lifetime in a beam experiment, we need some way to reconstruct the de-excitation curve. (Figure 1.1) When the nuclei de-excite, they emit gamma-rays at various distances downstream of the target. Because the recoil velocity is measured, distance travelled translates directly to time of flight, and hence emission time. The distribution of emission times will follow an exponential decay:

$$\begin{aligned} A(z) &= A_0 e^{-\mu z} && (1.4) \\ &= A_0 e^{-z/\gamma\beta c\tau_0} && (1.5) \end{aligned}$$

where β is the parent nucleus's speed in the lab frame, γ is the corresponding Lorentz factor, τ_0 is the proper lifetime of the nuclear state, and $\mu = 1/\gamma\beta c\tau_0$ gives the probability of de-excitation per unit length.

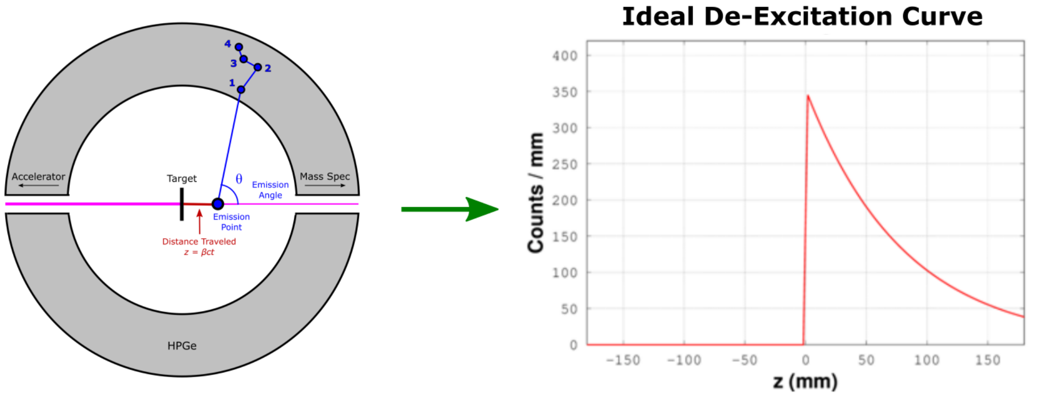

Photon Emitted at Angle θ

Hits multiple times in detector before absorption

Distribution of Emission Points

Locate emission points of many different photons; distribution follows an exponential decay function

Figure 1.1: Illustration of the lifetime measurement problem

The current state-of-the-art for measuring lifetimes is the **R**ecoil **D**istance **M**ethod, or RDM. The technique is discussed in detail in Section 2.3. The important point is how intensive the process is – building a de-excitation curve through RDM requires multiple runs, each of which can take hours or even *days* of beamtime. Beamtime is a very scarce and costly resource, and so there is marked interest in alternative methods for measuring lifetimes. My work here investigates using gamma-ray imaging for the purpose. One of the primary attractions to this approach is that the de-excitation curve is built in a *single* measurement. In addition, where RDM requires several dedicated runs, imaging can use data from a standard spectroscopy experiment. This means using *significantly* less beamtime.

Lawrence-Berkeley National Labs has developed a state-of-the-art photon detector array called GRETINA, which is used (among other things) for RDM measurements. This array consists of many large-volume segmented HPGe crystals. Because of its extraordinary efficiency and resolution, the array presents a very promising opportunity for gamma-ray imaging, specifically for lifetime measurements. More details on the GRETINA array are included in Section 2.4.

This work was made possible by a generous grant from the **N**ational **N**uclear **S**ecurity **C**onsortium, or NSSC. One of the missions of this organization is to prepare young scientists for careers in nuclear security. While lifetime measurements are not directly related to securing our nuclear stockpile or defending against radiological threats, gamma-ray imaging is a technique with broad applications in the field. Through my work with Compton imaging, I have gained skills that would be readily transferrable to security applications, and have added to the body of knowledge surrounding this valuable technique.

1.2 Chapter Overviews

In this section, I provide the reader with a general guide to the rest of the dissertation. The theory and background is all contained in Chapter 2, while Chapters 3 thru 6 represent the new contributions my work brings to the field.

This body of work seeks to use gamma-ray imaging to measure lifetimes of rare excited nuclei. There are several pieces to this puzzle – Compton Sequencing (Chapter 3), Compton Imaging (Chapter 4), Doppler-Shift Imaging (Chapter 5), and Lifetime Measurements (Chapter 6).

Chapter 2 provides the background and theory upon which the remaining chapters rest. In it the reader will find discussions of Compton Scattering and relativistic Doppler-Shifts, including derivations of some of the most important formulae involved. There is also a section on gamma-ray detector physics, with an in-depth look at the GRETINA detector array. Much of this discussion focuses on the signal decomposition which enables GRETINA to determine the locations of photon interactions within its crystals. The chapter concludes with a brief description of the simulation tools used in this study.

GRETINA's position sensitivity is a powerful asset. Combined with the array's excellent energy resolution, this sensitivity provides the basis for Doppler-shift correction, Compton sequencing, and two different gamma-ray imaging modes. On top of that, it enables us to perform lifetime measurements in a variety of ways. Chapters 3 thru 6 explore in detail how I implemented these techniques, and represent the new contributions this work brings to the field.

Chapter 3 is dedicated to interaction grouping and Compton tracking – the methods used to identify and sequence individual photon tracks. The detector's time resolution is not nearly good enough to sequence directly, so instead we take advantage of the physics of Compton scattering. Each potential sequence of measured energy depositions and scattering angles is tested against the kinematics described by the Compton formula. The one that best matches the kinematics is deemed the "correct" sequence.

Chapter 4 discusses the mechanics of Compton Imaging. Much of my research focused on optimizing the resolution achievable with this technique. There are multiple parameters that we can tune during post-processing. Some of the choices can be made independently of the imaging problem; but some, like the "Compton lever arm", are simply empirical optimizations of the end results. Imaging resolution and efficiency are also highly-dependent on the details of a given beam experiment, including beam velocity, CM-frame photon energy, and detector resolution (for both position and energy). I investigated the effects of these parameters on the final "detector imaging response", a distribution reflecting how well a given imaging modality locates the true photon emission points along the beamline.

Chapter 5 introduces a new gamma-ray imaging method, called Doppler-Shift imaging, which seems very promising for lifetime measurements. If we *know* the correct CM-frame emission energy, we can use the detected lab-frame energy to determine the emission angle. Combined with the location of the photon's first interaction in the detector, this uniquely determines the emission location. Requiring a single interaction point is an enormous advantage over Compton imaging, which requires both the 1st and 2nd hits. Compton imaging is therefore much more sensitive to detector position resolution. I evaluated this new imaging method using a similar approach to the one in Chapter 4.

In Chapter 6, I tackle the problem of measuring nuclear lifetimes through imaging. There are three main considerations: the imaging resolution, the number of counts available to build the de-excitation curve, and the "de-excitation parameter" (determined by the beam velocity and nuclear lifetime). Imperfect imaging resolution smears the true shape of an ideal de-excitation curve, and should be corrected for. Doing so requires calibration measurements to determine the detector imaging response for a particular setup. The chapter ends with an experimental validation of the two imaging techniques using two known states of ^{92}Mo.

Finally, in Chapter 7, I discuss my conclusions, with a comparison of the two imaging-based lifetime measurement techniques. The chapter concludes with refinements to imaging we could implement if given more time.

Chapter 2

Theoretical Basis

This chapter provides background and the theoretical basis of our work here. In it, we cover the prerequisite physics for Compton tracking and Doppler-shift corrections. The next sections describe the GRETINA detector array in some detail, including an overview of the signal-decomposition algorithm that enables its position sensitivity.

All of the information presented here is the result of others' work – it is included for reference and to provide a complete background for the work introduced in the next chapter. Much of it can of course be found in textbooks. However, it took a good while for me to reach my current understanding of everything that goes into the larger lifetime measurement problem. My hope is that by including all this material in one place the people who read this work won't have to go through such great lengths.

2.1 Physics of Compton Scattering

Compton scattering occurs when a photon scatters off an electron. The kinematics of this process allow us to properly sequence a photon track, a fact we will use extensively later on in gamma-ray imaging. Because these sequencing techniques rely on a track having three or more interactions, photonic cross-sections in HPGe can be used to estimate the energy range for which these techniques are most useful.

The derivation of the famous Compton Scattering formula is fairly straightforward and is presented here for reference. However, it makes an important simplification, assuming the electron is initially at rest when struck by the incoming photon. Because electrons in real materials are bound to atoms and thereby have non-zero energy and momentum, there is some inherent uncertainty in the energy transferred during the scatter.

There are three primary reactions for a photon traveling through a material. One such interaction is photoabsorption, wherein the photon transfers its full energy to an atomic electron. The reaction will leave the electron in an excited atomic state or potentially liberate it from the nucleus entirely (photoionization). A photon can also scatter off an electron while imparting only some of its energy in the process. This is called Compton scattering, which forms the very basis of my work here. The last of the common interactions is pair-production, wherein a gamma-ray of sufficient energy scatters off the nucleus and produces a matching electron-positron pair.

The famous Compton energy formula gives the final energy of a photon of initial energy after it has scattered off an electron at a given angle. The derivation is straightforward (see Appendix A.1), and the familiar result is:

$$E_{\gamma,f} = \frac{E_{\gamma,i}}{1 + (E_{\gamma,i}/m_e c^2)(1 - \cos\theta)} \tag{2.1}$$

Here, $E_{\gamma,i}$ is the photon's initial energy, $E_{\gamma,f}$ is its post-scatter energy, and θ is the scattering angle. The above equation makes an important assumption, though – that the scattering electron is initially at rest. In reality, this is certainly not the case. Electrons are bound to parent atoms with energies from several eV to several 10's of keV (and for high-Z elements, even more). In HPGe, the inner K-shell electrons have 14.1keV binding energy, and because e$^-$ are massive particles, even relatively small kinetic energy can correspond to significant initial momentum relative to the photon. Reference [40] gives an expression for Compton scattering that accounts for this momentum:

$$E_{\gamma,f} = \frac{E_{\gamma,i}(1 - \beta\cos\alpha_1)}{1 - \beta\cos\alpha_2 + (E_{\gamma,i}/\gamma m_e c^2)(1 - \cos\theta)} \tag{2.2}$$

$$\cos\alpha_1 = \frac{\boldsymbol{p_{e,i}} \cdot \boldsymbol{p_{\gamma,f}}}{|\boldsymbol{p_{e,i}}||\boldsymbol{p_{\gamma,f}}|} \qquad \cos\alpha_2 = \frac{\boldsymbol{p_{e,i}} \cdot \boldsymbol{p_{\gamma,i}}}{|\boldsymbol{p_{e,i}}||\boldsymbol{p_{\gamma,i}}|} \qquad \cos\theta = \frac{\boldsymbol{p_{\gamma,i}} \cdot \boldsymbol{p_{\gamma,f}}}{|\boldsymbol{p_{\gamma,i}}||\boldsymbol{p_{\gamma,f}}|} \tag{2.3}$$

where βc is the electron's speed and γ is its Lorentz factor. $\boldsymbol{p_{\gamma,i}}$ is the inital photon momentum, $\boldsymbol{p_{\gamma,f}}$ is the final photon momentum, $\boldsymbol{p_{e,i}}$ is the inital electron momentum, and $\boldsymbol{p_{e,f}}$ is the final electron momentum. (See Figure 2.1)

Figure 2.2 shows the relative cross-sections for the three primary photon interactions in Germanium. As we can see, photoabsorption dominates in the low-energy region ($E_\gamma <$ 150 keV). Compton scattering becomes the most probable interaction between 150 keV $< E_\gamma <$ 8 MeV, with pair production dominating the total cross-section at higher energies. The differential cross-section for Compton scattering is given by the Klein-Nishina formula:

$$\frac{\partial\sigma}{\partial\Omega} = \alpha^2 r_C^2 P(E_\gamma,\theta)^2 \left[P(E_\gamma,\theta) + P(E_\gamma,\theta)^{-1} - 1 + \cos^2\theta\right] \tag{2.4}$$

$$P(E_\gamma,\theta) = \frac{1}{1 + (E_\gamma/m_e c^2)(1 - \cos\theta)} \tag{2.5}$$

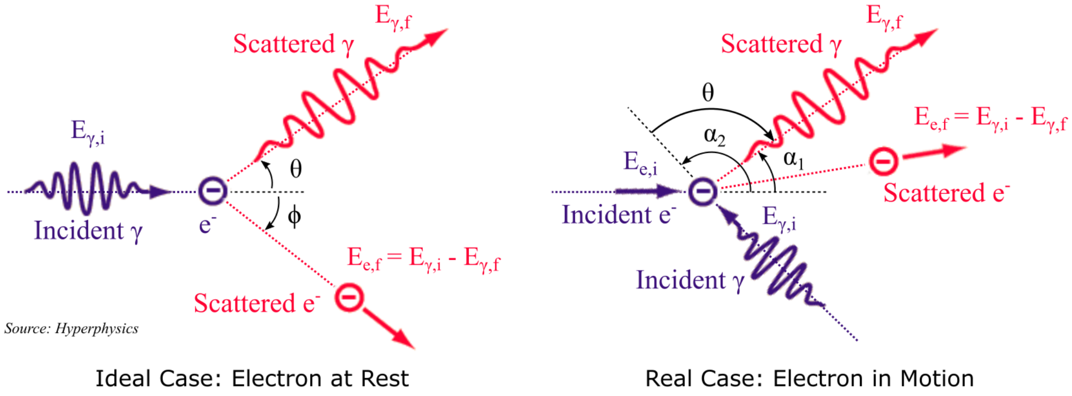

Ideal Case: Electron at Rest

Real Case: Electron in Motion

Figure 2.1: Illustration of Compton scattering

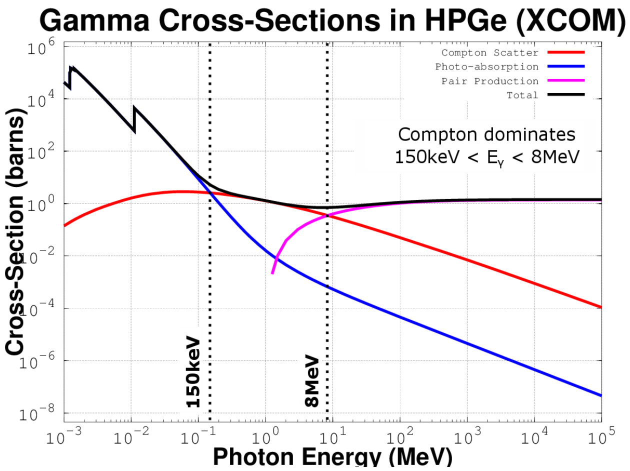

Figure 2.2: Photon cross-sections in HPGe

where α is the fine structure constant, $r_C = \hbar/m_e c$ is the classical electron radius, m_e is the electron mass, E_γ is the initial photon energy, and θ is the photon scattering angle. The derivation is beyond the scope of this work, but details are available in Reference [30].

Equation 2.4 above can be used to find the relative probability that a photon will scatter at a given angle. From there, we can use Equation 2.1 to find the probability that a photon scatters with final energy $E_{\gamma,f}$ (see Figure 2.3). R. Ribberfors took this a step farther, combining the corrected Compton formula (Eq. 2.2) with the Klein-Nishina formula:

$$\left(\frac{\partial^2\sigma}{\partial\Omega\partial E_{\gamma,f}}\right)_n = J_n(p_z)\left(\frac{m_e r_C^2}{2E_{\gamma,i}}\right)\left(\frac{E_C}{E_{\gamma,i}} + \frac{E_{\gamma,i}}{E_C} - \sin^2\theta\right)\left(\frac{E_{\gamma,f}}{\sqrt{E_{\gamma,i}^2 + E_{\gamma,f}^2 - 2E_{\gamma,i}E_{\gamma,f}\cos\theta}}\right) \tag{2.6}$$

Here, E_C is the ideal post-scatter photon energy given by Equation 2.1. $J_n(p_z)$ represents the distribution of electron momenta for the *nth* electron shell, also known as the Compton profile. For a given scattering angle, we can use a weighted average of Equation 2.6 for each shell to arrive at an energy distribution like the one shown in Figure 2.4. [27] The width of this distribution sets a physical minimum on the effective energy resolution of a detector. For example, K. Vetter et al. found this physical limit to be 1.7keV for 662keV photons in HPGe. [33]

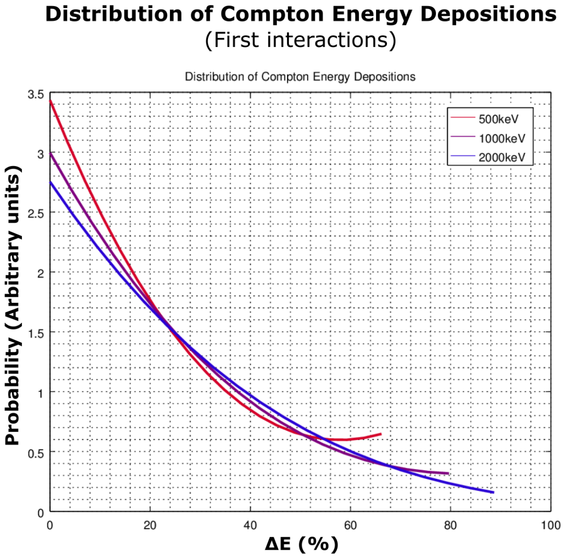

Figure 2.3: Some ideal ΔE distributions in Compton scattering

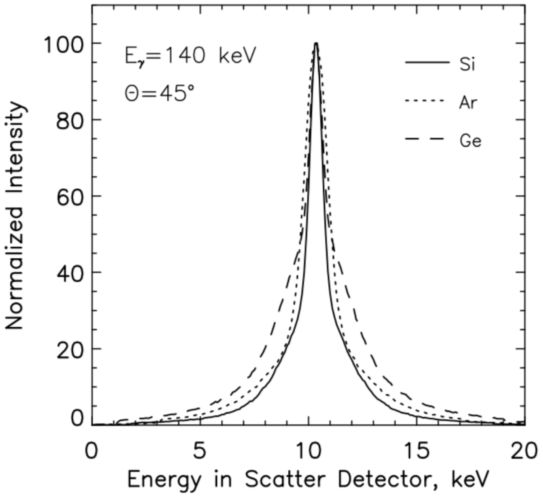

Figure 2.4: ΔE distribution for 140keV photons scattered at 45°
[27]

Equation 2.1 forms the basis of my imaging work. Photons typically interact several times in a detector before being fully-absorbed, but the detector electronics are not fast enough to resolve timing of individual interactions. Consider – from Figure 2.2, the total interaction cross-section for HPGe is between 10 and 20 barns for photons of energy 150 keV $< E_\gamma <$ 8 MeV. Germanium has a molar mass of 72.63 g/mol and mass density of 5.323 g/cm^3, or a number density of 4.413E22 atoms/cm^3. The macroscopic cross-section yields the mean-free-path: $MFP = 1/\Sigma = 1/\sigma n$. Taking $\sigma = 10$ b gives an MFP of 2.27 cm, a distance the photon can cover in 75.5 ps. Considering semiconductor detectors produce signals on 100 ns timescales, the entire track appears simultaneous to the detector. However – the kinematics relating photon energy and scattering angle provide a way to sequence tracks, which in turn allows us to image photon sources in GRETINA's central cavity. We will discuss this in much more detail in Chapter 3.

2.2 Physics of Doppler Shifts

Gamma rays emitted from moving sources are shifted both in energy and angular distribution. These changes are due to the relativistic Doppler effect. I derive the governing formulas for the shifts here.

GRETINA's primary purpose is as a high-efficiency, high-precision gamma-ray spectrometer. It serves to measure the emissions from excited exotic nuclei created in accelerator fusion experiments. In traditional spectroscopy applications, the parent nuclei are typically at rest in the lab-frame. But with in-beam experiments, the sources are moving relativistically – which means the emissions can be significantly up- or down-shifted in energy due to the relativistic Doppler effect. For a nucleus moving with speed βc in the lab frame:

$$E_{\gamma,Lab} = \frac{E_{\gamma,CM}}{\gamma(1-\beta\cos\phi)} \tag{2.7}$$

where γ is the nucleus's Lorentz factor and ϕ is the measured emission angle relative to the parent velocity in the lab frame. (See Appendix A.2 for a derivation of this equation.)

The Doppler shift can be quite pronounced. For a parent nucleus moving down the beam axis with a speed of 0.30c, a 1.00 MeV emission in the CM-frame can range anywhere from 1.36 MeV ($\phi = 0°$) down to 0.73 MeV ($\phi = 180°$). Obviously, we would want a much better level of certainty than that for spectroscopy, where 0.25% energy resolution is typical of an HPGe detector for stationary 1.0 MeV sources.

We can correct for the Doppler-shift if we can determine the source velocity and emission angle. The source velocity is readily measured using multichannel plate detectors downstream of the detector array (see Appendix A.6). The emission angle is more difficult – we need the emission location on the beamline ($\boldsymbol{X_0}$), plus the coordinates of the first interaction in the detector ($\boldsymbol{X_1}$). This defines the emission vector, $\boldsymbol{V_0} = \boldsymbol{X_1} - \boldsymbol{X_0}$, which in turn provides the emission angle:

$$\cos\phi = \frac{\boldsymbol{V_0} \cdot \boldsymbol{B}}{|\boldsymbol{V_0}||\boldsymbol{B}|} \tag{2.8}$$

where $\boldsymbol{B}$ is the vector representing the source velocity. (We generally assume that the source is a pencil beam, and use $\boldsymbol{B} = \boldsymbol{\hat{z}}$ by convention.)

Because GRETINA's detectors are position-sensitive, we can directly measure the coordinates of each interaction. Determining which is $\boldsymbol{X_1}$ is discussed more in Section 3.2. Finding $\boldsymbol{X_0}$ is the subject of much of Chapters 4 and 5 (see Sections 4.1 and 5.1). A common assumption is to simply set $\boldsymbol{X_0} =$ (0.0 mm, 0.0 mm, 0.0 mm) or the target location in GRETINA's inner cavity.

However, this is a good assumption only when the lifetime is very short. Consider a photon that registers its first hit at $\boldsymbol{X_1} =$ (0.0 mm, 190.0 mm, 190.0 mm) and deposits a total of 1.00 MeV in the detector. Suppose the parent nucleus moves with $\beta = 0.3$. Using $\boldsymbol{X_0} =$ (0.0 mm, 0.0 mm, 0.0 mm), we obtain a Doppler-corrected, CM-frame photon energy of 0.827 MeV. Using $\boldsymbol{X_0} =$ (0.0 mm, 0.0 mm, 10.0 mm) – a position just 1 cm downstream – yields a Doppler-corrected energy of 0.833 MeV. The nucleus travels this distance in 111 ps in the lab-frame, or 117 ps in proper time. So, lifetimes longer than this will introduce even larger uncertainties in the CM-frame photon energy.

A final note on Doppler shifts – the lab-frame emission angles tend to be far from isotropic. Let the photon's lab-frame momentum be $\boldsymbol{p_\gamma} = (p_x,\ p_y,\ p_z)$ and its CM-frame momentum be $\boldsymbol{p'_\gamma} = (p'_x,\ p'_y,\ p'_z)$. We can define the emission angle in the lab frame by $\tan\phi = p_y/p_z$, and in the CM-frame by $\tan\phi' = p'_y/p'_z$. From Equation A.21, we have:

$$\begin{aligned} p'_z &= \gamma p_z - \gamma\beta E_\gamma \qquad (2.9)\\ &= \gamma|\boldsymbol{p_\gamma}|\cos\phi - \gamma\beta|\boldsymbol{p_\gamma}| \qquad (2.10)\\ &= \gamma|\boldsymbol{p_\gamma}|(\cos\phi - \beta) \qquad (2.11) \end{aligned}$$

Similarly, $p'_y = p_y = |\boldsymbol{p_\gamma}|\sin\phi$. Therefore:

$$\begin{aligned} tan\phi' &= p'_y/p'_z \qquad (2.12)\\ &= \frac{|\boldsymbol{p_\gamma}|\sin\phi}{\gamma|\boldsymbol{p_\gamma}|(\cos\phi - \beta)} \qquad (2.13)\\ &= \frac{\sin\phi}{\gamma(\cos\phi - \beta)} \qquad (2.14) \end{aligned}$$

With some algebra, we can solve for the lab-frame angle, ϕ:

$$\sin\phi = \frac{-b \pm \sqrt{b^2 - 4ac}}{2a} \tag{2.15}$$

$$a = \gamma^2 \tan^2\phi' - 1 \tag{2.16}$$

$$b = -2\gamma\beta \tan\phi' \tag{2.17}$$

$$c = \gamma^2 \tan^2\phi'(1 - \beta^2) \tag{2.18}$$

With $\beta = 0.3$, a 45.0° emission in the lab frame corresponds to a 58.8° emission in the CM-frame. In general, the lab frame angle will be less than CM-frame angle, an effect called "Doppler focusing". This has important repercussions for detection efficiency in GRETINA, where we have less than 4π coverage and must choose where to place detector modules to maximize counts. The geometric efficiency is a complex function of both Doppler focusing and the lifetime of the parent nucleus.

2.3 Lifetime Measurements with RDM

This section describes a process by which lifetimes of nuclear states are currently measured. The technique is called the "Recoil Distance Method", or RDM.

Recall that a photon emitted with a given energy in the CM-frame of its parent will exhibit a Doppler-shifted energy in the lab frame. (See Section 2.2.) The magnitude of the shift depends on the emission angle and the parent velocity. By placing a degrader foil at a set distance downstream of the target, we can separate the emissions into two categories – those that occur upstream of the degrader, and those that occur downstream. With a thick enough foil, the parent nuclei can be slowed significantly, and thus exhibit noticeably different Doppler-shifts for the two categories.

The next step is to apply an estimated Doppler-shift correction to each emission, using:

$$E_{CM} = \gamma(1 - \beta\cos\theta)E_{Lab} \tag{2.19}$$

$$= \alpha E_{Lab} \tag{2.20}$$

where E_{CM} is the CM-frame photon emission energy, E_{Lab} is its corresponding lab-frame energy, θ is the emission angle, and the overall Doppler-shift correction factor is $\alpha = \gamma(1 - \beta\cos\theta)$. The emission angle is not known exactly, but it can be estimated by measuring the location of the first interaction of the photon in a nearby gamma-ray detector. (The emission point itself is generally **assumed** to be at the target.) Note that the velocity at emission is also not generally known, but can be calculated from the reaction kinematics in the target. This means that the recoil velocity β will be *overestimated* and emission angle θ will be *underestimated* for the nuclei that de-excite downstream of the degrader.

We can see from Equation 2.19 that these two effects will tend to underestimate the Doppler-shift correction factor. So, for any given measured lab-frame energy, the photon's CM-frame energy will be under-reported. Consider, for example, an emission downstream of the degrader with true parent velocity 0.1c and 90° emission angle. Suppose the parent velocity calculated from kinematics is 0.3c, and the estimate for emission angle is 60°. Then the true correction factor would be $alpha_{true} = 1.005$, but the guess would be $alpha_{guess} = 0.891$.

Figure 2.5 illustrates this. [17] RDM will populate two peaks in the corrected energy spectrum. The emissions downstream of the degrader (in green) will fall into the lower-energy peak, while the emissions from between the target and degrader (in blue) will fall into the higher-energy peak. By comparing the ratio of counts in the two peaks, then, we have a measure of how many of the parent nuclei de-excited prior to reaching the degrader. Each choice of degrader position gives a data point on the overall de-excitation curve.

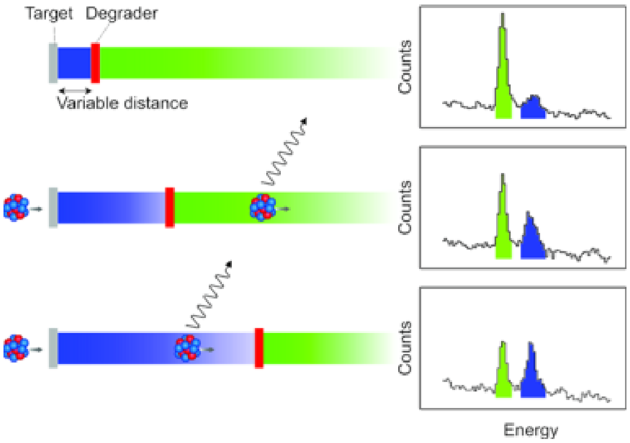

Figure 2.5: Illustration of the RDM lifetime technique
[17]

2.4 The GRET(IN)A Array

This section briefly describes the technical specifications of the GRET(IN)A detector array, including crystal size, segmentation, and arrangement.

GRETA, the **G**amma-**R**ay **E**nergy **T**racking **A**rray, is a yet-unbuilt set of detector modules that provide (nearly) full 4π coverage around a gamma-ray source or target. (Figure 2.6) The array is comprised of 30 separate detector modules, each containing 4 highly-segmented hexagonal HPGe crystals sharing a single cryostat. These modules are closely packed to form a spherical shell with 36 cm inner-diameter and 9 cm thickness. (An aluminum frame holds the modules in several concentric rings centered about and perpendicular to the beam axis.) Each crystal is segmented along 6 axial and 6 radial lines, giving

36 segments per crystal and 4,320 total segments across the array as a whole – each with separate readouts. The axial segments have varying thickness, with boundaries chosen to give approximately equal counts for 1.0 MeV gamma rays in the front 4 layers. Due to attenuation in the HPGe, the segments near the outer edge see far fewer photons per unit volume than those near the front face.

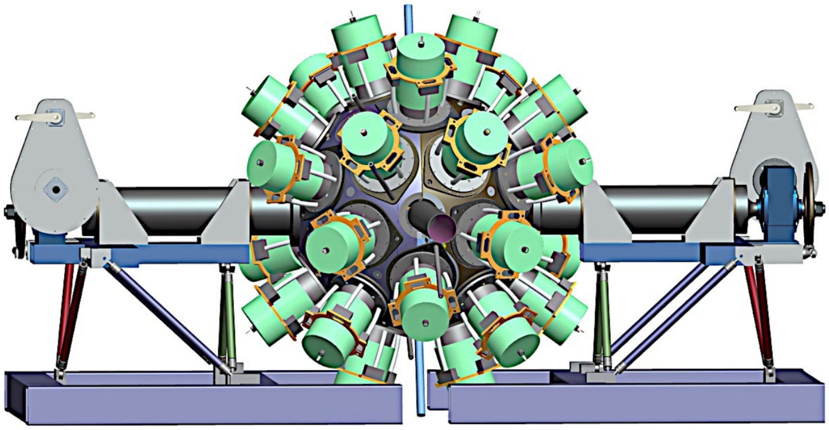

Figure 2.6: GRETA schematic
[5]

The design makes use of two distinct, tapered crystal shapes, necessary to achieve the close hexagonal packing of the HPGe shell. The shape and segmentation of the Type A and Type B can be seen in Figure 2.7. Both crystal types are 9 cm deep with 4 cm radii at their bases, but have different tapering. More technical details can be found in References [12] and [5].

GRETINA, or the **G**amma-**R**ay **E**nergy **T**racking **IN**-beam **A**rray, is a proof of concept of the larger GRETA array. The current iteration includes 8 of the 30 detector modules, covering approximately 1π of solid angle. Additional modules are currently under construction, but the work presented here uses a version of GRETINA with 7 modules. The incomplete nature of GRETINA therefore adds a geometric dependence to our results. As discussed in Section 2.2, the observed photon count rate is heavily influenced by Doppler focusing. While GRETINA was hosted at MSU in April 2013, the geometry clustered detectors near the exit beam pipe to maximize the detected countrate due to this focusing effect. (Figure 2.8) But there are other detector geometries available, such as populating the ring at 90°. This geometry yields the best imaging performance, for reasons that will be discussed in Sections 4.1 and 5.1.

In GRETA's lab-frame coordinate system, the $\hat{\boldsymbol{z}}$-axis points downstream along the beam axis. The $\hat{\boldsymbol{y}}$-axis points towards the floor – that is, in the same direction as gravity.

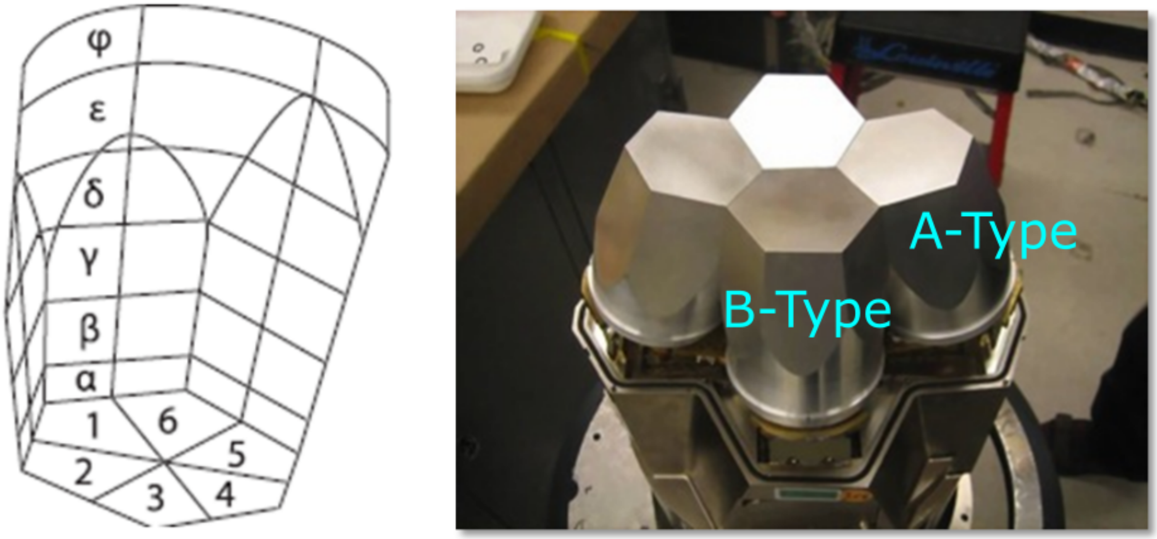

Figure 2.7: GRETINA crystal types

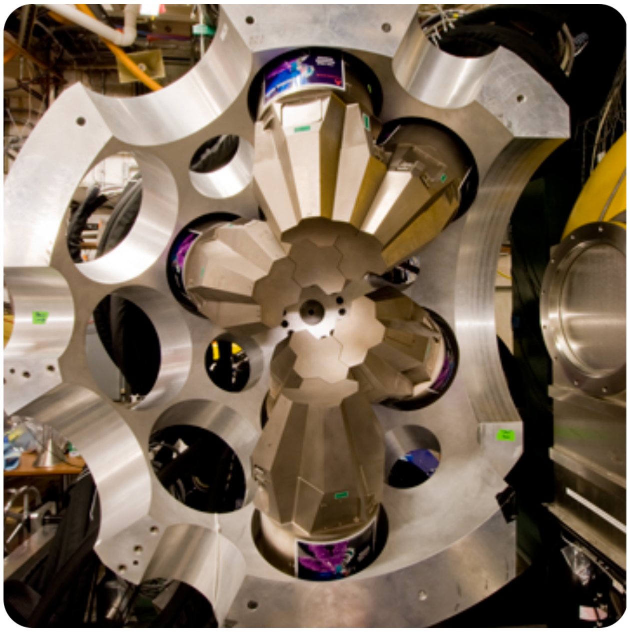

Figure 2.8: GRETINA with 7 modules populated (at MSU, Apr 2013) [26]

(This assumes of course that the beam runs parallel to the floor.) $\hat{\boldsymbol{x}}$ is a horizontal vector chosen such that $\hat{\boldsymbol{x}} \times \hat{\boldsymbol{y}} = \hat{\boldsymbol{z}}$. The origin is placed at the center of the inner cavity.

Note, however, that interaction coordinates are actually recorded in the "crystal frame". Each crystal places its origin in the center of its front face. The $\hat{\boldsymbol{z}}$-axis runs along the crystal's axial dimension, with $\hat{\boldsymbol{x}}$ and $\hat{\boldsymbol{y}}$ defining the radial plane. There exist separate transformation matrices for each crystal frame back into the larger GRETA lab frame.

2.5 Detectors and Signal Decomposition

GRETINA aims for 2.0 mm spatial resolution for the first hit in a photon track. This section describes how the array performs this localization, and goes into the many challenges facing the signal decomposition algorithm. A more complete discussion of GRETINA's signal decomposition can be found at Reference [28].

Traditionally, semiconductor detectors are used to gather information about the emission energy of radiation sources. GRETINA's HPGe detectors are finely segmented, so we can also measure the *locations* of interactions using pulse-shape analysis. This capability enables multiple applications that would not be possible from an energy measurement alone.

First, consider how signals are produced in a semi-conductor detector. When a photon interacts in HPGe, it deposits some amount of its energy at the site of the interaction. This elevates electrons to the conduction band and creates electron-hole pairs. Applying a bias voltage to the crystal's electrodes sets up an electric field which sweeps the charge carriers towards their respective electrodes. The charges induce a current (and corresponding voltage) in a coupled pre-amplifier as they move through the crystal. Solving for the exact time-dependent shape of this pulse is beyond the scope of this introduction, but is discussed in much greater detail in [13] and [20]. We must solve the Laplace Equation to calculate weighting potentials for a specific electrode geometry. From there, the Shockley-Ramo Theorem gives the instantaneous current (or charge) induced on an electrode by a charge q:

$$i(t) = q\boldsymbol{v(t)} \cdot \boldsymbol{E_0} \tag{2.21}$$

$$Q(t) = q\Delta\phi_0 \tag{2.22}$$

where $\boldsymbol{v}$ is the charge's velocity, $\boldsymbol{E_0} = -\nabla\phi_0$ is the "weighting field", and ϕ_0 is the weighting potential found by the Laplace Equation.

Figure 2.9 shows sample induced signals for two different interaction locations within a detector segment. [7] Note that signals are actually induced in both the primary segment that was struck, but also (to varying degrees) the other segments in the crystal. The integrated area of the current pulse in the struck segment is linearly-proportional to the total charge collected. Of course, this total charge is also proportional to the energy deposited by the photon in that segment, ΔE:

$$Q_{tot} = -qn = -q\Delta E/W \tag{2.23}$$

where n is the number of free carriers produced, W is the average energy required to create an electron-hole pair, and q is the charge on the respective carrier (-1.6 x 10^{-19} C for electrons). Charge-sensitive pre-amplifiers integrate each pulse, giving a signal whose height corresponds to the energy deposition. There is usually some loss of charge while the carriers move towards the electrodes, though, due to recombination with impurities in the crystal. Ideally, the loss is small enough such that the measured energy deposition does not change based on where an interaction took place.

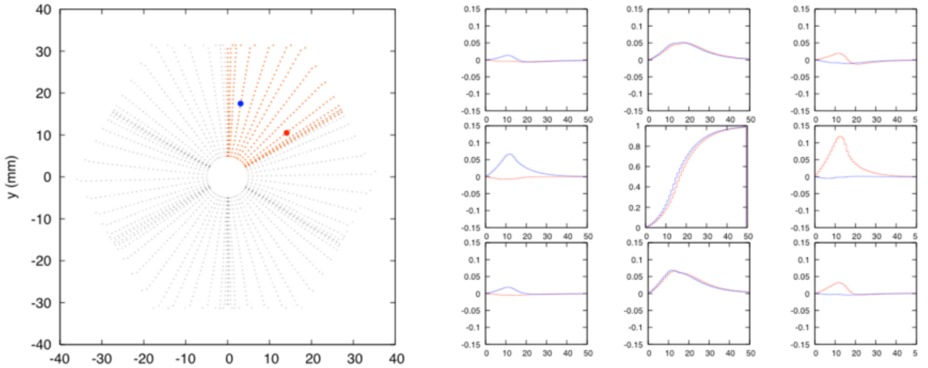

Images courtesy of Dr. Mario Cromaz, LBL

Figure 2.9: Illustration of signals produced in neighboring segments [7]

Obtaining position information requires a more complex signal-processing algorithm. As mentioned above, the Shockley-Ramo Theorem allows us to calculate the current (or charge) induced by electron-hole pairs drifting in a weighting potential. The shape of these pulses depends on where the charges are created, as well as their drift velocities. (Figure 2.9). Theoretically, we can then construct idealized “basis signals” for an energy deposition at any point in a crystal. A single basis “supersignal” is formed from the signals produced in each segment, not just the one that the photon struck. Note that the *shape* of a pulse is independent of the *magnitude* of energy deposited, assuming all charges from Equation 2.21 are created at a single point. This means we can normalize each basis set to the energy deposited in any given interaction. Then, by breaking each crystal into a grid of points and computing characteristic basis signals for each, finding the position of an interaction becomes a non-linear best-fit problem. We take the measured signal set and search for the closest match among the calculated basis signal sets.

In GRETINA, signal decomposition begins with a coarse 600-point grid search, followed by a fine 6000-point grid search around the point found by the first iteration. Theoretically, we could achieve further precision by interpolating *between* points, but that approach has not been implemented. There are many significant challenges to the decomposition algorithm which limit the effective position resolution more than the grid spacing does. [6]

It is relatively straightforward to match signals for single interactions. But when a photon interacts twice or more in the same detector, the output is a sum of overlapping signals. This is a complex problem – the overlapping signals are produced nearly simultaneously in the detector, and can only be distinguished by pulse shapes such as the rise time. (Again, the shape of the signal depends on where an energy deposition is made relative to an electrode.) To compare against the computed basis set, we must first separate the signals and determine where each begins in time. However, we do not know à priori the number of hits in any given segment (called the hit "multiplicity"). GRETINA's algorithm starts by *assuming* each trigger corresponds to two separate hits. The measured signals are fit against three independent parameters – the location of the first hit ($\boldsymbol{X_1}$), the location of the second hit ($\boldsymbol{X_2}$), and the ratio of the two hit energies, E_1/E_2. If the two best-fit interactions are located within a certain distance of each other (typically 6.0 mm), they are coalesced into a single combined interaction. However, by assuming a hit multiplicity of 2 like this, single physical hits will sometimes be erroneously decomposed into two unphysical hits. This is called "position bifurcation". The additional hits are typically low-energy (< 50 keV), serving as small adjustments to improve the quality of the fit between measured and basis signals. Conversely, two physical hits can also sometimes be regrouped into a single unphysical interaction. Both types of errors are highly detrimental to tracking and imaging. The addition or loss of hits from a track prevent it from being reliably sequenced with Compton kinematics (Section 3.2).

The accuracy of signal decomposition furthers depends upon the position sensitivity of the detector weighting field. As we can see from Figure 2.10 [24], ϕ_0 changes sharply near the segment boundaries, but much more gradually in the middle of the active volume. This makes it more difficult to resolve differences in signals away from the edges. Two hits of equal energy might be spaced a few mm apart but produce very similar signals. On top of this, differences in crystal impurities cause slight variations in charge velocity and trapping, and hence in the measured signals.

The detector electronics present other difficulties. "Differential cross-talk" is a problem that arises from tightly-packed wiring on the pre-amplifier outputs. Each crystal has 36 segments, each with their own pre-amplifier. Capacitance between wires and other electronics components induces noise that closely mimics the true induced signals in the crystal, both in shape and amplitude. The pre-amplifiers for each crystal also have slightly different capacitances, resulting in slightly different signal amplitudes for events of the same energy. This requires independent energy calibration for each crystal. Differences in trigger thresholds also cause some crystals to report significantly less counts than their neighbors. Trigger thresholds pose an especially difficult problem to tracking – many low-energy hits go unde-

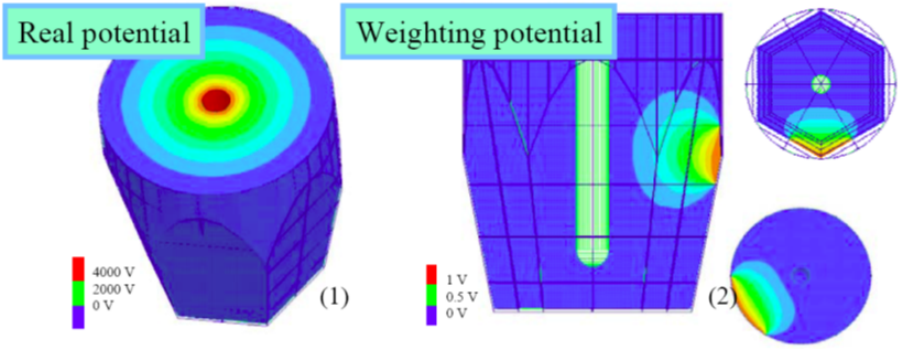

Figure 2.10: Illustration of weighting potentials in GRETINA crystal segments

tected. The loss of hits from this, and the hit multiplicity issues discussed above, is quite apparent. (Geant4 simulations of a stationary ^{60}Co source produce full-energy tracks with an average of 3.21 ± 0.12 hits each, while in real-world ^{60}Co calibration runs, the average track length is only 2.13 ± 0.02 hits.)

To correct for these effects, each crystal and its attendant electronics are characterized separately in a laborious process. There are two approaches – illustrated in Figure 2.11. Scanning and characterizing an entire crystal, millimeter by millimeter, can takes weeks to months.

To benchmark the end-to-end signal decomposition process, we can point a highly-collimated pencil beam of gamma rays through the detector, perpendicular to one of its crystal-frame planes (i.e. XY, XZ, or YZ). This creates a linear distribution of *detected* interaction points, each of which *most likely* corresponds to the first hit in a photon track. (The photons will scatter away from the central beam for all subsequent interactions.) By comparing the projected interaction locations from signal decomposition with the known location of the beam spot, we obtain the effective 2D detector position resolution in a given crystal plane. Fully characterizing the crystal requires scanning the beam across fine grids on multiple crystal planes.

It is possible to assay the position resolution in all three dimensions simultaneously with a different test. A pencil beam is again used, pointed axially down the detector. A finely-pixelated planar detector sits next to the GRETINA crystal, and both run on a synced clock. This second detector looks for photons that scatter in the GRETINA crystal at 90° and subsequently escape. Such photons will leave two coincident hits (one in either detector) with the same vertical position. The 90° scattering angle can be verified using Compton kinematics and the measured energy deposition in the GRETINA crystal. Between the beam spot location and the now-known vertical position, all three coordinates of the primary hit are known. This location can then be compared with the results from signal decomposition.

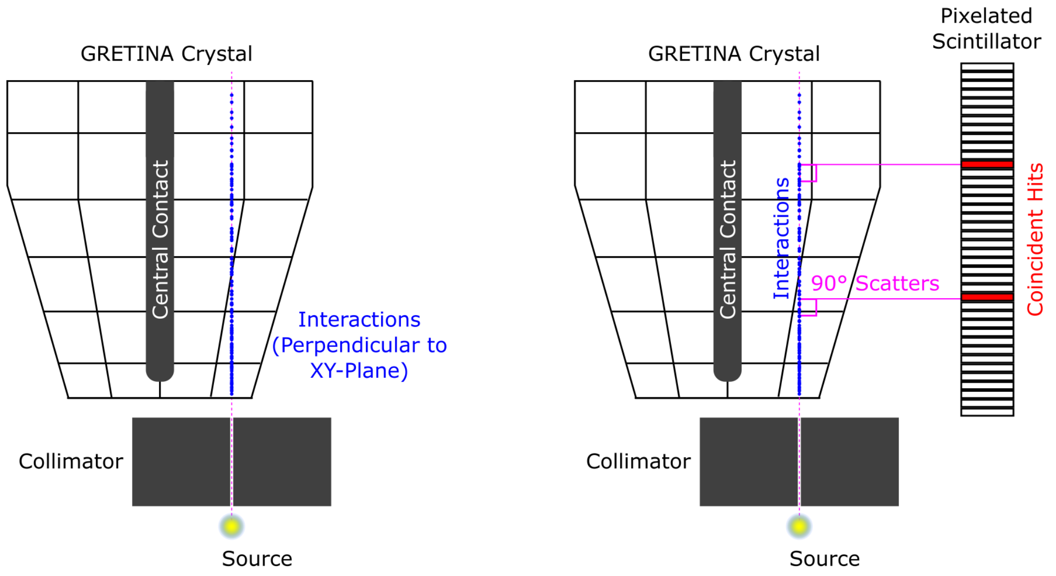

a.) 2D Characterization **b.) 3D Characterization**

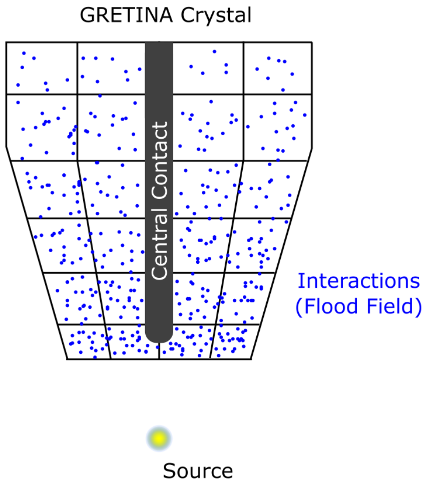

c.) Electronics Characterization

Figure 2.11: Detector characterization tests

Note that this method requires very long counting times – it is very rare for a gamma-ray to scatter 90° and then escape the GRETINA crystal, subsequently hitting the planar detector. As before, fully characterizing the detector requires scanning the beam across a grid of points, though only one plane need be scanned. Currently, GRETINA delivers close to 2.5 mm resolution for the *first* interaction in a photon track. [6]

The detector electronics are characterized indirectly through simulation. A ^{60}Co source is placed in front of the crystal, creating a flood-field of gamma-rays. The system saves the 3D position, energy deposition, and signal traces for each hit. These same hits are then entered into a simulation that calculates corresponding idealized signals from the Shockley-Ramo theorem. The idealized signals are compared with the measured traces, and used to fit 650+ independent electronics parameters (such as differential cross-talk coefficients). Once complete, the fit defines a transform from idealized signal traces to more realistic ones. This allows us to compute more realistic basis signals for any given hit position and energy deposition.

Yet for all these efforts, the search for the ideal signal match sometimes does not converge on a solution. In such cases, the hit is placed at the edge of a segment boundary. These edge effects are plainly visible when plotting interactions across a given crystal. Figure 2.12 shows reconstructed interaction positions in a few different crystals for a ^{60}Co flood-field measurement. We expect to see fairly uniform distributions, with a loosely exponential reduction in counts with increasing crystal depth. Some crystals are much worse than others; this highlights the individual differences in crystal properties and electronics, and the challenges that decomposition poses to Compton tracking and imaging. Note, however, that GRETINA is optimized for detection efficiency and spectroscopy, not imaging. More stringent fitting criteria would necessarily reduce the number of counts available for this.

GRETINA stores data in three main formats or "modes". Mode 3 contains raw signal traces, and requires by far the most storage space. Consider that a 100 MHz, 12-bit ADC can generate 150 MB of data every second, and each crystal segment has its own ADC. Storing 5.0 µs per trace requires 500 samples, multiplied by 36 to store traces for each segment in the crystal. One million events would thus require 27 GB.

These storage considerations make it advantageous to run the traces through signal processing in real time. The output is Mode 2 data, which contains coordinates and energy depositions for each interaction, as well as other miscellaneous information (like the χ^2 metric from the basis fit). In total, each record is 288 bytes and can store *up to* 16 interactions. (Each struck detector will produce its own 288-byte data block.) Note that photon tracks that cross crystal boundaries will produce multiple separate triggers. One million Mode 2 events require approximately 288 MB, a ˜94x reduction. Even still, longer runs will still produce datasets in the 10's of GB's.

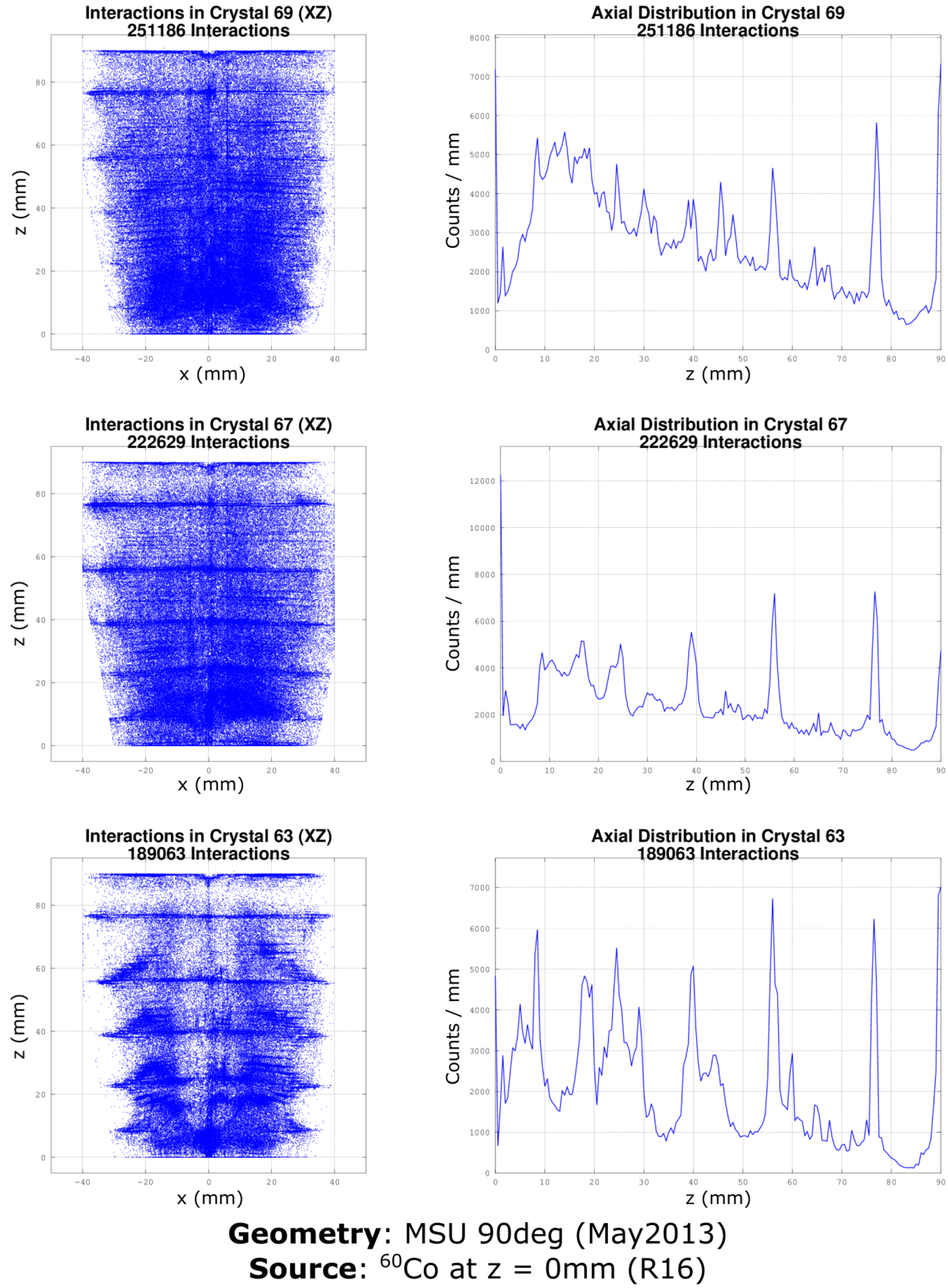

Figure 2.12: Reconstructed interaction positions in multiple crystals
Axial & XZ projections

Mode 1 requires the least space but the most processing power. A tracking algorithm combines events from a Mode 2 dataset to produce full, sequenced photon tracks. Because a 1.0 MeV photon track typically has fewer than 5-6 hits, a Mode 1 dataset can be 1/3 the size of its Mode 2 counterpart (which always reserves space for 16 hits per event).

Complete descriptions of GRETINA's data formats can be found at Reference [11].

2.6 Geant4 Simulations of GRETINA

This section describes the simulation tools I used for the majority of this study. The GRETINA team has developed a detailed model of the array for Geant4, called UCGretina. It allows us to simulate detected photon tracks from both stationary and moving sources. (Many thanks to C. Campbell, L. Riley, and H. Crawford for helping me with the simulation software.)

Much of my work rests on simulation results generated by a Geant4 model of the GRETINA detector. This detailed model was developed jointly by at LBL and MSU. [29] The Geant4 simulations allow us to generate "detected" photon tracks for a wide range of experimental scenarios. For example, we can specify the CM energies for photon emissions, their parent velocities and lifetimes, and the particular geometric loadout of the GRETINA detector modules.

I make use of a combination of stationary and moving sources throughout this study. In Section 3.2, I place a stationary 1.0 MeV photon point source at the origin to evaluate the effectiveness of Compton tracking. For Sections 4.1, 5.1, and 6.1, I use the same 1.0 MeV CM-frame photons, but emitted from nuclei traveling at various speeds in the lab-frame. For example, in one such test, the source nuclei have 859 ps proper lifetime. The source velocity is set at 0.3 ± 0.001 c, with a beam spread of $\sigma_\theta = 0.25°$ and spot size of $\sigma_{beam,x} = \sigma_{beam,y} =$ 0.25 mm. The target is placed at z = 0.0 mm. In all tests the geometry is kept constant; Figure 2.13 shows a stereographic projection of the detector modules as seen from the target position in the center of GRETINA's inner cavity.

The Geant4 model accounts for Compton profiles but otherwise follows basic Compton scattering kinematics. (Refer to Section 2.1.) The output photon tracks are pre-sequenced, and the detector is assumed to have perfect energy and position resolution. To simulate a more realistic detector scenario, I randomly reshuffle the tracks and apply uniform Gaussian noise to the position and energy at each hit. A typical run might have $\sigma_{xyz} = 3.0$ mm spatial resolution and $\sigma_E = 2.0$ keV energy resolution (standard deviation, not FWHM). The 2.0 keV energy resolution here is slightly worse than what was measured for ^{60}Co engineering runs performed on 12Jul2011. And as noted earlier, GRETINA yields roughly 2.5 mm resolution on the *first* hit in a track, but degrades for subsequent hits. I chose a uniform 3.0 mm resolution to better represent the track as a whole, which is obviously a simplification.

Because the simulations return the true emission locations for each photon, we are able to directly compare the true source distributions with the results from gamma-ray imaging. From this information we can deduce the “detector response”, $P(z, z_0)$, or the probability that a photon emitted at z_0 will be traced back to z from imaging. We also get picosecond timestamps for each interaction, which allows us to evaluate the results of Compton tracking directly. From the timestamps, we know the true sequence of events, and can compare this to the sequences given by the tracking algorithm.

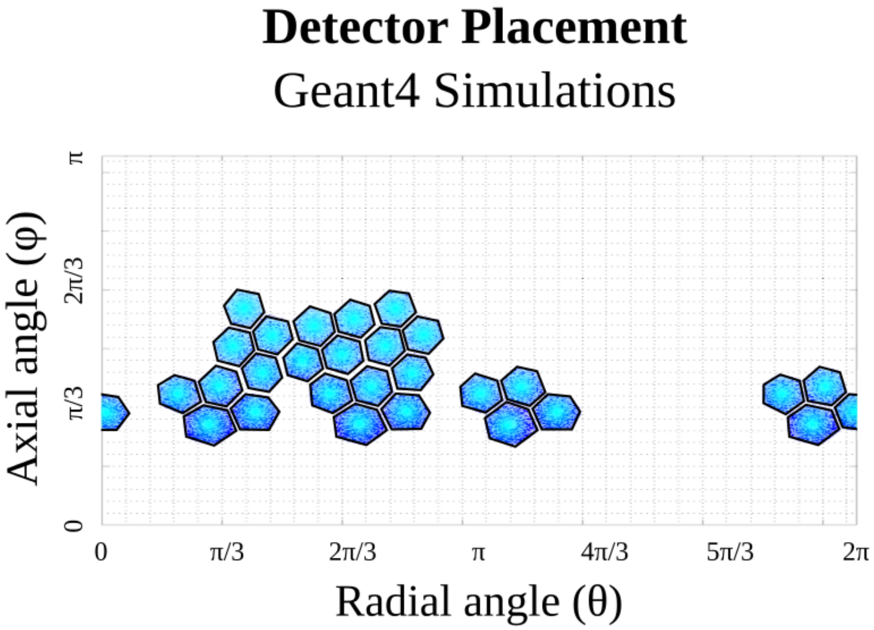

Figure 2.13: Stereographic projection of detector loadout in simulations

Chapter 3

Sequencing and Tracking

3.1 Interaction Grouping

Hits from a single photon track are often split across multiple crystals and segments, and therefore need to be regrouped to assemble the full track. This section discusses the motivations for doing so, as well as an algorithm that accomplishes the task. Events are first grouped by their timestamps, forming tracks from their combined photon hits. These composite tracks can be broken down again if groups of hits are more than several cm's apart.

As discussed in Section 2.2, GRETINA is primarily used for gamma-ray spectrscopy in beam experiments. The array combines excellent energy resolution and high efficiency. More importantly, its position sensitivity allows researchers to correct for Doppler shifts in emitted photon energy. Once we know the locations of both the emission point and the first hit in the detector, we can calculate the emission angle and translate the emission's lab-frame energy back into a true CM-frame photopeak energy:

$$E_{CM} = \gamma(1 - \beta \cos\theta) E_{Lab} \tag{3.1}$$

where βc is the relativistic speed of the parent nucleus in the lab frame, γ is the corresponding Lorentz factor, and θ is the emission angle relative to the parent's velocity (as measured in the lab frame).

One difficulty is determining which hit in a photon track is actually first. A 1.0 MeV photon traveling through HPGe has a mean-free-path of several centimeters, and this decreases exponentially for lower energies. Moving at the speed of light, the photon covers the distance between interactions in mere picoseconds (1.0 cm = 33 ps). Yet the electronics for the detector operate on timescale of 10's to 100's of nanoseconds. Because of this, the detector cannot distinguish the time sequence of interactions directly – all the photon hits, from the initial scatter to the final photoabsorption – appear to happen more or less simultaneously. Figure 3.1 illustrates the general sequencing problem, which will be discussed in much greater detail in Section 3.2.

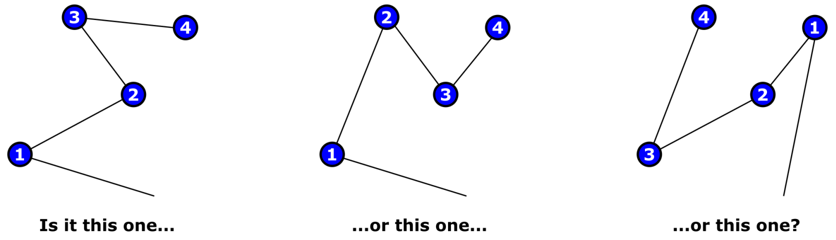

Figure 3.1: Illustration of the sequencing problem

The simplest approach is to assume that the first hit is the one with the highest energy deposition. Based on Compton kinematics and scattering cross-sections, this is valid much of the time, but is far from certain. For example, a 1.0 MeV photon that scatters at 30° deposits 208 keV in the detector. The scattered 792 keV photon has a 36% chance to make a greater deposit with the next hit.

Knowing the interaction sequence is useful for another reason – reduction of Compton background. Previous-generation gamma detector arrays use Compton suppression layers to reject partial-energy counts. In such setups, detector regions are surrounded by a thick shell of secondary detector material. If a photon scatters out of the sensitive HPGe region and subsequently interacts in the secondary layer, the array rejects the event as Compton background. This is crucial for accurate and precise measurement of photopeak energies, especially in complex spectra with multiple peaks. (Note that the peaks may overlap by tens of hundreds of keV due to the Doppler-shifting discussed above. This of course makes it difficult to distinguish Compton background from Doppler-shifted photopeak counts, hence the need for Compton suppression.) The downside to this approach is a drastic reduction in counts.

Thanks to GRETINA's position sensitivity, another option is available – one which can reject background without throwing out nearly so much data. Recall that each crystal in the GRETINA array is heavily segmented into 36 individual regions. These segments are relatively small (approx. 1.5 cm in depth), which means it's unlikely for a high-energy gamma-ray to deposit its full energy into any single segment. However, because the array is position-sensitive, it is possible to group interactions from nearby segments to re-form a photon track as a whole. We refer to this process as interaction "grouping" or "clustering".

The clustering process consists of several steps, illustrated in Figure 3.2. First, interactions are grouped by trigger time. GRETINA's electronics sample at 100 MHz, with all segments are synced to the same clock. When a photon scatters from one segment into another, GRETINA records separate events for each triggered segment. Note that an event can contain multiple hits when the photon interacts multiple times within a single crystal segment. Because the clocks are synced, we can then apply a timing gate to group ”simultaneous” events and hits. (As discussed in Section 2.5, determining multiple hits within a segment is very challenging work. This is currently one of the primary focuses of the signal decomposition team.)

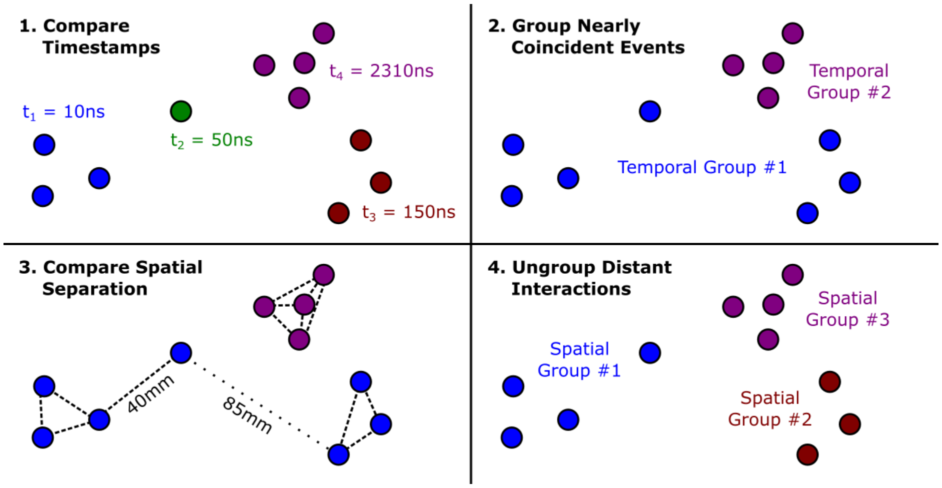

Figure 3.2: Illustration of interaction grouping

A secondary effect arises from this, though. Any coincident gamma rays will be falsely clumped together, producing a single track with a completely unphysical energy. To mitigate problems from such event pileup, a secondary layer of clustering can be applied to re-separate interactions by spatial proximity. Basically, if two interactions are more than several MFP’s apart, then they most likely do not belong to the same track. The software algorithm to accomplish the separation is somewhat complicated, but the end result is that temporally-clustered events are regrouped into a larger number of spatially-distinct tracks.

Implementations differ based on how “proximity” is defined. We can define it in a solid-angle sense, or by using the 3D lab coordinates of each photon hit. My analysis uses this second approach. I set a hard gate on the physical distance between points in a given group. As long as a point is close enough to *any* other point in the group, it remains in the group. However, my approach is somewhat simplified – it is based on absolute distance between points. This can incorrectly ungroup tracks for which the photon scattered from one detector into another by crossing GRETINA’s inner cavity. A more correct algorithm would use only the travel distance in the *HPGe*.

Optimal timing gates and spatial clustering thresholds can be obtained through energy spectra. We would expect interaction grouping to improve P/T ratios, because it assembles photopeak tracks from events that would otherwise have fallen into the Compton background.

Spatial re-separation recovers some of the photopeak counts that are erroneously grouped with other tracks.

Because the distance between hits depends on cross-section, spatial clustering should vary by photon energy. We used several different calibration sources to study this dependence:

Source	**Photon Energies**	**GRETINA Dataset**
^{152}Eu	121.8, 344.3, 1408.0 keV	MSU_May2013_90deg__R29
^{60}Co	1173.3 keV	MSU_May2013_90deg__R16
^{88}Y	898.0, 1836.1 keV	MSU_May2013_90deg__R44
^{22}Na	511 keV	MSU_May2013_90deg__R48

Table 3.1: Sources used to optimize clustering thresholds

Tables 3.2 and 3.3 list the P/T ratios we obtained for a range of temporal and spatial clustering thresholds. For the spatial threshold study, we kept the temporal threshold constant at 250 ns, while for the temporal threshold study, we kept the spatial threshold constant at 70.0 mm. (Peak counts were taken from 10-12 keV regions centered about the known photopeak energies. Background was defined by averaging counts over the regions immediately to the left and right of the peaks, and was then subtracted from the peak counts using a trapezoidal approximation.)

Figure 3.3 illustrates how the peak-to-total (P/T) ratio improves with both types of clustering. The improvements are modest but welcome – in this case, a 26% total improvement in P/T and 22% reduction in the Compton background for a ^{60}Co source. The effect of spatial clustering threshold on the P/T ratio is not as pronounced as we had expected, and generally, 300ns / 80mm thresholds will work well for all photons between 120keV and 1.8MeV. The bolded elements in the tables show where a P/T ratio reaches 99% of its maximum value for a given peak energy. One can see there are strong diminishing returns here. We also looked at signal-to-noise (SNR) ratios, defined as:

$$SNR = \frac{\text{[Gross Peak Counts] - [Background Counts]}}{\text{[Background Counts]}} \tag{3.2}$$

Background under each peak was estimated with a trapezoidal approximation, using average counts to either side of the peak. As we saw, the effects were fairly small for thresholds above 80mm. For example, the SNR for the 1836.1keV ^{88}Y peak showed a maximum of 68.8 at 40mm, but fell to 57.1 at 120mm. Therefore, we conclude that the data quality is not harmed by excessively large clustering thresholds.

A final note – interaction clustering only applies for *measured* Mode 2 data. (See Section 2.5.) However, the majority of our imaging work uses data simulated by a Geant4

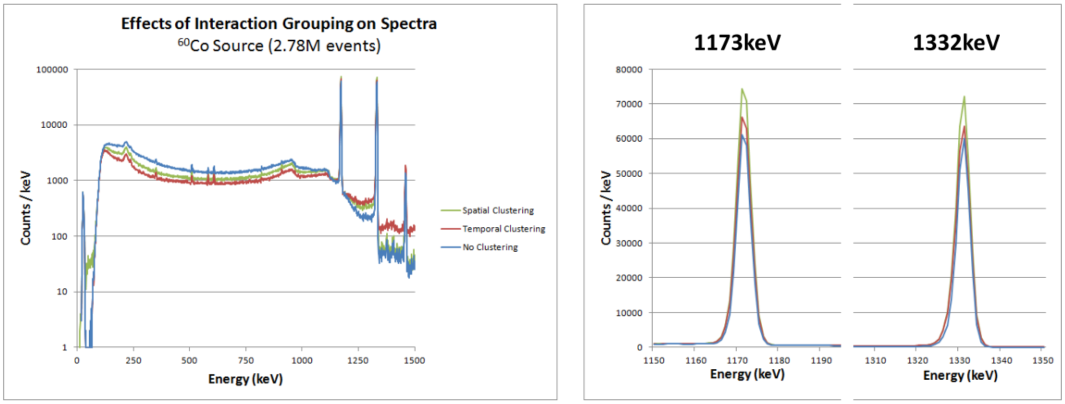

Figure 3.3: Energy spectra for no grouping, temporal grouping and temporal+spatial grouping

model of GRETINA. The simulations produce pre-sequenced photon tracks akin to Mode 1 data, and therefore do not require subsequent clustering.

3.2 Compton Sequencing

HPGe detectors are simply not fast enough to measure the sequence of hits in a photon track. Hits are generally a few centimeters apart, which translates to 100 picoseconds or less of travel time. Drift times in HPGe are on the order of 100's of nanoseconds, and GRETINA's 100MHz digitizer takes samples every 10 ns. However, by clever use of Compton kinematics and GRETINA's position sensitivity, it becomes possible to resequence the detected tracks. There are multiple ways to do this, using different algorithms and figures of merit to select the best order of interactions.

While we cannot measure the sequence directly, we can deduce it using the energy and position sensitivity of the detector. The technique, called Compton Tracking, is now widely used in astrophysics, nuclear security, and other scientific work. As discussed in Section 2.1, photons undergo three main types of interactions: pair production, photoabsorption, and Compton scattering. It's this last one that we take advantage of in Compton Tracking.

Consider a photon track with N_{hits} total interactions. For each of these interactions, we measure its 3D coordinates $\boldsymbol{X_j} = (x_j, y_j, z_j)$ and energy deposition ΔE_j. $\boldsymbol{X_1}$ and ΔE_1 correspond to the first hit in the detector, $\boldsymbol{X_2}$ and ΔE_2 with the second, and so on. The total track energy is defined as $E_{tot} = \sum \Delta E_j$. Note that below a photon energy of about 4.0 MeV, pair production is rare (refer to Figure 2.2 for a comparison of relative cross-sections in HPGe). For energies between 200 keV and 4.0 MeV, then, we can assume the track is composed of one or more Compton scatters, possibly ending with a photoabsorption.

Threshold	**121.8.1 keV**	**344.3 keV**	**511.0 keV**
10.0mm	0.03568 ± 0.00013	0.01408 ± 0.00008	0.01822 ± 0.00005
20.0mm	0.06614 ± 0.00017	0.03919 ± 0.00012	0.06001 ± 0.00009
30.0mm	0.09503 ± 0.00021	0.06328 ± 0.00017	0.10762 ± 0.00014
40.0mm	0.10613 ± 0.00023	0.07390 ± 0.00018	0.13327 ± 0.00016
50.0mm	0.10999 ± 0.00024	0.07865 ± 0.00019	0.14599 ± 0.00017
60.0mm	**0.11215 ± 0.00024**	0.08124 ± 0.00020	0.15319 ± 0.00018
70.0mm	0.11332 ± 0.00024	**0.08255 ± 0.00020**	0.15694 ± 0.00018
80.0mm	0.11388 ± 0.00024	0.08312 ± 0.00020	**0.15866 ± 0.00018**
90.0mm	0.11411 ± 0.00025	0.08337 ± 0.00020	0.15940 ± 0.00019
100.0mm	0.11414 ± 0.00025	0.08347 ± 0.00020	0.15967 ± 0.00019
110.0mm	0.11410 ± 0.00025	0.08349 ± 0.00020	0.15972 ± 0.00019
120.0mm	0.11403 ± 0.00025	0.08344 ± 0.00020	0.15963 ± 0.00019

Threshold	**898.0 keV**	**1173.3 keV**	**1332.5 keV**
10.0mm	0.00888 ± 0.00003	0.00858 ± 0.00004	0.00768 ± 0.00004
20.0mm	0.03443 ± 0.00007	0.03518 ± 0.00010	0.03179 ± 0.00009
30.0mm	0.06885 ± 0.00011	0.07328 ± 0.00017	0.06758 ± 0.00015
40.0mm	0.09160 ± 0.00013	0.09966 ± 0.00021	0.09265 ± 0.00019
50.0mm	0.10461 ± 0.00014	0.11545 ± 0.00023	0.10777 ± 0.00022
60.0mm	0.11236 ± 0.00015	0.12493 ± 0.00024	0.11691 ± 0.00023
70.0mm	0.11665 ± 0.00016	0.13029 ± 0.00025	0.12201 ± 0.00024
80.0mm	0.11883 ± 0.00016	0.13303 ± 0.00026	0.12465 ± 0.00024
90.0mm	**0.11988 ± 0.00016**	**0.13433 ± 0.00026**	**0.12589 ± 0.00024**
100.0mm	0.12033 ± 0.00016	0.13489 ± 0.00026	0.12644 ± 0.00025
110.0mm	0.12051 ± 0.00016	0.13517 ± 0.00026	0.12669 ± 0.00025
120.0mm	0.12055 ± 0.00016	0.13526 ± 0.00026	0.12677 ± 0.00025

Threshold	**1408.0 keV**	**1836.1 keV**
10.0mm	0.00253 ± 0.00002	0.00487 ± 0.00002
20.0mm	0.01018 ± 0.00005	0.02051 ± 0.00005
30.0mm	0.02118 ± 0.00009	0.04588 ± 0.00008
40.0mm	0.02848 ± 0.00010	0.06454 ± 0.00011
50.0mm	0.03273 ± 0.00011	0.07554 ± 0.00012
60.0mm	0.03525 ± 0.00012	0.08220 ± 0.00013
70.0mm	0.03668 ± 0.00012	0.08595 ± 0.00013
80.0mm	0.03746 ± 0.00013	0.08789 ± 0.00013
90.0mm	0.03788 ± 0.00013	**0.08885 ± 0.00013**
100.0mm	**0.03810 ± 0.00013**	0.08928 ± 0.00013
110.0mm	0.03823 ± 0.00013	0.08948 ± 0.00013
120.0mm	0.03833 ± 0.00013	0.08955 ± 0.00014

Table 3.2: P/T ratios vs. spatial grouping threshold
Temporal threshold set at 250ns

Threshold	**121.8.1 keV**	**344.3 keV**	**511.0 keV**
50ns	0.10762 ± 0.00024	0.07470 ± 0.00019	0.13428 ± 0.00016
100ns	0.11031 ± 0.00024	0.07820 ± 0.00019	0.14269 ± 0.00017
150ns	0.11160 ± 0.00025	0.07994 ± 0.00020	0.14770 ± 0.00017
200ns	**0.11290 ± 0.00025**	0.08178 ± 0.00020	0.15423 ± 0.00018
250ns	0.11332 ± 0.00025	0.08255 ± 0.00020	0.15694 ± 0.00018
300ns	0.11344 ± 0.00025	**0.08324 ± 0.00020**	**0.15897 ± 0.00018**
350ns	0.11341 ± 0.00025	0.08350 ± 0.00020	0.15958 ± 0.00018
300ns	0.11341 ± 0.00025	0.08373 ± 0.00020	0.16004 ± 0.00019
450ns	0.11343 ± 0.00025	0.08383 ± 0.00020	0.16023 ± 0.00019
500ns	0.11347 ± 0.00025	0.08393 ± 0.00020	0.16042 ± 0.00019

Threshold	**898.0 keV**	**1173.3 keV**	**1332.5 keV**
50ns	0.09379 ± 0.00013	0.10276 ± 0.00021	0.09577 ± 0.00020
100ns	0.10356 ± 0.00014	0.11471 ± 0.00023	0.10715 ± 0.00022
150ns	0.10881 ± 0.00015	0.12089 ± 0.00024	0.11298 ± 0.00022
200ns	0.11443 ± 0.00015	0.12752 ± 0.00025	0.11932 ± 0.00023
250ns	0.11665 ± 0.00016	0.13029 ± 0.00025	0.12201 ± 0.00024
300ns	**0.11825** ± 0.00016	**0.13230 ± 0.00025**	**0.12401 ± 0.00024**
350ns	0.11869 ± 0.00016	0.13282 ± 0.00026	0.12452 ± 0.00024
400ns	0.11901 ± 0.00016	0.13321 ± 0.00026	0.12488 ± 0.00024
450ns	0.11914 ± 0.00016	0.13336 ± 0.00026	0.12503 ± 0.00024
500ns	0.11925 ± 0.00016	0.13349 ± 0.00026	0.12514 ± 0.00024

Threshold	**1408.0 keV**	**1836.1 keV**
50ns	0.02944 ± 0.00011	0.06653 ± 0.00011
100ns	0.03269 ± 0.00012	0.07500 ± 0.00012
150ns	0.03427 ± 0.00012	0.07915 ± 0.00012
200ns	0.03598 ± 0.00012	0.08386 ± 0.00013
250ns	0.03668 ± 0.00012	0.08595 ± 0.00013
300ns	**0.03714 ± 0.00013**	0.08757 ± 0.00013
350ns	0.03724 ± 0.00013	**0.08800 ± 0.00013**
400ns	0.03732 ± 0.00013	0.08830 ± 0.00013
450ns	0.03736 ± 0.00013	0.08841 ± 0.00013
500ns	0.03739 ± 0.00013	0.08850 ± 0.00013

Table 3.3: P/T ratios vs. temporal grouping threshold
Spatial threshold set at 70mm

The kinematics of Compton scattering are well-defined. That is, if we know the incident photon energy and the scattering angle, we can deduce the outgoing photon energy and the energy imparted to the scattering electron. This energy deposition is measured by the detector and is equal to:

$$\Delta E = E_i - E_f = E_i - \frac{E_i}{1 + \frac{E_i}{m_e c^2}(1 - \cos\theta)} \tag{3.3}$$

Alternately, if we know the incident photon energy and the energy deposition for the scatter, we also know the cosine of the corresponding scattering angle:

$$\mu = \cos\theta = 1 - m_e c^2 \left(\frac{1}{E_f} - \frac{1}{E_i} \right) = 1 - \frac{m_e c^2 \Delta E}{E_i(E_i - \Delta E)} \tag{3.4}$$

Note that there is a one-to-one mapping of energy deposition to scattering angle – no two angles will yield the same energy deposition for the same initial photon energy. This fact is the crux of Compton sequencing.

So, suppose the first $N_{scatters} = N_{hits} - 1$ interactions are all Compton scattering. We don't necessarily know where the photon originated from, so we can't (yet) say anything about the original photon heading vector V_0, from the emission point to the first hit in the detector. However, the locations of subsequent hits are known. We can define the photon's incidence vector on $\boldsymbol{X_j}$ as $\boldsymbol{V_j} = \boldsymbol{X_j} - \boldsymbol{X_{j-1}}$. If $\boldsymbol{X_j}$ is not the last hit in the track, we can further define the outgoing photon vector at $\boldsymbol{X_j}$ as $\boldsymbol{V_{j+1}} = \boldsymbol{X_{j+1}} - \boldsymbol{X_j}$. Point $\boldsymbol{X_j}$ represents a Compton scatter, and the *measured* scattering angle is simply equal to:

$$\mu_{meas,j} = \frac{\boldsymbol{V_j} \cdot \boldsymbol{V_{j+1}}}{\|\boldsymbol{V_{j+1}}\| \|\boldsymbol{V_j}\|}. \tag{3.5}$$

In other words, $\mu_{meas,j}$ is the angle between the incident and outgoing photon directions as given by the coordinates of points $\boldsymbol{X_{j-1}}$ to $\boldsymbol{X_{j+1}}$. This gives us a direct comparison to the theoretical value given by the incident photon energy and energy deposition at $\boldsymbol{V_j}$. Note that because a scattering interaction is anchored by three points, this approach necessarily only applies to tracks with three or more interactions. For a track of length N_{hits}, we only have $N_{hits} - 2$ anchored scatterings for which the comparison to theory can be made.

Of course, we don't know the track sequence á priori. But using the combination of theoretical Compton kinematics and the measured coordinates and energy depositions, we can decide which sequences would not make physical sense. Essentially, we can simply try all *possible* sequences and find the one that best matches the Compton formula. This means evaluating a Figure of Merit (FoM) for each permutation of the track sequence.

This approach can become very computationally-intensive, because the number of possible sequences scales factorially with the length of the track. An 8-hit track (5,040 permutations) takes 210 times longer to sequence than a 4-hit track (24 permutations). However, 8-hit tracks are also fairly rare at the energies where Compton tracking applies (below 4.0 MeV). For example, they account for less than 1.4% of all full-energy tracks at 1.0 MeV. The real worry is if interaction grouping registers a track with 12 or more hits, which will effectively halt a sequencing algorithm. For this reason, it is wise to limit the length of tracks. In this study I have limited the scope to tracks with 6 or fewer interactions.

There are multiple figures of merit we can use to deduce the sequence of interactions. One common FoM compares the cosines of the measured and theoretical scattering angles (Eq. 3.5 and Eq. 3.4, respectively) for each scattering in the track:

$$FoM = \frac{1}{(N_{scatters} - 1)} \sum_{j=2}^{N_{hits}-1} (\mu_{meas,j} - \mu_{calc,j})^2 \tag{3.6}$$

This figure of merit is unitless and normalized to the number of compared scattering points. $\mu_{calc,j}$ is the angle predicted by the incident photon energy and measured energy deposition (Eq. 3.5), and depends on $E_{i,j-1}$, the incident photon energy at $\boldsymbol{X_j}$. $E_{i,j-1}$ is calculated from the total energy of the track, minus all previous energy depositions:

$$E_{i,j-1} = E_{tot} - \sum_{k=1}^{k=j-1} \Delta E_k = \sum_{k=j}^{k=N_{hits}} \Delta E_k \tag{3.7}$$

This is where incorrect sequences get thrown out. Suppose we are testing a 4-hit track sequence with hits #2 and #3 swapped. (Figure 3.4) In this case, the incident headings on $\boldsymbol{X_2}$ and $\boldsymbol{X_3}$ are both incorrect. This means $E_2 = \Delta E_2 + \Delta E_4$ instead of the correct $E_2 = \Delta E_3 + \Delta E_4$, and the calculated scattering angles at $\boldsymbol{X_2}$ and $\boldsymbol{X_3}$ will reflect the inaccuracy.

We can define a second FoM using the energy depositions instead of scattering angle:

$$FoM = \frac{1}{(N_{scatters} - 1)} \sum_{j=2}^{N_{hits}-1} \frac{(\Delta E_{meas,j} - \Delta E_{calc,j})^2}{\Delta E_{meas,j}^2} \tag{3.8}$$

Here, $\Delta E_{meas,j}$ is the measured energy deposition at $\boldsymbol{X_j}$. $\Delta E_{calc,j}$ is the measured energy deposition at $\boldsymbol{X_j}$. To obtain a unitless figure of merit, the observed difference in measured vs. calculated energy depositions is divided by $E_{meas,j}$. Normalizing in this fashion weights each scatter equally, regardless of the magnitude of the energy deposition. However, in most cases we want to prioritize accuracy on the first (and sometimes second) interactions. As noted earlier, these early interactions tend to have much higher energy depositions than subsequent hits in the track. Normalizing by total track energy weights these high-energy scatters over the small-energy ones near the end of a track:

$$FoM = \frac{1}{E_{total}^2 (N_{scatters} - 1)} \sum_{j=2}^{N_{hits}-1} (\Delta E_{meas,j} - \Delta E_{calc,j})^2 \tag{3.9}$$

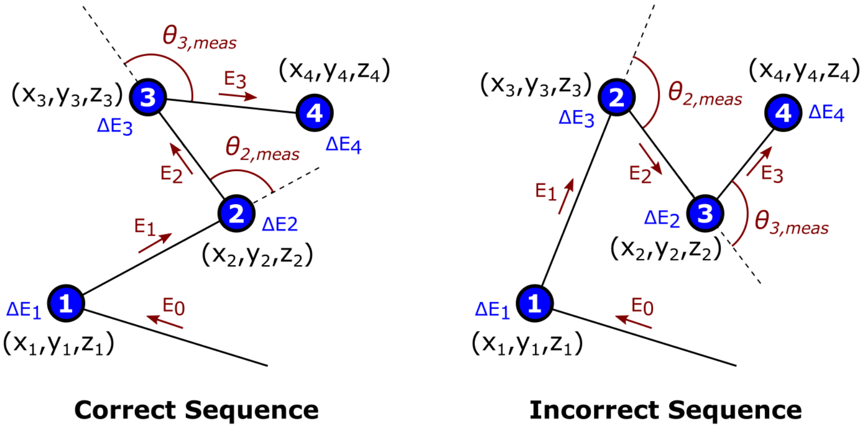

Figure 3.4: Evaluating two different sequences

This is the normalization and figure of merit used for sequencing in this study. However, there certainly may be better choices. An ideal figure-of-merit would provide better discrimination between Compton background and photopeaks counts. We might also choose a different FoM based on the reliability of sequencing it provides.

Note that other sequencing methods are sometimes used. Appendix A.3 gives a brief discussion of some of them.

3.3 Sequencing Efficiency and Effectiveness

The ability to use Compton kinematics for sequencing depends heavily on photon energy. Higher energies give longer tracks and hence more data to work with, but also more potential sequences from which to choose. Below a certain energy, Compton sequencing cannot be used because too many tracks will have one or two hits. We can map the fraction of sequenceable tracks as a function of energy, and determine the probability of a critical sequencing error based on detector resolution and track length.

While these sequencing methods may sound straightforward in theory, in practice they are not full-proof. Real detectors have finite position and energy resolution. This means that the measured interaction coordinates $\boldsymbol{X_j}$ are only approximations of the true locations. Therefore, the measured scattering angles we compute from these positions are themselves uncertain, and the FoMs calculated in Equation 3.9 will be nonzero – even for the *correct* sequence of hits.

On top of that, even with perfect detector resolution, basic Compton kinematics are also only an approximation. As discussed in Section 2.1, electrons in real materials are not at rest in a vacuum. They have characteristic binding energies that give them nonzero momentum prior to an interaction with a photon. This extra momentum can cause a scattered photon to have significantly different energy from that predicted by the Compton formula. Because the electron momentum is inherently stochastic in nature, a deterministic calculation is impossible – we can never be completely certain of any sequence deduced from kinematics. This is especially true of the two Maximum-Likelihood methods discussed, which are based on probabilities in the first place. In other words, there is always some probability that a track has been mis-sequenced.

The severity of the problem depends on the goal of sequencing. Mis-sequencing errors cause serious problems in gamma-ray imaging. (A more detailed discussion of this will follow in Sections 4.1 and 5.1.) Doppler-shift corrections are also affected – a mis-sequenced track changes the calculated emission angle. Consider – hits in a 1.0 MeV track will typically be a few cm apart. Therefore, a mis-sequenced interaction will result in an angular deviation of 10° or less with GRETINA's 18 cm inner radius. The Doppler correction (from Equation 3.1) for a 90° emission from a nucleus moving at 0.3c is $E_{CM}/E_{Lab} = 0.962$. The same correction for a 80° emission is $E_{CM}/E_{Lab} = 1.01$, i.e. a difference of 4.8%. In this particular case, the corrected photon energy is nearly 50 keV off.

As discussed, if the source location is unknown, then Compton sequencing requires three or more photon hits to work. The more hits in a photon track, the more scattering points we'll have to compare to kinematics. Intuitively, this should allow us to sequence longer tracks with more certainty. However, longer tracks also have more potential ways to be mis-sequenced. (All things being equal, the probability of guessing a 6-hit sequence correctly is only 0.14%, versus 17% for a 3-hit track.) Longer tracks also have more low-energy hits, which are disproportionately affected by the detector's finite position and energy resolution. While we might be able to sequence the first few interactions reliably, the tail end of a photon track is more difficult.

It's important to note that the percentage of sequenceable tracks depends heavily on photon energy. Low-energy photons tend to leave shorter tracks with fewer scatters. On the other hand, high-energy photons have a lower probability of full-energy deposition in the detector. Because we assume full-energy deposition in sequencing, these Compton background counts may not sequence properly.

To study the effects of finite detector resolution on sequencing, I used the GRETINA Geant4 model (Section 2.6) to generate pre-sequenced photon tracks from a stationary 1.0MeV point source. Only the *full-energy* tracks were accepted for processing (±6keV), or approximately 39% of the 100K simulated tracks. Figure 3.5 shows the breakdown of the simulated tracks by length and energy. Note that a 1.0 MeV photon typically must scatter 3-4 times before being of low enough energy for photoabsorption. A large majority of the 1- and 2-hit tracks correspond to partial-energy detections (shown in green). The full-energy detections become more common above three hits. However, the tracks we can sequence with our Compton tracking algorithm account for only 29.9% of the total. (Recall that we disregard tracks with 7 or more hits for computational efficiency.) Including 2-hit tracks increases this number to 34.4%, though such tracks cannot be sequenced through tracking (unless the source location is known).

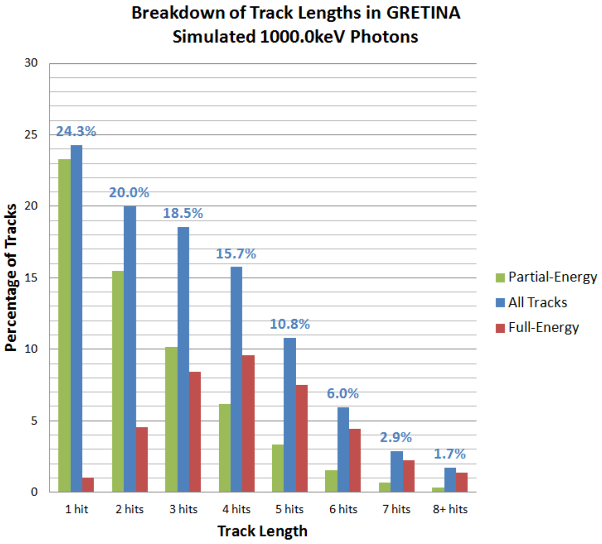

Figure 3.5: Track breakdown by length
(Relative errors are all within 0.15%)

To better reflect the response of a real detector, I randomly re-ordered the interactions in each track, then added *uniform* Gaussian noise to the position and energy of each hit. The intentionally randomized tracks were then run through the sequencing algorithm. I compared the known tracks with the Compton-sequenced versions to see how frequently errors arose. Tables 3.4 and 3.5 show the mis-sequencing probability as functions of simulated detector resolution for tracks with 2 to 6 hits. Table 3.6 gives similar numbers for a typical detector as a function of the photon track length. (For these runs, detector resolution was kept constant with standard deviations of $\sigma_{xyz} = 3.0$ mm and $\sigma_E = 2.0$keV for position and energy resolution, respectively.) Note that we're generally most interested in the first interaction, because this is what is used for Doppler-shift corrections. Additionally, the second interaction comes into play when using the sequence for Compton imaging. All 3 tables give separate probabilities for mis-sequencing the first hit alone, the first and second hits together, and for the track as a whole.

The results of Table 3.6 suggest some important points. First, given 3.0 mm position- and 2.0 keV energy-resolution in the detector, nearly half of all full-energy tracks – 46% – show an error in the first two hits. This has serious repercussions for Compton imaging – without some kind of filter, every other track will contribute noise to the final image. The situation is somewhat improved for Doppler-shift correction and imaging (Section 5.1), both of which only require the first hit in a track. Still, a full 1/3rd of tracks yield incorrect results here. Note that the situation is greatly improved for 2-hit tracks, which are sequenced by assuming the higher-energy hit came first. (The ratio of correctly-sequenced to mis-sequenced 2-hit tracks is 5.5, whereas for 4-hit tracks it is 0.78.) Because of this, Compton sequencing is ignored entirely in some implementations. If all we care about is getting the first interaction right, it can be advantageous to assume it's simply the highest-energy hit.

While a photon's emission point is an unknown in lifetime experiments, using stationary point sources allows us to benchmark the sequencing algorithm further. Here, the emission point is known, which establishes the initial photon heading. This lets us to now use the first scatter in each track for sequencing. In the Geant4 simulations discussed above, I placed the 1.0 MeV source at the origin. For a detector with perfect position and energy resolution, I found that a mere 1.17 ± 0.06% of 3- to 6-hit tracks had an incorrect vertex after Compton sequencing. Additionally, only 3.81 ± 0.12% had errors affecting Compton imaging while a full 93.88 ± 0.78% were correctly sequenced in their entirety. This is certainly encouraging.

Position Resolution	**Error in Hit 1**	**Error in Hits 1-2**	**Error in Any Hit**	**Correctly Sequenced**
0.0 mm	10.15 ± 0.18 %	13.07 ± 0.21 %	14.68 ± 0.22 %	85.32 ± 0.68 %
0.25 mm	13.64 ± 0.21 %	18.00 ± 0.25 %	20.78 ± 0.27 %	79.22 ± 0.64 %
0.50 mm	17.28 ± 0.24 %	23.06 ± 0.29 %	26.86 ± 0.31 %	73.14 ± 0.61 %
0.75 mm	20.32 ± 0.27 %	27.31 ± 0.32 %	31.83 ± 0.35 %	68.17 ± 0.58 %
1.0 mm	22.89 ± 0.29 %	30.87 ± 0.34 %	35.96 ± 0.38 %	64.04 ± 0.55 %
1.5 mm	26.89 ± 0.31 %	36.70 ± 0.38 %	42.37 ± 0.42 %	57.63 ± 0.51 %
2.0 mm	29.75 ± 0.33 %	40.66 ± 0.41 %	46.83 ± 0.45 %	53.17 ± 0.49 %
2.5 mm	31.78 ± 0.35 %	43.60 ± 0.43 %	50.07 ± 0.47 %	49.93 ± 0.47 %
3.0 mm	33.54 ± 0.36 %	45.98 ± 0.44 %	52.76 ± 0.48 %	47.24 ± 0.45 %
4.0 mm	36.35 ± 0.38 %	49.85 ± 0.47 %	56.70 ± 0.51 %	43.30 ± 0.42 %
5.0 mm	38.18 ± 0.39 %	52.53 ± 0.48 %	59.32 ± 0.52 %	40.68 ± 0.41 %
7.5 mm	41.05 ± 0.41 %	56.51 ± 0.51 %	63.21 ± 0.55 %	36.79 ± 0.38 %
10.0 mm	42.63 ± 0.42 %	58.98 ± 0.52 %	65.55 ± 0.56 %	34.45 ± 0.37 %

Table 3.4: Probability of sequencing errors vs. position resolution
1000.0 ± 6.0 keV track energy, 2.0 keV energy resolution

Not having that first scattering point available for FoM calculations may be the largest issue with our approach. As discussed earlier, the first hit usually corresponds to the highest energy deposition. This also means that the first hit is also likely to contribute the largest amount to the sequencing FoM. At high photon energies, small deviations in scattering angle can yield 10's of keV difference in energy deposition. Not so with lower-energy photons. Since

Position Resolution	**Error in Hit 1**	**Error in Hits 1-2**	**Error in Any Hit**	**Correctly Sequenced**
0.0 keV	33.73 ± 0.36 %	45.93 ± 0.44 %	52.59 ± 0.48 %	47.41 ± 0.45 %
1.0 keV	33.60 ± 0.36 %	45.95 ± 0.44 %	52.72 ± 0.48 %	47.28 ± 0.45 %
2.5 keV	33.59 ± 0.36 %	46.04 ± 0.44 %	52.81 ± 0.48 %	47.18 ± 0.45 %
5.0 keV	33.67 ± 0.36 %	46.28 ± 0.44 %	53.11 ± 0.49 %	46.90 ± 0.45 %
7.5 keV	34.07 ± 0.36 %	46.72 ± 0.45 %	53.67 ± 0.49 %	46.33 ± 0.44 %
10.0 keV	34.60 ± 0.37 %	47.44 ± 0.45 %	54.47 ± 0.49 %	45.53 ± 0.44 %

Table 3.5: Probability of sequencing errors vs. energy resolution
1000.0 ± 6.0 keV track energy, 3.0 mm position resolution

Track Length	**Error in Hit 1**	**Error in Hits 1-2**	**Error in Any Hit**	**Correctly Sequenced**
2 hits	15.31 ± 0.62 %	15.31 ± 0.62 %	15.31 ± 0.62 %	84.69 ± 1.85 %
3 hits	28.18 ± 0.66 %	38.88 ± 0.80 %	38.88 ± 0.80 %	61.12 ± 1.08 %
4 hits	38.03 ± 0.74 %	52.56 ± 0.91 %	56.20 ± 0.96 %	43.80 ± 0.81 %
5 hits	40.67 ± 0.87 %	56.89 ± 1.09 %	70.20 ± 1.26 %	29.80 ± 0.72 %
6 hits	40.68 ± 1.14 %	58.34 ± 1.45 %	80.79 ± 1.82 %	19.21 ± 0.72 %
(All)	33.54 ± 0.36 %	45.98 ± 0.44 %	52.76 ± 0.48 %	47.24 ± 0.45 %

Table 3.6: Probability of sequencing errors vs. track length
1000.0 ± 6.0 keV track energy, (3.0 mm, 2.0 keV) detector resolution

our FoM is normalized to the *total* track energy, this means sequencing mistakes for low-energy hits are less noticeable in the final FoM. This is by design, since we want to priotize getting the first (i.e. higher-energy) hits right.

Table 3.7 shows a sample mis-sequenced track. Note that sequencing on this 6-hit track gave an incorrect location for the first interaction, despite perfect detector position and energy resolution. This rare occurrence would have clearly been avoided if we had been able to use our á priori knowledge of the source location. The FoM contribution from the first hit in the computed sequence is enormous relative to the rest of the FoM contributions. The remaining hits happened to be arranged in such a way to allow the subsequent hits to still match Compton kinematics. This may not be as unbelievable as it appears at first glance – it can take fairly large deviations in angle to skew the energy deposition more than a few keV. Consider that the measured scattering angle is calculated thus:

$$\theta_{meas,i} = \cos^{-1}(\boldsymbol{\hat{V}_{i-1}} \cdot \boldsymbol{\hat{V}_i}) \tag{3.10}$$

$$\boldsymbol{\hat{V}_i} = (\boldsymbol{X_{i+1}} - \boldsymbol{X_i})/|\boldsymbol{X_{i+1}} - \boldsymbol{X_i}| \tag{3.11}$$

Again, $\boldsymbol{\hat{X}_0}$ is the photon emission point and $\boldsymbol{\hat{X}_1}$ is the first hit in the detector. We find $\theta_{meas,1} = 2.285$ radians at $\boldsymbol{\hat{X}_1}$ in the true sequence, while the angle calculated by Compton kinematics is $\theta_{calc,1} = 2.204$ radians. This is a difference of 3.51%, yet the corresponding difference in measured vs. calculated energy deposition is only -0.93% (757.012 keV vs 764.042 keV). Even a 10.00% difference in the initial scattering angle would only produce a 3.00% in energy deposition (779.726 keV vs. 764.042 keV).

I explored a few modifications to the FoM definition. Table 3.8 summarizes the results for four different FoMs:

$$FoM_1 = \sum(\mu_{meas,i} - \mu_{calc,i})^2/N_{scatters} \tag{3.12}$$

$$FoM_2 = \sum(\Delta E_{meas,i} - \Delta E_{calc,i})^2/(N_{scatters}E_{total}^2) \tag{3.13}$$

$$FoM_3 = \sum(\Delta E_{meas,i} - \Delta E_{calc,i})^2/(N_{scatters}\Delta E_i^2) \tag{3.14}$$

$$FoM_4 = \sum(\Delta E_{meas,i} - \Delta E_{calc,i})^2/(N_{scatters}E_{total}^2), \text{ with a guess for } \boldsymbol{X_0} \tag{3.15}$$

FoMs 1, 2, and 3 used hits 2 to $N_{hits} - 1$, while FoM 4 took all hits 1 to $N_{hits} - 1$. I found that comparing energy depositions and normalizing to the total track energy (FoM 2) provides better results than comparing cosines of scattering angles (FoM 1). Normalizing to *total* track energy is also better than normalizing to the measured energy deposition at each hit (FoM 3). FoM 4 did offer some improvement for (3.0 mm, 2.0 keV) detector resolution. For this test, I placed the guess for $\boldsymbol{X_0}$ at (0.0 mm, 0.0 mm, 60.0 mm), or 60.0 mm away from the true source location. I did not study this approach in great detail, although the performance numbers in Table 3.8 are promising. The results improved markedly as the guess for $\boldsymbol{X_0}$ came closer to the true source location at (0.0 mm, 0.0 mm, 0.0 mm), approaching near-100% accuracy when the guess was spot-on. However, in lifetime measurements the emission

Hit	**X**	**Y**	**Z**	$\mathbf{E_i}$	μ_{meas}	$\Delta\mathbf{E_{meas}}$	$\Delta\mathbf{E_{calc}}$	**FoM**
True Sequence								
(Src)	0.000	0.000	0.000	–	–	–	–	–
1	-77.921	170.052	103.876	1000.000	-0.654642	757.012	764.042	**(9.885E-06)**
2	-77.193	168.620	96.225	242.988	0.855815	34.633	15.591	7.252E-05
3	-81.571	165.890	87.314	208.355	0.727474	21.966	20.837	2.549E-07
4	-81.686	166.218	86.609	186.389	-0.637781	82.652	69.705	3.352E-05
5	-81.948	166.648	87.717	103.737	0.651133	8.124	6.861	3.189E-07
6	-81.976	166.710	87.737	95.613	–	95.615	–	–
Computed Sequence								
(Src)	0.000	0.000	0.000	–	–	–	–	–
1	-77.193	168.620	96.225	1000.000	0.632993	34.633	418.000	**(2.939E-02)**
2	-77.921	170.052	103.876	965.367	-0.944982	757.012	758.845	6.722E-07
3	-81.948	166.648	87.717	208.355	0.885275	8.124	9.311	2.818E-07
4	-81.686	166.218	86.609	200.231	-0.637860	82.652	78.272	3.835E-06
5	-81.571	165.890	87.314	117.579	-0.021635	21.966	22.380	3.422E-08
6	-81.976	166.710	87.737	95.613	–	95.615	–	–

Table 3.7: Sample Compton-Sequenced Photon Track (1000.0keV, 6 hits)
All positions in mm and energies in keV.

FoM Type	**Error in Hit 1**	**Error in Hits 1-2**	**Error in Any Hit**	**Correctly Sequenced**
Type 1	40.22 ± 0.43 %	47.91 ± 0.49 %	52.25 ± 0.52 %	47.75 ± 0.49 %
Type 2	33.28 ± 0.38 %	45.11 ± 0.47 %	51.27 ± 0.51 %	48.73 ± 0.49 %
Type 3	56.16 ± 0.54 %	62.47 ± 0.58 %	67.91 ± 0.62 %	32.09 ± 0.38 %
Type 4	13.79 ± 0.23 %	34.10 ± 0.39 %	43.44 ± 0.46 %	56.56 ± 0.54 %

Table 3.8: Performance of multiple FoM definitions

	Error in Hit 1	**Error in Hits 1-2**	**Error in Any Hit**	**Correctly Sequenced**
Full-Energy	33.54 ± 0.36 %	45.98 ± 0.44 %	52.76 ± 0.48 %	47.24 ± 0.45 %
Partial-Energy	47.31 ± 0.44 %	58.81 ± 0.50 %	61.13 ± 0.52 %	38.87 ± 0.38 %

Table 3.9: Probability of sequencing errors for full-energy vs. partial-energy tracks
1000.0 ± 6.0 keV track energy, (3.0 mm, 2.0 keV) detector resolution

points can be spread over a wide range (100 mm or more). This FoM type can actually degrade sequencing performance if the guess is too far off, so I chose to use FoM 3 as the working definition for all subsequent work.

A final observation about sequencing – the figure-of-merit *ought* to be correlated with whether or not a track deposits its full energy in the detector. We'd expect partial energy tracks to match Compton kinematics relatively poorly and thus have a worse FoM than a full-energy track. Because of this, the figure-of-merit is a potential way to further reduce background counts, thereby improving P/T ratios for imaging or spectroscopy purposes. Receiver-operating characteristic (ROC) curves are a standard method for evaluating the effectiveness of a given filter. [37] We are interested in the system sensitivity (true positive rate) and specificity (true negative rate) as functions of a maximum FoM limit. In this case, tracks were accepted if their sequencing FoM is under a given threshold. A true positive is a full-energy event for which the first two hits are sequenced correctly; a true negative is any partial-energy or incorrectly-sequenced track. Unfortunately, as Figure 3.6 shows, the method's sensitivity is not very high for realistic values of detector position resolution. The ROC curve for (3.0 mm, 2.0 keV) resolution is barely above the "random guess" line. This is consistent with Table 3.9, which shows that roughly 45% of *full-energy* tracks contain sequencing errors in the first two hits. Tightening the sequencing FoM limit greatly reduces the number of accepted counts, but has little affect on the sensitivity. A different choice of FoM might yield more promising results.

There are a number of metrics we could use to select an optimal filtering parameter. The Youden index is one such metric, and is given by the sum of sensitivity and specificity. [38] [39] The maximum value of this index provides a reasonable choice for the parameter value. As we can see in Figure 3.6, this gives an "ideal" FoM limit of 2.66×10^{-4} for 1.0 MeV tracks with (3.0 mm, 2.0 keV) detector resolution. We will discuss this choice in more detail in Sections 4.3 and 5.3. Optimizing image quality provides another empirical approach to setting the FoM threshold.

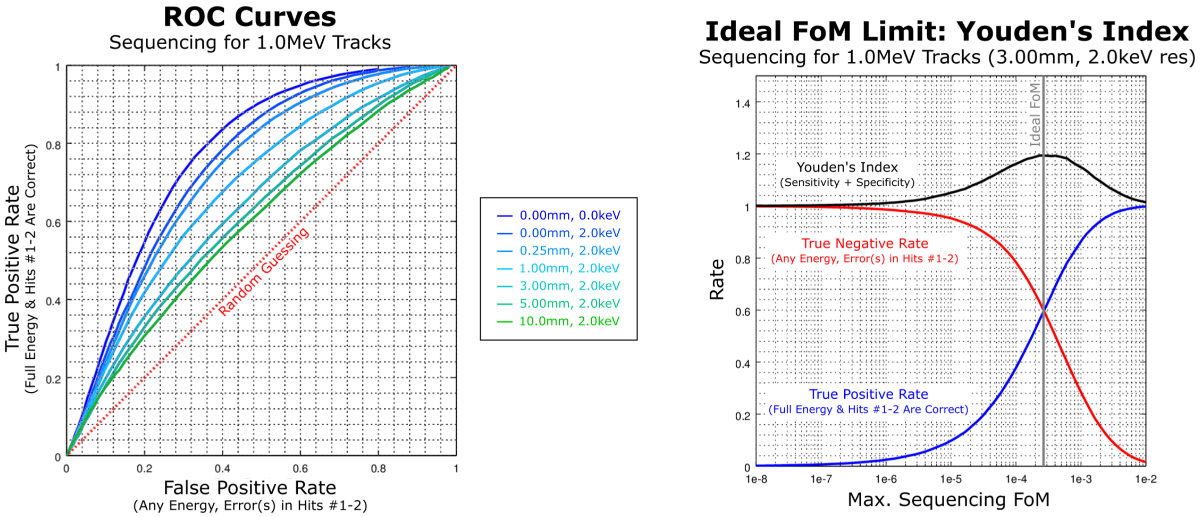

Figure 3.6: ROC curves and choosing a sequencing FoM limit

Chapter 4

Compton Imaging

4.1 Introduction to Compton Imaging

This section describes the fundamentals of Compton imaging, and how it can be used to locate the emission points of photons produced during in-beam experiments. What makes Compton imaging so powerful is that we get the data for "free" from other experiments. But while it's potentially useful for lifetime experiments, this approach also has its limitations – including the Compton profile in HPGe, non-idealities in the ion beam, and imperfect detector resolution.

The ability to sequence a photon track not only makes it possible to correct energy spectra, it also enables the use of gamma-ray imaging. Knowing the complete path a photon takes through a detector allows us to backtrack to where the photon originated from before entering the detector. Consider a track with interaction locations $\boldsymbol{X_1}, ..., \boldsymbol{X_N}$ and energy depositions $E_1, ..., E_N$. Applying Compton tracking to hits 2 through N-1 gives a best-fit interaction sequence. Below a photon energy of several MeV, Hit 1 is generally also a Compton scatter. We can use kinematics here, too, to deduce the initial scattering angle.

The total energy of the track, assuming the photon deposited its full energy in the detector, is equal to:

$$E_{total} = \sum_{n=1}^{N} \Delta E_n \tag{4.1}$$

This is the initial energy of the photon before it enters the detector. Because we also know the energy deposition at the first scattering point, we can calculate the cosine of the initial scattering angle from Equation 3.4:

$$\mu_1 = 1 - \frac{m_e c^2 \Delta E_1}{E_{total}(E_{total} - \Delta E_1)} \tag{4.2}$$

This is the cosine of the angle between the photon's final and initial headings at $\boldsymbol{X_1}$. Note that the final heading is simply defined as a unit vector from $\boldsymbol{X_1}$ towards $\boldsymbol{X_2}$, i.e.:

$$\hat{\boldsymbol{V}}_{\boldsymbol{1}} = \frac{\boldsymbol{X_2} - \boldsymbol{X_1}}{\|\boldsymbol{X_2} - \boldsymbol{X_1}\|} \tag{4.3}$$

We can thus say that:

$$\hat{\boldsymbol{V}}_{\boldsymbol{0}} \cdot \hat{\boldsymbol{V}}_{\boldsymbol{1}} = \mu_1 \tag{4.4}$$

where $\hat{\boldsymbol{V}}_{\boldsymbol{0}}$ is the unit vector that defines the photon's incident heading on $\boldsymbol{X_1}$.

Equation 4.4 defines a *cone* of possible directions for the incident photon vector. This is referred to as the "Compton Cone", with opening angle $\theta_C = \cos^{-1}\mu_C = \cos^{-1}\mu_1$, central axis $\hat{\boldsymbol{V}}_{\boldsymbol{C}} = -\hat{\boldsymbol{V}}_{\boldsymbol{1}}$, and vertex $\boldsymbol{X_C} = \boldsymbol{X_1}$. Note that the photon must have originated from a point somewhere on the *forward* sheet of this cone. This observation is the essence of Compton imaging.

In imaging, the goal is to determine the source locations for emitted photons – the "source distribution". In many experiments, this is limited to an angular distribution, because the distance to any emission point is unknown. By projecting the cones from many events onto a containing sphere, we obtain a set of overlapping ellipses (a stereographic projection). Point sources can be picked out by noting where the ellipses intersect; the more ellipses that intersect a given pixel in the projection, the stronger the source in that direction. Note that in near-field imaging applications, we can voxelize space in a similar manner in order to localize sources in 3D. (See References [14], [15], and [3] for many more details on stereographic projections and Compton imaging.)

GRETINA's source geometry is uniquely constrained compared to other applications of Compton imaging. In lifetime experiments, an accelerator delivers high-energy projectiles to a thin target, creating exotic excited nuclei through fusion or other nuclear reactions. These products recoil out of the target in a highly-collimated beam travelling at relativistic speeds (typically 0.05-0.4c, depending on kinematics). They de-excite a short time later, emitting one or more characteristic gamma-rays. This means, for our imaging problem, we can assume our photons originate somewhere along the beamline, downstream of the target.

Instead of trying to locate arbitrary source points in 3D, we just need to find the intersections of our Compton cones with the beamline. Assuming a pencil beam, there can only be up to two such locations per cone. Ideally, one of these intersections is upstream of the target, ruling it out as unphysical. In such case, reconstruction yields a single unambiguous origin for the photon. See Figure 4.1 for an illustration. Note that it is quite possible for both intersections to be downstream of the target. In these ambiguous cases, the reconstruction is simply thrown out.

Appendix A.4 gives a detailed derivation of the cone-beam intersection points. In the end, we arrive at a quadratic equation that depends on the beam axis and the Compton

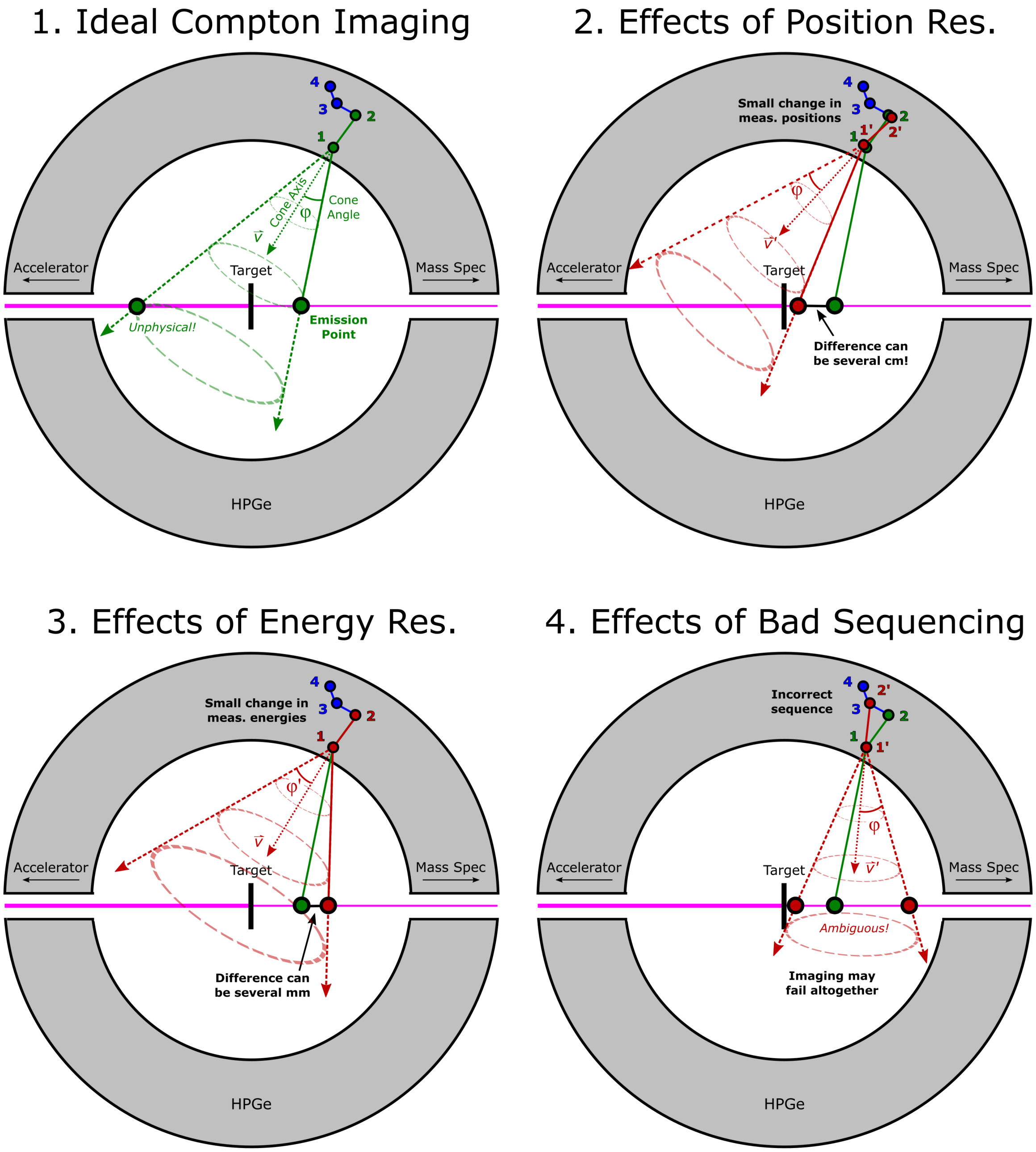

1. Ideal Compton Imaging

2. Effects of Position Res.

3. Effects of Energy Res.

4. Effects of Bad Sequencing

Figure 4.1: Ideal Compton imaging and detector effects

cone axis, vertex, and opening angle. The intersections are $\boldsymbol{X_{0,1}} = t_1\hat{\boldsymbol{B}}$ and $\boldsymbol{X_{0,2}} = t_2\hat{\boldsymbol{B}}$, where t_1 and t_2 are the solutions to that equation and $\hat{\boldsymbol{B}}$ is the beam axis.

While on paper this is very promising, Compton imaging with real detectors is not nearly so clean. Finite detector position and energy resolution limits how well we know the hit coordinates $\boldsymbol{X_1}$, ..., $\boldsymbol{X_N}$ and energy depositions E_1, ..., E_N. Both the Compton cone axis ($\boldsymbol{V_C} = \boldsymbol{X_1} - \boldsymbol{X_2}$) and the cone angle (Equation 4.2) are directly affected by these quantities. Figure 4.1 illustrates the effects that detector performance has for the imaging problem.

Energy resolution changes the cone angle, but the difference is generally very small. Consider a 1.0 MeV photon that initially scatters at 45° in the detector, leaving a 364 keV energy deposition at $\boldsymbol{X_1}$. Suppose with 0.2% energy resolution, this deposition registers as 363keV while the full photon energy registers 1002 keV. The scattering angle computed in this scenario would then be 44.7° (shifting the cone-beam intersection by approximately 0.3° or 0.7 mm).

Position resolution creates much more serious problems for Compton imaging. Figure 4.2 shows a simple estimate for angular resolution based on how position resolution skews the Compton cone axis. Consider a track where the first two hits are $\boldsymbol{X_1}$ and $\boldsymbol{X_2}$. Suppose the detector registers hits at $\boldsymbol{X_1'}$ and $\boldsymbol{X_2'}$, which are a distance L' apart. (Here, L' is referred to as the "Compton lever arm".) In the worst case, the shifts are perpendicular to the *new* beam axis $\boldsymbol{V_C'} = \boldsymbol{X_1'} - \boldsymbol{X_2'}$. The maximum angular error can be simply expressed as:

$$\Delta\theta_C = \arctan\sqrt{2}\sigma_{xyz}/L' \tag{4.5}$$

where σ_{xyz} is the position resolution and $L' = \|\boldsymbol{X_1} - \boldsymbol{X_2}\|$. (Note that the position resolution at both points sums in quadrature.) With typical $\sigma_{xyz} = 3.0$ mm position resolution and a measured lever arm of $L' = 30.0$ mm, the shift is 8.0°. At a 90° nominal emission angle and a cone vertex 180 mm from the beamline, this corresponds to a 25.2 mm shift from the true emission point.

Mis-sequencing errors can also shift the cone axis. (Any sequence that mis-identifies Hit #1 or Hit #2 will do so.) However, the errors may be even more severe, as the distance between points is generally several times greater than the position resolution.

Beam properties present another complication to imaging. In my analysis I've assumed an ideal pencil beam, but real beams have a finite angular divergence and spot size on target. Typically, the divergence is $< 1°$ and the spot size can be modeled as a 2D Gaussian with $\sigma = 4$ mm in both dimensions. Because I assume all nuclei travel along the $\hat{z}$-axis in my calculations of the cone-beam intersections, this can lead to significant errors in the imaged source distribution. With the proper instrumentation downstream of GRETINA, it is possible to measure the true beam heading and correct for these effects. [4] However, this instrumentation is not always available, and so I've ignored this complication for this study. Please refer to Appendix A.6 for more details.

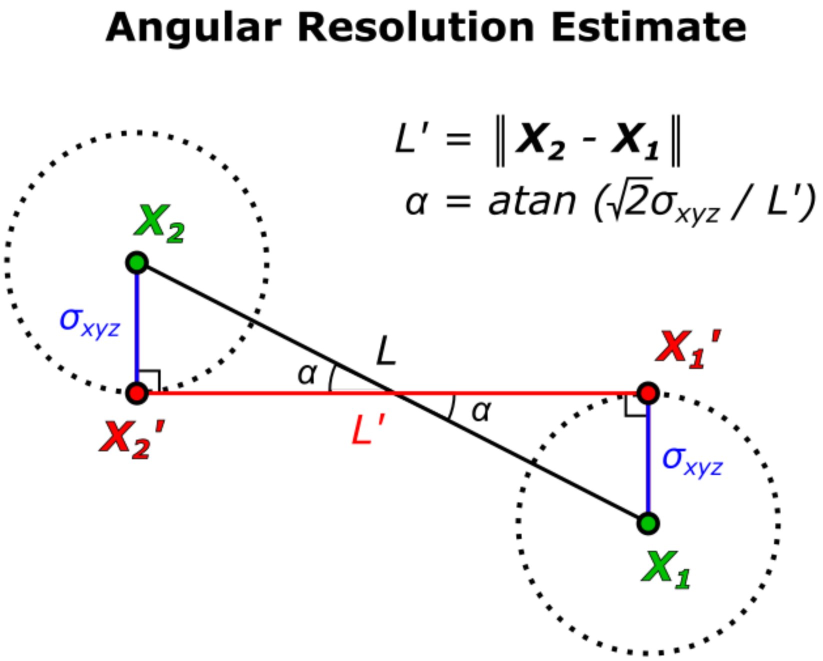

Figure 4.2: Estimate of angular resolution from position resolution and Compton lever arm

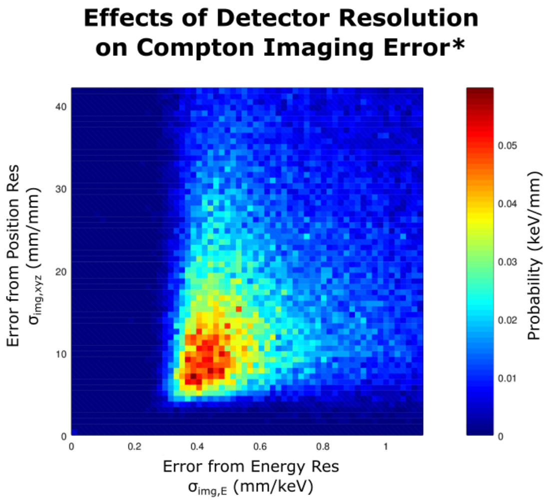

* Analytic error estimates, with $\sigma_{img,total}^2 = \sigma_E^2\sigma_{img,E}^2 + \sigma_{xyz}^2\sigma_{img,xyz}^2$

Figure 4.3: Analytical error estimates for Compton imaging
$\sigma_{xyz} = 3.0$mm, $\sigma_E = 2.0$keV detector resolution
Geant4 simulation with $E_{\gamma,CM} = 1000$keV, $\beta = 0.3$c, and $\tau_0 = 3.0$ns

In all these cases, it is possible for a Compton reconstruction to yield ambiguous, incorrect, or unphysical solutions, or no solutions at all. (A Compton cone may not intersect the beamline when it is too far off-axis.) It is easy to see that the errors become more pronounced at shallower emission angles. As the distance between the cone vertex and the calculated emission point increases, the angular resolution translates to larger shifts along the beamline.

Still, before dismissing Compton imaging for these potential issues, it is important to have a quantitative handle on what they mean for final imaging resolution. I explored this analytically using error propagation on the solutions to Equation A.44. Appendix A.7 provides the derivation of the error formulas, which involves a very large set of complicated partial derivatives. (I studied only the effects of detector energy and position resolution for simplicity.) To get a realistic picture of the imaging errors, I simulated a set of 1.0 MeV photon tracks using the Geant4 model introduced in Section 2.6. Running the tracks through sequencing gave me a set of Compton cones to plug into the error formulas from Appendix A.7. This let me compute uncertainty estimates for a range of detector resolutions.

Figure 4.3 shows the distribution of errors calculated for a detector with $\sigma_{xyz} = 3.0$ mm position- and $\sigma_E = 2.0$ keV energy-resolution. The colormap shows the normalized contributions from detector position and energy resolution, which I denote $\sigma_{img,xyz}$ and $\sigma_{img,E}$, respectively. (These contributions sum in quadrature to get the total analytic error, $\sigma^2_{img,total} = \sigma^2_{img,xyz}\sigma^2_{xyz} + \sigma^2_{img,E}\sigma^2_E$) As noted before, σ_{xyz} and σ_E are applied uniformly to each photon hit, regardless of hit energy. Appendix A.7 discusses these calculations in detail. We can immediately see that position resolution dominates as the major factor in the final imaging resolution – by a factor of about 20x. The distribution peaks around $\sigma_{img,xyz} = 10$ mm/mm and $\sigma_{img,E} = 0.4$ mm/keV. As discussed in Section 2.5, detector resolution depends on the magnitude of the energy deposition, but I ignored this for simplicity.

4.2 Detector Performance

Compton imaging is affected by several experimental factors, including detector resolution and beam properties. As expected, detector position resolution is much more limiting than energy resolution. The results can be used to get a sense of performance requirements for effective Compton imaging.

It is clear that Compton Imaging is not without its challenges. Much of this study was therefore dedicated to optimizing the image quality achievable with GRETINA. There are many experimental parameters that can affect this image quality, as shown in Table 4.1 below. Some are intrinsic characteristics of the experiment, such as the resolution of the detector. Others, however, are tunable parameters that are used in data post-processing. We can try to improve imaging quality by selecting appropriate values for these analytical parameters.

To test the effects of these parameters, I used the GRETINA Geant4 model to generate idealized track data for a beam source. The source nuclei had an 2.7525 ns lifetime and emitted 1.0 MeV CM-frame gamma rays. The source speed was set at 0.3 ± 0.001c, with a beam spread of $\sigma_\theta = 0.25°$ and spot size of $\sigma_{beam,x} = \sigma_{beam,y} = 0.25$ mm. The target was placed at z = 0.0 mm. Each track was then sent through the Compton sequencing and image reconstruction algorithm to obtain a computed emission point, $\boldsymbol{X_{0,calc}}$. As Geant4 provided the true emission point $\boldsymbol{X_{0,true}}$ for each track, I readily obtained the imaging error $\boldsymbol{\Delta X_0} = \boldsymbol{X_{0,calc}} - \boldsymbol{X_{0,true}}$ of each reconstruction. For simplicity, I ignored beam deviations and used only the z-component of the errors to evaluate imaging. (The properties of the beam certainly affect the quality of the output image, however – see Appendix A.6 for details. For all of my simulations, though, I assumed a near-pencil beam with very little angular, spatial, or velocity spread.)

Experimental Parameters	**Analytical Parameters**
Photon energy	Compton "lever arm"
Position resolution	Sequencing FoM
Energy resolution	Corrected CM-frame energy
Beam velocity	Proximity to segment bounds

Table 4.1: Parameters that affect Compton imaging quality

Image quality is characterized by two factors – imaging resolution and efficiency. I estimated resolution by fitting Gaussians to the distributions of imaging errors, $\boldsymbol{\Delta X_0}$. While Compton imaging responses are not completely Gaussian, the simplification yielded fairly accurate FWHMs. The fitting process and a few sample Compton images are shown in Figure 4.4. From there, I defined the imaging resolution as $\sigma_{img} = FWHM/2\sqrt{2ln2}$. Appendix A.9 provides details about the uncertainty calculations for the fits.

Photon tracks can be rejected for use in an image for many reasons. For example, a track may be too short or too long, or result in ambiguous or unphysical emission points. Before sending a track through sequencing and subsequent imaging, however, we first check its measured lab-frame energy. This helps remove Compton background counts. Because sources move relativistically in lifetime measurements, the emission energy can be broadened by up to several hundred keV (see Section 2.2). However, we can still reject tracks whose energy lies outside the range of possibilities set by the imaging window. Consider a track with first hit at $\boldsymbol{X_1}$ = (200.0 mm, 0.0 mm, 100.0 mm). For these experiments, I restrict emissions to GRETINA's central cavity, where the upstream limit is the beam target, generally at $\boldsymbol{X_{0,L}}$ = (0.0 mm, 0.0 mm, 0.0 mm), and the downstream limit is $\boldsymbol{X_{0,R}}$ = (0.0 mm, 0.0 mm, 180.0 mm). The emission vectors $\boldsymbol{V_{0,L}} = \boldsymbol{X_1} - \boldsymbol{X_{0,L}}$ and $\boldsymbol{V_{0,R}} = \boldsymbol{X_1} - \boldsymbol{X_{0,R}}$ define the minimum and maximum possible emission angles, respectively, relative to the beam axis. This angular range corresponds to a range of permissible lab-frame energies for the photon, so that any tracks outside that window can be rejected.

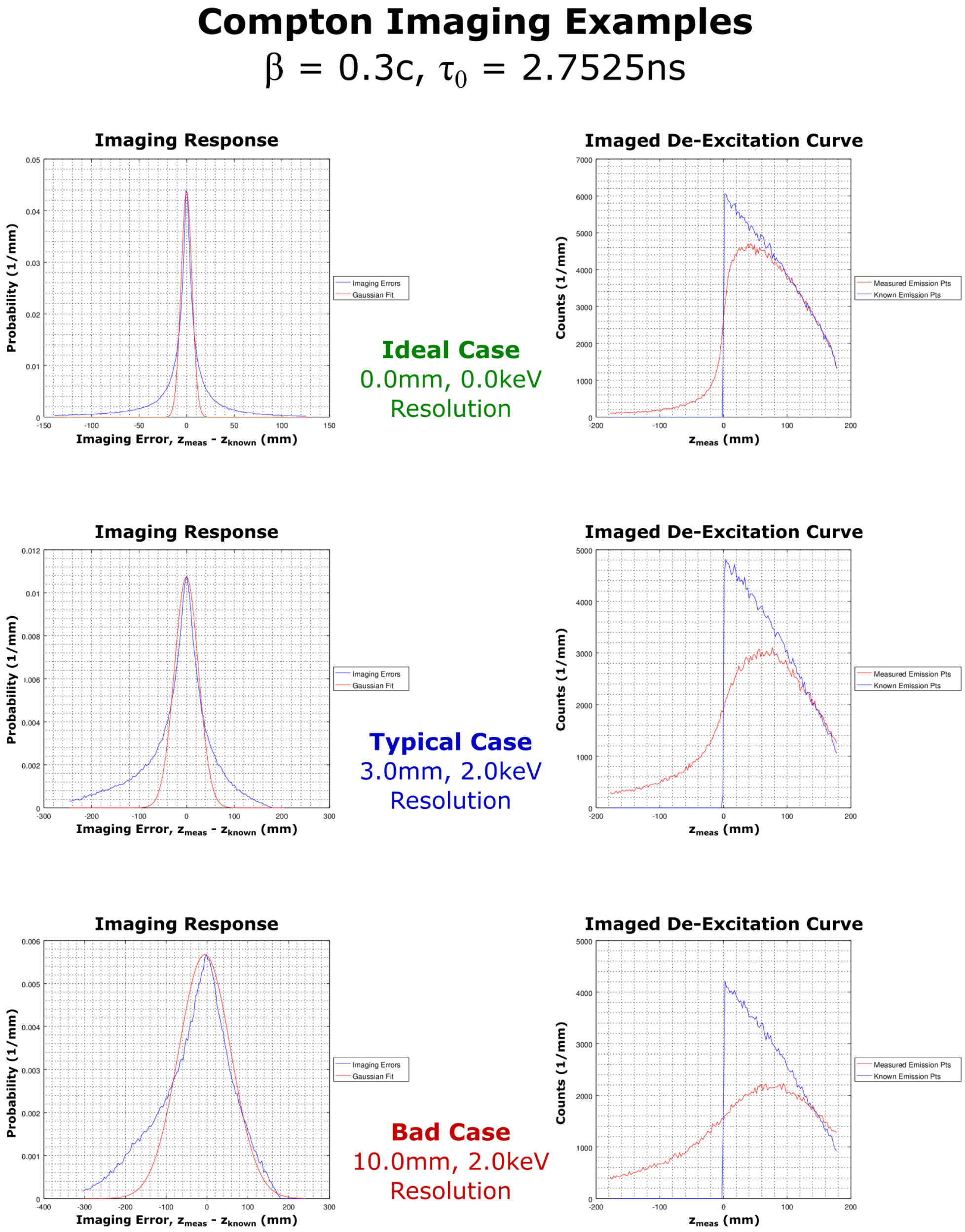

Compton Imaging Examples

$\beta = 0.3c$, $\tau_0 = 2.7525\text{ns}$

Imaging Response

Imaged De-Excitation Curve

Ideal Case
0.0mm, 0.0keV
Resolution

Typical Case
3.0mm, 2.0keV
Resolution

Bad Case
10.0mm, 2.0keV
Resolution

Figure 4.4: Sample Compton images
For a range of detector position and energy resolutions

This first data filter sets the baseline number of tracks that we have to work with for imaging. In my simulations, I began with $N_{total} = 2.365$M total tracks, of which $N_{Compton} = 1.529$M tracks were rejected by the above energy filter. This left $N_{imaging} = 0.836$M tracks for imaging. From there, subsequent data filters further reduce the number of counts used to create the output Compton image (N_{good}). We define the absolute imaging efficiency as the ratio $\epsilon = N_{good}/N_{imaging}$. Tables 4.2 and 4.3 below also provide "relative" efficiencies. These numbers represent quantities normalized to the ideal cases in their respective tables. As detector resolution degrades, it becomes more likely for Compton imaging to produce ambiguous or unphysical emission points, resulting in fewer counts in the final image. For example, at 3.0 mm position resolution, the output image contains only 70.0% as many counts as a detector with perfect position resolution.

Detector resolution is perhaps the most critical of the experimental properties for imaging resolution. As shown in Figure 4.1, detector resolution can cause multiple errors in Compton reconstruction. The deviations between true and calculated emission points can range from several millimeters to several centimeters or more. Table 4.2 and Figure 4.5 show the effects of detector position resolution (σ_{xyz}) on the imaging resolution and efficiency, while Table 4.3 and Figure 4.6 show similar data for varying detector energy resolution (σ_E). We can see that position resolution dominates for realistic values of energy resolution in HPGe. In fact, energy resolution hardly affects imaging resolution or efficiency. It is important to note that detector resolution was applied uniformly to each hit, regardless of energy deposition. This approach could be improved – detector position resolution depends on the energy of a photon hit. While the effect was demonstrated in the AGATA array (the European cousin to GRETA) [32], similar effects are expected for GRETINA. I ignored this energy-dependence for simplicity.

There were a couple effects I did not have time to investigate in great detail, but which may further affect imaging quality. The first of these is the lab-frame energy of the photon. 200 keV photons yield fewer hits per track than 1.0 MeV ones, and the hits from the lower-energy tracks leave smaller energy depositions. This reduces not only the detector resolution, but also the accuracy and efficiency of sequencing. (As pointed out in Section 3.3, only 29.9% of 1.0 MeV photon detections are full-energy events with between 3 and 6 hits.) By simulating datasets for many photon CM-frame energies, we could identify a range for which Compton imaging would be most effective.

Detector geometry plays a role, too, further complicating the imaging problem. Consider a photon that is emitted nearby a detector (as opposed to one emitted near the center of the GRETINA inner cavity). The total distance traveled from emission to the first hit is then relatively small, which means angular resolution translates to a smaller spatial deviation on the beam-line. Because of this, emissions from either end of the inner cavity will be located more precisely than those in the center.

Position Resolution	**Imaging Resolution (mm)**	**Efficiency (Absolute, %)**	**Efficiency (Relative, %)**
0.0 mm	6.57 ± 0.27	42.818 ± 0.086	100.000 ± 0.283
0.25 mm	8.28 ± 0.33	40.972 ± 0.083	95.690 ± 0.272
0.50 mm	9.62 ± 0.35	39.017 ± 0.081	91.124 ± 0.262
0.75 mm	10.88 ± 0.36	37.391 ± 0.078	87.331 ± 0.253
1.0 mm	13.01 ± 0.42	36.006 ± 0.077	84.092 ± 0.245
1.5 mm	15.51 ± 0.49	33.848 ± 0.074	79.052 ± 0.234
2.0 mm	18.78 ± 0.57	32.259 ± 0.071	75.341 ± 0.225
2.5 mm	22.00 ± 0.64	30.985 ± 0.070	72.366 ± 0.218
3.0 mm	25.17 ± 0.65	29.957 ± 0.068	69.964 ± 0.212
4.0 mm	31.75 ± 0.81	28.325 ± 0.066	66.152 ± 0.203
5.0 mm	36.53 ± 0.87	27.126 ± 0.064	63.353 ± 0.196
7.5 mm	48.26 ± 1.11	25.263 ± 0.062	59.002 ± 0.186
10.0 mm	63.89 ± 1.21	24.084 ± 0.060	56.248 ± 0.179

Table 4.2: Compton image quality & efficiency vs. position resolution
$E_{CM} = 1000$ keV, $\beta = 0.3$, $\tau_0 = 2.7525$ ns, $\sigma_E = 2.0$ keV
Total Tracks: 2.365M, Plausible Energy: 0.832M-0.836M, Imaged Tracks: 0.200M-0.359M

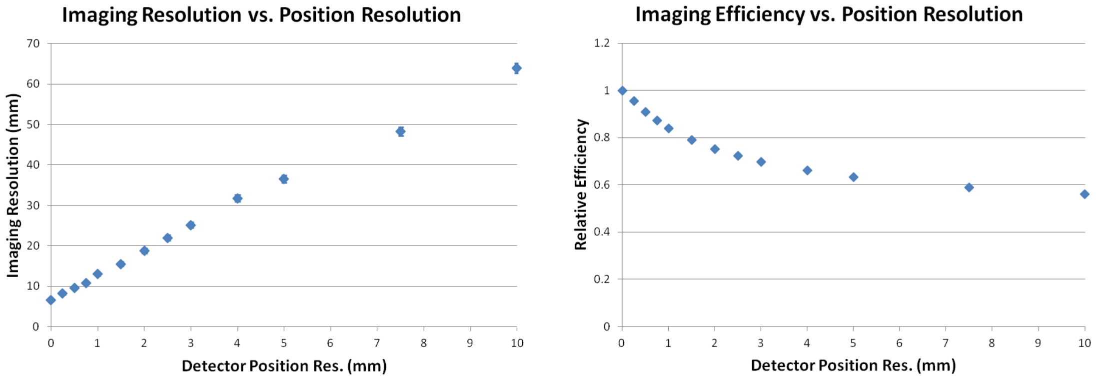

Figure 4.5: Compton image quality & efficiency vs. detector position resolution
See Table 4.2

Energy Resolution	**Imaging Resolution (mm)**	**Efficiency (Absolute, %)**	**Efficiency (Relative, %)**
0.0 keV	24.76 ± 0.71	30.057 ± 0.068	100.000 ± 0.322
0.25 keV	25.19 ± 0.74	30.019 ± 0.068	99.874 ± 0.322
0.50 keV	23.50 ± 0.66	30.018 ± 0.068	99.870 ± 0.322
0.75 keV	25.06 ± 0.75	29.983 ± 0.068	99.751 ± 0.321
1.0 keV	24.17 ± 0.72	30.070 ± 0.068	100.042 ± 0.322
1.5 keV	25.09 ± 0.68	29.961 ± 0.068	99.680 ± 0.321
2.0 keV	25.17 ± 0.65	29.957 ± 0.068	99.666 ± 0.321
2.5 keV	26.32 ± 0.67	29.947 ± 0.068	99.631 ± 0.321
3.0 keV	25.42 ± 0.65	29.893 ± 0.068	99.453 ± 0.320
4.0 keV	25.83 ± 0.67	29.809 ± 0.068	99.172 ± 0.320
5.0 keV	27.16 ± 0.65	29.705 ± 0.068	98.829 ± 0.319
7.5 keV	28.21 ± 0.61	29.339 ± 0.067	97.609 ± 0.316
10.0 keV	31.85 ± 0.71	28.959 ± 0.067	96.344 ± 0.312

Table 4.3: Compton image quality & efficiency vs. energy resolution
E_{CM} = 100 0keV, $\beta = 0.3$, $\tau_0 = 2.7525$ ns, $\sigma_{xyz} = 3.0$ mm
Total Tracks: 2.365M, Plausible Energy: 0.834M-0.835M, Imaged Tracks: 0.242M-0.251M

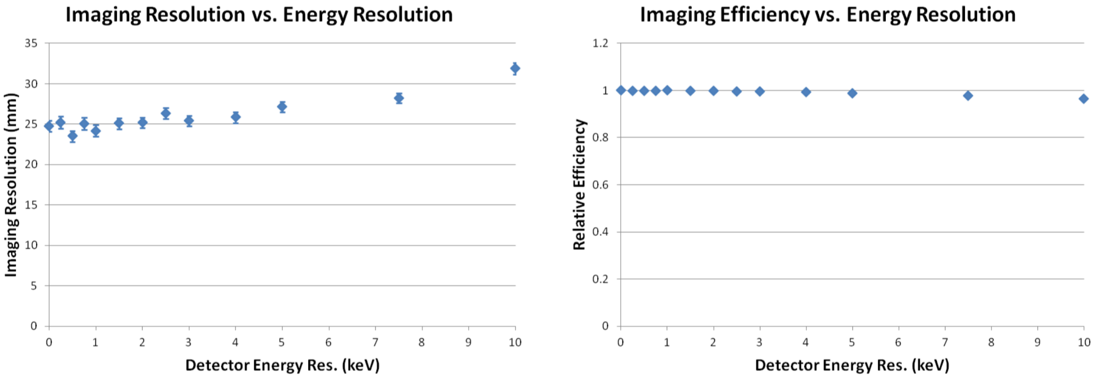

Figure 4.6: Compton image quality & efficiency vs. detector energy resolution
See Table 4.3

4.3 Image Quality Cuts

There are several data quality cuts we can make to improve imaging resolution in post-processing. I studied imaging filters using the Compton lever arm, sequencing FoM, and corrected CM-frame energy. As with all such filters, there is a trade-off between data quality and imaging efficiency (i.e. the fraction of tracks used in the final image reconstruction). In this section I show the effects of the various cuts and optimize for a 1.0 MeV beam source.

The factors discussed in Section 4.2 are intrinsic to the experiment and the detector used. There are also multiple data cuts that can be made in post-processing to improve image quality. Using the same simulation data as before, I studied the effects of a few of these factors, keeping detector position and energy resolution constant at $\sigma_{xyz} = 3.0$ mm and $\sigma_E = 2.0$ keV. For each run, I modified a single data filter at a time, keeping the others constant at their most permissive values (discussed below).

As illustrated already in Figure 4.2, the angular resolution not only depends on the detector position resolution (σ_{xyz}), but also the distance between the first and second hits in a photon track, L' (the Compton "lever arm"). From Equation 4.5, the larger L' is compared to σ_{xyz}, the smaller the average angular error is expected to be. Therefore, the Compton lever arm is a convenient filter to remove tracks with high imaging uncertainty (see also Appendix A.7). Of course, there is a trade-off between data quality and imaging efficiency. Requiring lever arms to exceed a certain threshold sets a maximum angular deviation for a given Compton reconstruction. The larger this threshold, the better-constrained the cone axis is. However, the distance a photon travels in the detector is a function of photon cross-section. The probability that a photon travels at least a distance x in the detector before interacting is:

$$P(x, E) = 1 - e^{-x/d(E)} \tag{4.6}$$

where $d(E)$ is the attenuation length (or mean-free-path) for a photon of energy E in HPGe. Note that the decrease in counts will not be a simple exponential, though, since the photons in question will not be mono-energetic after the first scatter at $\boldsymbol{X_1}$. Still, it is plain to see that as we increase the lever arm threshold, fewer photon tracks will qualify for use in the final image. (Setting the minimum Compton lever arm to $L_{min} = 0.0$ mm accepts all tracks.) Table 4.4 and Figure 4.7 provide results gathered for our typical setup. The improvements in imaging quality are noticeable but modest. For example, imposing a minimum lever arm limit of 20.0 mm improves resolution by a factor of 1.31x. Imaging efficiency is simultaneously reduced by 56.9%, which makes for a somewhat unfavorable trade-off. (Statistical uncertainty is increased by a factor of 1.52x in this case.)

The sequencing FoM provides another such filter. We found in Section 3.3 that tracks with larger FoMs are less likely to have been sequenced properly, thereby introducing potential error in the Compton reconstruction. So, by rejecting tracks with sequencing FoMs over a set limit, we *should* see an improvement in image quality. (Setting the maximum sequencing FoM to $FoM_{max} = 1.0$ accepts all tracks.) Table 4.5 and Figure 4.8 show results for the same setup as before. Unfortunately, the gains in imaging resolution are insignifcant compared to the loss in imaging efficiency. Rejecting tracks with sequencing FoM above 3E-5 improves resolution by a scant 1.06x, while reducing the number of available counts by 84%.

Doppler-shift corrections provide a third way to improve things. Here, the goal is to compare the Doppler-corrected CM-frame energy with the known photopeak energy of the source. Anything outside a few keV from a photopeak is likely to be an incomplete energy deposition, and therefore not a Compton-sequenceable track. We want to remove such tracks from the final image. To identify them, we use the emission angle calculated via imaging and the known parent velocity to find the photon's Doppler-corrected CM-frame energy. The track can then be rejected by checking against the known photopeak energy; in other words, only tracks within a given CM-frame energy range are accepted for the final image. (Setting the maximum deviation to $\Delta E_{corrected,max} = 1000$ keV accepts all tracks.) Table 4.6 and Figure 4.9 present the results. It is immediately clear how effective this data filter is. For example, constraining counts to be within 10.0 keV of the 1000 keV CM-frame photopeak improves resolution by a factor of 4.44x. The corresponding reduction in imaging efficiency (85.3%) increases statistical uncertainty by a factor of 2.61x, making for a *very* favorable trade-off. The overall imaging response also begins to follow a much more Gaussian shape as the energy window is narrowed.

Figure 4.10 shows a few sample images using the above filters. However, choosing appropriate filtering thresholds is difficult. One approach is to balance the improvement in imaging resolution against the loss in Poisson statistics. Let $\sigma_{img,0}$ be the imaging resolution prior to filtering, and let $N_{counts,0}$ be the corresponding number of tracks accepted for image reconstruction. Then let $\sigma_{img,filt}$ and $N_{counts,filt}$ denote these same quantities after the data filter is applied. Because statistical uncertainty scales with the square root of the number of counts, we want to choose our filter parameter such that:

$$\frac{\sigma_{img,filt}}{\sigma_{img,0}} < \frac{\sqrt{N_{counts,filt}}}{\sqrt{N_{counts,0}}} \tag{4.7}$$

For example, if imaging efficiency is dropped by a factor of 4x, the cut should improve imaging resolution by at least 2x. Narrowing the corrected energy window from 1000.0 ± 20.0 keV to 1000.0 ± 10.0 keV drops imaging efficiency by 1.85x (from 7.97% to 4.32%) while improving imaging resolution by 1.86x (from 10.5 mm to 5.63 mm). However, further narrowing the window to 1000.0 ± 5.0 keV reduces efficiency another 1.96x while improving image resolution by only 1.39x. So, this suggests that a cut at 10.0 keV is advantageous, while 5.0 keV is too restrictive. However, the decision of where to cut ultimately depends on the total number of tracks available for a given lifetime measurement. (Section 6.3 discusses this exact problem in much greater detail.)

Minimum “Lever Arm”	**Imaging Resolution (mm)**	**Efficiency (Absolute, %)**	**Efficiency (Relative, %)**
0.0 mm	25.13 ± 0.68	29.359 ± 0.067	100.000 ± 0.325
5.0 mm	23.33 ± 0.64	25.991 ± 0.063	88.526 ± 0.295
10.0 mm	21.15 ± 0.57	20.416 ± 0.054	69.537 ± 0.244
15.0 mm	20.55 ± 0.57	16.015 ± 0.047	54.548 ± 0.204
20.0 mm	19.14 ± 0.56	12.657 ± 0.041	43.111 ± 0.172
25.0 mm	16.66 ± 0.54	10.050 ± 0.036	34.232 ± 0.147
30.0 mm	16.48 ± 0.51	8.061 ± 0.032	27.455 ± 0.127
35.0 mm	15.17 ± 0.51	6.474 ± 0.029	22.050 ± 0.110
40.0 mm	15.74 ± 0.74	5.214 ± 0.026	17.759 ± 0.096
45.0 mm	14.42 ± 0.68	4.194 ± 0.023	14.283 ± 0.084
50.0 mm	14.68 ± 0.69	3.374 ± 0.020	11.494 ± 0.074

Table 4.4: Compton image quality & efficiency vs. minimum lever arm
$E_{CM} = 1000$ keV, $\beta = 0.3$, $\tau_0 = 2.7525$ ns, $\sigma_{xyz} = 3.0$ mm, $\sigma_E = 2.0$ keV
$FoM_{max} = 1E0$, $\Delta E_{corrected,max} = 1000$ keV
Total Tracks: 2.365M, Plausible Energy: 0.836M, Imaged Tracks: 0.028M-0.245M

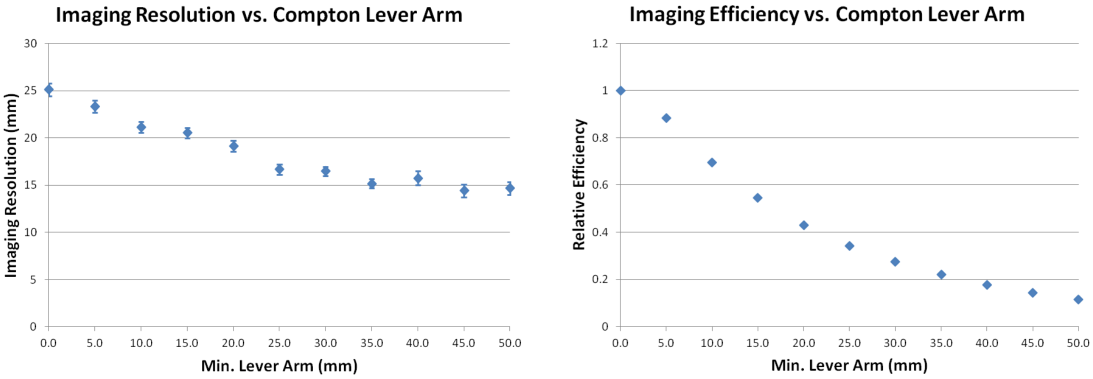

Figure 4.7: Compton image quality & efficiency vs. min. Compton lever arm
See Table 4.4

Maximum Sequencing FoM	**Imaging Resolution (mm)**	**Efficiency (Absolute, %)**	**Efficiency (Relative, %)**
1.0E-1	25.17 ± 0.65	29.359 ± 0.067	100.000 ± 0.325
1.0E-2	25.13 ± 0.65	29.216 ± 0.067	99.511 ± 0.323
3.0E-3	24.23 ± 0.71	28.112 ± 0.066	95.751 ± 0.314
1.0E-3	24.40 ± 0.70	24.561 ± 0.060	83.655 ± 0.282
3.0E-4	23.97 ± 0.68	16.938 ± 0.049	57.691 ± 0.212
1.0E-4	24.33 ± 0.74	9.670 ± 0.036	32.938 ± 0.143
3.0E-5	23.65 ± 1.00	4.555 ± 0.024	15.513 ± 0.089
1.0E-5	25.86 ± 1.05	2.319 ± 0.017	7.896 ± 0.060

Table 4.5: Compton image quality & efficiency vs. maximum sequencing FoM
$E_{CM} = 1000$ keV, $\beta = 0.3$, $\tau_0 = 2.7525$ ns, $\sigma_{xyz} = 3.0$ mm, $\sigma_E = 2.0$ keV
$L_{min} = 0.0$ mm, $\Delta E_{corrected,max} = 1000$ keV
Total Tracks: 2.365M, Plausible Energy: 0.836M, Imaged Tracks: 0.019M-0.245M

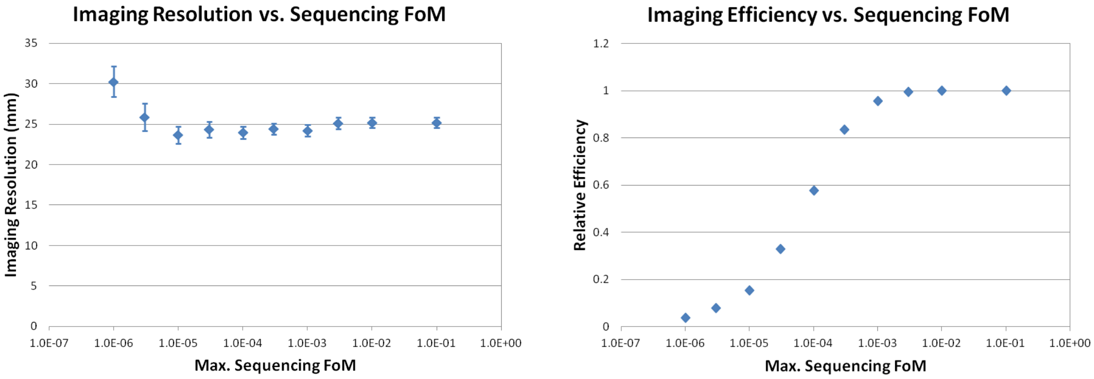

Figure 4.8: Compton image quality & efficiency vs. max. sequencing FoM
See Table 4.5

Maximum Energy Error	Imaging Resolution (mm)	Efficiency (Absolute, %)	Efficiency (Relative, %)
1000.0 keV	25.17 ± 0.65	29.359 ± 0.067	100.000 ± 0.325
200.0 keV	24.68 ± 0.60	27.398 ± 0.065	93.321 ± 0.307
150.0 keV	23.56 ± 0.56	25.247 ± 0.062	85.994 ± 0.288
100.0 keV	24.04 ± 0.48	21.723 ± 0.056	73.989 ± 0.256
75.0 keV	23.20 ± 0.45	19.038 ± 0.052	64.844 ± 0.232
50.0 keV	21.29 ± 0.34	15.320 ± 0.046	52.181 ± 0.197
40.0 keV	18.67 ± 0.23	13.353 ± 0.043	45.480 ± 0.179
30.0 keV	14.96 ± 0.14	10.940 ± 0.038	37.263 ± 0.155
25.0 keV	12.65 ± 0.18	9.522 ± 0.035	32.431 ± 0.141
20.0 keV	10.53 ± 0.19	7.974 ± 0.032	27.158 ± 0.126
15.0 keV	8.12 ± 0.14	6.235 ± 0.028	21.238 ± 0.108
10.0 keV	5.67 ± 0.06	4.321 ± 0.023	14.717 ± 0.086
7.5 keV	4.74 ± 0.07	3.275 ± 0.020	11.156 ± 0.073
5.0 keV	4.09 ± 0.05	2.202 ± 0.016	7.501 ± 0.058
2.5 keV	3.78 ± 0.04	1.103 ± 0.012	3.756 ± 0.040
1.0 keV	3.82 ± 0.05	0.440 ± 0.007	1.499 ± 0.025

Table 4.6: Compton image quality & efficiency vs. max. error in corrected energy
$E_{CM} = 1000$ keV, $\beta = 0.3$, $\tau_0 = 2.7525$ ns, $\sigma_{xyz} = 3.0$ mm, $\sigma_E = 2.0$ keV
$L_{min} = 0.0$ mm, $FoM_{max} = 1E0$
Total Tracks: 2.365M, Plausible Energy: 0.836M, Imaged Tracks: 0.004M-0.245M

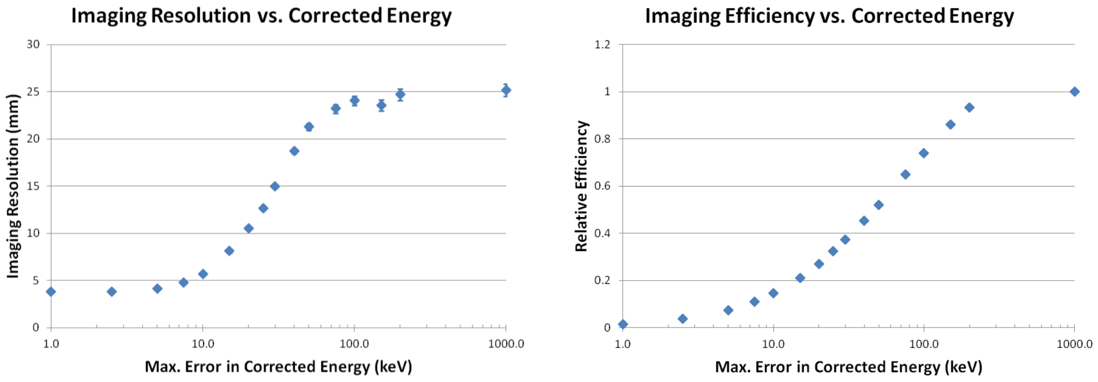

Figure 4.9: Compton image quality & efficiency vs. max. error in corrected energy
See Table 4.6

There are other data quality cuts we could make for *measured* track data. Recall from Section 2.5 that interaction coordinates in GRETINA tend to register near crystal segment boundaries (Figure 2.12). This clustering is of course completely unphysical, calling into question the reliability of tracks with hits near segment boundaries. We might therefore define "exclusion zones" about each segment boundary, rejecting any track with one or more hits in these zones. I explored this briefly with real-world datasets, but unfortunately did not see any marked improvement in image quality as a result of the data filter. (Note that these effects do not show up in simulations, which skip the complex signal decomposition problem.) The analytic error estimates calculated in Appendix A.7 might also prove useful here – we could reject tracks for which the estimated uncertainty is too large. This would make an interesting future study.

We can conclude that the Compton lever arm cut has a much greater effect on image quality than does the sequencing figure-of-merit. The Doppler-corrected energy cut outperforms both of these handily. However, since these three cuts are not entirely independent, I chose to only apply the Doppler-correction energy cut in subsequent Compton imaging runs.

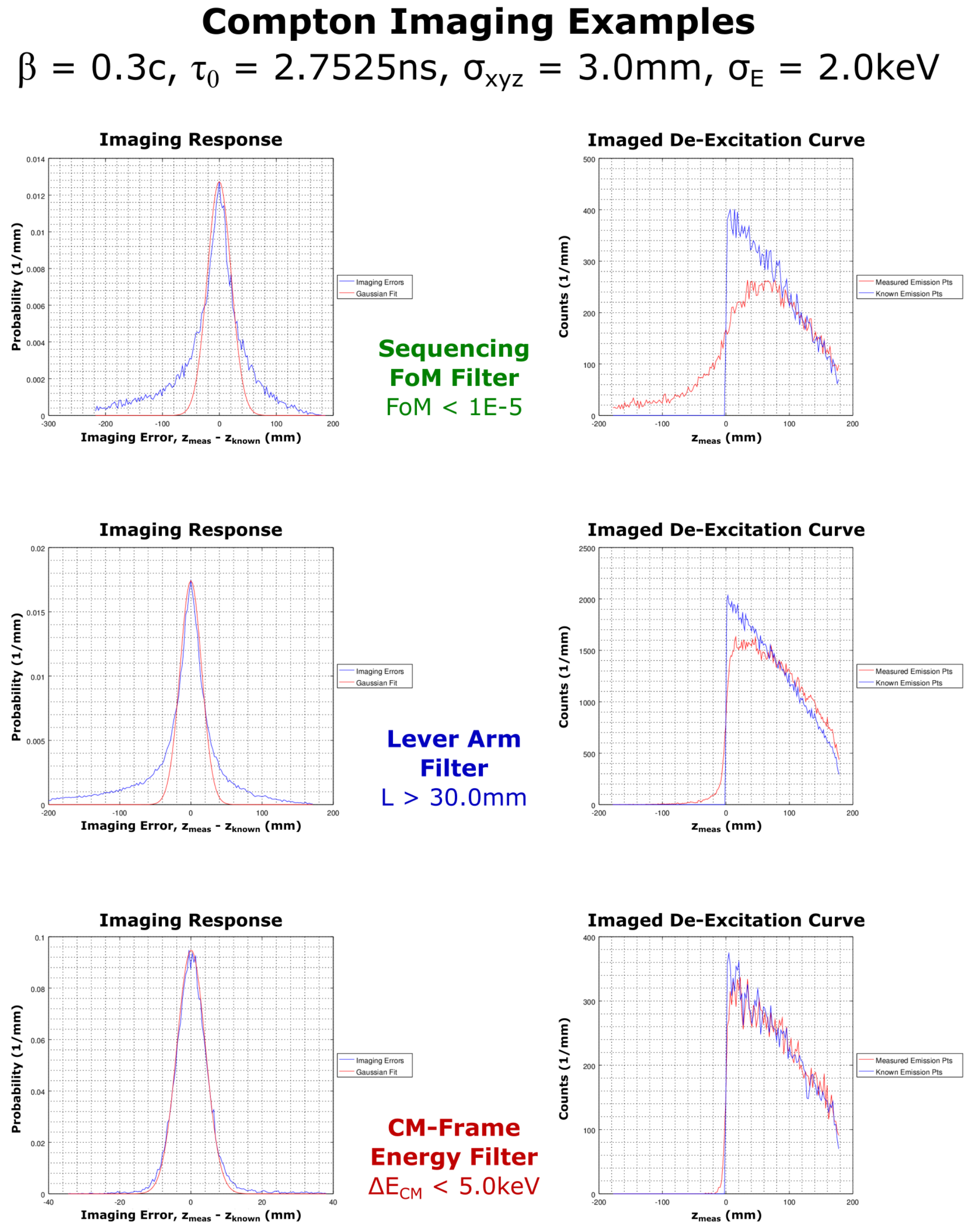

Figure 4.10: Sample Compton images (with data filters)
With various data filters applied

Chapter 5

Doppler-Shift Imaging

5.1 Introduction to Doppler-Shift Imaging

While contemplating the limitations of Compton imaging, I came up with a completely separate solution to the imaging problem. We can obtain a photon's emission point using three pieces of data: 1.) The location of the first interaction, 2.) The CM-frame energy of the emission (i.e. the photopeak energy), and 3.) The lab-frame energy of the photon. This avoids many of the problems associated with the Compton imaging method. Detector position resolution has a much smaller effect on the imaging resolution, and total imaging efficiency is a factor of 4-5x better. Because this novel technique relies on the physics of Doppler shifts, I dubbed it "Doppler-Shift imaging".

The studies in Sections 4.3 and 4.2 make the limitations of Compton imaging abundantly clear. Its effective imaging resolution and efficiency are not particularly exciting, for reasons that will be discussed in Section 6.1. However, while ruminating on the problem I found sudden inspiration in the Doppler-shift corrections that GRETINA was purpose-built for. Would it be possible to reverse the process to trace an emission back to its source?

Consider – the Doppler-shift is determined by the emission angle and lab-frame velocity of the parent nucleus. The properties of the beam are known quantities, and the cosine of the emission angle is simply:

$$\mu = \cos\phi = \frac{\boldsymbol{V_0} \cdot \boldsymbol{B}}{\|\boldsymbol{V_0}\| \|\boldsymbol{B}\|} \tag{5.1}$$

where $\boldsymbol{V_0} = \boldsymbol{X_1} - \boldsymbol{X_0}$ is the vector from the emission point to the first hit in the detector, and $\boldsymbol{B}$ is the beam axis. Now, the physics of Doppler-shifts gives an independent measure of the emission angle cosine:

$$\mu = \frac{1}{\beta}\left(1 - \frac{E_{CM}}{\gamma E_{Lab}}\right) \tag{5.2}$$

If we *assume* that we know the true photopeak energy E_{CM}, then we can solve for the emission angle with the photon energy measured in the lab, E_{Lab}. (This of course assumes that the photon deposits its full energy in the detector, an assumption we already made for sequencing. We must also be able to attribute the detected photons to the specific isotope of interest. This requires the parent nuclei to pass through an isotope separator synced with GRETINA.) $\boldsymbol{X_1}$ is itself a known quantity – it's just the location of the first hit in the detector. That means the only unknown in Equation 5.1 is $\boldsymbol{X_0}$, the emission location!

Appendix A.5 derives the expressions used to calculate $\boldsymbol{X_0}$. By comparison to Compton Imaging, the math is quite simple. And where Compton imaging requires knowledge of both $\boldsymbol{X_1}$ and $\boldsymbol{X_2}$, this new "Doppler-shift" imaging technique only requires $\boldsymbol{X_1}$. This is truly excellent news from the perspective of detector position resolution. In Compton imaging, the angular resolution is largely determined by position resolution and Compton lever arm. Small shifts in the cone-axis can be blown up to large errors on the beam-axis (see Figure 4.1). Doppler-shift imaging, in comparison, does not suffer from this problem. A shift in $\boldsymbol{X_1}$ results in a comparable translation of the Doppler-shift cone along the beam axis. For any given emission angle, the error in $\boldsymbol{X_0}$ depends only linearly on σ_{xyz}. Figure 5.1 illustrates this new technique.

For example, suppose a photon is emitted from $\boldsymbol{X_0} = (0.00\text{ mm}, 0.00\text{ mm}, 45.0\text{ mm})$ with an emission angle of $\theta = 30°$. The photon travels 150 mm before scattering at $\boldsymbol{X_1} = (0.00\text{ mm}, 75.0\text{ mm}, 175.0\text{ mm})$ in the detector. Suppose the detector reports this hit at $\boldsymbol{X_1'} = (0.00\text{ mm}, 80.0\text{ mm}, 170.0\text{ mm})$, a full 7.1 mm away from its true location. Carrying out the computation, the calculated emission point would then be $\boldsymbol{X_0'} = (0.00\text{ mm}, 0.00\text{ mm}, 31.4\text{ mm})$ – just 13.6 mm from the true emission point. Correct sequencing is much less important for a similar reason – an incorrect sequence would ultimately have the same effect as shifting $\boldsymbol{X_1}$ by some distance.

One of the main strengths of the Doppler-Shift technique is its high efficiency, particularly at low energies. Because the reconstruction only requires a single interaction to determine an emission point, we could use this method even where photoabsorption dominates (< 150 keV). Compared to Compton imaging, there are also fewer situations where reconstruction can fail. As long as the measured lab-frame energy is within a range of physically-possible Doppler-shifts, this method will always return a single, unambiguous emission point on the beamline. Compton cones can skew off-axis and fail to intersect the beamline entirely, or they can intersect in two positions downstream of the target.

The flip side to this, however, is that Doppler-shift imaging offers poor discrimination of Compton background. Consider a 1.0 MeV CM-frame emission from a nucleus moving at 0.3c in the lab frame. As noted earlier, the emitted energy can vary anywhere from 733 keV to 1.36 MeV. So, any track that registers in the range of physically-possible energies (determined by the detector geometry) will be accepted for imaging. Background becomes

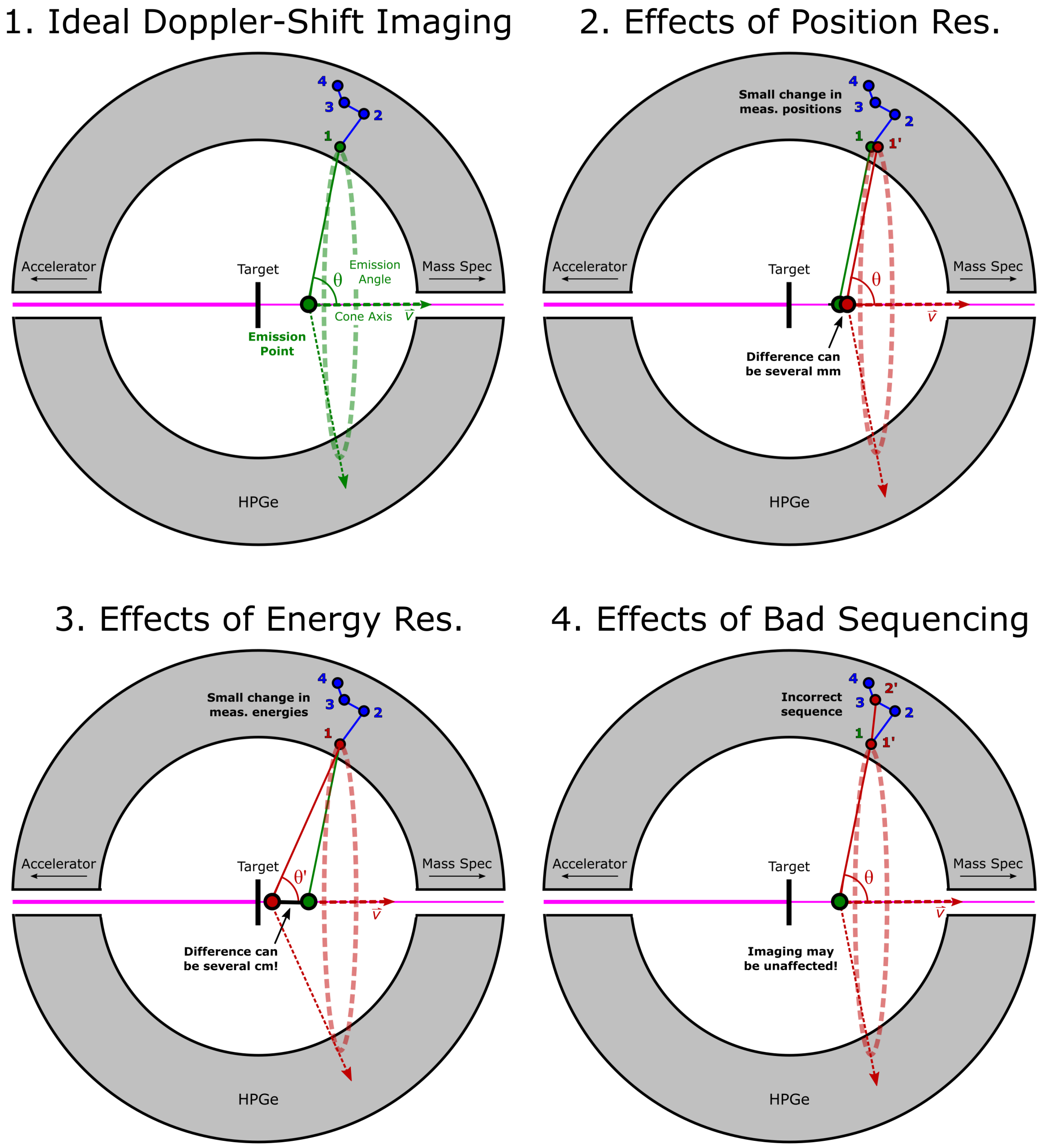
1. Ideal Doppler-Shift Imaging

2. Effects of Position Res.

3. Effects of Energy Res.

4. Effects of Bad Sequencing

Figure 5.1: Doppler-shift imaging and detector effects

especially challenging where multiple gamma lines are present simultaneously. This would be the case, for example, when trying to measure gammas populated through de-excitation chains. There can be significant overlap of peaks in the spectrum, which becomes more pronounced as beam velocity increases. (Consider – the same 1.0 MeV CM-frame emission with $\beta = 0.45$ yields an energy range of 616 keV to 1.62 MeV in the lab frame.) So we must do extra work to ensure a given photon actually belongs to the photopeak we think it does. For example, we might reject tracks for having large sequencing FoM's or for having too few interactions (refer to Sections 3.3 and 5.3). This turns out to be the biggest challenge to using Doppler-shift imaging to measure lifetimes.

As with Compton Imaging, I used error propagation to estimate the imaging resolution of this imaging method. The results were *extremely* promising, suggesting that Doppler-Shift imaging delivers 5-10x better resolution than its Compton counterpart, at least for the detector resolution we expect from GRETINA. Figure 5.2 gives the results for a 1.0 MeV CM-frame emission and 0.3c beam velocity. (See Appendix A.8 for a detailed derivation of the analytic error estimates.) For typical detector performance, position resolution is still the most important factor. Note that it holds roughly constant – for every 1.0 mm that detector position resolution increases, so too does its analytic error contribution. The energy resolution adds approximately 0.6 - 0.7 mm error per keV. As discussed in Appendix A.8, Doppler-shift imaging depends on both the CM-frame emission energy, as well as the velocity of the beam. I ignored both effects for simplicity.

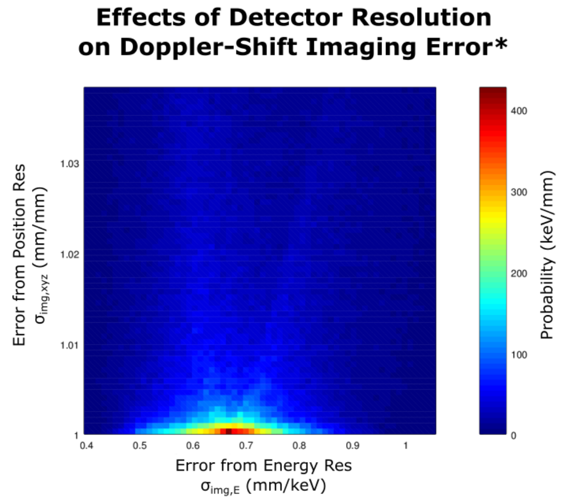

* Analytic error estimates, with $\sigma_{img,total}^2 = \sigma_E^2\sigma_{img,E}^2 + \sigma_{xyz}^2\sigma_{img,xyz}^2$

Figure 5.2: Analytical error estimates for Doppler-Shift imaging
$\sigma_{xyz} = 3.0$ mm, $\sigma_E = 2.0$ keV detector resolution
Geant4 simulation with $E_{\gamma,CM} = 1000$ keV, $\beta = 0.3$c, and $\tau_0 = 3.0$ ns

5.2 Detector Performance

This is very similar to the analysis I did in Section 4.2 for Compton imaging. Detector position and energy resolution both affect the overall imaging resolution, as do the beam velocity and CM-frame energy of the emissions. In general, Doppler-shift imaging is not as sensitive as Compton imaging to position resolution, but it is more sensitive to energy resolution and beam velocity.

In Section 4.2, I quantified effects that certain experimental parameters had on Compton imaging quality and efficiency. Unlike with Compton imaging, though, I expect Doppler-shift imaging to be much more affected by detector energy resolution than position resolution. (See Appendix A.8 for a detailed derivation.) I employed the same simulation data from Section 5.3 to generate track data and perform the analysis.

Tables 5.1 and 5.2 show that imaging resolution is indeed dominated by the detector energy resolution. Note that, again, resolution was simulated as a Gaussian smearing applied uniformly to each hit in a photon track. The detector energy resolution does not reflect the full width of the Doppler-shifted peak in an uncorrected spectrum – it is simply the uncertainty in measuring the energy deposition for a specific interaction.

The results are very promising – Gaussian estimates of imaging resolution (σ_{img}) range from a mere 3.03 mm at perfect detector position resolution to 6.77 mm at 10.0 mm position resolution (with constant $\sigma_E = 2.0$ keV detector energy resolution). For comparison, the Compton imaging resolution increased from 6.57 mm to 63.89 mm over the same range. As expected, detector energy resolution plays a greater role in Doppler-shift imaging. With constant $\sigma_{xyz} = 3.0$ mm detector position resolution, σ_{img} ranges from 2.18mm to 14.43 mm for σ_E between 0.0 keV and 10.0 keV. For a typical detector with 3.0 mm position- and 2.0 keV energy-resolution, Doppler-shift imaging yields 6.3x better imaging resolution and 2.4x better efficiency than Compton imaging.

Doppler-shift imaging also highly-sensitive to the CM-frame photopeak energy of the photon – though this is something I did not study in great detail. For example, if we knew the photopeak energy only to within 10's of keV, Doppler-shift images would likely be significantly worse than the corresponding Compton images (assuming the same detector position resolution). On the other hand, since we only need the first hit in a track, we can use much lower-energy photons than we can in Compton imaging. The imaging efficiency of this method is much higher than for Compton imaging across all energies from 150 keV to 4 MeV. Incorrect sequencing also has much less of an effect. However, we still use Compton tracking to determine the quality of fit to kinematics – this is one of the few ways to reject background counts in Doppler-shift imaging.

The imaging response also depends on the true location of emissions along the beamline, as noted already for Compton imaging. I was able to extract this z-dependence by

Position Resolution	**Imaging Resolution (mm)**	**Efficiency (Absolute, %)**	**Efficiency (Relative, %)**
0.0 mm	3.03 ± 0.02	72.151 ± 0.122	100.000 ± 0.239
0.25 mm	3.06 ± 0.02	72.111 ± 0.122	99.944 ± 0.239
0.50 mm	3.11 ± 0.02	72.079 ± 0.122	99.901 ± 0.239
0.75 mm	3.17 ± 0.03	72.053 ± 0.122	99.864 ± 0.239
1.0 mm	3.33 ± 0.04	72.0276 ± 0.122	99.829 ± 0.239
1.5 mm	3.47 ± 0.04	71.996 ± 0.122	99.785 ± 0.239
2.0 mm	3.63 ± 0.03	71.971 ± 0.122	99.751 ± 0.238
2.5 mm	3.80 ± 0.03	71.952 ± 0.122	99.724 ± 0.238
3.0 mm	3.97 ± 0.03	71.934 ± 0.122	99.699 ± 0.238
4.0 mm	4.35 ± 0.04	71.909 ± 0.122	99.664 ± 0.238
5.0 mm	4.70 ± 0.05	71.873 ± 0.122	99.614 ± 0.238
7.5 mm	5.83 ± 0.08	71.818 ± 0.122	99.538 ± 0.238
10.0 mm	6.77 ± 0.12	71.756 ± 0.122	99.452 ± 0.238

Table 5.1: Doppler-shift image quality & efficiency vs. position resolution
$E_{CM} = 1000$ keV, $\beta = 0.3$, $\tau_0 = 2.7525$ ns, $\sigma_E = 2.0$ keV
Total Tracks: 2.365M, Plausible Energy: 0.832M-0.836M, Imaged Tracks: 0.597M-0.605M

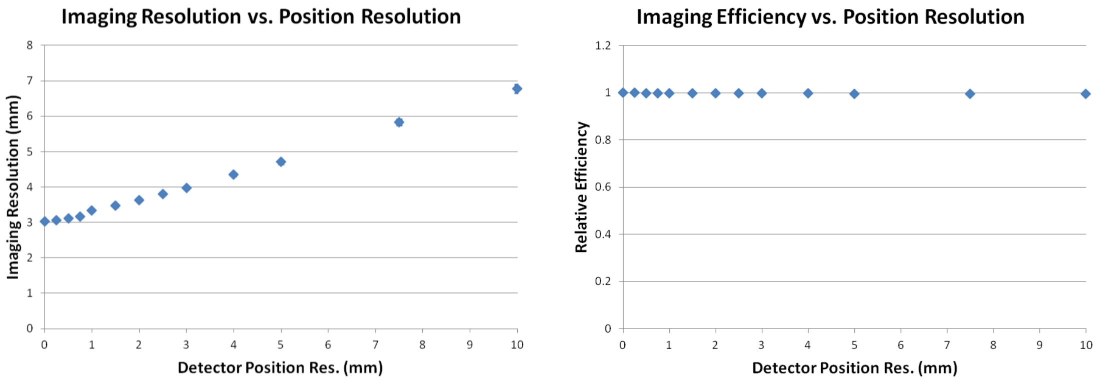

Figure 5.3: Doppler-shift image quality & efficiency vs. detector position resolution
See Table 5.1

Energy Resolution	**Imaging Resolution (mm)**	**Efficiency (Absolute, %)**	**Efficiency (Relative, %)**
0.0 keV	2.18 ± 0.06	72.099 ± 0.122	100.000 ± 0.239
0.25 keV	2.22 ± 0.06	72.093 ± 0.122	99.992 ± 0.239
0.50 keV	2.32 ± 0.05	72.084 ± 0.122	99.978 ± 0.239
0.75 keV	2.64 ± 0.05	72.076 ± 0.122	99.968 ± 0.239
1.0 keV	2.82 ± 0.04	72.037 ± 0.122	99.914 ± 0.239
1.5 keV	3.39 ± 0.04	72.010 ± 0.122	99.877 ± 0.239
2.0 keV	3.97 ± 0.03	71.934 ± 0.122	99.771 ± 0.239
2.5 keV	4.59 ± 0.04	71.861 ± 0.122	99.669 ± 0.238
3.0 keV	5.23 ± 0.04	71.814 ± 0.122	99.604 ± 0.238
4.0 keV	6.59 ± 0.05	71.677 ± 0.121	99.414 ± 0.238
5.0 keV	7.92 ± 0.05	71.549 ± 0.121	99.236 ± 0.238
7.5 keV	11.21 ± 0.06	71.236 ± 0.121	98.802 ± 0.237
10.0 keV	14.43 ± 0.07	70.860 ± 0.120	98.282 ± 0.236

Table 5.2: Doppler-shift image quality & efficiency vs. energy resolution
$E_{CM} = 1000$ keV, $\beta = 0.3$, $\tau_0 = 2.7525$ ns, $\sigma_{xyz} = 3.0$ mm
Total Tracks: 2.365M, Plausible Energy: 0.834M-0.835M, Imaged Tracks: 0.591M-0.605M

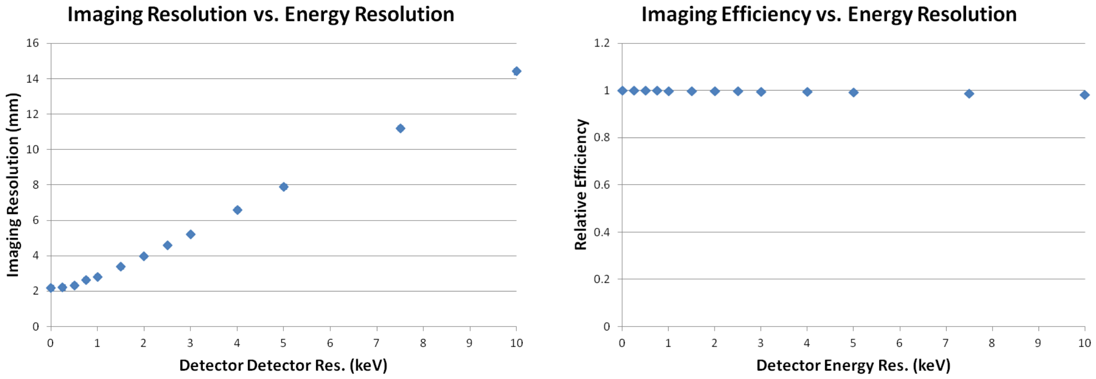

Figure 5.4: Doppler-shift image quality & efficiency vs. detector energy resolution
See Table 5.2

binning the z-axis and drawing comparisons of $|z_{true} - z_{calc}|$ for several 10.0 mm-wide bins. Figure 5.5 shows this effect – the imaging resolution improves from 4.67 ± 0.16 mm at z_0 = 0.0 mm to 3.90 ± 0.05 mm at z_0 = 90.0 mm. (Imaging efficiency also rose from 6.221 ± 0.028% to 8.165 ± 0.033% over this same range.) However, I did not study it in great detail or account for it in subsequent work in lifetime measurements.

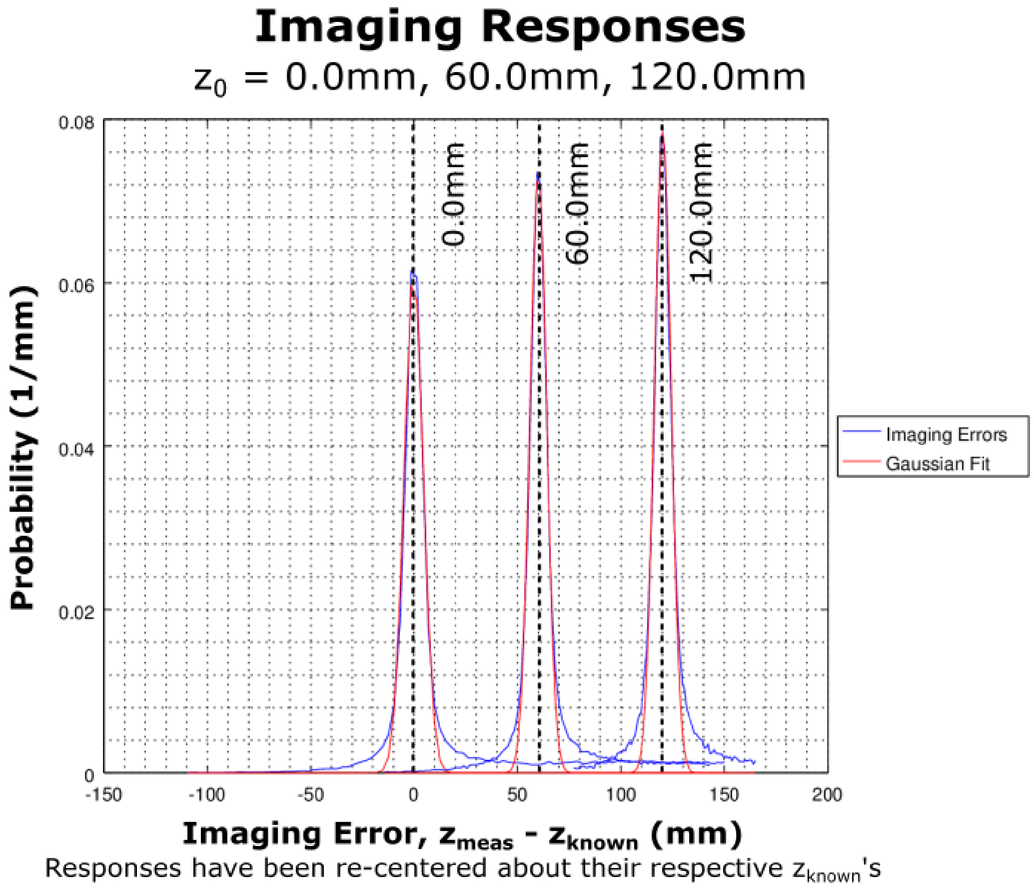

Figure 5.5: Doppler-shift image quality at various points along the beam axis

In addition, the properties of the parent beam affect Doppler-shift reconstructions more directly than they do Compton reconstructions. The parent lab-frame velocity, βc, is explicitly required to solve for the emission point. By contrast, Compton imaging in principle should yield a similar imaging resolution and efficiency regardless of beam velocity (even down to stationary sources). Because Doppler-shift imaging is sensitive to beam velocity, it works best when the beam itself is tightly constrained about a single velocity. β should vary only slightly; in our simulations, we use $\beta = 0.3 \pm 0.001$. The uncertainty here is a combination of kinematics and straggling in the target. Nuclear reactions with two or more products always have some angular distribution for the outgoing particles. On top of that, the charged products interact with the target itself on their way out, causing small changes in their headings. Thicker targets will produce more straggling in the recoil nuclei, yielding less-constrained beams (both in terms of velocity and angle) for a given incident particle energy. As with Compton imaging, the same issues apply here when emissions do not occur directly on the $\hat{\boldsymbol{z}}$-axis. (See Section A.6.)

Despite the apparently excellent imaging performance of this method, images of de-excitation curves are visibly inaccurate. In Figure 5.6, the blue curves are the known emission distributions for *detected* photons, while the red curves are their corresponding images. The imaged curves tend to underestimate counts near the target while overestimating them farther downstream. This problem is caused by the Compton background counts used in the reconstruction. (Recall that we must initially accept *all* counts where the measured lab-frame energy lies in the Doppler-shifted energy range of the photopeak.) Now, the emission angle θ is *calculated* from the detected lab-frame energy (E_{Lab}) and known CM-frame photopeak energy (E_{CM}) of the photon:

$$\mu = \cos\theta = \frac{1}{\beta}\left(1 - \frac{E_{CM}}{\gamma E_{Lab}}\right) \tag{5.3}$$

where βc is the parent nucleus's speed in the lab frame. Consider that photons from the Compton background deposit only part of their energy in the detector. From this formula, we can see that μ decreases as E_{Lab} decreases. Therefore, θ *increases* with decreasing measured E_{Lab} (at least over the range 0° to 180°). In other words, we tend to overestimate the emission angles for Compton background counts.

Referring back to Figure 5.1, $\boldsymbol{X_0}$ is the photon's emission point and $\boldsymbol{X_1}$ is the location of track's first hit in the detector. If we keep $\boldsymbol{X_1}$ fixed while increasing θ, we can see that $\boldsymbol{X_0}$ gets shifted downstream. So, photons that deposit less than their full energy in the detector will produce computed emission points downstream of their true locations. It is somewhat difficult to see in Figure 5.6, but the imaging responses each have long "tails" in which $z_{meas} - z_{known}$ is fairly large. For the ideal case with perfect detector resolution, the tail contains about 10% of the total counts. The deviation between the measured and known emission distribution is – not coincidentally – also about 10% of the total counts. (We can verify that this is the case with simulations, where we know the true emitted lab-frame energies for each track. By filtering out partial-energy tracks, the long tail of the imaging response disappears, and the known and imaged source distributions line up precisely.)

Note that these imaging deviations are not the end of the world for lifetime measurements. As long as the imaging response is well-characterized, we can correct for systematic errors in output images. It is important to retain the full shape of the response – including both the Gaussian-shaped peak and the long tail from the Compton background. We will discuss this in greater detail in Section 6.2.

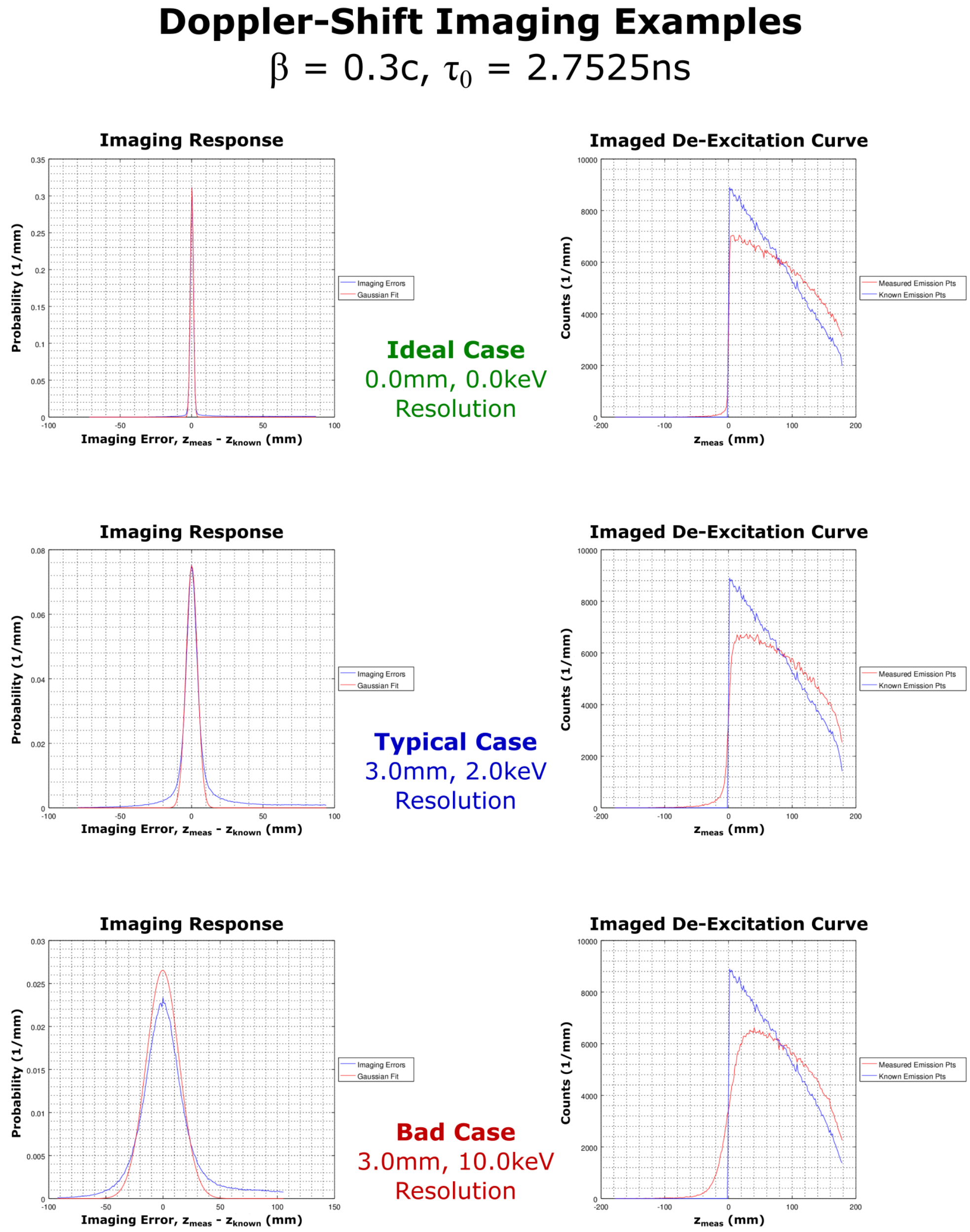

Figure 5.6: Sample Doppler-shift images
For a range of detector position and energy resolutions

5.3 Image Quality Cuts

In Compton imaging, there are multiple parameters that can be tuned in post-processing to optimize imaging quality and efficiency. Doppler-shift imaging offers less flexibility in this regard – we cannot use corrected CM-frame energy to reject background counts, for example. Even still, Doppler-shift imaging generally offers much better imaging performance than its Compton counterpart. There are also multiple data filters available to reduce Compton background.

Doppler-shift imaging faces a different set of challenges than does Compton imaging. However, we face a similar problem in trying to optimize imaging quality. As before, there are some parameters that can be tuned in data analysis, and some that are characteristics of the experimental setup. Table 5.3 categories the parameters that affect imaging into these two camps. This section is dedicated to the parameters we can optimize in post-processing.

Experimental Parameters	**Analytical Parameters**
Photon energy	Sequencing FoM
Position resolution	Track length
Energy resolution	Emission angle
Beam velocity	Proximity to segment bounds

Table 5.3: Parameters that affect Doppler-Shift imaging quality

I used the same simulated data as in Section 4.3. The parent nuclei have a 2.7525 ns lifetime, 0.3 ± 0.001c lab-frame velocity, and 1.0 MeV CM-frame gamma-ray emission energy. The detector was assumed to have $\sigma_{xyz} = 3.0$ mm and $\sigma_E = 2.0$ keV position and energy resolution. As before, each track was sent through Compton sequencing. I then applied the Doppler-shift image reconstruction algorithm to obtain a computed emission point, $X_{0,calc}$, and compared this to the true emission point $X_{0,true}$ that Geant4 provided for each track. (The imaging error is thus given by $\Delta X_0 = X_{0,calc} - X_{0,true}$.) Lastly, I estimated the imaging resolution σ_{img} by fitting a Gaussian to these computed imaging errors.

Note that since we only use the first hit in a photon track, there are no Compton lever arms to account for. In addition, I did not have experimental data to test quality of reconstruction vs. proximity of hits to crystal segment boundaries. Compton imaging works with stationary calibration sources. Doppler-shift imaging does not. As with Compton imaging, analytic error estimates might be useful here too (refer to Appendix A.8), but I did not have time to study it further as a data filter.

The main challenge is removing Compton background events. Recall from Section 5.1 that Doppler-shift imaging *assumes* that each track is a full-energy event. We can still restrict tracks to a range of possible energies, as discussed in Section 4.3. However, unlike in Compton Imaging, we can't use the calculated emission point to perform a sanity check on the Doppler-shifted energy. We're using that Doppler-shift itself to calculate the emission point. Therefore, we must rely on other filters to throw out these partial-energy photons.

The FoM used in Compton sequencing provides one such filter. Tracks with higher sequencing FoMs do not match Compton kinematics very well, suggesting that they may not actually be full-energy events. As in Section 4.3, I set a maximum FoM limit for photon tracks. The results are shown in Table 5.4 and Figure 5.7. Overall, there is only a small improvement in the estimated imaging resolution. However, this metric is only one way to gauge imaging quality. A visual inspection of the output images shows they match the known emission distributions more closely. While I did not explore other metrics in detail, an R^2 calculation would prove useful to quantify the similarity between the measured and known emission distributions.

Another possibility for removing Compton background lies in track length. Recall from Section 3.2 that high-energy photons generally must scatter one or more times before photo-absorption becomes likely. This means that tracks with few hits often correspond to partial-energy depositions. Figure 3.5 shows the distribution for 1.0 MeV photons. Near this energy, any tracks with three or fewer hits are more likely to be partial- rather than full-energy events. To explore this further, I set a gate on the minimum track length used for imaging. Table 5.5 and Figure 5.8 provide the results. It is somewhat surprising here that imaging resolution actually *worsens* slightly as we increase the required track length. However, the reason is straightforward – longer tracks are also more likely to introduce sequencing errors (refer to Table 3.6). As with the sequencing FoM filter, however, there are notable visual improvements in the imaged source distributions.

The final data cut I explored works through the calculated emission angle. As noted towards the end of Section 5.2, Compton background counts tend to overestimate the emission angle relative to the beamline. Therefore, we can preferentially reject partial-energy tracks by requiring emission angles to be below a given limit. Fundamentally, this is an energy gate – emission angles are calculated directly using the measured lab-frame energy and Equation 5.2. In Table 5.6 and Figure 5.9, I varied the minimum value of $\mu = \cos\theta$ to see the effects on imaging quality. As with the other two filters, the imaging resolution is largely unaffected despite huge numbers of counts being thrown out. However, the imaged source distributions do start to match the true distributions much more closely as we lower the maximum emission angle (i.e. increase minimum μ).

Maximum Sequencing FoM	**Imaging Resolution (mm)**	**Efficiency (Absolute, %)**	**Efficiency (Relative, %)**
1E-1	3.98 ± 0.04	71.858 ± 0.122	100.000 ± 0.239
1E-2	3.98 ± 0.04	71.440 ± 0.121	99.418 ± 0.238
3E-3	3.90 ± 0.04	68.123 ± 0.117	94.802 ± 0.229
1E-3	3.88 ± 0.04	58.040 ± 0.105	80.770 ± 0.200
3E-4	3.87 ± 0.04	38.432 ± 0.080	53.483 ± 0.143
1E-4	3.80 ± 0.05	20.998 ± 0.055	29.221 ± 0.091
3E-5	3.71 ± 0.04	9.589 ± 0.035	13.344 ± 0.054
1E-5	3.88 ± 0.07	4.818 ± 0.025	6.705 ± 0.036
3E-6	4.30 ± 0.17	2.383 ± 0.017	3.316 ± 0.024
1E-6	4.31 ± 0.21	1.300 ± 0.013	1.810 ± 0.018

Table 5.4: Doppler-shift image quality & efficiency vs. maximum sequencing FoM
E_{CM} = 1000 keV, $\beta = 0.3$, $\tau_0 = 2.7525$ ns, $\sigma_{xyz} = 3.0$ mm, $\sigma_E = 2.0$ keV
N_{hits} = 3 - 6, $\cos\theta_{max}$ = -1
Total Tracks: 2.365M, Plausible Energy: 0.836M, Imaged Tracks: 0.011M-0.601M

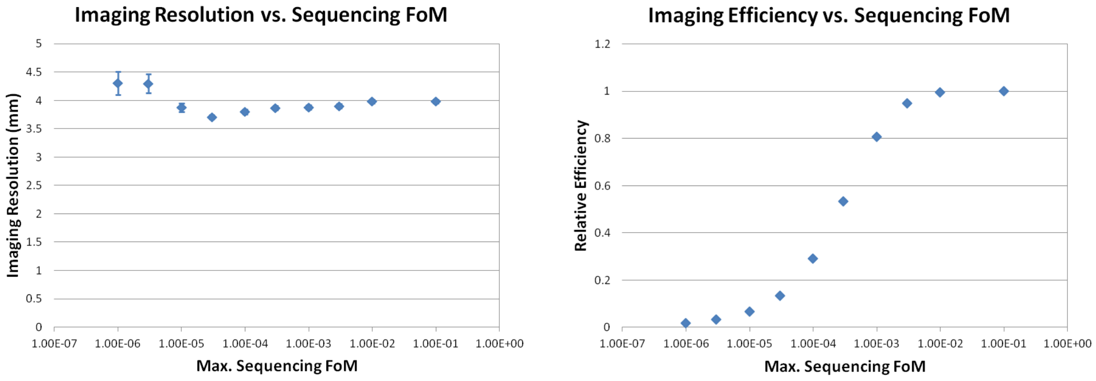

Figure 5.7: Doppler-shift image quality & efficiency vs. max. sequencing FoM
See Table 5.4

Minimum Track Length	**Imaging Resolution (mm)**	**Efficiency (Absolute, %)**	**Efficiency (Relative, %)**
1 hit	3.76 ± 0.04	94.816 ± 0.149	100.000 ± 0.222
2 hits	3.89 ± 0.04	91.607 ± 0.145	96.615 ± 0.216
3 hits	4.02 ± 0.04	79.349 ± 0.131	83.688 ± 0.191
4 hits	4.22 ± 0.04	58.056 ± 0.105	61.230 ± 0.147
5 hits	4.36 ± 0.04	35.209 ± 0.076	37.134 ± 0.099
6 hits	4.69 ± 0.05	17.614 ± 0.050	18.577 ± 0.060
7 hits	4.74 ± 0.08	7.184 ± 0.030	7.577 ± 0.034
8 hits	5.34 ± 0.11	2.102 ± 0.016	2.217 ± 0.017

Table 5.5: Doppler-shift image quality & efficiency vs. maximum sequencing FoM
$E_{CM} = 1000$ keV, $\beta = 0.3$, $\tau_0 = 2.7525$ ns, $\sigma_{xyz} = 3.0$ mm, $\sigma_E = 2.0$ keV
$FoM_{max} = 1\text{E}0$, $\cos\theta_{max} = -1$
Total Tracks: 2.365M, Plausible Energy: 0.831M, Imaged Tracks: 0.017M-0.788M

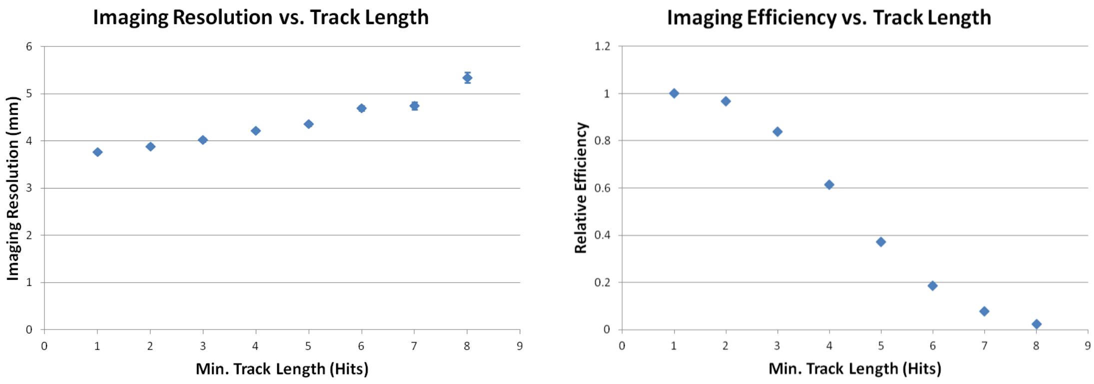

Figure 5.8: Doppler-shift image quality & efficiency vs. min. track length
See Table 5.5

Maximum $\cos\theta$	**Imaging Resolution (mm)**	**Efficiency (Absolute, %)**	**Efficiency (Relative, %)**
-1.00	3.98 ± 0.04	71.858 ± 0.122	100.000 ± 0.239
-0.85	3.98 ± 0.04	71.858 ± 0.122	100.000 ± 0.239
-0.70	3.98 ± 0.04	71.641 ± 0.121	99.698 ± 0.239
-0.55	3.87 ± 0.03	69.733 ± 0.119	97.043 ± 0.233
-0.40	3.88 ± 0.03	65.371 ± 0.114	90.972 ± 0.221
-0.25	3.73 ± 0.04	57.932 ± 0.105	80.620 ± 0.199
-0.10	3.72 ± 0.03	48.045 ± 0.092	66.860 ± 0.171
0.00	3.70 ± 0.03	40.760 ± 0.083	56.723 ± 0.150
0.10	3.69 ± 0.03	33.316 ± 0.073	46.363 ± 0.128
0.25	3.74 ± 0.03	22.231 ± 0.057	30.938 ± 0.095
0.40	3.98 ± 0.04	11.867 ± 0.040	16.515 ± 0.062
0.55	4.33 ± 0.06	3.959 ± 0.022	5.509 ± 0.032
0.70	5.68 ± 0.23	0.270 ± 0.006	0.375 ± 0.008

Table 5.6: Doppler-shift image quality & efficiency vs. maximum emission angle
E_{CM} = 1000 keV, $\beta = 0.3$, $\tau_0 = 2.7525$ ns, $\sigma_{xyz} = 3.0$ mm, $\sigma_E = 2.0$ keV
FoM_{max} = 1E0, N_{hits} = 3 - 6
Total Tracks: 2.365M, Plausible Energy: 0.831M, Imaged Tracks: 0.017M-0.788M

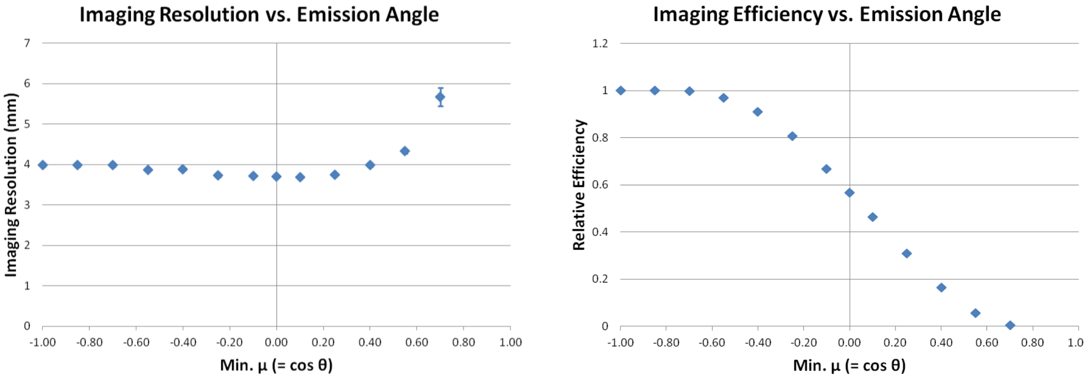

Figure 5.9: Doppler-shift image quality & efficiency vs. max. emission angle
See Table 5.6

Unlike the other two data cuts, though, this last filter brings about some interesting geometric effects. Generally, the farther downstream an emission occurs, the larger its emission angle must be in order to hit a detector. Filtering tracks above a set emission angle limit therefore has a greater affect on emissions farther downstream on the beamline. Above any given limit, it is no longer possible to observe emissions past a certain point. To illustrate, suppose GRETINA's detectors are placed in a ring perpendicular to the beamline and centered about the target at $z = 0.0$ mm. A photon detected at $z = 135.0$ mm would register an emission angle around $\theta = 235°$ ($\mu = -0.57$). So, setting $\mu > -0.55$ would throw out all emissions that are 135.0 mm (or more) downstream of the target.

Figure 5.10 shows sample images for the three data filters. The image where emission angle has been restricted to $\mu > 0.4$ appears to have a much shorter lifetime than the other two, because the downstream counts have all been removed. However, the remaining curve matches very closely with the known emission points, with very little noise from Compton background. As long as we characterize the detector response precisely, we *should* theoretically be able to use such images in lifetime measurements. However, for lack of time I did not study this angular filter further than this simple test.

Lastly, note that the usual statistics trade-off is especially difficult to apply here. Ideally, we want any reduction in counts to improve imaging resolution more than the corresponding degradation from loss of statistics:

$$\frac{\sigma_{img,filt}}{\sigma_{img,0}} < \frac{\sqrt{N_{counts,filt}}}{\sqrt{N_{counts,0}}} \tag{5.4}$$

where $\sigma_{img,0}$ and $N_{counts,0}$ are the unfiltered results and $\sigma_{img,filt}$ and $N_{counts,filt}$ are the corresponding filtered results. However, we can see from Tables 5.4 to 5.6 that none of the data cuts offer significant improvements to imaging resolution. As we discussed at the end of Section 5.2, the peaks in the imaging responses correspond almost entirely to the full-energy tracks. It's the Compton background that creates the long tails we observe (where $z_{meas} - z_{known}$ is large). So the main advantage of our data filters here lie in the reduction of this Compton background. It is therefore more difficult to quantify ideal choices for each data cut.

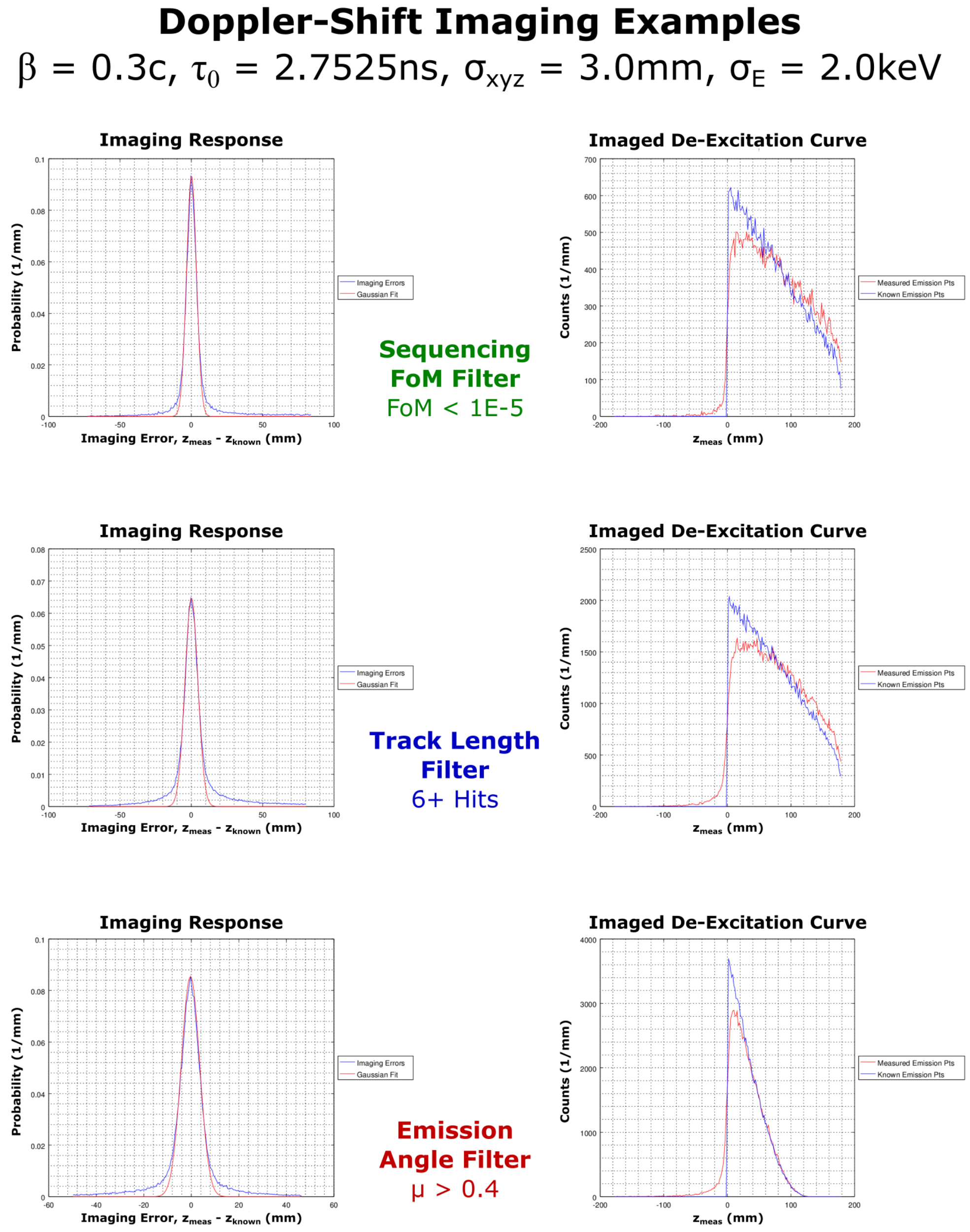

Figure 5.10: Sample Doppler-shift images (with data filters)
With various data filters applied

Chapter 6

Lifetime Measurements

6.1 Introduction to Lifetime Measurements

The simplest lifetime measurement involves a parent nucleus with proper lifetime τ_0 and lab-frame velocity β, which emits a single characteristic photon of energy E_0 in the CM-frame. The random de-excitation of these parent nuclei produces an exponential source distribution along the beamline. (Note that a nucleus's travel distance directly corresponds to its emission time.) Our job is to gather enough statistics to produce an image of this exponential decay, and then extract the lifetime from it. Doing so is largely independent of our choice of imaging mode – what matters is the imaging response and effective imaging resolution. Images from known calibration measurements or simulations can be used to characterize this resolution.

All methods of measuring nuclear lifetimes involve sampling a decay curve in some fashion. In the recoil-distance method (RDM), one places a degrader foil downstream of the target, which slows the parent nuclei to a lower speed. Photons emitted upstream of this degrader will have a measurable Doppler-shift in the lab frame (see Equation 2.19). Photons emitted downstream of the degrader will have little to no shift. So, by comparing the number of Doppler-shifted counts to the number of counts with lesser or no shift, one obtains the fraction of nuclei that de-excite upstream of the degrader. Note that because the beam recoil velocity is known, the distance between the target and degrader directly translates to flight time. Accounting for relativistic time dilation, the proper de-excitation time in the CM-frame (t_0) is:

$$z = vt = (\beta c)(\gamma t_0) = \gamma\beta c t_0 \tag{6.1}$$

where βc is the lab-frame velocity of the parent nucleus, γ is the corresponding Lorentz factor, and τ_0 is the parent's lifetime in the CM-frame. Each position along the beamline corresponds to a different time. So, by moving the degrader to several positions and repeating the measurement, one obtains the fraction of nuclei that de-excite as a function of distance (i.e. flight time). Fitting an exponential decay function to these samples then yields the proper lifetime, τ_0. As the reader can surmise, this technique is rather laborious and requires beamtime for each additional sample of the de-excitation curve.

Alternately, we could conceivably measure lifetimes electronically – if the nuclear lifetime and travel times are long enough. The method is well-known, and uses a combination of synced HPGe and multichannel plate detectors. First, the ions produced in the target go through a magnetic separator to select only the parent nuclei of interest. The selected nuclei then pass through a pair of plate detectors, which record a timestamp $t_{1,n}$ and velocity $\beta_n c$ for the nth nucleus that passes through. After that the particles are caught in a beam stop, where they sit until they de-excite. Finally, the de-excitations are measured by an HPGe detector, which records a timestamp $t_{2,n}$ for each detected photon. If the distance from the target to the multichannel detectors is x_{mcd}, then the time-of-flight is simply $t_{flight,n} = x_{mcd}/\beta_n c$. The total de-excitation time (as measured in the lab frame) for the nth parent nucleus is thus:

$$
\begin{aligned}
t_{lab,n} &= t_{flight,n} + (t_{2,n} - t_{1,n}) && (6.2)\\
&= x_{mcd}/\beta_n c + (t_{2,n} - t_{1,n}) && (6.3)
\end{aligned}
$$

Finally, accounting for time dilation, the proper time of the nth de-excitation is:

$$
t_{lab,n} = \frac{x_{mcd}}{\gamma \beta_n c} + \frac{1}{\gamma}(t_{2,n} - t_{1,n}) \tag{6.4}
$$

From here we can build a distribution of de-excitation times and extract the lifetime. Note, however, that we are limited by the travel distances involved. (Consider that an ion moving at 0.1c takes 100 ns to travel 3.0 m, which is about the minimum length needed to install all the necessary components.) Therefore, this method is not well-suited for the gamma de-excitations we aim to study through imaging, which occur on timescales of 10's of picoseconds to a few nanseconds.

Measuring lifetimes is much simpler with gamma-ray imaging. Here, we trace each photon back to its emission point along the beamline, converting each distance to a time-of-flight. With enough counts, we can build a de-excitation curve and extract the lifetime. The appeal of this technique is that it can reconstruct an entire de-excitation curve with a single measurement, without any additional equipment.

In the simplest case, we measure a single nuclear transition that neither feeds – nor is fed by – any other transitions. In such situations, there is a single lifetime τ_0 to consider, and the density of emissions downstream of the target will follow a simple exponential decay:

$$
\begin{aligned}
S(z) &= Ae^{-\mu z} && (6.5)\\
&= Ae^{-z/\gamma\beta c\tau_0} && (6.6)
\end{aligned}
$$

where z is the distance from the target, $\mu = 1/\gamma\beta c\tau_0$, and A is a scaling factor. This factor is found by normalizing the curve to the number of emissions N_{counts} observed between the target and end of imaging window (z_{end}):

$$N_{counts} = \int_0^{z_{end}} Ae^{-\mu z} dz \tag{6.7}$$

$$= -(A/\mu)e^{-\mu z}\Big|_0^{z_{end}} = (A/\mu)(1 - e^{-\mu z_{end}}) \tag{6.8}$$

$$A = N_{counts} \frac{\mu}{1 - e^{-\mu z_{end}}} \tag{6.9}$$

Note that A has the correct units for a density function (counts per length).

When the state of interest is part of a de-excitation chain, however, the shape of the curve no longer follows a simple exponential. For example, consider a simple two-state system where the parent state has lifetime $\tau_{0,p} = 1/\gamma\beta c\mu_p$ and the daughter state has lifetime $\tau_{0,d} = 1/\gamma\beta c\mu_d$. This is a textbook problem (see pages 170-172 in Ref. [21]). The source distribution $S_d(z)$ is found:

$$S_p(z) = A_p e^{-\mu_p z} \tag{6.10}$$

$$S_d(z) = A_d(e^{-\mu_p z} - e^{-\mu_d z}) \tag{6.11}$$

$$A_d = A_p \left(\frac{\mu_p}{\mu_d - \mu_p}\right) \tag{6.12}$$

$$= N_{counts} \left(\frac{\mu_p}{1 - e^{-\mu z_{end}}}\right) \left(\frac{\mu_p}{\mu_d - \mu_p}\right) \tag{6.13}$$

The shape is ultimately determined by the the relative lifetimes of the parent and daughter. For example, in a system where the parent is very long-lived compared to the daughter, such that $\mu_d >> \mu_p$:

$$S_d(z) = N_{counts} \left(\frac{\mu_p}{1 - e^{-\mu z_{end}}}\right) \left(\frac{\mu_p}{\mu_d}\right) (1 - e^{-\mu_d z}) \tag{6.14}$$

This leads to secular equilibrium, where the countrate from the daughter is fundamentally limited by the de-excitations of the parent. If the parent lifetime is too long, then we will not be able to use imaging to study the lifetime of either state. The source distributions will simply appear flat across the entire imaging range, and we will likely have low statistics to work from.

The source distributions of more complex de-excitation chains can be solved using the Bateman equations. (Pg. 173 in Reference [21]) In such cases, we must have prior knowledge of the lifetimes for all parent states feeding the state of interest. Complex chains may also produce significant background. Recall that relativistic Doppler-shifts can cause peaks to overlap even if they are several hundred keV apart in the CM-frame. For this study, I avoid such complications and focus on simple single-transition systems.

6.2 Curve Fitting and the Inverse Imaging Problem

Our goal in lifetime measurements is to reproduce the exponential source distribution for photons along the beamline. Once we have that curve, we can fit an exponential to it to determine the nuclear lifetime. As with all imaging problems, however, we must deal with the effects of finite resolution. For any true emission point z_0, there is some probability that the emission will instead register at z. We call this probability function the "detector response". Because we can measure or simulate the detector response beforehand, it is possible to correct for it in lifetime measurements. I chose the χ^2 Minimization method over Singular-Value-Decomposition (SVD) due to the better stability of the former algorithm.

We seek to use gamma-ray imaging to reproduce the source distribution for nuclei that de-excite downstream of the target. As mentioned earlier, the ideal distribution is a simple exponential decay function given by Equation 6.5. However, imaging does not recreate source distributions with perfect accuracy. This is clearly seen in Figure 6.1, which shows the differences in true versus imaged emission points for a Compton imaging test. (However, the concept applies equally to Doppler-shift images as well.) For any true emission point z_0, there is a distribution $P(z, z_0)$ that reflects the probability that the emission will instead register at z. We call this probability density function the "detector response". For the rest of this discussion, we will divorce ourselves from the specific type of imaging method used, and focus instead on the imaging *resolution* as the primary parameter of interest.

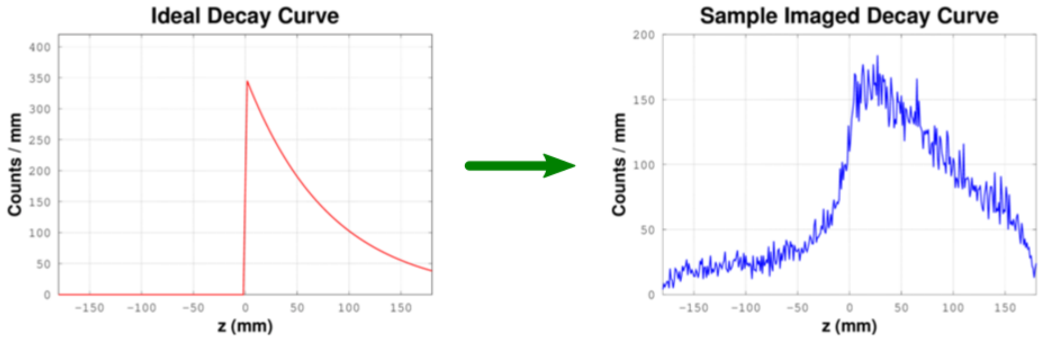

Figure 6.1: Sample comparison of true and imaged source distributions
$\tau_0 = 0859$ ns, $\beta = 0.3$, $\sigma_{xyz} = 3.0$ mm, $\sigma_E = 2.0$ keV
The "transformation kernel" is the detector response matrix, $P(z, z_0)$

The detector response serves to smear the true source distribution into an imaged one. By discretizing z and z_0 into bins, this convolution can be represented by the matrix equation:

$$R(z) = P(z, z_0)S(z_0) \tag{6.15}$$

where $R(z)$ gives the imaged source distribution. Note that $R(z)$ is an $M \times 1$ column vector, where M is the number of distinct bins forming the imaging space on the beam axis. $S(z_0)$ is an $N \times 1$ column vector, where N is the number of distinct z's for which a detector response distribution is measured. This makes $P(z, z_0)$ an $M \times N$ matrix, where the *nth* column represents the detector response function for the *nth* z_0 bin.

Depending on how bad the imaging resolution is, the imaged de-excitation curve may deviate significantly from an exponential shape. (Again, see Figure 6.1.) This of course complicates the curve-fitting process we would use to extract the lifetime. Generally speaking, the convolution in Equation 6.15 will move counts from the peak of the exponential to somewhere upstream of the beam target, rounding the top of the imaged source distribution and making the slope of the decay more shallow. Therefore, fitting a simple exponential to this shape will return a measured lifetime longer than the true lifetime.

Geometric efficiency also plays a role here. GRETINA is not a full 4π array, and so emissions can escape the central cavity without passing through a detector. GRETINA's geometric efficiency is 25% for an isotropic point source at the center of the array, but things are more complicated for moving sources. Recall that emissions become more and more forward-directed in the lab frame as the source velocity increases. In addition, the detector solid angle "seen" by a parent nucleus changes as the nucleus moves down the beamline. Geometric efficiency is therefore a function of both source velocity and emission location. Because of this, the measured source distribution will not be perfectly exponential – even with perfect imaging resolution. The effect can be seen clearly in Figure 6.2. The thin lines represent the measured emission points in three categories – total emissions, *detected* emissions, and emissions which missed the detectors entirely. The thicker lines are idealized de-excitation curves for each category, given the number of emissions and the known parent lifetime and velocity. One can see that the detected emissions fall short of the exponential shape due to losses in geometric efficiency. In general, each detector response function $S(z_0)$ should be renormalized to the geometric efficiency at z_0. For simplicity, I ignored this correction in my simulations.

There are a couple common methods to correct for smearing in the source distribution. $P(z, z_0)$ is a measurable property of the specific detector and imaging method employed. We could obtain it through a calibration experiment using a nucleus of known lifetime. Here, though, I obtained simulated detector response curves from the Geant4 GRETINA model. Once we have the $P(z, z_0)$ matrix, we can then use either Singular-Value-Decomposition (SVD) or a χ^2 Minimization to account for the imaging response. [1] [34]

In SVD, the goal is to find the pseudo-inverse of the detector response, $P^{-1}(z_0, z)$, in order to calculate the "true" source distribution:

$$S(z_0) = P^{-1}(z_0, z)R(z) \tag{6.16}$$

Theoretically, this correction should let us fit an exponential directly to the curve $S(z_0)$.

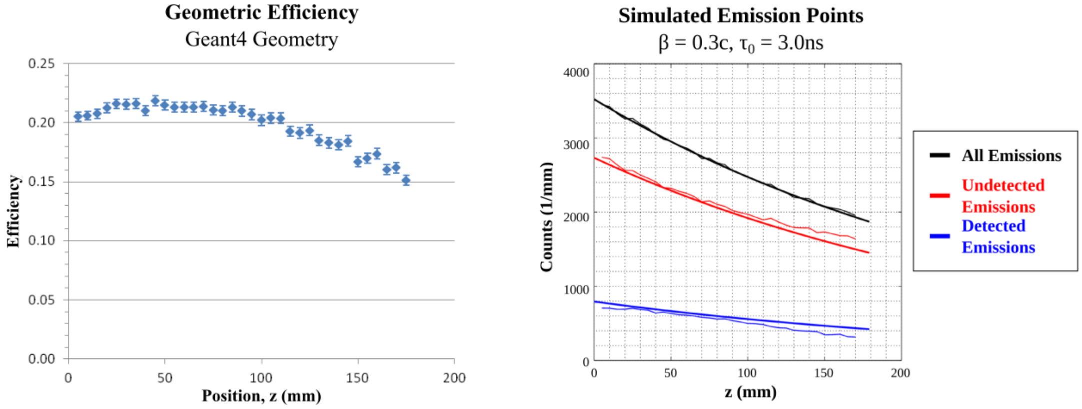

Figure 6.2: Geometric efficiency in GRETINA

However, noise amplification is a well-known problem in SVD. [31] We therefore found it ill-suited for our simulated lifetime measurements. The algorithm is highly-sensitive to our choice of z and z_0 bins, which obviously have nothing to do with the underlying data. [19] Yet SVD imposes an arbitrary requirement to optimize binning for the output images.

The χ^2 Minimization method avoids these issues entirely, though conceptually it is more complicated (and *significantly* more computationally-intensive). In SVD, we work backwards from the image $R(z)$ to calculate an approximate source distribution $S(z_0)$. The χ^2 approach is almost the opposite – we start with a hypothetical source $S'(z_0)$, then convolve it with the response matrix $P(z, z_0)$ to arrive at a hypothetical image, $R'(z)$. (See Figure 6.3) We then compare this hypothetical $R'(z)$ image with the measured image, $R(z)$, computing a χ^2 value:

$$\chi^2 = \sum_{n=1}^{N} \frac{(R(z_n) - R'(z_n))^2}{\sigma^2_{R'(z_n)}} \tag{6.17}$$

$$= \sum_{n=1}^{N} \frac{(R(z_n) - R'(z_n))^2}{R'(z_n)} \tag{6.18}$$

Here, $\sigma^2_{R'(z_n)} = R'(z_n)$, and N is the number of z bins used to characterize image distributions. To avoid edge effects from histogram binning in the images, I omitted the first and last bins from the comparison.

Conceptually, this approach has similarities to the signal decomposition algorithm discussed in Section 2.5. Where GRETINA uses a grid of computed basis signals to compare against a measured signal, here we compare a set of hypothetical imaged de-excitation curves to the measured image. We begin by hypothesizing values of τ_0, then use an iterative method

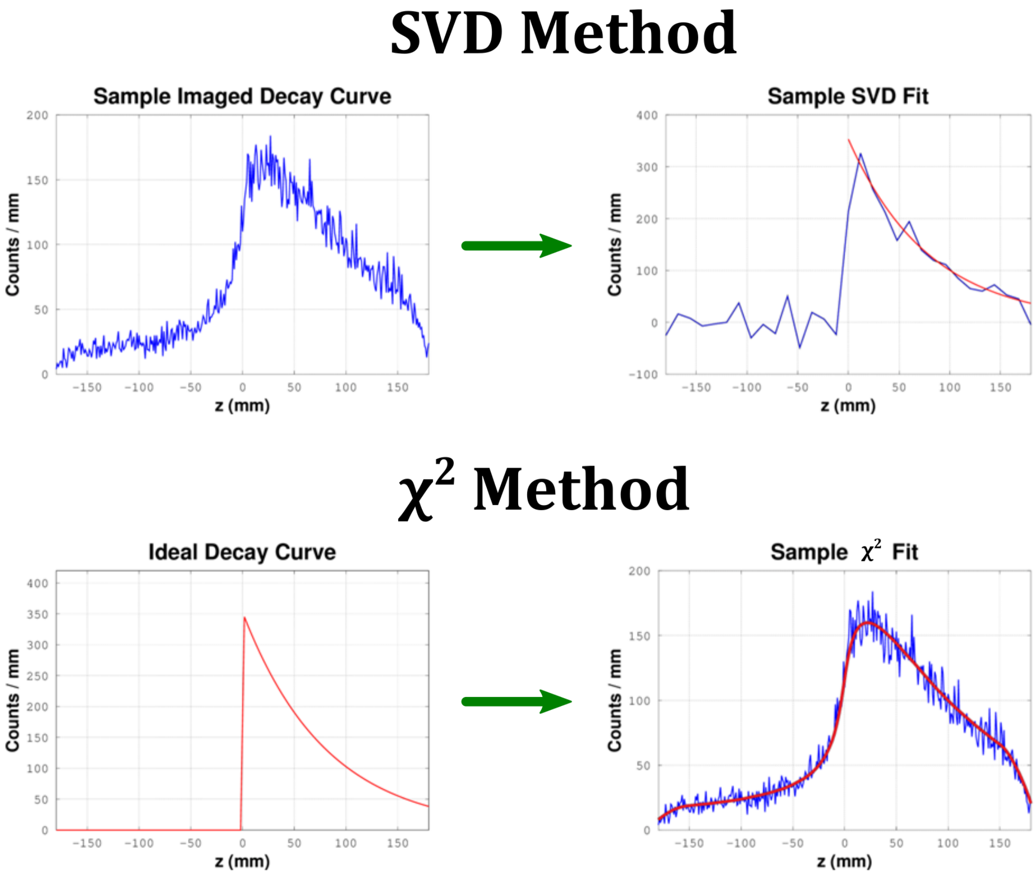

Figure 6.3: SVD vs. χ^2 Minimization curve-fitting methods

to rapidly narrow down on the best-fit value of τ_0. For the first iteration, we create 20 evenly-spaced points within a range of possible lifetimes for the state (for example, 250 ps to 4 ns). Once we find the point with the minimum χ^2 value, we construct a new range of 20 points evenly-spaced between the left- and right-hand neighbors of that point. This is repeated until the answer converges to within 0.1 ps, which generally occurs after 5-6 iterations. The best-fit curve is the one with the smallest χ^2 value computed using Eq. 6.17 (hence "χ^2 Minimization").

At the end of this process, we have χ^2 as a function of hypothetical values of τ_0. This curve enables a nifty trick – it allows us to estimate the uncertainty in the best-fit lifetime from a single measurement. To do so, we find the values of τ_0 for which $\chi^2 = \chi^2_{min} + 1$. These represent the $\pm 1\sigma$ error bars for the lifetime. One must use *unnormalized* χ^2 for this to work, instead of the standard $\chi^2/(N_{pts} - 1)$.

Figure 6.4 shows a sample χ^2 fit. On the left side, the hypothesized images (red and

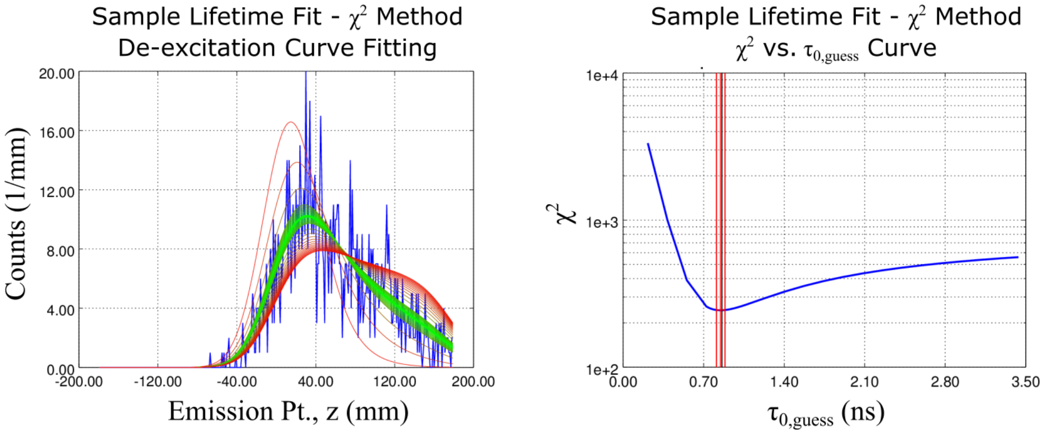

Figure 6.4: A sample χ^2 Minimization Fit

green) are compared to the raw data (blue). The green lines have the smallest χ^2 values, while the red ones are generally poor fits to the measured de-excitation curve. In other words, the green lines converge to our best guess for the true value of τ_0. The right half of the figure shows the χ^2 vs. $\tau_{0,guess}$ curve. The pink lines show the limits of the $\chi^2 + 1$ estimate on the uncertainty.

6.3 Precision in Lifetime Measurements

Our primary goal in this project was to evaluate uncertainty in lifetime measurements using gamma-ray imaging. There are three main factors that affect the quality of the curve-fitting described in Section 6.2: the imaging resolution, σ_{img}; the number of imaged emissions, N_{img}; and the decay parameter, $\mu = 1/\gamma\beta c\tau_0$, a combination of the beam velocity and proper lifetime.

As discussed in Section 6.2, creating a de-excitation curve from gamma-ray imaging is directly limited by the system's imaging resolution. In addition, both the the lifetime of the de-excitation and the number of successful image reconstructions limit the accuracy of the measurement.

Gathering enough counts is a major challenge in our lifetime measurements. A nuclear state of interest may have a very small production cross-section. On top of that, not every nucleus thus produced will necessarily emit a photon within the imaging range. (The fraction depends on the beam velocity and the nuclear lifetime.) The detector also has less-than-perfect geometric and intrinsic efficiencies, and therefore will not detect every photon emission. (Note: GRETINA covers about 1π steradians as seen from the center of its inner cavity, and has approximately 60% P/T for ^{137}Cs. The placement of detector modules is an extremely important consideration here. Because the parent nuclei are moving relativistically, the lab-frame emissions will tend to be forward-directed. The exact angular distribution depends on the beam velocity and the angular distribution in the CM-frame. See Section 2.2.)

Moreover, both gamma-ray imaging methods have imperfect imaging efficiency. Not every track with full energy deposition yields an emission point. In Compton imaging, tracks are rejected for giving ambiguous emission points or emission points outside the imaging range (-180 mm $< z <$ 180 mm). They can also be rejected for having small Compton lever arms, for example. In Doppler-shift imaging, tracks are rejected if they yield emission points outside the imaging range. When no data filters are applied, typical imaging efficiency for 1.0 MeV CM-frame emissions at 0.3c is 30% for Compton imaging and 72% for Doppler-shift imaging. These numbers drop to 5-10% for Compton imaging and 10-20% for Doppler-shift imaging depending on the choice of data cut(s).

To illustrate this problem, consider an experiment with beam intensity I, production cross-section σ, atom density n, target thickness x, geometric efficiency ϵ_g, intrinsic efficiency of ϵ_i, and imaging efficiency ϵ_m. Suppose the parent nuclei have velocity βc and proper lifetime τ_0, with a branching ratio B for the transition of interest. If the beam runs for time t, then the total number of nuclei produced is:

$$N_{tot} = tIB(1 - e^{-\Sigma x}) \simeq tIB\Sigma x \tag{6.19}$$

where $\Sigma = n\sigma$. The total number of emissions created within the imaging window depends on the target position. Suppose the target is placed at z = (0.0 mm, 0.0 mm, 0.0 mm) and the right edge of the imaging window is at z_r. Then the number of emissions that *could* be detected is:

$$N_{emit} = N_{tot}(1 - e^{-\mu z_r}) = N_{total}(1 - e^{-z_r/\gamma\beta c\tau_0}) \tag{6.20}$$

Of these, the number that finally are accepted for imaging is:

$$\begin{aligned} N_{img} &= N_{emit}(\epsilon_g \epsilon_i \epsilon_m) & (6.21) \\ &= (tIB\Sigma x)(1 - e^{-\mu z_r})(\epsilon_g \epsilon_i \epsilon_m) & (6.22) \end{aligned}$$

In other words, the amount of beamtime needed to collect N_{img} counts for building a de-excitation curve is:

$$t_N = \frac{N_{img}}{(IB\Sigma x)(1 - e^{-\mu z_r})(\epsilon_g \epsilon_i \epsilon_m)} \tag{6.23}$$

For example, consider a typical secondary beam (1.5 × 10^4 particles/s) with a reaction of cross-section of σ = 10.0 mb. Suppose the target is x = 1.0 mm thick with density n = 1.50 × 10^{22} atoms/cm^3, and let B = 0.1, β = 0.30, τ_0 = 1.0 ns, z_r = 180 mm, ϵ_g = 0.25, ϵ_i = 0.60, and ϵ_m = 0.20. All told, gathering 100 good reconstructions requires 48 hrs of beamtime.

In addition to statistics and imaging resolution, the decay parameter $\mu = 1/\gamma\beta c\tau_0$ also plays a part in how well we can extract lifetimes. Consider – as de-excitation lifetime and/or the beam velocity decreases, the source distribution will appear more and more like a point source located at the target (like in Figure 6.1). This will naturally make it difficult or impossible to identify a de-excitation curve in the image. On the other hand, if the lifetime is too long or the beam velocity too great, then the source distribution will appear as a flat line across the entire imaging range. Of course, this also prevents us from reliably fitting a de-excitation curve to the image.

Essentially, in order to image a de-excitation curve we need a sufficient fraction of emissions to occur relatively far from the target, while also still being in the imaging range. As a first-order estimate, for example, we might want a minimum fraction F of emissions to occur beyond $z_{min} = 1\sigma_{img}$ of the target, where σ_{img} is our imaging resolution. This lets us put a lower limit on the lifetime we can measure ($\tau_{0,min}$). The number of emissions between the target ($z = 0$) and z_{min} is given by:

$$\int_{z_{min}}^{\infty} A_0 e^{-\mu z} dz = F \int_{0}^{\infty} A_0 e^{-\mu z} dz \tag{6.24}$$

$$\left(\frac{A_0}{\mu}\right)\left(e^{-\mu z_{min}}\right) = F\left(\frac{A_0}{\mu}\right) \tag{6.25}$$

$$z_{min} = \frac{\ln\left(1/F\right)}{\mu} \tag{6.26}$$

We want to solve this for the minimum viable lifetime, $\tau_{0,min}$. Given that $\mu = 1/(\gamma\beta c\tau)$:

$$z_{min} = \gamma\beta c\tau_{0,min} \ln\left(1/F\right) \tag{6.27}$$

$$\tau_{0,min} = \frac{z_{min}}{\gamma\beta c \ln\left(1/F\right)} \tag{6.28}$$

Suppose the beam velocity is 0.30c and the imaging resolution is $\sigma_{img} = 30.0$ mm. Setting $z = \sigma_{img}$ and $F = 0.25$ yields a minimum lifetime of 230 ps. We can perform a very similar calculation for the opposite extreme – here we might want some fraction F of emissions to occur within the imaging window, $0 < z < 180mm$. In this case we'd get:

$$\tau_{0,max} = \frac{z_{max}}{\gamma\beta c \ln\left[1/(1-F)\right]} \tag{6.29}$$

If we want half of all counts to fall between the target and $z = 180$ mm, we'd set $F = 0.5$ and find a maximum viable lifetime of 2.7 ns. So, if we have 30 mm imaging resolution (and unlimited statistics), we would expect to be able to reliably measure lifetimes between 0.23 ns and 2.7 ns.

My primary goal with this study was to evaluate the precision achievable in τ_0 as a function of the various imaging parameters (i.e. σ_{img}, N_{img}, and μ). I explored this parameter space through a large series of Monte Carlo simulations, generating 1000 hypothetical source images for each combination of σ_{img}, N_{img}, and μ.

Generating hypothetical source images is fairly straightforward. First, we define values for τ_0 and β to formulate an ideal de-excitation curve. This allows us to sample the de-excitation curve for a true emission point, z_0. Once we have that, we sample the detector response distribution at z_0 to find the *imaged* emission point, z. This process is repeated until the desired number of counts $N_{samples}$ is reached to construct a simulated de-excitation curve. From there, we use the curve-fitting described in Section 6.2 to extract a lifetime from the simulated curve. Finally, to get an accurate handle on the precision of the calculated lifetime, we must run this process for a large number of simulated de-excitation curves (such as $N_{runs} = 1000$).

For my purposes, I assumed simple Gaussian detector response curves with the desired imaging resolution, σ_{img}. As we can see from Figure 6.1, however, the imaging responses do deviate from this idealized shape. Compton imaging responses have long tails to either end of the imaging window (and the peaks sit atop wide backgrounds). Doppler-shift imaging responses have much more Gaussian peaks, but also have a long, low tail downstream of the true emission point.

The repeat simulations produce a large distribution of calculated lifetimes for a given imaging resolution, number of counts, and decay parameter (μ). The standard deviation of this distribution is by definition the precision we seek. However, this approach requires multiple simulations of the same lifetime experiment. Fortunately, we can also estimate uncertainty from a single run using the $\chi^2_{min} + 1$ method from curve fitting. The single-run estimates for σ_τ are largely in agreement with the actual standard deviations we find from the multi-simulation tests. Figure 6.5 illustrates this – the single- and multi-measurement σ_τ values are within a 10% margin (less than the standard deviation of the single-measurement estimates). This therefore gives us confidence that we can trust the $\chi^2_{min} + 1$ method in real-world experiments, where we do not have the luxury of running 1000 test cases.

Tables 6.1 to 6.7 show how overall precision in lifetime depends on statistics and detector resolution. For these simulations, I kept the parent CM-frame lifetime and lab-frame velocity constant at 0.859 ns and 0.3c, respectively. I varied the number of reconstructions ($N_{samples}$) in each de-excitation curve from 100 to 50K samples. For each value of $N_{samples}$, I then varied the detector's Gaussian imaging resolution (σ_{img}) from 1.0 mm to 75.0 mm. In sum, I studied 19 values of σ_{img} and 21 values of $N_{samples}$, for a total of 399 data points. Figure **??** shows the dependence on $N_{samples}$ for two imaging resolutions – 10.0 mm and 25.0 mm. These values reflect the observed imaging resolution of Doppler-Shift and Compton imaging, respectively. For each imaging resolution, I've highlighted the number of counts required to achieve $< 10\%$ relative uncertainty in the measured τ_0.

As we can see, there is some fluctuation in the measured value of τ_0 in the low-count regime ($N_{samples} < 1000$). In addition, there is significant systematic error in many of the fits. In Figure **??**, I attribute the error to normal statistical fluctuations. The apparent monotonic

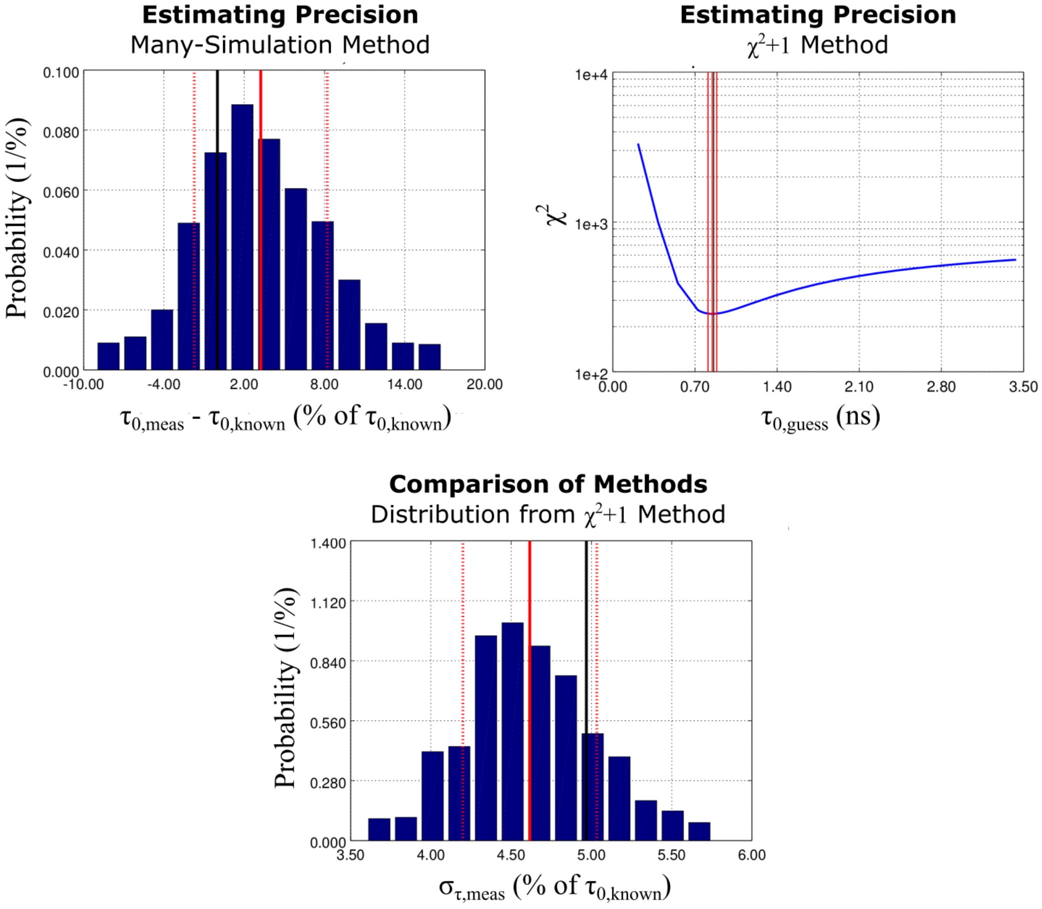
Estimating Precision
Many-Simulation Method

Estimating Precision
χ^2+1 Method

Comparison of Methods
Distribution from χ^2+1 Method

Figure 6.5: Estimating precision for lifetime measurements

convergence is the result of the random number generator I used. At the beginning of each set of lifetime simulations, I reset the random number seed to an initial value. This was done to preserve reproducibility in the simulations. Using a different seed between runs removes the monotonic trend, although the measured lifetime still converges as expected to the nominal value (0.859 ns).

Figures 6.7, 6.9, and 6.10 also show a monotonically-decreasing systematic error for the same reason. However, here the fits do **not** converge to the correct lifetime. This is caused by edge effects in the fitting process – the response functions in the $P(z, z_0)$ matrix are cut off towards the edges of the imaging window. (See Figure 6.6) Rather than having full, symmetric Gaussian shapes at $z_0 = 180$ mm, for example, the responses are only half-Gaussians. Because I did not renormalize the response functions to account for potential cut-off, emissions near the edges carry artifically less weight than emissions closer to the target. This causes sharp dips in counts in the idealized lifetime curves near the downstream imaging limit. The effect becomes more pronounced with long lifetimes and very poor imaging resolution. (In the first case, because more emissions occur near the imaging limit; and in the second case, because more of each detector response function is cut off, especially for those nearer to the downstream edge of the imaging window.) To improve on the results presented here, we would need to confine curve fitting to a range smaller than the imaging window, where the detector response curves are not cut off. For example, rather than using comparing measured and ideal counts between 0 mm $< z <$ 180 mm, as I have, we might instead fit only to 0 mm $< z <$ 150 mm. We could also extend the imaging window itself and calculate detector responses beyond the $z = 180$ mm limit that I used here.

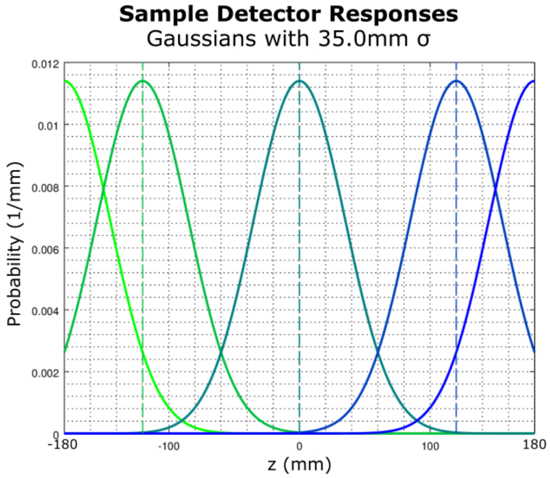

Figure 6.6: Sample cut-off detector responses

Figure 6.7 similarly illustrates the dependence on σ_{img} for two distinct values of $N_{samples}$. The systematic error in the average measured value of τ_0 is very pronounced for $N_{samples} = 1000$, but decreases to generally less than 2% with $N_{samples} = 5000$. Meanwhile, the precision σ_τ steadily worsens with increasing width of detector imaging resolution, as expected. The dependence is surprisingly weak, however – even with an *abysmal* 75.0mm imaging resolution, the precision is still within 10% for $N_{samples} = 5000$. So, if we can accurately characterize the detector imaging resolution, we can use the χ^2 fitting method to largely correct for poor imaging performance.

As discussed above, the decay parameter $\mu = 1/\gamma\beta c\tau_0$ also affects the measurement precision. To study this, I ran two series of simulations for lifetimes varying from 0.029 ns to 6.872 ns (21 values total), with β kept constant at 0.3c. (The τ_0 range corresponds to a μ range of 0.365 / mm to 0.00154 / mm.) For the first set, I kept $N_{samples}$ constant at 5000 counts and picked 5 different imaging resolutions – $\sigma_{img} = \{5.0$ mm, 10.0 mm, 25.0 mm, 35.0 mm, and 50.0 mm$\}$, for a total of 105 test runs. Tables 6.8 and 6.9 provide the detailed results, which are illustrated in Figure 6.10. In the second set of simulations, I did the reverse – keeping σ_{img} constant at 25.0 mm while varying $N_{samples}$. I chose 5 values to study the effects of statistics on σ_τ: $\{$500 counts, 1K counts, 5K counts, 10K counts, 50K counts$\}$, for another 105 data points. Tables 6.10 and 6.11 provide the results. Figure 6.9 illustrates the dependence of lifetime precision on τ_0 for two different values of $N_{samples}$.

As expected, the uncertainty in the measured τ_0 value is most pronounced for very short and very long lifetimes. This suggests an effective range of lifetimes that we could measure through imaging, although of course the actual sensitivity range will depend on the specific counting statistics and uncertainty tolerated in the measured lifetime. In the tables, I've marked the first and last values of τ_0 for which the relative uncertainty is $\leq$ 10% of the lifetime. I then used linear interpolation to estimate where lifetime uncertainty would be exactly 10%. Figures 6.12 and 6.11 plot the resulting sensitive ranges as a function of beam velocity from 0.05c to 0.50c. (Again, the decay parameter μ is a combined function of β and τ_0. As beam velocity increases, the effective range of lifetimes we can measure shifts downward.) The shaded regions indicate the lifetimes for which we would theoretically measure less than 10% uncertainty, given a specific imaging resolution and number of counts. Note that some of the ranges are cut off. For example, with 5K counts and 10.0mm imaging resolution, the observed uncertainty in measured lifetime is less than 10% even at 29 ps – the shortest lifetime for which I ran simulations. (Refer to Table 6.8.) This is certainly promising, although I did not have time to pursue the investigation further.

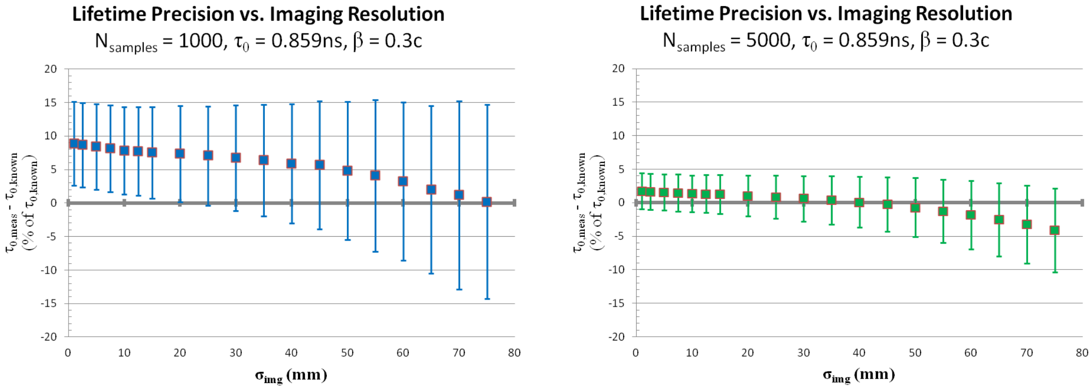

Figure 6.7: Lifetime precision vs. imaging resolution
σ_{img} = 1.0 mm to 75.0 mm, 1000 & 5000 samples
τ_0 = 0.859 ns, β = 0.3c, 1000 trials
See Tables 6.1 to 6.7

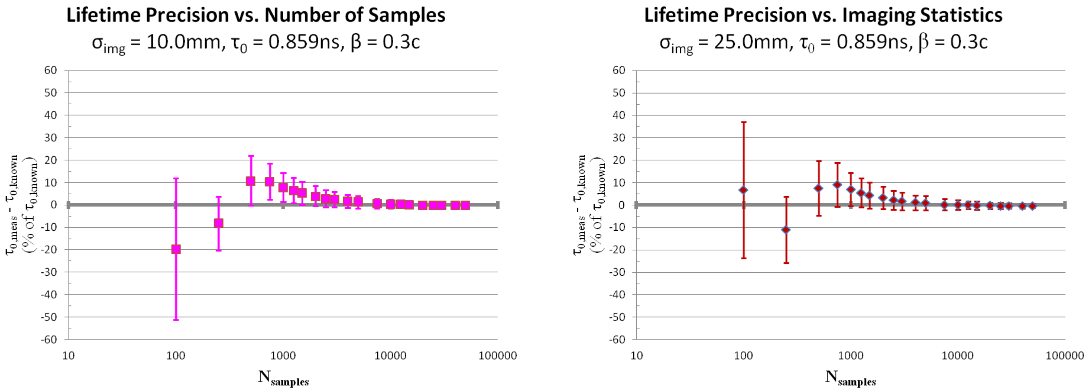

Figure 6.8: Lifetime precision vs. number of samples
σ_{img} = 10.0 mm & 25.0 mm, 100 to 50K samples
τ_0 = 0.859 ns, β = 0.3c, 1000 trials
See Tables 6.2 and 6.3

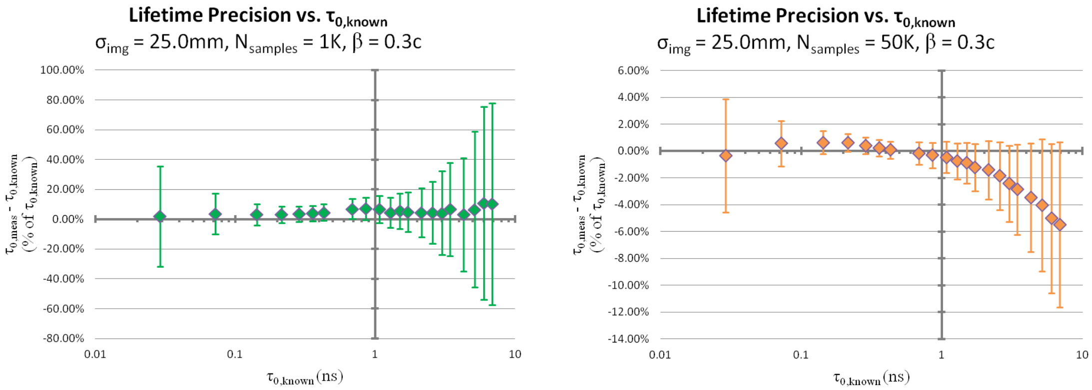

Figure 6.9: Lifetime precision vs. decay parameter, $\mu = 1/\gamma\beta c\tau_0$
σ_{img} = 25.0 mm, 1K & 50K samples
τ_0 = 0.029 ns to 6.872 ns, β = 0.3c, 1000 trials
See Tables 6.10 and 6.11

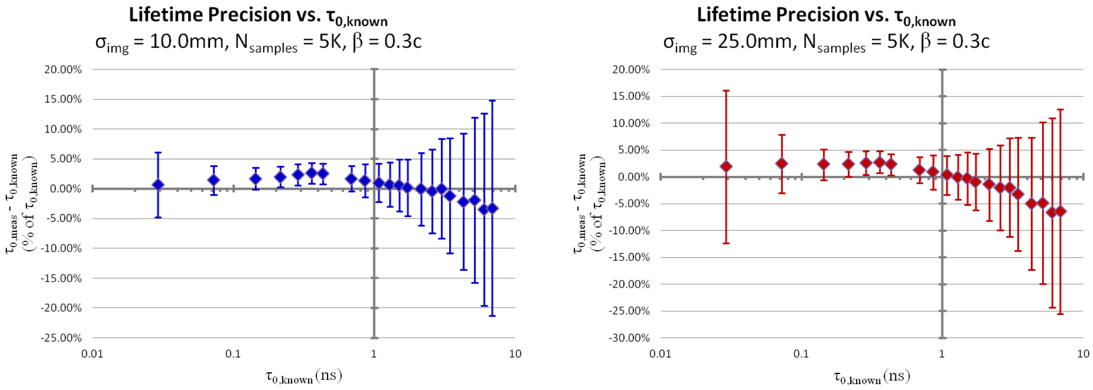

Figure 6.10: Lifetime precision vs. decay parameter, $\mu = 1/\gamma\beta c\tau_0$
σ_{img} = 10.0 mm & 25.0 mm, 5K samples
τ_0 = 0.029 ns to 6.872 ns, β = 0.3c, 1000 trials
See Table 6.8

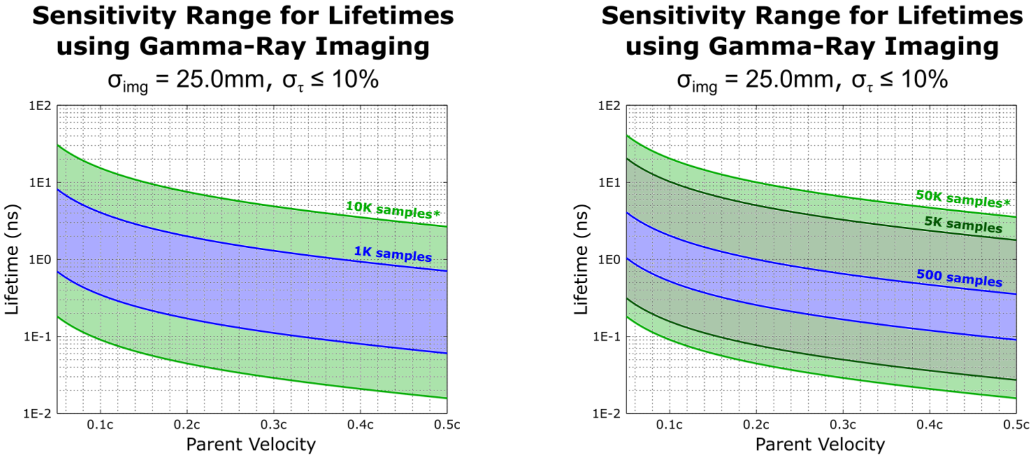
Sensitivity Range for Lifetimes using Gamma-Ray Imaging
σ_{img} = 25.0mm, $\sigma_\tau \leq$ 10%

Sensitivity Range for Lifetimes using Gamma-Ray Imaging
σ_{img} = 25.0mm, $\sigma_\tau \leq$ 10%

* 10K range extends below 0.029ns at 0.3c by an unknown amount

* 50K range extends below 0.029ns and above 6.495ns at 0.3c by unknown amounts

Figure 6.11: Lifetime sensitivity vs. number of samples
σ_{img} = 25.0 mm, 500 to 50K samples
Lifetime precision $\sigma_\tau \leq 10\%$

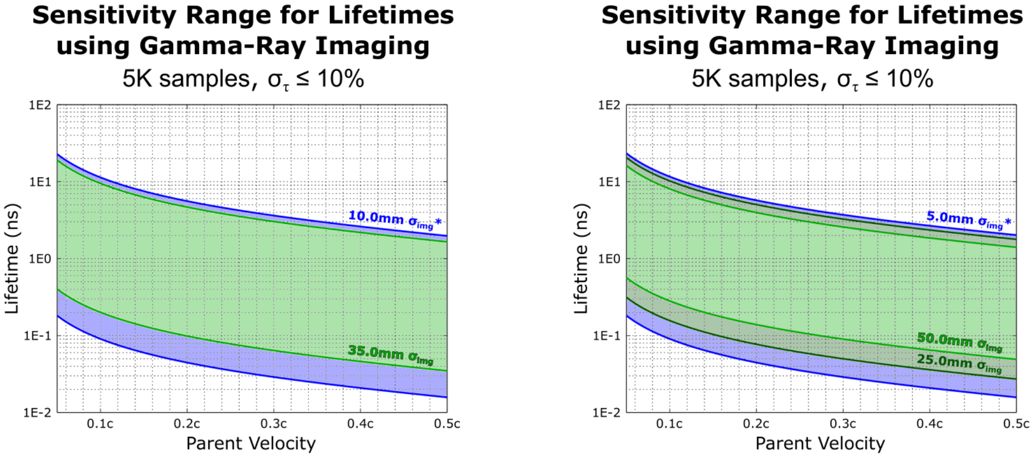
Sensitivity Range for Lifetimes using Gamma-Ray Imaging
5K samples, $\sigma_\tau \leq$ 10%

Sensitivity Range for Lifetimes using Gamma-Ray Imaging
5K samples, $\sigma_\tau \leq$ 10%

* 10.0mm range extends below 0.029ns at 0.3c by an unknown amount

* 5.0mm range extends below 0.029ns at 0.3c by an unknown amount

Figure 6.12: Lifetime sensitivity vs. imaging resolution
σ_{img} = 5.0 mm to 50.0 mm, 5K samples
Lifetime precision $\sigma_\tau \leq 10\%$

# of Samples	σ_{img} **= 1.0 mm**	σ_{img} **= 2.5 mm**	σ_{img} **= 5.0 mm**
100	0.6307 ± 0.1592	0.6317 ± 0.1669	0.6391 ± 0.1952
250	0.8034 ± 0.0975	0.8012 ± 0.0960	0.7985 ± 0.1009
500	0.9788 ± 0.1053	0.9733 ± 0.1026	0.9647 ± 0.0976
750	**0.9637 ± 0.0644**	**0.9596 ± 0.0650**	**0.9549 ± 0.0667**
1000	0.9352 ± 0.0535	0.9332 ± 0.0542	0.9312 ± 0.0551
1250	0.9225 ± 0.0468	0.9204 ± 0.0463	0.9178 ± 0.0471
1500	0.9112 ± 0.0432	0.9099 ± 0.0435	0.9081 ± 0.0437
2000	0.8992 ± 0.0373	0.8982 ± 0.0377	0.8959 ± 0.0377
2500	0.8887 ± 0.0319	0.8873 ± 0.0318	0.8859 ± 0.0320
3000	0.8849 ± 0.0290	0.8837 ± 0.0289	0.8824 ± 0.0290
4000	0.8777 ± 0.0242	0.8766 ± 0.0242	0.8753 ± 0.0242
5000	0.8741 ± 0.0229	0.8730 ± 0.0230	0.8723 ± 0.0232
7500	0.8674 ± 0.0181	0.8662 ± 0.0182	0.8655 ± 0.0184
10000	0.8651 ± 0.0157	0.8643 ± 0.0158	0.8637 ± 0.0161
12500	0.8637 ± 0.0135	0.8628 ± 0.0136	0.8623 ± 0.0135
15000	0.8617 ± 0.0128	0.8611 ± 0.0128	0.8606 ± 0.0130
20000	0.8606 ± 0.0106	0.8599 ± 0.0105	0.8596 ± 0.0106
25000	0.8593 ± 0.0098	0.8587 ± 0.0099	0.8583 ± 0.0099
30000	0.8593 ± 0.0088	0.8587 ± 0.0088	0.8583 ± 0.0089
40000	0.8587 ± 0.0077	0.8582 ± 0.0077	0.8578 ± 0.0078
50000	0.8584 ± 0.0070	0.8578 ± 0.0070	0.8575 ± 0.0070

Table 6.1: Simulated Lifetime Measurement Results, $\sigma_{img} = 1.0$ mm to 5.0 mm
$\tau_0 = 0.859$ ns, $\beta = 0.3$c, $N_{trials} = 1000$, $N_{samples} = 100$ to 50K
Values are given in ns

# of Samples	σ_{img} **= 7.5 mm**	σ_{img} **= 10.0 mm**	σ_{img} **= 12.5 mm**
100	0.6577 ± 0.2344	0.6902 ± 0.2711	0.7232 ± 0.2942
250	0.7937 ± 0.1014	0.7889 ± 0.1034	0.7842 ± 0.1053
500	0.9604 ± 0.0984	0.9522 ± 0.0959	0.9471 ± 0.0960
750	**0.9503 ± 0.0677**	**0.9486 ± 0.0696**	**0.9438 ± 0.0708**
1000	0.9291 ± 0.0556	0.9262 ± 0.0563	0.9254 ± 0.0570
1250	0.9163 ± 0.0478	0.9150 ± 0.0489	0.9128 ± 0.0493
1500	0.9064 ± 0.0436	0.9046 ± 0.0441	0.9032 ± 0.0453
2000	0.8956 ± 0.0381	0.8932 ± 0.0383	0.8929 ± 0.0386
2500	0.8848 ± 0.0320	0.8833 ± 0.0324	0.8826 ± 0.0329
3000	0.8806 ± 0.0293	0.8800 ± 0.0302	0.8796 ± 0.0304
4000	0.8746 ± 0.0247	0.8738 ± 0.0254	0.8729 ± 0.0255
5000	0.8717 ± 0.0236	0.8707 ± 0.0237	0.8704 ± 0.0243
7500	0.8650 ± 0.0186	0.8645 ± 0.0188	0.8638 ± 0.0190
10000	0.8632 ± 0.0164	0.8628 ± 0.0165	0.8625 ± 0.0171
12500	0.8619 ± 0.0137	0.8616 ± 0.0138	0.8612 ± 0.0138
15000	0.8602 ± 0.0132	0.8599 ± 0.0135	0.8596 ± 0.0137
20000	0.8592 ± 0.0108	0.8590 ± 0.0109	0.8588 ± 0.0111
25000	0.8581 ± 0.0100	0.8578 ± 0.0102	0.8577 ± 0.0104
30000	0.8581 ± 0.0090	0.8579 ± 0.0092	0.8578 ± 0.0093
40000	0.8576 ± 0.0079	0.8574 ± 0.0080	0.8573 ± 0.0081
50000	0.8573 ± 0.0071	0.8571 ± 0.0072	0.8569 ± 0.0073

Table 6.2: Simulated Lifetime Measurement Results, $\sigma_{img} = 7.5$ mm to 12.5 mm
$\tau_0 = 0.859$ ns, $\beta = 0.3$c, $N_{trials} = 1000$, $N_{samples} = 100$ to 50K

# of Samples	σ_{img} **= 15.0 mm**	σ_{img} **= 20.0 mm**	σ_{img} **= 25.0 mm**
100	0.7789 ± 0.3088	0.8762 ± 0.2816	0.9166 ± 0.2600
250	0.7789 ± 0.1056	0.7703 ± 0.1144	0.7648 ± 0.1262
500	0.9405 ± 0.0972	0.9326 ± 0.1027	0.9243 ± 0.1043
750	**0.9447 ± 0.0756**	**0.9387 ± 0.0771**	**0.9370 ± 0.0833**
1000	0.9237 ± 0.0586	0.9222 ± 0.0616	0.9196 ± 0.0636
1250	0.9120 ± 0.0508	0.9096 ± 0.0532	0.9065 ± 0.0564
1500	0.9017 ± 0.0453	0.8996 ± 0.0480	0.8962 ± 0.0491
2000	0.8912 ± 0.0395	0.8885 ± 0.0403	0.8868 ± 0.0427
2500	0.8819 ± 0.0336	0.8803 ± 0.0351	0.8776 ± 0.0360
3000	0.8781 ± 0.0311	0.8761 ± 0.0327	0.8744 ± 0.0343
4000	0.8721 ± 0.0258	0.8708 ± 0.0271	0.8689 ± 0.0283
5000	0.8697 ± 0.0250	0.8679 ± 0.0259	0.8666 ± 0.0274
7500	0.8632 ± 0.0192	0.8620 ± 0.0203	0.8608 ± 0.0214
10000	0.8619 ± 0.0173	0.8611 ± 0.0178	0.8599 ± 0.0189
12500	0.8607 ± 0.0142	0.8600 ± 0.0146	0.8592 ± 0.0154
15000	0.8592 ± 0.0138	0.8588 ± 0.0143	0.8578 ± 0.0152
20000	0.8585 ± 0.0113	0.8580 ± 0.0118	0.8574 ± 0.0124
25000	0.8575 ± 0.0105	0.8570 ± 0.0108	0.8566 ± 0.0115
30000	0.8576 ± 0.0095	0.8571 ± 0.0100	0.8567 ± 0.0106
40000	0.8571 ± 0.0082	0.8567 ± 0.0085	0.8564 ± 0.0089
50000	0.8568 ± 0.0074	0.8565 ± 0.0077	0.8562 ± 0.0081

Table 6.3: Simulated Lifetime Measurement Results, $\sigma_{img} = 15.0$ mm to 25.0 mm
$\tau_0 = 0.859$ ns, $\beta = 0.3$c, $N_{trials} = 1000$, $N_{samples} = 100$ to 50K

# of Samples	σ_{img} **= 30.0 mm**	σ_{img} **= 35.0 mm**	σ_{img} **= 40.0 mm**
100	0.9292 ± 0.2802	0.9403 ± 0.3105	0.9518 ± 0.3406
250	0.7596 ± 0.1359	0.7543 ± 0.1462	0.7508 ± 0.1600
500	0.9201 ± 0.1121	0.9192 ± 0.1203	0.9173 ± 0.1336
750	0.9367 ± 0.0886	0.9361 ± 0.0939	0.9373 ± 0.0994
1000	**0.9171 ± 0.0677**	**0.9138 ± 0.0714**	**0.9094 ± 0.0765**
1250	0.9031 ± 0.0591	0.9012 ± 0.0631	0.8965 ± 0.0679
1500	0.8937 ± 0.0527	0.8900 ± 0.0558	0.8860 ± 0.0601
2000	0.8840 ± 0.0451	0.8815 ± 0.0474	0.8778 ± 0.0508
2500	0.8757 ± 0.0388	0.8734 ± 0.0411	0.8695 ± 0.0451
3000	0.8715 ± 0.0363	0.8684 ± 0.0384	0.8649 ± 0.0417
4000	0.8666 ± 0.0304	0.8640 ± 0.0325	0.8608 ± 0.0345
5000	0.8644 ± 0.0291	0.8621 ± 0.0309	0.8598 ± 0.0326
7500	0.8593 ± 0.0225	0.8575 ± 0.0238	0.8552 ± 0.0253
10000	0.8589 ± 0.0202	0.8576 ± 0.0216	0.8557 ± 0.0228
12500	0.8582 ± 0.0163	0.8570 ± 0.0175	0.8558 ± 0.0188
15000	0.8568 ± 0.0160	0.8559 ± 0.0172	0.8548 ± 0.0186
20000	0.8568 ± 0.0131	0.8561 ± 0.0140	0.8551 ± 0.0152
25000	0.8560 ± 0.0123	0.8553 ± 0.0132	0.8547 ± 0.0143
30000	0.8561 ± 0.0113	0.8554 ± 0.0121	0.8545 ± 0.0129
40000	0.8560 ± 0.0095	0.8556 ± 0.0100	0.8550 ± 0.0107
50000	0.8558 ± 0.0085	0.8554 ± 0.0090	0.8549 ± 0.0096

Table 6.4: Simulated Lifetime Measurement Results, $\sigma_{img} = 30.0$ mm to 40.0 mm
$\tau_0 = 0.859$ ns, $\beta = 0.3$c, $N_{trials} = 1000$, $N_{samples} = 100$ to 50K

# of Samples	**σ_{img} = 45.0 mm**	**σ_{img} = 50.0 mm**	**σ_{img} = 55.0 mm**
100	0.9661 ± 0.3797	0.9812 ± 0.4264	0.9973 ± 0.4812
250	0.7578 ± 0.1861	0.7674 ± 0.2250	0.7853 ± 0.2658
500	0.9235 ± 0.1526	0.9364 ± 0.1752	0.9505 ± 0.2019
750	0.9354 ± 0.1030	0.9352 ± 0.1109	0.9303 ± 0.1224
1000	**0.9076 ± 0.0820**	0.9005 ± 0.0884	0.8942 ± 0.0970
1250	0.8926 ± 0.0743	**0.8862 ± 0.0786**	**0.8794 ± 0.0843**
1500	0.8802 ± 0.0637	0.8744 ± 0.0683	0.8667 ± 0.0726
2000	0.8729 ± 0.0538	0.8672 ± 0.0586	0.8596 ± 0.0618
2500	0.8653 ± 0.0476	0.8601 ± 0.0514	0.8548 ± 0.0559
3000	0.8613 ± 0.0443	0.8561 ± 0.0486	0.8510 ± 0.0525
4000	0.8572 ± 0.0372	0.8535 ± 0.0400	0.8483 ± 0.0422
5000	0.8568 ± 0.0348	0.8530 ± 0.0379	0.8482 ± 0.0406
7500	0.8525 ± 0.0271	0.8497 ± 0.0290	0.8462 ± 0.0313
10000	0.8539 ± 0.0245	0.8512 ± 0.0268	0.8483 ± 0.0292
12500	0.8542 ± 0.0201	0.8522 ± 0.0217	0.8496 ± 0.0235
15000	0.8535 ± 0.0201	0.8513 ± 0.0211	0.8494 ± 0.0225
20000	0.8543 ± 0.0164	0.8527 ± 0.0175	0.8509 ± 0.0190
25000	0.8536 ± 0.0154	0.8526 ± 0.0167	0.8510 ± 0.0181
30000	0.8537 ± 0.0139	0.8528 ± 0.0150	0.8516 ± 0.0163
40000	0.8545 ± 0.0116	0.8537 ± 0.0126	0.8530 ± 0.0137
50000	0.8544 ± 0.0104	0.8537 ± 0.0112	0.8528 ± 0.0121

Table 6.5: Simulated Lifetime Measurement Results, $\sigma_{img} = 45.0$ mm to 55.0 mm
$\tau_0 = 0.859$ ns, $\beta = 0.3$c, $N_{trials} = 1000$, $N_{samples} = 100$ to 50K

# of Samples	σ_{img} **= 60.0 mm**	σ_{img} **= 65.0 mm**
100	1.0140 ± 0.5334	1.0317 ± 0.5894
250	0.8275 ± 0.3685	0.8726 ± 0.4793
500	0.9635 ± 0.2193	0.9884 ± 0.2453
750	0.9266 ± 0.1324	0.9209 ± 0.1427
1000	0.8869 ± 0.1014	0.8762 ± 0.1071
1250	0.8706 ± 0.0903	0.8648 ± 0.0980
1500	**0.8597 ± 0.0770**	**0.8491 ± 0.0818**
2000	0.8513 ± 0.0658	0.8429 ± 0.0705
2500	0.8475 ± 0.0602	0.8409 ± 0.0654
3000	0.8444 ± 0.0554	0.8371 ± 0.0595
4000	0.8428 ± 0.0454	0.8365 ± 0.0493
5000	0.8432 ± 0.0440	0.8372 ± 0.0468
7500	0.8420 ± 0.0337	0.8380 ± 0.0364
10000	0.8449 ± 0.0309	0.8414 ± 0.0326
12500	0.8473 ± 0.0256	0.8442 ± 0.0278
15000	0.8469 ± 0.0245	0.8443 ± 0.0262
20000	0.8487 ± 0.0206	0.8465 ± 0.0223
25000	0.8494 ± 0.0196	0.8479 ± 0.0210
30000	0.8501 ± 0.0177	0.8486 ± 0.0192
40000	0.8521 ± 0.0149	0.8514 ± 0.0160
50000	0.8520 ± 0.0133	0.8518 ± 0.0144

Table 6.6: Simulated Lifetime Measurement Results, $\sigma_{img} = 60.0$ mm to 65.0 mm
$\tau_0 = 0.859$ ns, $\beta = 0.3$c, $N_{trials} = 1000$, $N_{samples} = 100$ to 50K

# of Samples	σ_{img} **= 70.0 mm**	σ_{img} **= 75.0 mm**
100	1.0468 ± 0.6484	1.0468 ± 0.6785
250	0.9376 ± 0.6018	1.0284 ± 0.7160
500	1.0060 ± 0.2580	1.0345 ± 0.2980
750	0.9183 ± 0.1556	0.9181 ± 0.1727
1000	0.8691 ± 0.1210	0.8605 ± 0.1245
1250	0.8560 ± 0.1045	0.8493 ± 0.1129
1500	0.8377 ± 0.0891	0.8258 ± 0.0960
2000	**0.8354 ± 0.0763**	**0.8268 ± 0.0801**
2500	0.8313 ± 0.0700	0.8239 ± 0.0729
3000	0.8301 ± 0.0634	0.8221 ± 0.0674
4000	0.8296 ± 0.0523	0.8214 ± 0.0565
5000	0.8311 ± 0.0500	0.8237 ± 0.0537
7500	0.8323 ± 0.0389	0.8263 ± 0.0415
10000	0.8373 ± 0.0356	0.8331 ± 0.0386
12500	0.8410 ± 0.0300	0.8380 ± 0.0321
15000	0.8415 ± 0.0284	0.8397 ± 0.0304
20000	0.8447 ± 0.0241	0.8444 ± 0.0260
25000	0.8471 ± 0.0223	0.8464 ± 0.0242
30000	0.8484 ± 0.0209	0.8482 ± 0.0225
40000	0.8514 ± 0.0176	0.8512 ± 0.0191
50000	0.8518 ± 0.0157	0.8519 ± 0.0171

Table 6.7: Simulated Lifetime Measurement Results, $\sigma_{img} = 70.0$ mm to 75.0 mm
$\tau_0 = 0.859$ ns, $\beta = 0.3$c, $N_{trials} = 1000$, $N_{samples} = 100$ to 50K

$\tau_{0,known}$ **(ns)**	**σ_{img} = 5.0 mm**	**σ_{img} = 10.0 mm**	**σ_{img} = 25.0 mm**
0.029	**0.0291 ± 0.0008**	**0.0292 ± 0.0016**	0.0295 ± 0.0041
0.072	0.0728 ± 0.0013	0.0730 ± 0.0018	**0.0738 ± 0.0039**
0.143	0.1452 ± 0.0023	0.1454 ± 0.0026	0.1463 ± 0.0041
0.215	0.2191 ± 0.0035	0.2193 ± 0.0038	0.2201 ± 0.0049
0.286	0.2926 ± 0.0048	0.2927 ± 0.0050	0.2935 ± 0.0061
0.358	0.3675 ± 0.0061	0.3673 ± 0.0063	0.3677 ± 0.0073
0.430	0.4408 ± 0.0073	0.4408 ± 0.0076	0.4399 ± 0.0086
0.687	0.6996 ± 0.0144	0.6985 ± 0.0145	0.6960 ± 0.0167
0.859	0.8723 ± 0.0232	0.8707 ± 0.0237	0.8666 ± 0.0274
1.074	1.0867 ± 0.0336	1.0848 ± 0.0341	1.0776 ± 0.0389
1.289	1.3011 ± 0.0463	1.2977 ± 0.0479	1.2880 ± 0.0538
1.503	1.5151 ± 0.0633	1.5117 ± 0.0655	1.4989 ± 0.0736
1.718	1.7266 ± 0.0812	1.7208 ± 0.0820	1.7022 ± 0.0907
2.148	2.1557 ± 0.1280	2.1463 ± 0.1297	2.1176 ± 0.1439
2.577	2.5807 ± 0.1784	2.5657 ± 0.1807	2.5252 ± 0.2052
3.007	3.0250 ± 0.2458	3.0067 ± 0.2516	**2.9472 ± 0.2762**
3.436	**3.4123 ± 0.3241**	**3.3952 ± 0.3306**	3.3242 ± 0.3619
4.295	4.2436 ± 0.4836	4.2008 ± 0.4904	4.0825 ± 0.5280
5.154	5.1074 ± 0.6934	5.0545 ± 0.7140	4.9037 ± 0.7743
6.013	5.8767 ± 0.9449	5.8025 ± 0.9697	5.6116 ± 1.0619
6.872	6.7413 ± 1.2257	6.6490 ± 1.2419	6.4272 ± 1.3127

Table 6.8: Simulated Lifetime Measurement Results, $\sigma_{img} = 5.0$ mm to 25.0 mm
$\tau_0 = 0.029$ ns to 6.872 ns, $\beta = 0.3$c, $N_{samples} = 5$K, $N_{trials} = 1000$

$\tau_{0,known}$ **(ns)**	σ_{img} **= 35.0 mm**	σ_{img} **= 50.0 mm**
0.029	0.0296 ± 0.0059	0.0299 ± 0.0086
0.072	**0.0742 ± 0.0056**	0.0748 ± 0.0083
0.143	0.1470 ± 0.0055	**0.1480 ± 0.0079**
0.215	0.2209 ± 0.0062	0.2226 ± 0.0089
0.286	0.2942 ± 0.0073	0.2946 ± 0.0095
0.358	0.3679 ± 0.0083	0.3649 ± 0.0111
0.430	0.4390 ± 0.0101	0.4357 ± 0.0131
0.687	0.6932 ± 0.0188	0.6873 ± 0.0246
0.859	0.8621 ± 0.0309	0.8530 ± 0.0379
1.074	1.0721 ± 0.0432	1.0581 ± 0.0531
1.289	1.2790 ± 0.0603	1.2571 ± 0.0748
1.503	1.4884 ± 0.0834	1.4639 ± 0.1003
1.718	1.6871 ± 0.1014	1.6529 ± 0.1215
2.148	2.0953 ± 0.1569	2.0381 ± 0.1819
2.577	**2.4877 ± 0.2262**	**2.4094 ± 0.2577**
3.007	2.8964 ± 0.2981	2.7962 ± 0.3409
3.436	3.2594 ± 0.3892	3.1447 ± 0.4555
4.295	4.0033 ± 0.5953	3.8272 ± 0.6821
5.154	4.7842 ± 0.8281	4.5347 ± 0.9387
6.013	5.4361 ± 1.1540	5.1376 ± 1.4534
6.872	6.1945 ± 1.3860	5.7834 ± 1.5259

Table 6.9: Simulated Lifetime Measurement Results, $\sigma_{img} = 35.0$ mm to 50.0 mm
$\tau_0 = 0.029$ ns to 6.872 ns, $\beta = 0.3c$, $N_{samples} = 5K$, $N_{trials} = 1000$

$\tau_{0,known}$ **(ns)**	$N_{samples}$ **= 500**	$N_{samples}$ **= 1000**	$N_{samples}$ **= 5000**
0.029	0.0300 ± 0.0142	0.0296 ± 0.0098	0.0295 ± 0.0041
0.072	0.0736 ± 0.0144	0.0746 ± 0.0099	**0.0738 ± 0.0039**
0.143	0.1444 ± 0.0155	**0.1475 ± 0.0100**	0.1463 ± 0.0041
0.215	**0.2164 ± 0.0177**	0.2220 ± 0.0119	0.2201 ± 0.0049
0.286	0.2880 ± 0.0219	0.2959 ± 0.0150	0.2935 ± 0.0061
0.358	0.3611 ± 0.0272	0.3725 ± 0.0185	0.3677 ± 0.0073
0.430	**0.4357 ± 0.0332**	0.4500 ± 0.0233	0.4399 ± 0.0086
0.687	0.7231 ± 0.0714	0.7352 ± 0.0451	0.6960 ± 0.0167
0.859	0.9243 ± 0.1043	0.9196 ± 0.0636	0.8666 ± 0.0274
1.074	1.1838 ± 0.1614	**1.1456 ± 0.0962**	1.0776 ± 0.0389
1.289	1.4371 ± 0.2280	1.3469 ± 0.1284	1.2880 ± 0.0538
1.503	1.7081 ± 0.3111	1.5868 ± 0.1791	1.4989 ± 0.0736
1.718	1.9790 ± 0.4143	1.8015 ± 0.2258	1.7022 ± 0.0907
2.148	2.5362 ± 0.7025	2.2457 ± 0.3547	2.1176 ± 0.1439
2.577	3.0681 ± 1.0121	2.6874 ± 0.5352	2.5252 ± 0.2052
3.007	3.7695 ± 1.7073	3.1308 ± 0.8451	**2.9472 ± 0.2762**
3.436	4.3022 ± 2.1353	3.6650 ± 1.0767	3.3242 ± 0.3619
4.295	6.0336 ± 3.8683	4.4276 ± 1.6359	4.0825 ± 0.5280
5.154	7.6861 ± 5.4939	5.4942 ± 2.6923	4.9037 ± 0.7743
6.013	9.2424 ± 6.9364	6.6701 ± 3.8876	5.6116 ± 1.0619
6.872	11.4505 ± 8.7428	7.5749 ± 4.6503	6.4272 ± 1.3127

Table 6.10: Simulated Lifetime Measurement Results, $N_{samples} = 500$ to 5K
$\sigma_{img} = 25.0$ mm, $\tau_0 = 0.029$ ns to 6.872 ns, $\beta = 0.3$c, $N_{trials} = 1000$

$\tau_{0,known}$ **(ns)**	$N_{samples}$ **= 10000**	$N_{samples}$ **= 50000**
0.029	**0.0293 ± 0.0027**	**0.0289 ± 0.0012**
0.072	0.0730 ± 0.0029	0.0724 ± 0.0012
0.143	0.1454 ± 0.0028	0.1439 ± 0.0012
0.215	0.2185 ± 0.0035	0.2163 ± 0.0014
0.286	0.2912 ± 0.0040	0.2871 ± 0.0017
0.358	0.3634 ± 0.0049	0.3588 ± 0.0022
0.430	0.4349 ± 0.0062	0.4303 ± 0.0027
0.687	0.6904 ± 0.0122	0.6859 ± 0.0058
0.859	0.8599 ± 0.0189	0.8562 ± 0.0081
1.074	1.0730 ± 0.0274	1.0690 ± 0.0124
1.289	1.2825 ± 0.0376	1.2791 ± 0.0170
1.503	1.4925 ± 0.0501	1.4895 ± 0.0223
1.718	1.6976 ± 0.0663	1.6970 ± 0.0298
2.148	2.1113 ± 0.0975	2.1177 ± 0.0460
2.577	2.5185 ± 0.1343	2.5293 ± 0.0640
3.007	2.9292 ± 0.1933	2.9337 ± 0.0830
3.436	3.3267 ± 0.2488	3.3376 ± 0.1123
4.295	**4.0994 ± 0.3752**	4.1457 ± 0.1680
5.154	4.8874 ± 0.5469	4.9453 ± 0.2431
6.013	5.6760 ± 0.7411	5.7109 ± 0.3168
6.872	6.4187 ± 0.9624	**6.4951 ± 0.3992**

Table 6.11: Simulated Lifetime Measurement Results, $N_{samples}$ = 10K to 50K
σ_{img} = 25.0 mm, τ_0 = 0.029 ns to 6.872 ns, β = 0.3c, N_{trials} = 1000

6.4 Experimental Validation

Simulations only get us so far. I also performed an experimental validation of the techniques I developed, using known excited states of ^{92}Mo. This work suggests that it is indeed possible to use gamma-ray imaging for lifetime measurements, though difficulties arise for nuclei with complex energy spectra. As expected, Doppler-shift imaging yields superior performance over Compton imaging.

As a final test, I applied my imaging and lifetime measurement methods to a real, non-simulated experiment. I chose to study two known transition in ^{92}Mo, populated in the ^{12}C[^{84}Kr, 4n]^{92}Mo reaction. The experiment was performed at ANL's ATLAS facility, using a ^{84}Kr projectile on a ^{12}C target. The experimental detector geometry is shown in Figure 6.13. [23] The ^{84}Kr projectiles were accelerated to 394 MeV *total* kinetic energy, resulting in a pre-collision speed of 0.100c. The ^{92}Mo nuclei thus produced had a maximum recoil speed of 0.085c. Because the source was moving, I was able to test both types of gamma-ray imaging.

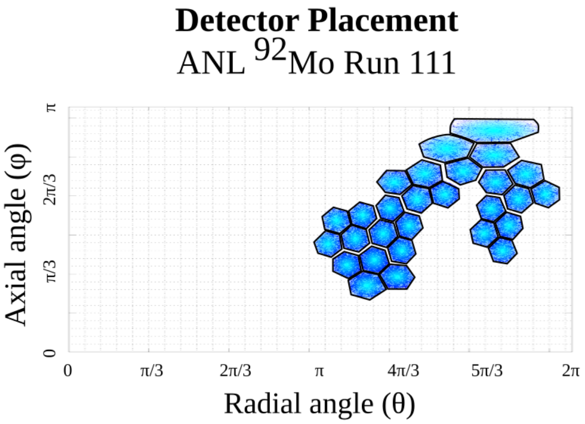

Figure 6.13: Detector placement in ANL ^{92}Mo experiment

The first step was to compute the Doppler-corrected emission spectrum of the excited ^{92}Mo nuclei. To do so, I assumed all gamma rays were emitted from the target and used Compton sequencing to find the first hit in each detected photon track. From the corresponding estimate for the emission angle, and the detected lab-frame energy, I then computed the CM-frame energy spectrum (shown in Figure 6.14). A 2064.1 keV line is plainly visible along with many lower-energy lines.

I searched this corrected energy spectrum for states suitable for lifetime measurements with gamma-ray imaging. Brookhaven National Laboratory maintains an extensive database of such information in its Chart of Nuclides. [22] The first requirement was a strong gamma peak – something that stood out of the spectrum and did not overlap with nearby peaks. (The signal-to-noise ratio quantifies this.) The second requirement was a lifetime that *conceivably*

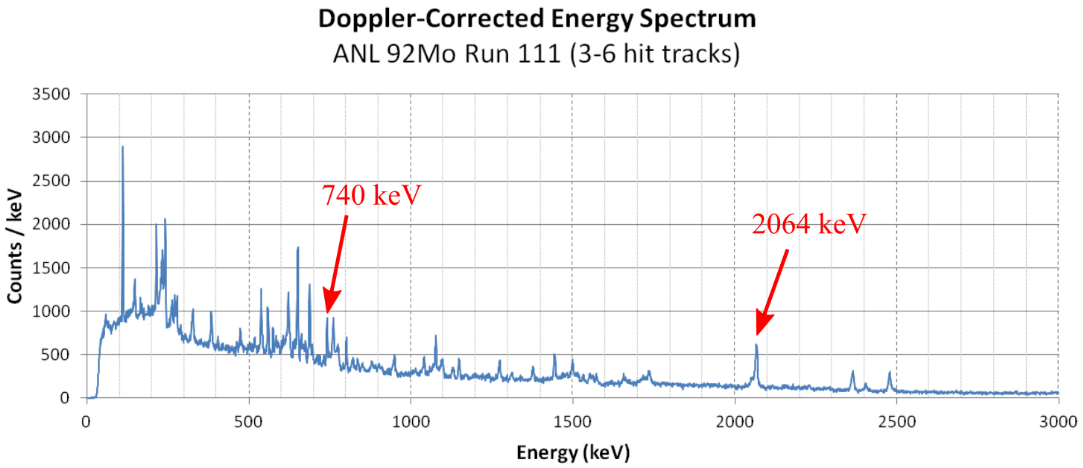

Figure 6.14: Doppler-Corrected ^{92}Mo Spectrum

was long enough to discern with imaging. Table 6.12 lists several initial candidates I found. It includes energy windows used to define each peak, as well as the peak-to-totals and signal-to-noise ratios for those windows.

Energy	**Lifetime**	**Energy Window**	**Peak-to-Total***	**SNR****
111.2 ± 0.2 keV	22 ± 3 ps	107 keV to 115 keV	4.95E-3 ± 1.5E-4	0.579 ± 0.018
740.3 ± 0.2 keV	35 ± 3 ps	736 keV to 745 keV	1.57E-3 ± 1.0E-4	0.325 ± 0.021
800.7 keV	22 ± 3 ps	795 keV to 807 keV	1.41E-3 ± 1.0E-4	0.298 ± 0.023
1374.7 keV	35 ± 3 ps	1370 keV to 1384 keV	8.78E-4 ± 9.0E-5	0.262 ± 0.027
2064.1 ± 0.3 keV	< 0.7 ps	2058 keV to 2074 keV	3.66E-3 ± 1.0E-4	1.102 ± 0.036

Table 6.12: Common gamma-ray lines in ^{92}Mo
* Defined as the ratio of peak net counts to **total** counts between 0 - 3000keV
** Defined as the ratio of peak net counts to peak background counts

Of these, I decided to use the 740.3 keV and 2064.1 keV transitions. While the 111.2 keV peak is the strongest one in the spectrum, it is too low-energy for Compton imaging. The state's lifetime is also on the extreme low-end of what we expect to be able to see with either imaging mode. (The decay parameter of $\mu = 1.8$ mm^{-1} means that 99.9% of the nuclei de-excite within 3.9 mm of the target.) I ruled out the 800.7 keV peak for the same reason. Lastly, while the 740.3 keV and 1347.7 keV transitions share the same lifetime, the peak-to-total for 740.3 keV is significantly higher.

The 2064 keV transition has a *very* short known lifetime of < 0.7 ps. Combined with the low 0.085c parent velocity, this gives a decay parameter of $\mu > 56$ mm^{-1}. This is short enough for the source to appear like a stationary point source at the target. Neither gamma-ray imaging method has sufficiently good resolution to distinguish such a short de-excitation curve. (Consider that 99.9% of the nuclei de-excite within the first 0.12 mm downstream of the target.) This is actually extremely advantageous – it means the true emission points can all be approximated as coming from the target location ($z_0 = 0.0$ mm). We can thus treat the gamma-ray *image* as the imaging *response*, i.e. the difference between the measured and true emission points. Characterizing this detector response is of course essential to accurate lifetime measurements.

For this experiment, my goal was to use the measured imaging responses at 2064.1 keV to correct the images produced at 740.3 keV. This assumes that the responses are similar at both energies. However, as we can see from Figures 6.15 and 6.16, this is not at all a good assumption. At 2064 keV, both imaging methods produce single-peak images, but they have somewhat different shapes than those we produced in our simulations of the 1.0 MeV beam source. There is also significantly higher background. The Doppler-shift image, in particular, resembles a Gaussian sitting atop a nearly uniform background. Unlike in simulations, the energy spectrum continues past the photopeak energy. Recall that lower-energy background below a peak causes a low tail of counts on the right side of the image. Similarly, higher-energy background gives rise to a low tail on the *left* half of the image.

The images at 740 keV are *much* less well-behaved. The Doppler-shift image still exhibits a clear peak near the target; this reflects the sharp de-excitation curve for the 740 keV transition. However, the background is far from uniform across the imaging range. In fact, there appears to be a second, broader peak to the left of the target. This is due to another nearby photopeak at 762.9 keV, which is too close in energy to be rejected directly. The Compton image is also much degraded compared to the corresponding image at 2064 keV. From Figure 6.14 and Table 6.12, we can see that the Compton background at 740 keV is significantly higher than at 2064 keV. While many of these background counts can be rejected by data filters, the ones that remain will blur the output images.

I was thus left with a question – how to deal with the very different imaging backgrounds for the two energies? To apply the detector response at 2064 keV to measure the lifetime at 740 keV, I needed to reduce the two imaging responses to comparable forms. Figures 6.15 and 6.16 illustrate my approach to the problem. The first step was to obtain a raw gamma-ray image (top row). After that, I identified the imaging background by defining a peak window (middle row). I simply set these windows by eye. Lastly, I performed a background subtraction to isolate the "true" image (bottom row). This subtracted all counts outside the peak window. I required counts to go to zero at the window boundaries, subtracting a trapezoidal approximation of the background within the peak area. I took the remaining peak as the final image. In the case of the 2064 keV transition, this became the imaging response I used in the lifetime measurement.

This is admittedly a very crude approach. However, I did not have time to develop a

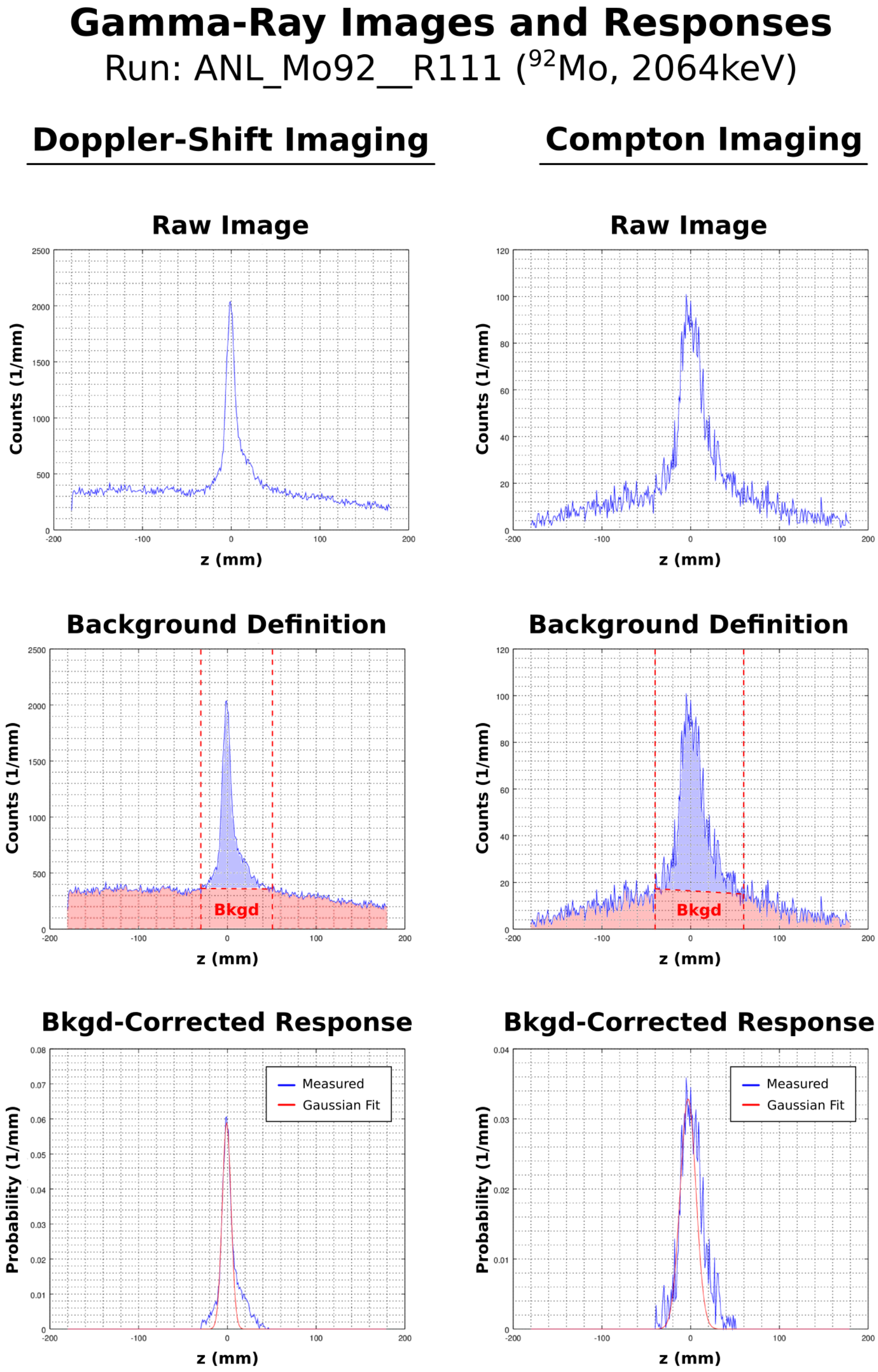

Figure 6.15: Gamma-ray imaging responses for the 2064 keV transition of ^{92}Mo

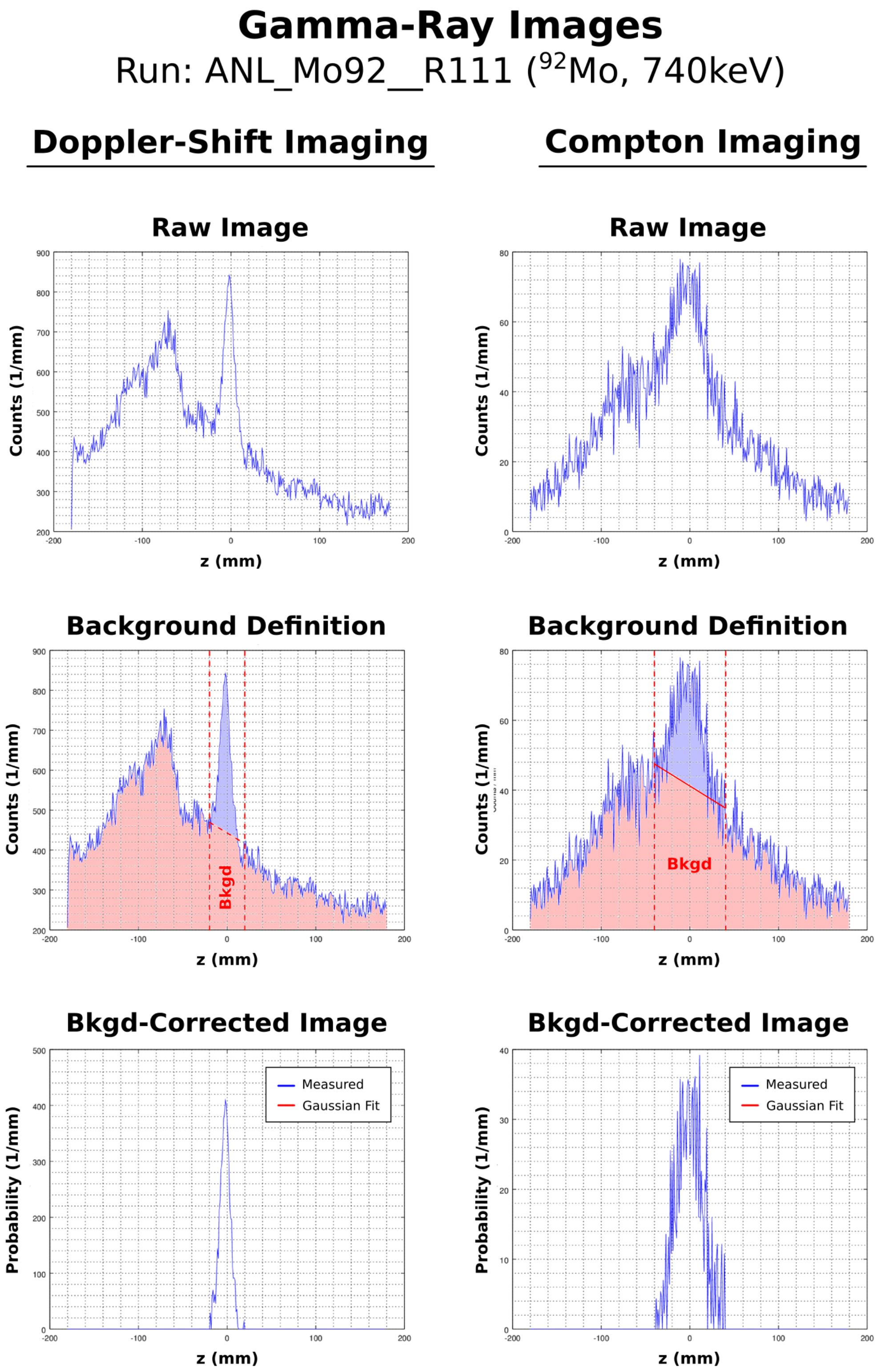

Figure 6.16: Gamma-ray imaging responses for the 740 keV transition of ^{92}Mo

more rigorous method. Imaging response depends on more than a photon's CM-frame energy or the properties of the parent nuclei. It also depends on the highly complex structure of the background in the allowed energy range (in this case, roughly 680 - 795 keV). This makes it very difficult to use imaging responses at other energies or from other nuclei as surrogates in lifetime measurements. It is also unclear how we would use this method for de-excitation curves that span more of the total imaging window (i.e. long lifetime and/or high parent velocity). As the 740 keV images show, we might not be able to use a trapezoidal estimate for background in such cases.

Table 6.13 shows the results of the experimental measurements. I restricted tracks to 3-6 hits in length and the CM-frame energies to those in Table 6.12, but otherwise did not apply any data cuts. I only calculated imaging resolution for the 2064 keV transition, where I could treat the source as stationary and fit a Gaussian to the images. I then obtained imaging efficiencies using the ratio of successful reconstructions to the number of counts in their respective peak energy windows. I found that Doppler-shift imaging yields close to 5x better resolution and 10x better imaging efficiency than Compton imaging, and therefore seems the clear choice to use for these kinds of measurements.

2064 keV Transition

	Compton Imaging	**Doppler-Shift Imaging**
Imaging Peak Window	-40.0mm to 40.0mm	-20.0mm to 20.0mm
Imaging Resolution	20.90 ± 2.23 mm	4.96 ± 0.07 mm
Imaging Efficiency	1.057E-2 ± 4.9E-8	1.279E-1 ± 6.6E-7

740 keV Transition

	Compton Imaging	**Doppler-Shift Imaging**
Imaging Peak Window	-40.0mm to 60.0mm	-30.0mm to 50.0mm
Imaging Efficiency	2.061E-2 ± 7.6E-8	4.480E-3 ± 1.6E-8
Measured Lifetime	*N/A*	*N/A*

Table 6.13: Lifetime and imaging performance for ^{92}Mo

Unfortunately, the lifetime measurement was unsuccessful. In the Doppler-shift imaging case, the 2064 keV imaging response was wider than the "peak" I defined for the 740 keV line. Because of this, the χ^2 algorithm described in Section 6.2 converged to a zero lifetime. In the Compton imaging case, I observed the opposite problem. This perhaps reflects the stark difference in shape of the imaging responses at 2064 keV and 740 keV, even after background subtraction.

Clearly, more work needs to be done to refine these measurement techniques. The main problem lies in accurately characterizing the detector response for the transition under study. There are a few methods we might try to improve this characterization. For example, Compton imaging is able to image stationary sources. We can therefore place a calibration point source (like ^{60}Co) at a fixed location on the beam axis, and use the measured image as the detector response. This method does assume, however, that the velocity of the beam has little effect on the overall imaging response. This method therefore does *not* work for Doppler-shift imaging.

We could also make use of the χ^2 fitting technique used in lifetime measurements (Section 6.2). Instead of starting with a *known* detector response and an unknown lifetime, we could use a transition with known *lifetime* to deduce the detector response. (The 2064 keV transition of ^{92}Mo is a good example.) The goal is to find a hypothesized response that most closely transforms the known source distribution (determined by lifetime and parent velocity) into the measured image. We would have to propose the *shape* of the response, and decide whether to account for geometric complications such as detector placement. Once we have a properly-parametrized detector response, we could then construct a χ^2 curve to find the best-fit value for each parameter. However, this method assumes the surrogate response thus produced is applicable to the state under study.

Lastly, we could potentially compute the detector response with a sufficiently-realistic simulation. Due to time constraints, I only explored a simple 1.0 MeV beam source in Chapters 4 and 5. We could readily simulate any other specific experimental setup. We would need to assume values for the detector energy and position resolution, as well as the nuclear lifetime and velocity. But once these properties were known, we'd be able to simulate photon tracks with known emission points, and construct images from there. The goal would be to run such simulations for a range of lifetimes, producing a different response matrix for each, and then find the one that produced the best experimental results. One could potentially quantify this by looking for the response that yielded the smallest uncertainty on the measured lifetime. This method seems the most promising of the three.

Despite the negative results of this experimental validation, I still have hope. The 740 keV transition of ^{92}Mo has a very short lifetime. Combined with the low recoil velocity of the parent nuclei, this de-excitation was on the extreme low-end of what I expected to be able to resolve. It's likely there are other states that would be more conducive to study with gamma-ray imaging. We'll discuss them in more detail in Section 7.2.

Chapter 7

Conclusions

7.1 Comparing Compton and Doppler-Shift Imaging

Doppler-shift imaging avoids many of the issues with Compton imaging, and seems much more promising for lifetime measurements with GRETINA. It delivers better resolution and significantly higher imaging efficiency, especially at low photon energies. However, Doppler-shift imaging also rests on multiple assumptions which make it much less versatile than Compton imaging in other applications.

Both the Compton and Doppler-Shift imaging methods have their strengths and weaknesses, which we went over in detail in Sections 4.1 and 5.1. Table 7.1 summarizes the comparison between the two. Note that both imaging methods require full energy-deposition in the detector.

Figures 7.1 and 7.2 provide an apples-to-apples comparison of the two imaging methods for a typical experiment, taken from Chapters 4 and 5. Again, these results are for a simulated beam source with 1.0 MeV CM-frame photon energy and 0.3c parent velocity. A uniform (3.0 mm, 2.0 keV) detector resolution was applied to every simulated photon interaction. We found that Compton imaging achieved 25.17 ± 0.65 mm imaging resolution and 29.96 ± 0.07% absolute imaging efficiency, while Doppler-shift imaging delivered 3.97 ± 0.03 mm imaging resolution and 71.93 ± 0.12% imaging efficiency.

Note that in Figure 7.2, no data filters were used to improve imaging quality. By contrast, Figure 7.3 shows some of the better results achieved when filters were applied. By far the most effective way to improve Compton imaging is the comparison of measured and known CM-frame photon energies. (After a photon's emission point is calculated, we can use the corresponding measured emission angle to compute the corrected CM-frame energy.) Using the same detector setup as above, I was able to narrow imaging resolution to 4.09 ± 0.05 mm. This massive improvement came at a fairly high cost, however – absolute imaging

	Compton Imaging	**Doppler-Shift Imaging**
Strengths	Largely insensitive to σ_E Does spectroscopy & imaging	Largely insensitive to σ_{xyz} Only requires a single hit Usable for low-energy γ's High imaging efficiency
Weaknesses	Highly-sensitive to σ_{xyz} Highly-sensitive to sequencing Requires two sequenced hits Low imaging efficiency	Highly-sensitive to σ_E Highly-sensitive to beam velocity Requires a relativistic source Requires prior spectroscopy Poor Compton bkgd rejection

Table 7.1: Strengths & Weaknesses of Compton and Doppler-Shift Imaging

efficiency dropped to 2.202 ± 0.016% (7.501 ± 0.058% relative to the unfiltered case).

Doppler-shift imaging did not see such large improvements in its imaging resolution. Here, it's not detector resolution but rejection of Compton background that most limits the fidelity of the output images. Of the data cuts I studied in my simulations, the most effective one accepted or rejected counts based on emission angle. (Refer to Section 5.3.) It does cause the shape of the imaging response to change significantly due to geometric effects, although this can be adjusted for in the detector response. A more important issue arises in realistic experiments with complex energy spectra. Here, most photopeaks will lie above a Compton background from higher-energy peaks. The angle-rejection technique does not help as much in such situations. In fact, it may even be a hindrance, as it will reduce the number of true photopeak reconstructions without removing higher-energy background.

In general, Doppler-shift imaging appears more promising for lifetime measurements with the GRETINA detector, where Compton imaging is limited by the detector's position resolution and short Compton lever arms. But because the Doppler-shift method also requires á priori knowledge of the source's velocity vector and specifc CM energy, its applications outside of lifetime measurements appear limited. Compton imaging is much more versatile, with applications in nuclear security, astrophysics, and nuclear medicine.

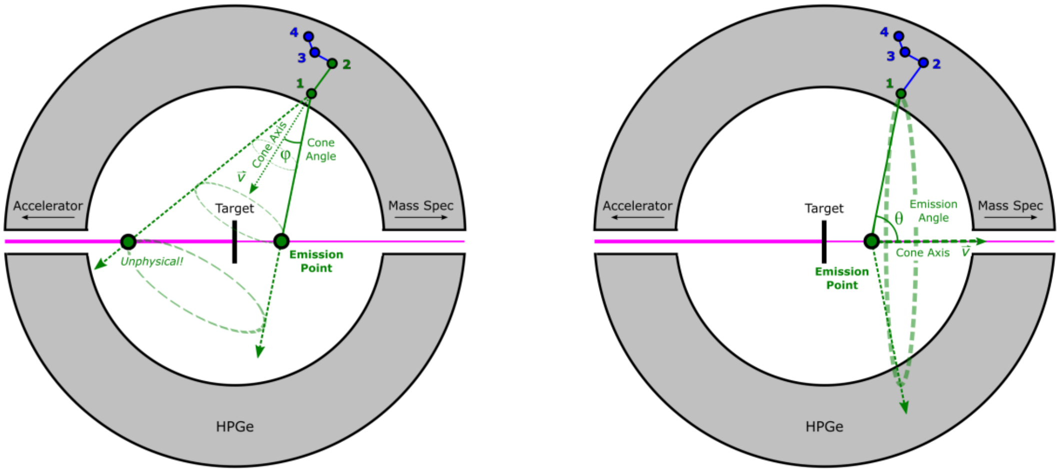

Compton Imaging

Requires 1st & 2nd hits in detector, including (x,y,z,ΔE)

Doppler-Shift Imaging

Requires 1st hit in detector, plus E_{CM} of emission

Figure 7.1: Side-by-side illustration of the Compton and Doppler-Shift imaging techniques

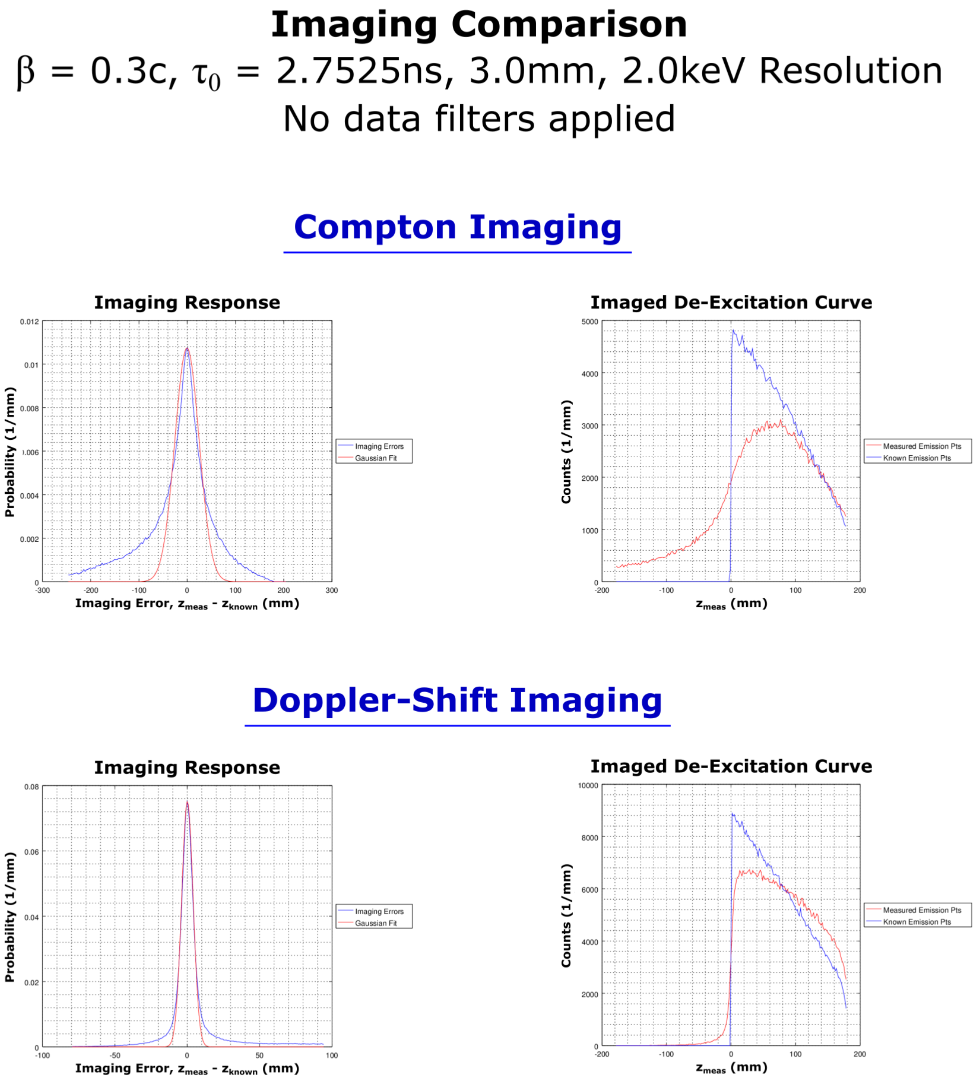

Figure 7.2: Comparison of Compton & Doppler-Shift imaging responses, no data filters
For a typical detector and lifetime

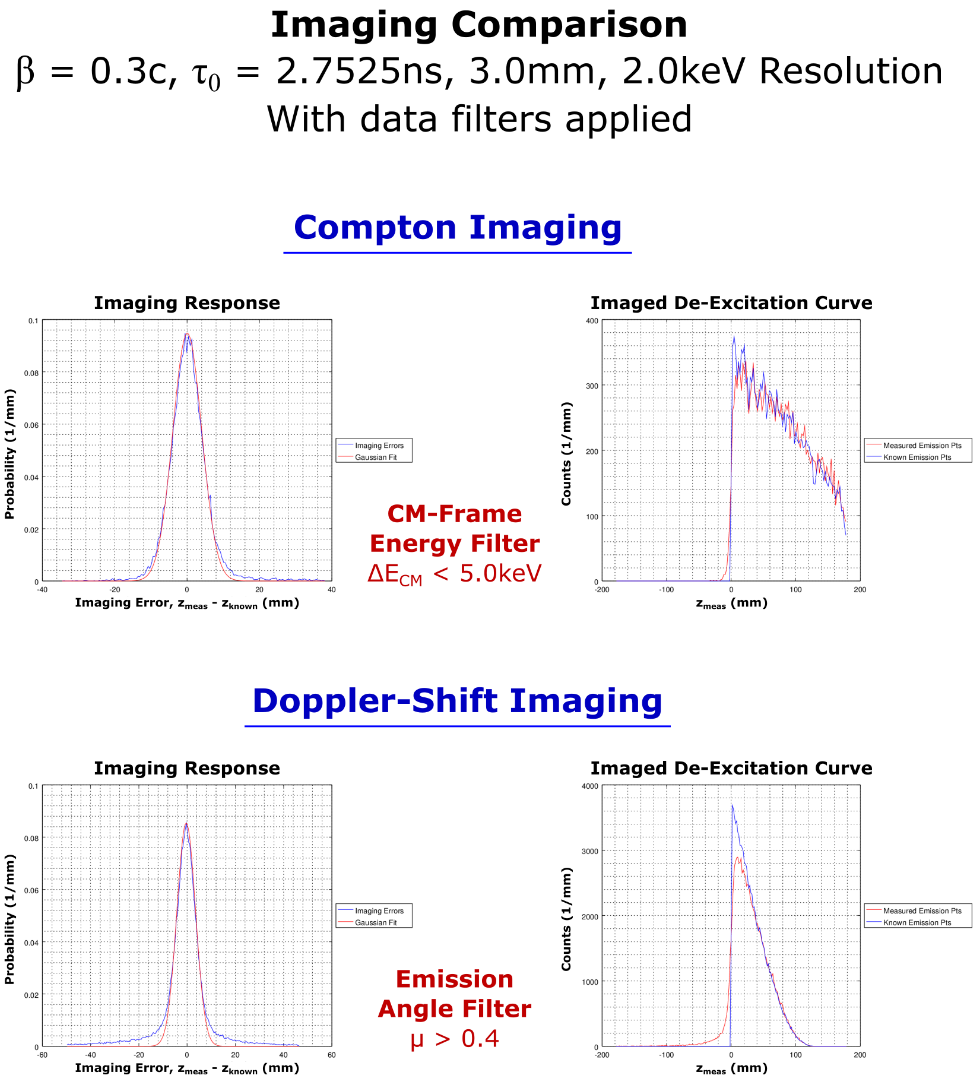

Imaging Comparison

$\beta = 0.3c$, $\tau_0 = 2.7525$ns, 3.0mm, 2.0keV Resolution
With data filters applied

Compton Imaging

CM-Frame Energy Filter
$\Delta E_{CM} < 5.0$keV

Doppler-Shift Imaging

Emission Angle Filter
$\mu > 0.4$

Figure 7.3: Comparison of Compton & Doppler-Shift imaging responses, with data filters
Reducing Compton bkgd enhances image quality

7.2 Conclusions About Lifetime Measurements

The simulated lifetime measurements from Chapter 6 are very encouraging. They suggest that, even with relatively poor imaging resolution, we can still determine lifetime fairly precisely (< 10% relative uncertainty). An experimental validation turned out to be much more challenging than I had expected, however. In this section we discuss the reasons for this and what can be done to improve future real-world measurements.

In Chapter 6, I sought to understand the effects of imaging resolution and statistics on lifetime measurements. I did a semi-exhaustive 2D parameter search, varying imaging resolution from 1.0 mm to 75.0 mm and statistics from 100 counts to 50K counts. A surprising result was that, even with *abysmal* imaging resolution, it is still possible to measure a lifetime within 1% uncertainty if given enough statistics. Tables 6.1 to 6.7 provide a detailed breakdown of the simulation results. In a second set of calculations, I also looked into lifetime precision over a range of lifetimes. Here, I kept the parent velocity constant at 0.3c, and varied imaging resolution and number of counts separately. Again, the results appear quite good. Figure 7.4 shows some of the lifetime precision curves obtained through simulation.

I also used the data to describe sensitive ranges for lifetime measurements with imaging. These ranges show the lifetimes we could measure to within 10% uncertainty, given a set imaging resolution and number of counts per de-excitation curve. Figure 7.5 provides several examples. In all cases, statistics seems to be the limiting factor in lifetime measurements – not imaging resolution. In other words, improving GRETINA's position resolution is not as important as it might appear for this application. Suppose that, instead of 3.0 mm detector position resolution, we had the 0.5 mm resolution typical of double-sided strip detectors (or DSSDs). [25] With no data filters applied, Compton imaging would deliver 9.62 mm imaging resolution instead of 25.17 mm (Table 4.2). However, this would only extend our sensitive range from roughly 0.05 ns $< \tau_0 <$ 3.27 ns to 0.03 $< \tau_0 <$ 3.62 at $\beta = 0.3$c and $N_{samples} =$ 5000 counts. (Table 6.8) And from Table 5.1, it is clear that Doppler-shift imaging resolution is even less affected, only improving from 3.97 mm to 3.11 mm. It's unclear exactly how much this would improve lifetime sensitivity, but the gains would likely be very modest.

In the follow-up experimental validation, I sought to measure the lifetime of the 740 keV transition in ^{92}Mo. I was hopeful that I could use the imaging response from the 2064 keV transition as a surrogate for the unknown response at 740 keV. However, the imaging responses varied much more than anticipated between the 740 keV and 2064 keV emissions. I attribute these differences to the differences in the energy spectrum near the two photopeaks. The 2064 keV line stands alone on a relatively small Compton background (SNR = 1.102), with no other photopeaks on either side for several hundred keV. As a result, the gamma-ray images for this transition show a single clear peak (though it's much sharper with Doppler-shift imaging). By contrast, the 740 keV line sits atop a much higher relative background (SNR = 0.325), and has a nearby peak at 763 keV which shows up prominently as noise in

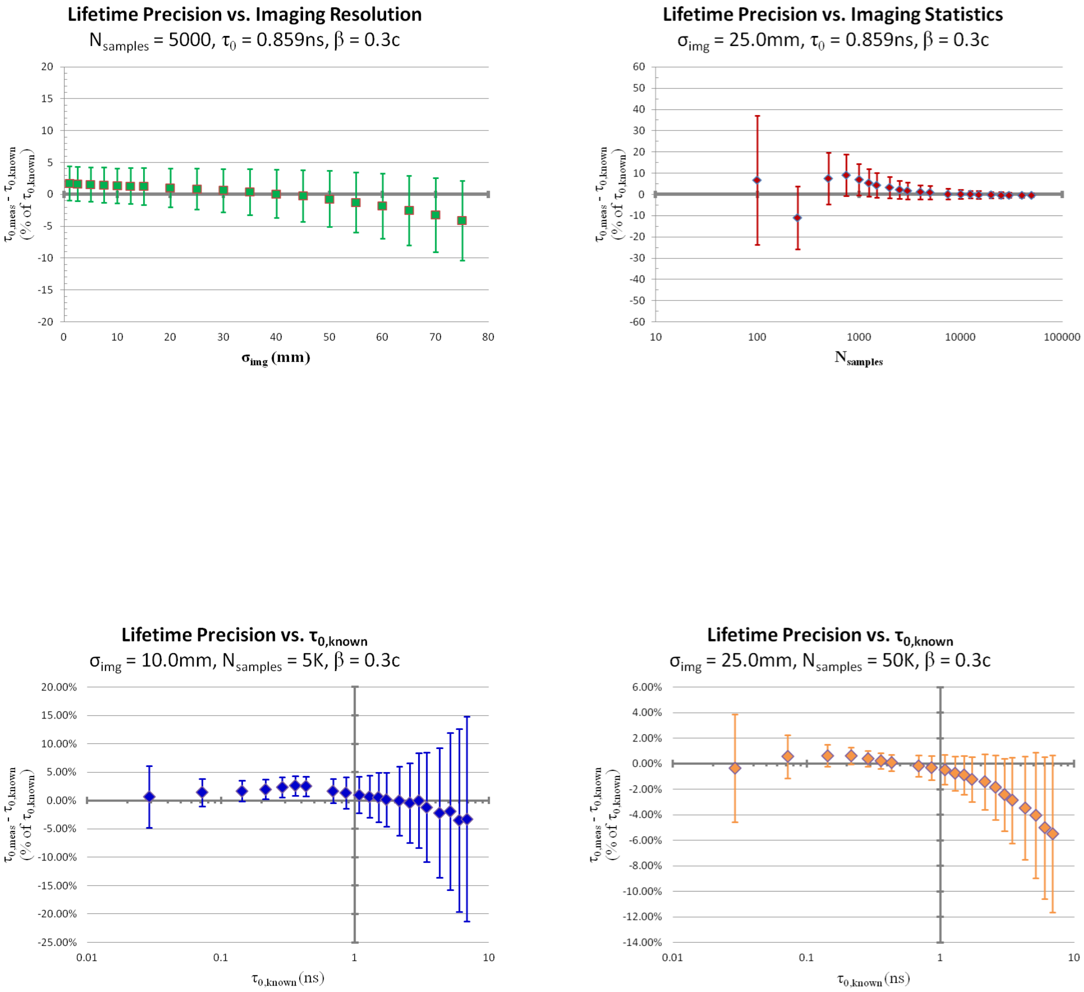

Figure 7.4: Lifetime measurement precision from simulations

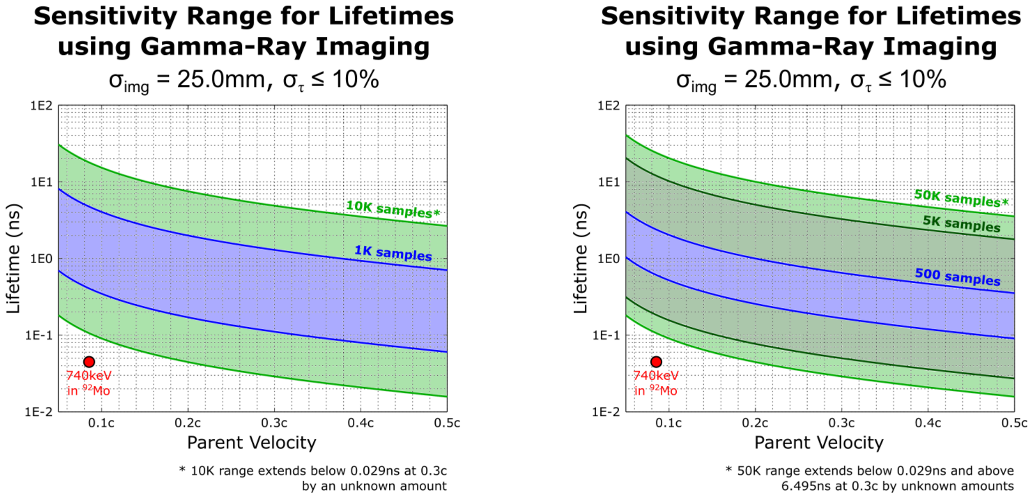

* 10K range extends below 0.029ns at 0.3c by an unknown amount

* 50K range extends below 0.029ns and above 6.495ns at 0.3c by unknown amounts

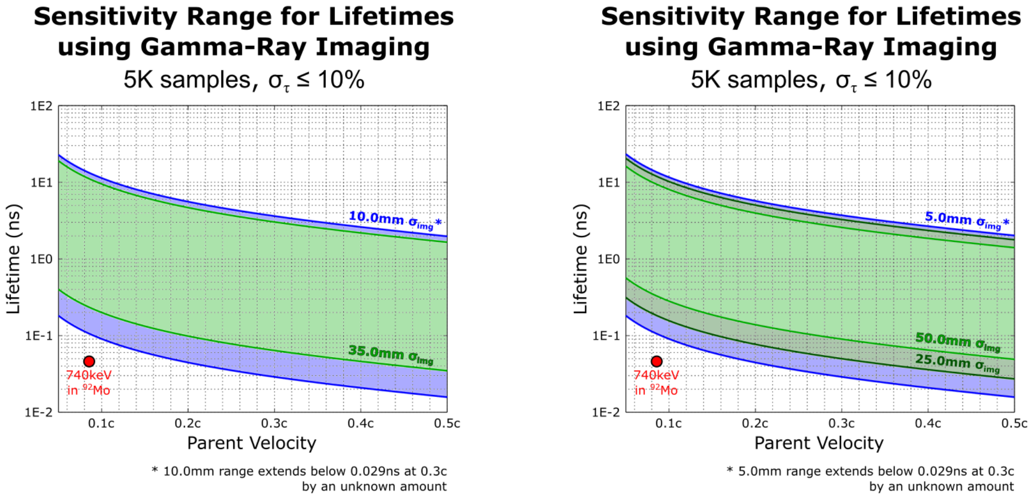

* 10.0mm range extends below 0.029ns at 0.3c by an unknown amount

* 5.0mm range extends below 0.029ns at 0.3c by an unknown amount

Figure 7.5: Lifetime sensitivity ranges from simulations

both the Compton and Doppler-shift images.

A large part of the difficulty is in correcting for this background imaging noise. The complete dissimilarity in the images at 740 keV and 2064 keV frustrated my efforts to come up with a standard approach to the problem. The background-reduction methods I developed from simulations of a 1.0 MeV beam source were inadequate. Instead, I more or less had to "eyeball" the background and subtract it to arrive at a "corrected" image. As I then found out, the responses thus produced for the 2064 keV transition were not applicable to the 740 keV case, and so I did not arrive at a valid measure of the lifetime. That said, this particular experimental validation was an ambitious one. With a 35 ps lifetime and 0.085c parent velocity, the 740 keV state lies well outside the estimated sensitivity ranges. (I've marked the transition in red on Figure 7.5.)

To get better results in future experiments, a few things would need to hold true. We might sum up these requirements with the following "rules of thumb":

1. **A de-excitation parameter between 0.003 / mm $< \mu <$ 0.365 / mm**
   There is no hard and fast rule here, but a combination of low parent velocity and short lifetime will make it very difficult to resolve a de-excitation curve even under the best of circumstances. The 740 keV transition of ^{92}Mo had a value of $\mu = 1.1$ / mm, meaning that over 99% of emissions occurred less than 5.0 mm downstream of the beam target.

2. **A gamma line in an uncrowded portion of its parent energy spectrum**
   The 2064 keV line from ^{92}Mo has no other photopeaks around it for hundreds of keV. By contrast, the 740 keV line sits atop a large Compton background from nearby peaks, the closest of which is only 20 keV away (763 keV). As a result, photons from the 2064 keV transition are much easier to isolate and therefore produce a much cleaner imaging response.

3. **A comparable imaging response from a known surrogate state**
   Correcting for imaging effects requires the imaging response to be well-characterized. However, to characterize the imaging response we need to find a surrogate state to use. The surrogate should have a very short lifetime (behaving like a point-source) and come from a *comparable* energy spectrum to the state under study. I simply did not have this for the 740 keV ^{92}Mo transition.

4. **At least 25K net counts in the photopeak on the parent energy spectrum**
   To obtain 10% lifetime uncertainty with 25.0 mm Gaussian imaging resolution, I found that we'd need approximately 1000 counts *in the final image*. Accounting for imaging efficiency, which can be as low as a few percent for Compton imaging, we would therefore want close to 25K *net* counts in the photopeak. If the Compton background was

particularly high below the peak in question (low "signal-to-noise"), we would want to aggressively filter the data. This would further increase the statistics requirement.

5. **A lab-frame gamma-ray energy between 500 keV and 8.0 MeV**
It's actually a bit unclear what photon energy is ideal for imaging. To use Compton sequencing, we need tracks to have 3+ interactions, which becomes increasingly rare as photon energy decreases. That said, as we saw in Section 3.3, mis-sequencing errors become more prevalent as track length increases. We can also technically use Doppler-shift imaging for single-hit tracks and Compton imaging for tracks with just 2 hits. However, it is easier to filter Compton background counts when using longer tracks. High-energy photopeaks tend to have larger signal-to-noise ratios than low-energy peaks.

With these requirements satisfied, GRETINA's detector performance should be sufficient to measure lifetimes via gamma-ray imaging. Finding states to measure is a complex question, however. Not only should the emitted gamma ray satisfy the above requirements, but the parent state must also be reasonably easy to populate in a beam experiment.

7.3 Future Work and Lessons Learned

This section concludes my presentation on lifetime measurements with gamma-ray imaging. It brings up some of the most important findings, as well as the next steps I recommend taking to further this research. This future work is left open to anyone who may be interested in carrying on the torch.

The results presented here are extensive but far from complete. There is plenty of opportunity for others to extend my work.

In Chapters 4 and 5, I used a series of simulations to study the effects of various experimental parameters on Compton and Doppler-shift imaging quality. I quantified imaging performance for a typical detector using both imaging methods, assuming a uniform 3.0 mm position resolution and 2.0 keV energy resolution for photon interactions. However,Ie only did so for a very simple test case – photons of 1.0 MeV CM-frame energy, emitted by parent nuclei with a 2.7525 ns lifetime and 0.3c lab-frame velocity. The results thus obtained cannot be extrapolated or applied to all subsequent imaging problems, as I found in Section 6.4. Differences in energy spectra and detector responses make it very difficult to do so. Rather, I have developed a *framework* for studying such problems further. We could use these models to simulate a great many other specific lifetime experiments, and from there attempt to identify those worthy of pursuit with gamma-ray imaging.

Another of my goals, discussed in Sections 4.3 and 5.3, was to identify a choice of data cuts to optimize imaging quality. This also proved to be too large in scope to tackle here – there simply is no one-size-fit-all solution. The 1.0 MeV-photon toy problem proved successful enough. I proposed a small set of potential filters for both Compton and Doppler-Shift imaging, and found the ones which *individually* offered the most substantial improvements to imaging quality. However, I did not study combinations of data cuts in any detail. Nor did I come up with objectively-optimal choices for things like Compton lever arm and sequencing FoM. These choices would depend on the specific experiment in question, hinging on things like the photon energy, the number of counts that would be available, and the desired precision in the measured lifetime. Fully exploring such a large parameter space would keep a grad student busy for a *very* long time.

I also ran into limitations simply trying to define "optimum". It was clear from my imaging simulations that Doppler-shift imaging offers much better FWHM imaging resolution than its Compton imaging counterpart, at least for the typical detector we have described. But that single figure cannot account for subtleties in the imaging response, particularly the long "tails" caused by Compton background in Doppler-shift images. The data cuts I investigated for this imaging method did not actually affect the FWHM all that much, and yet they often noticeably improved the output images of the de-excitation curves. However, I did not use any other metrics to quantify these improvements, and so I did not draw conclusions about the optimal filtering limits to be used with Doppler-shift or Compton imaging. I can say, though, that Doppler-shift imaging is more promising, especially when background is low.

In Chapter 6, I ran a series of simulations to investigate how lifetime measurements are affected by imaging resolution and statistics. The findings were extremely encouraging. This said, I made a few important assumptions. First, I set the parent nuclei's proper lifetime to 0.859 ns and lab-frame velocity to 0.3c. This combination is close to an ideal case, as it means that 90% of the de-excitations occur within the imaging range (0.0 mm $< z <$ 180.0 mm). Second, and perhaps more importantly, I assumed the imaging responses are purely Gaussian in shape. This is true in some cases, especially if we ignore the high-error tails on Doppler-shift imaging responses. However, subtleties like these can impact the measured images quite significantly (see Figure 5.6). Third, I also ignored complications from specific detector geometries, which affect imaging efficiency along the beam-line. To improve on the methods here, it would be useful to study more complex and realistic detector responses.

One of the goals with the lifetime measurement simulations was to identify an effective range for which Doppler-shift or Compton imaging might be advantageous compared to RDM. I performed one set of simulations on this front, using a $\sigma = 25.0$ mm Gaussian imaging response, a 0.3c parent velocity, and 50K samples per de-excitation curve. These more or less confirmed my back-of-the-envelope estimates for the effective range (approximately 0.23 ns to 2.7 ns). I found that, with sufficient statistics like this, the range could be extended significantly. I saw $< 4\%$ relative uncertainty between approximately 0.35 ns and 4.0 ns. Obviously, this is another case where a one-size-fits-all solution does not exist. The effective range really depends on the required uncertainty, the parent lifetime, and the particular imaging response. If I were to continue this study, I would use my framework to perform sensitivity studies for a much broader range of experimental parameters.

The experimental validation (Section 6.4) illustrated some limitations in my current approach to the problem. I expected to be able to see the 35 ps lifetime of the 740 keV transition in ^{92}Mo – both Doppler-shift and Compton imaging gave significantly better than 25.0 mm imaging resolution with the 2064 keV transition, and the available datasets contained a sizable number of counts for imaging. However, as discussed above in Section 7.2, it proved difficult to make such an apples-to-apples translation. The two photopeaks in question sat atop large Compton backgrounds from other higher-energy peaks. In the case of the 740 keV line, there was also a nearby photopeak that added to the imaging noise. The non-uniformity of this noise made it difficult to quantify the imaging response, hence frustrating my efforts to measure the lifetime of the 740 keV transition. Neither the Compton nor Doppler-shift imaging techniques proved reliable here.

The next step is to assemble a list of candidate states to measure the lifetimes of. The 740 keV transition in ^{92}Mo made for a particularly difficult experimental validation, but it is what I had data for at the time. There are no doubt many other states that would prove more successful with gamma-ray imaging methods. Experimental data exists for dozens of isotopes, from which we might be able to draw a better candidate than ^{92}Mo. Beyond that, the NNDC Chart of Nuclides [22] could be used to identify thousands of other states which satisfy the guidelines given in Section 7.2. As discussed in Section 7.2, we're looking for states with > 1.0 MeV emissions and lifetimes > 200 ps. We need relatively strong emission lines with low Compton backgrounds and no nearby photopeaks on the energy spectrum.

After obtaining a list of candidate states, we could then either use existing experimental data to run through the imaging framework I've developed, or else propose a new experiment. And then, once the validity of the gamma-ray imaging lifetime technique is confirmed, we could look for as-yet unmeasured states for future experiments. The researchers at FRIB (Michigan State University) specialize in the study of rare isotope beams. They are an authority on which states are currently of most interest to the community, and could provide guidance on ones whose lifetimes likely fall in our feasibility range.

With that, I conclude my study of lifetime measurements with gamma-ray imaging. I invite anyone who is interested to reach out to me, whether for help understanding a general concept presented here, or to take over the reins of my work with lifetime measurements. It has been a thoroughly engrossing project from which I've learned a great deal. My greatest hope is that this dissertation has been useful to the reader, and I thank you for your interest in my small corner of the world.

Appendix A

Appendix

A.1 Derivation of the Compton Formula

The derivation of the Compton energy formula is straightforward, and included here for reference.

Deriving the energy of a photon after Compton scattering is fairly straightforward. Let the photon have initial 3-momentum $\boldsymbol{p_{\gamma,i}}$ and final 3-momentum $\boldsymbol{p_{\gamma,f}}$, and let the scattering electron have corresponding momenta $\boldsymbol{p_{e,i}}$ and $\boldsymbol{p_{e,f}}$. If we assume the electron is initially at rest, then $\boldsymbol{p_{e,i}} = 0$, and conservation of momentum gives:

$$\boldsymbol{p_{\gamma,i}} = \boldsymbol{p_{\gamma,f}} + \boldsymbol{p_{e,f}} \tag{A.1}$$

Conservation of energy yields

$$\begin{aligned} E_{\gamma,i} + m_e c^2 &= E_{\gamma,f} + E_{e,f} && \text{(A.2)} \\ &= E_{\gamma,f} + \sqrt{(p_{e,f}c)^2 + (m_e c^2)^2} && \text{(A.3)} \end{aligned}$$

where m_e is the rest mass of the electron (511keV). The next step is to solve for $\boldsymbol{p_{e,f}}$ from Equation A.1:

$$\begin{aligned} \boldsymbol{p_{e,f}} &= \boldsymbol{p_{\gamma,i}} - \boldsymbol{p_{\gamma,f}} && \text{(A.4)} \\ \boldsymbol{p_{e,f}} \cdot \boldsymbol{p_{e,f}} &= (\boldsymbol{p_{\gamma,i}} - \boldsymbol{p_{\gamma,f}}) \cdot (\boldsymbol{p_{\gamma,i}} - \boldsymbol{p_{\gamma,f}}) && \text{(A.5)} \\ &= \boldsymbol{p_{\gamma,i}} \cdot \boldsymbol{p_{\gamma,i}} + \boldsymbol{p_{\gamma,f}} \cdot \boldsymbol{p_{\gamma,f}} - 2\boldsymbol{p_{\gamma,i}} \cdot \boldsymbol{p_{\gamma,f}} && \text{(A.6)} \\ p_{e,f}^2 &= p_{\gamma,i}^2 + p_{\gamma,f}^2 - 2p_{\gamma,i}p_{\gamma,f}\cos\theta && \text{(A.7)} \\ &= E_{\gamma,i}^2/c^2 + E_{\gamma,f}^2/c^2 - 2(E_{\gamma,i}E_{\gamma,f}/c^2)\cos\theta && \text{(A.8)} \end{aligned}$$

where θ is the angle between $\boldsymbol{p_{\gamma,i}}$ and $\boldsymbol{p_{\gamma,f}}$, i.e. the scattering angle of the photon. Note that we used the standard relation between photon energy and momentum: $E_\gamma = p_\gamma c$. From

Equation A.1 we now get:

$$\sqrt{(p_{e,f}c)^2 + (m_ec^2)^2} = E_{\gamma,i} - E_{\gamma,f} + m_ec^2 \tag{A.9}$$

$$\begin{aligned}(p_{e,f}c)^2 + (m_ec^2)^2 &= (E_{\gamma,i} - E_{\gamma,f})^2 + 2m_ec^2(E_{\gamma,i} - E_{\gamma,f}) \\ &\quad + (m_ec^2)^2\end{aligned} \tag{A.10}$$

$$\begin{aligned}E_{\gamma,i}^2 + E_{\gamma,f}^2 - 2E_{\gamma,i}E_{\gamma,f}\cos\theta + (m_ec^2)^2 &= E_{\gamma,i}^2 + E_{\gamma,f}^2 - 2E_{\gamma,i}E_{\gamma,f} \\ &\quad + 2m_ec^2(E_{\gamma,i} - E_{\gamma,f}) + (m_ec^2)^2\end{aligned} \tag{A.11}$$

$$-2E_{\gamma,i}E_{\gamma,f}\cos\theta = -2E_{\gamma,i}E_{\gamma,f} + 2m_ec^2(E_{\gamma,i} - E_{\gamma,f}) \tag{A.12}$$

$$-E_{\gamma,i}E_{\gamma,f}\cos\theta/m_ec^2 = -E_{\gamma,i}E_{\gamma,f}/m_ec^2 + (E_{\gamma,i} - E_{\gamma,f}) \tag{A.13}$$

$$E_{\gamma,f} + E_{\gamma,f}E_{\gamma,i}/m_ec^2 - E_{\gamma,f}E_{\gamma,i}\cos\theta/m_ec^2 = E_{\gamma,i} \tag{A.14}$$

$$E_{\gamma,f}\left[1 + \frac{E_{\gamma,i}}{m_ec^2}(1 - \cos\theta)\right] = E_{\gamma,i} \tag{A.15}$$

$$E_{\gamma,f} = \frac{E_{\gamma,i}}{1 + (E_{\gamma,i}/m_ec^2)(1 - \cos\theta)} \tag{A.16}$$

This last result is the famous Compton energy formula.

A.2 Derivation of Relativistic Doppler Shift

Doppler-shift correction is one of the primary features of GRETINA. Here we derive the formula relating a photon's lab- and CM-frame energies.

Consider a nucleus traveling with velocity $\boldsymbol{v_p} = \beta c\hat{x'}$ in the lab frame, $\boldsymbol{S}$. Suppose this nucleus emits a gamma at an angle ϕ relative to its velocity. Without loss of generality, we can choose a coordinate system where the photon travels in the xy-plane. In natural units, then, we can denote the photon's lab-frame 4-momentum as:

$$\begin{aligned}p_{\mu,Lab} &= (E_\gamma, p_x, p_y, p_z) &\text{(A.17)}\\ &= (E_\gamma, |\boldsymbol{p_\gamma}|\cos\phi, |\boldsymbol{p_\gamma}|\sin\phi, 0) &\text{(A.18)}\end{aligned}$$

where $\boldsymbol{p_\gamma} = (p_x, p_y, p_z)$ is the photon's 3-momentum. By the Lorentz transformation, the photon's 4-momentum in the CM-frame $\boldsymbol{S'}$ of its parent nucleus is then:

$$\begin{aligned}p_{\mu,CM} &= (E'_\gamma, p'_x, p'_y, p'_z) &\text{(A.19)}\\ &= (\gamma E_\gamma - \gamma\beta p_x, \gamma p_x - \gamma\beta E_\gamma, p_y, p_z) &\text{(A.20)}\\ &= (\gamma E_\gamma - \gamma\beta|\boldsymbol{p_\gamma}|\cos\phi, \gamma|\boldsymbol{p_\gamma}|\cos\phi - \gamma\beta E_\gamma, |p_\gamma|\sin\phi, 0) &\text{(A.21)}\end{aligned}$$

From the energy coordinate, we see that:

$$E'_\gamma = \gamma E_\gamma - \gamma\beta|\boldsymbol{p_\gamma}|\cos\phi \tag{A.22}$$

Note that for photons, $E_\gamma = |\boldsymbol{p_\gamma}|$, so we have:

$$E'_\gamma = \gamma E_\gamma - \gamma\beta E_\gamma \cos\phi \tag{A.23}$$

$$E'_\gamma = \gamma E_\gamma (1 - \beta\cos\phi) \tag{A.24}$$

In other words, recalling that $\boldsymbol{S}$ is the lab frame and $\boldsymbol{S'}$ is the CM frame:

$$E_{\gamma,Lab} = \frac{E_{\gamma,CM}}{\gamma(1-\beta\cos\phi)} \tag{A.25}$$

A.3 Other Methods of Sequencing

Photon tracks can be sequenced deterministically or stochastically. This section describes multiple stochastic approaches.

The Compton kinematics approach discussed in Section 3.2 is only one approach to sequencing a photon track. Other common sequencing methods make use of Maximum-Likelihood (ML) techniques.

One approach uses the energy-dependence of the Klein-Nishina formula (Equation 2.4) to determine a sequence. Let $\frac{d\sigma(E)}{d\theta}$ be the differential Compton scattering cross-section and let $\sigma_C(E)$ be the integrated cross-section for a photon of energy E. Then the normalized probability for scattering at an angle between θ and $\theta + d\theta$ is:

$$\frac{dP(\theta)}{d\theta} = \left(\frac{1}{\sigma_C(E)}\right)\left(\frac{d\sigma(E)}{d\theta}\right) \tag{A.26}$$

Picking a sufficiently small $\Delta\theta$ such that the cross-sections are constant over the angular range, we get:

$$P(\theta) = \left(\frac{1}{\sigma_C(E)}\right)\left(\frac{d\sigma(E)}{d\theta}\right)\Delta\theta \tag{A.27}$$

The next step is to find the total probability for all scatters in the track. Since $\Delta\theta$ is arbitrary, we can write:

$$P_{total} = \prod_{j=2}^{N_{hits}-1} P(\theta_j) \propto \prod_{j=2}^{N_{hits}-1} \left(\frac{1}{\sigma_C(E)}\right)\left(\frac{d\sigma(E)}{d\theta}\right) \tag{A.28}$$

$$FoM = \prod_{j=2}^{N_{hits}-1} \left(\frac{1}{\sigma_C(E)}\right)\left(\frac{d\sigma(E)}{d\theta}\right) \tag{A.29}$$

As before, we just go through every possible sequence of hits and find the one that maximizes this quantity.

A second ML approach takes advantage of the energy-dependence of mean-free-paths in the detector. Roughly speaking, a low-energy photon should travel less distance than a high-energy photon before undergoing an interaction. (This is not strictly true, since the total interaction cross-section increases again above the pair-production threshold.) The probability that a photon of energy E will travel a distance between x and $x + dx$ in a detector volume is:

$$\frac{dP(E)}{dx} = \frac{1}{L(E)} e^{-x/L(E)} \tag{A.30}$$

$$= \frac{1}{n\sigma(E)} e^{-xn\sigma(E)} = \frac{M}{N_A \rho \sigma(E)} e^{-\frac{xN_A\rho\sigma(E)}{M}} \tag{A.31}$$

With small enough Δx, the integrated probability becomes:

$$P(E) = \frac{M\Delta x}{N_A \rho \sigma(E)} e^{-\frac{xN_A\rho\sigma(E)}{M}} \tag{A.32}$$

Here, $L(E) = 1/n\sigma(E)$ is the photon's mean-free-path, $\sigma(E)$ is the *total* interaction cross-section (including photoabsorption, etc.), n is the detector's atom density, ρ is its mass density, N_A is Avogradro's Number, and M is the material's molar mass. In HPGe, $\rho =$ 5.32 g/cm^3, $M =$ 72.6 g/mol, and $n =$ 4.4 x 10^{22} atoms/cm^3. Using similar arguments as above, we define a FoM by the total probability of the photon traveling the full length of the observed track:

$$FoM = \prod_{j=1}^{N_{hits}-1} P(E_j) = \prod_{j=1}^{N_{hits}-1} \frac{1}{L(E_j)} e^{-x_j/L(E_j)} \tag{A.33}$$

where x_j is the distance from $\boldsymbol{X_j}$ to $\boldsymbol{X_{j+1}}$ and E_j is the outgoing photon energy from $\boldsymbol{X_j}$. As before, we seek to find the sequence that maximizes this figure-of-merit. Note that this last approach can be used to sequence 2-hit tracks.

It is possible to combine multiple approaches into a single FoM. For example, we might use the product of Eq. A.29, A.33, and 3.9:

$$\begin{aligned} FoM = &\left(\frac{1}{(N_{scatters}-1)} \sum_{j=2}^{N_{hits}-1} \frac{(\Delta E_{meas,j} - \Delta E_{calc,j})^2}{\Delta E_{meas,j}^2} \right) \times \\ &\left(\prod_{j=2}^{N_{hits}-1} \left(\frac{1}{\sigma_C(E)} \right) \left(\frac{d\sigma(E)}{d\theta} \right) \right) \left(\prod_{j=1}^{N_{hits}-1} P(E_j) \right) \end{aligned} \tag{A.34}$$

In Section 3.3, we discuss the effectiveness of deterministic sequencing methods. It would be very interesting to do a comparison with the stochastic approaches described above.

A.4 Cone-Beam Intersections in Compton Imaging

This section provides the algebra behind the cone-beam intersections in Compton imaging. It requires a little matrix math, but nothing too fancy.

In Compton imaging, we need to find where the Compton cones intersect the beam axis. Reference [9] provides a general geometric expression for this problem, which we can adapt here for our specific problem.

As noted in Section 4.1, a Compton cone is defined by its vertex $\boldsymbol{X_C}$, central axis $\boldsymbol{\hat{V}_C}$, and cosine of opening angle $\mu_C = \cos\theta_C$. A point $\boldsymbol{Z}$ lies on the cone if:

$$\boldsymbol{\hat{V}_C} \cdot \frac{(\boldsymbol{Z} - \boldsymbol{X_C})}{\|\boldsymbol{Z} - \boldsymbol{X_C}\|} = \mu_C \tag{A.35}$$

Re-arranging terms, we can rewrite this equation as:

$$\boldsymbol{\hat{V}_C} \cdot (\boldsymbol{Z} - \boldsymbol{X_C}) = \mu_C \|\boldsymbol{Z} - \boldsymbol{X_C}\| \tag{A.36}$$

Squaring both sides, we get:

$$(\boldsymbol{\hat{V}_C} \cdot (\boldsymbol{Z} - \boldsymbol{X_C}))^2 = \mu_C^2 \|\boldsymbol{Z} - \boldsymbol{X_C}\|^2 \tag{A.37}$$

Noting the vector identities $(\boldsymbol{a}\cdot(\boldsymbol{b}-\boldsymbol{c}))^2 = (\boldsymbol{b}-\boldsymbol{c})^T\boldsymbol{a}\boldsymbol{a}^T(\boldsymbol{b}-\boldsymbol{c})$ and $(\boldsymbol{b}-\boldsymbol{c})^T(\boldsymbol{b}-\boldsymbol{c}) = \|\boldsymbol{b}-\boldsymbol{c}\|^2$, the above becomes:

$$(\boldsymbol{Z} - \boldsymbol{X_C})^T \boldsymbol{\hat{V}_C}\boldsymbol{\hat{V}_C^T}(\boldsymbol{Z} - \boldsymbol{X_C}) = \mu_C^2 (\boldsymbol{Z} - \boldsymbol{X_C})^T(\boldsymbol{Z} - \boldsymbol{X_C}) \tag{A.38}$$

$$(\boldsymbol{Z} - \boldsymbol{X_C})^T M (\boldsymbol{Z} - \boldsymbol{X_C}) = 0 \tag{A.39}$$

where $M = \boldsymbol{\hat{V}_C}\boldsymbol{\hat{V}_C^T} - \mu_C^2 I_3$ is a 3×3 symmetric matrix. We seek an emission point $\boldsymbol{X_0}$ somewhere on the beam, which can be parametrized as $\boldsymbol{X_0}(t) = \boldsymbol{B_0} + \boldsymbol{\hat{B}}t$ with beam axis $\boldsymbol{\hat{B}}$ and beam anchor point $\boldsymbol{B_0}$. In GRETINA, the beamline lies along the $\boldsymbol{\hat{z}}$-axis and passes through the origin of the lab frame, so we can simply set $\boldsymbol{B_0} = (0,0,0)$ and $\boldsymbol{\hat{B}} = (0,0,1)$. This simplifies our expression for the emission point to $\boldsymbol{X_0}(t) = \boldsymbol{\hat{B}}t$. Substituting this expression for $\boldsymbol{X_0}(t)$ for $\boldsymbol{Z}(t)$ into Equation A.39, we get:

$$(\boldsymbol{\hat{B}}t - \boldsymbol{X_C})^T M (\boldsymbol{\hat{B}}t - \boldsymbol{X_C}) = 0 \tag{A.40}$$

$$\boldsymbol{\hat{B}}^T M \boldsymbol{\hat{B}} t^2 - (\boldsymbol{\hat{B}}^T M \boldsymbol{X_C} - \boldsymbol{X_C^T} M \boldsymbol{\hat{B}})t + \boldsymbol{X_C^T} M \boldsymbol{X_C} = 0 \tag{A.41}$$

With the matrix identity $(DEF)^T = F^T E^T D^T$, we note that:

$$(\boldsymbol{X_C^T} M \boldsymbol{\hat{B}})^T = \boldsymbol{\hat{B}}^T M^T \boldsymbol{X_C} = \boldsymbol{\hat{B}}^T M \boldsymbol{X_C} \tag{A.42}$$

because M is symmetric. Since M is a 3 × 3 matrix, we know $\boldsymbol{X_C}$ is a 3 × 1 column vector and $\boldsymbol{\hat{B}}^T$ is a 1 × 3 row vector. Therefore, $\boldsymbol{\hat{B}}^T M \boldsymbol{X_C}$ and $\boldsymbol{X_C}^T M \boldsymbol{\hat{B}}$ are both 1 × 1 scalars. So,

$$\boldsymbol{\hat{B}}^T M \boldsymbol{X_C} = (\boldsymbol{X_C}^T M \boldsymbol{\hat{B}})^T = \boldsymbol{X_C}^T M \boldsymbol{\hat{B}} \tag{A.43}$$

This fact lets us rewrite Equation A.41 as a quadratic equation:

$$\boldsymbol{\hat{B}}^T M \boldsymbol{\hat{B}} t^2 - 2\boldsymbol{\hat{B}}^T M \boldsymbol{X_C} t + \boldsymbol{X_C}^T M \boldsymbol{X_C} = 0 \tag{A.44}$$

Let $a = \boldsymbol{\hat{B}}^T M \boldsymbol{\hat{B}} = \boldsymbol{\hat{B}} \cdot (M\boldsymbol{\hat{B}})$, $b = -2\boldsymbol{\hat{B}}^T M \boldsymbol{X_C} = -2\boldsymbol{\hat{B}} \cdot (M\boldsymbol{X_C})$, and $c = \boldsymbol{X_C}^T M \boldsymbol{X_C} = \boldsymbol{X_C} \cdot (M\boldsymbol{X_C})$, so $at^2 + bt + c = 0$. This can be readily solved for t, and from there the cone-beam intersections are given by $\boldsymbol{X_{0,1}} = t_1\boldsymbol{\hat{B}}$ and $\boldsymbol{X_{0,2}} = t_2\boldsymbol{\hat{B}}$. (Note: With imperfect detectors, a Compton cone may not intersect the beamline at all. This is the situation when $b^2 - 4ac < 0$.)

A.5 Cone-Beam Intersections in Doppler-Shift Imaging

This section provides the algebra for finding cone-beam intersections in Doppler-shift imaging. Things are considerably simpler here than for Compton imaging.

Finding the emission point in Doppler-shift imaging is a straightforward geometry exercise. The emission angle μ defines the opening angle of a "Doppler" cone – the set of photon vectors with the same Doppler-shift. Unlike in Compton imaging, the cone axis here is simply defined by the beam axis, $\boldsymbol{\hat{B}}$. The emission point $\boldsymbol{X_0}$ is the vertex of the cone, and of course lies on the beamline. The point $\boldsymbol{X_1}$ is a point on the forward sheet of the cone. These constraints limit us to a single solution for $\boldsymbol{X_0}$. Figure A.1 illustrates the geometry.

First, define a right triangle from the three points $\boldsymbol{X_0}$, $\boldsymbol{X_1}$, and $\boldsymbol{Z_0}$. Here, $\boldsymbol{Z_0}$ is the point of closest approach on the beamline to $\boldsymbol{X_1}$. The lengths of the three sides are given by:

$$h = \|\boldsymbol{X_1} - \boldsymbol{Z_0}\| \tag{A.45}$$

$$r = \|\boldsymbol{X_1} - \boldsymbol{X_0}\| \tag{A.46}$$

$$s = \|\boldsymbol{X_0} - \boldsymbol{Z_0}\| \tag{A.47}$$

The height and emission angle, θ, are related by $h = r\sin\theta$ and $s = r\cos\theta$. So:

$$\frac{h}{s} = \tan\theta = \frac{\sqrt{1-\mu^2}}{\mu} \tag{A.48}$$

$$s = \frac{\mu h}{\sqrt{1-\mu^2}} \tag{A.49}$$

where $\mu = \cos\theta$. This gives the distance between $\boldsymbol{X_0}$ and the point of closest approach. Now that we have s, the emission point is given simply by:

$$\boldsymbol{X_0} = \boldsymbol{Z_0} - s\hat{\boldsymbol{B}} \tag{A.50}$$

Note that s will be positive if the emission angle is acute, and negative if θ is acute. This sign is determined by μ in the numerator of Equation A.49.

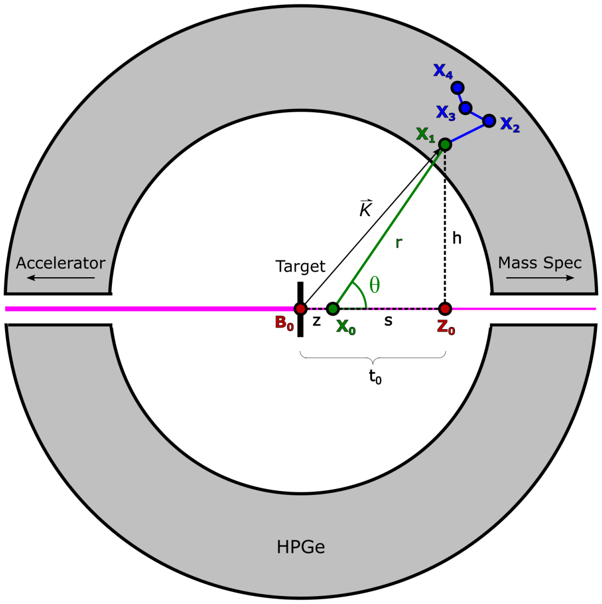

Figure A.1: Deriving the cone-beam intersection in Doppler-shift imaging

So now we just need to find h, which turns out to also be quite straightforward. [8] Define the beam-line as $\boldsymbol{A(t)} = \boldsymbol{B_0} + t\hat{\boldsymbol{B}}$, where $\boldsymbol{B_0}$ is a set point on the beamline and $\hat{\boldsymbol{B}}$ is a unit vector defining the beam axis. (We put $\boldsymbol{B_0}$ at the lab-frame origin for simplicity.) The point of closest approach can be written $\boldsymbol{Z_0} = \boldsymbol{B_0} + t_0\hat{\boldsymbol{B}}$. Let $\boldsymbol{K} = \boldsymbol{X_1} - \boldsymbol{B_0}$ be the vector from the beam set point to the first interaction point in the photon track. Referring again to Figure A.1, we see that the distance between $\boldsymbol{B_0}$ and $\boldsymbol{Z_0}$ is:

$$t_0 = \|\boldsymbol{K}\| \cos\theta = \boldsymbol{K} \cdot \hat{\boldsymbol{B}} \tag{A.51}$$

Now that we have the 3D coordinates of $\boldsymbol{Z_0}$, we can solve Equation A.45 for h.

A.6 Imaging Effects from Non-Ideal Beams

Here we discuss imaging errors that arise from realistic product beams. While beams generally are very highly-focused, parent nuclei still do not form a pencil beam downstream of the target.

From the derivations from Appendices A.4 and A.5, a photon's calculated emission point depends on the beam axis. In my imaging reconstruction code, I've assumed a strict pencil beam directed along $\boldsymbol{A}(t) = \boldsymbol{B_0} + t\hat{\boldsymbol{B}} = (0,0,0) + t(0,0,1)$ in the lab-frame. However, the actual angular distribution for the reaction products will have a finite spread. Reactions are *highly* forward-directed in the lab-frame, but the degree to which this is true depends on the specific kinematics of the reaction. Depending on the target thickness, the product nuclei may also undergo significant straggling as they exit the target.

Consider a projectile that hits at a point $\boldsymbol{B_0'} = (x', y')$ in the plane of the target, and subsequently reacts. Suppose the recoil nucleus (the parent of the photon we'll measure) heads off at an angle θ relative to the nominal beam axis, $\hat{\boldsymbol{B}}$. For the sake of generality, suppose also that the nucleus has a radial angle of η as measured in the target XY-plane. We can define this heading vector as $\boldsymbol{A'}(t) = \boldsymbol{B_0'} + t\hat{\boldsymbol{B}}'$, where $\hat{\boldsymbol{B}}' = (\sin\theta\cos\eta, \sin\theta\sin\eta, \cos\theta)$. This is the line along which the photon will be emitted.

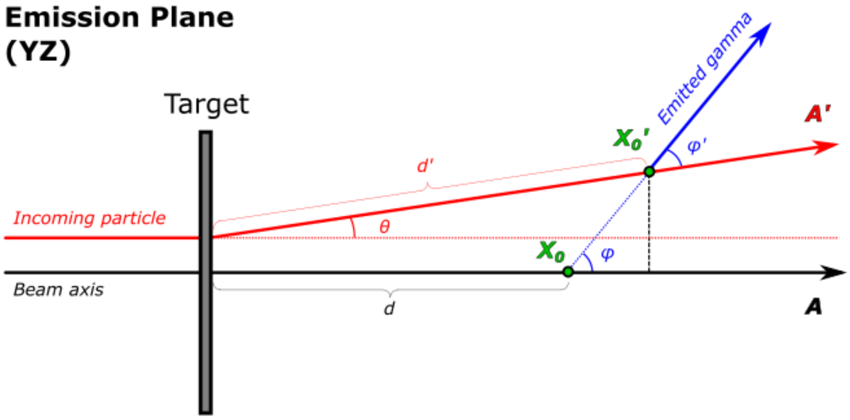

Figure A.2: Estimated effects of beam deviations on imaged emission point

Because our imaging techniques use $\boldsymbol{A}(t)$ instead of $\boldsymbol{A'}(t)$ as the emission vector, there will be some intrinsic imaging error associated with each calculated cone-beam intersection. Figure A.2 provides a simplified illustration to estimate these errors. For example, consider a parent nucleus that is created 4.00 mm above center on the target, and which recoils at 0.3c with a 1.00° divergence from the nominal beam axis ($\hat{\boldsymbol{B}} = \hat{\boldsymbol{z}}$). For simplicity, assume the beam divergence and photon emission are both in the YZ-plane. Suppose this nucleus de-excites after traveling 100.0 mm, emitting a photon at 29.0° relative to its line of motion (or 30.0° relative to $\hat{\boldsymbol{B}}$). At the emission point, the parent nucleus is 5.75 mm away from the beam axis. The true emission point is $\boldsymbol{X_0'} =$ (0.00 mm, 5.75 mm, 99.98 mm), but tracing the emission vector back to $\hat{\boldsymbol{B}}$ yields an intersection at $\boldsymbol{X_0} =$ (0.00 mm, 0.00 mm, 90.04 mm). The difference in true vs. imaged travel distance is $|d - d'| = 9.96$ mm, which corresponds to a full *105 ps* difference in apparent emission time. To rigorously quantify this error in the more general case, we would need to re-run full beam-cone calculations using the adjusted trajectory of the parent nucleus.

The adjusted trajectories can be measured with a pair of microchannel plate detectors. [4] These detectors are thin, highly-pixelated scintillators which record timing and position of ions as they pass through. The detectors ideally should be thin enough to detect an incident particle's passing without affecting its trajectory. Figure A.3 illustrates how this information can be used to deduce the beam properties. Consider an ion which passes through the first detector at position $\boldsymbol{Z_1}$ and time t_1, and through the second detector at $\boldsymbol{Z_2}$ and time t_2. The adjusted heading vector for this particle is thus:

$$
\begin{aligned}
\hat{\boldsymbol{A}}' &= \boldsymbol{B}'_0 + t\hat{\boldsymbol{B}}' && \text{(A.52)}\\
&= \boldsymbol{Z_1} + t(\boldsymbol{Z_2} - \boldsymbol{Z_1})/\|\boldsymbol{Z_2} - \boldsymbol{Z_1}\| && \text{(A.53)}
\end{aligned}
$$

Furthermore, the measured speed of the ion is:

$$\beta = \frac{\|\boldsymbol{Z_2} - \boldsymbol{Z_1}\|}{t_2 - t_1} \tag{A.54}$$

With this information, it is straightforward to re-run the beam-cone calculations to produce adjusted emission times for each parent nucleus.

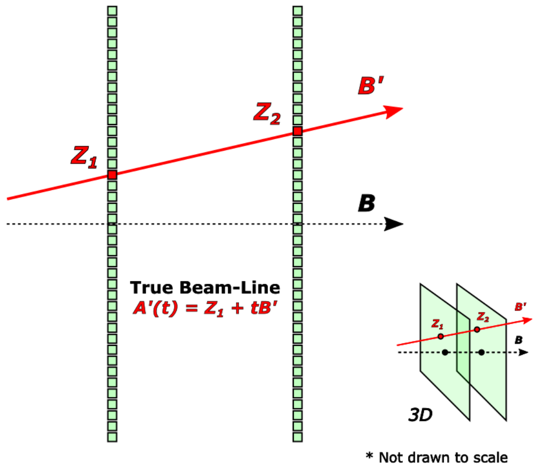

Figure A.3: Microchannel plate detectors

A.7 Error Propagation in Compton Imaging

This section describes computing analytical error estimates for Compton imaging. These estimates can be used to judge the reliability of the reconstruction for an individual photon *track. The full derivation contains 20 pages of partial derivatives – those have been omitted and "left as an exercise to the reader".*

We are interested in estimating imaging resolution in Compton Imaging. One way to do so is through analytic error propagation. Recall the general formula for computing these errors:

$$\sigma_z^2 = \sum_{j=1}^{N} \left(\frac{\partial z}{\partial x_j} \right)^2 \sigma_{x_j}^2 \tag{A.55}$$

where $(x_1, ..., x_N)$ are the independent variables in our measurement. For this imaging problem, there are 8 such variables needed to define a given Compton cone. The cone vertex is given by $\boldsymbol{X_C} = \boldsymbol{X_1} = (x_1, x_2, x_3)$, and the second hit is at $\boldsymbol{X_2} = (x_4, x_5, x_6)$. These two points define the cone axis:

$$\hat{\boldsymbol{V}}_{\boldsymbol{C}} = \frac{\boldsymbol{X_1} - \boldsymbol{X_2}}{\|\boldsymbol{X_1} - \boldsymbol{X_2}\|} = (\frac{x_1 - x_4}{L}, \frac{x_2 - x_5}{L}, \frac{x_3 - x_6}{L}) = (v_1, v_2, v_3) \tag{A.56}$$

where $L = \sqrt{(x_1 - x_4)^2 + (x_2 - x_5)^2 + (x_3 - x_6)^2}$ is the Compton lever arm. Lastly, the cone angle is determined by:

$$\mu_C = 1 - m_e c^2 \left(\frac{1}{E_1} - \frac{1}{E_0} \right) \tag{A.57}$$

where E_0 is the photon's lab-frame emission energy and E_1 is the energy after the initial scatter in the detector. Therefore, the eight independent variables (i.e what we measure) are $(x_1, x_2, x_3, x_4, x_5, x_6, E_0, E_1)$.

Note that this analysis ignores the beam properties of the parent nuclei. To account for variations in the beam, we would have to add the photon parent's trajectory to the list of independent variables. The velocity component is 4 variables: $\beta\hat{\boldsymbol{B}} = (\beta b_1, \beta b_2, \beta b_3)$, where $\hat{\boldsymbol{B}}$ is the heading for a particular recoil nucleus and βc is its speed. We would also need a beam setpoint, $\boldsymbol{B_0} = (b_{0,1}, b_{0,2}, b_{0,3})$ that the nucleus passes through. In all, this would add another 7 independent variables to the analysis: $(b_1, b_2, b_3, b_{0,1}, b_{0,2}, b_{0,3}, \beta)$. For simplicity, and because the variations in the beam are typically not large, I have ignored these.

In Appendix A.4 we went over the math behind finding emission points using Compton imaging. The goal was to calculate the t in $z(t) = \boldsymbol{B_0} + t\hat{\boldsymbol{B}}$. In the end, we arrived at a quadratic equation:

$$t = \frac{-b \pm \sqrt{b^2 - 4ac}}{2a} \tag{A.58}$$

$$a = \hat{\boldsymbol{B}} \cdot (M\hat{\boldsymbol{B}}) \tag{A.59}$$

$$b = -2\hat{\boldsymbol{B}} \cdot (M\boldsymbol{X_C}) \tag{A.60}$$

$$c = \boldsymbol{X_C} \cdot (M\boldsymbol{X_C}) \tag{A.61}$$

Again, $M = \boldsymbol{\hat{V}_C}\boldsymbol{\hat{V}_C^T} - \mu_C^2 I_3$ is a 3 × 3 symmetric matrix:

$$M = \begin{pmatrix} v_1^2 - \mu_C^2 & v_1 v_2 & v_1 v_3 \\ v_1 v_2 & v_2^2 - \mu_C^2 & v_2 v_3 \\ v_1 v_3 & v_2 v_3 & v_3^2 - \mu_C^2 \end{pmatrix} \tag{A.62}$$

To get scalar expressions for error analysis, we evaluate a, b, and c with known quantities for the beam:

$$\boldsymbol{B_0} = (0,0,0) \qquad\qquad \boldsymbol{\hat{B}} = (0,0,1) \tag{A.63}$$

The matrix algebra is straightforward, yielding the following:

$$a = v_3^2 - \mu_C^2 \tag{A.64}$$

$$b = -2[v_1 v_3 x_1 + v_2 v_3 x_2 + (v_3^2 - \mu_C^2) x_3] \tag{A.65}$$

$$\begin{aligned} c = {} & x_1^2(v_1^2 - \mu_C^2) + x_2^2(v_2^2 - \mu_C^2) + x_3^2(v_3^2 - \mu_C^2) \\ & + 2(v_1 v_2 x_1 x_2 + v_1 v_3 x_1 x_3 + v_2 v_3 x_2 x_3) \end{aligned} \tag{A.66}$$

Furthermore, note that $\boldsymbol{Z(t)} = \boldsymbol{B_0} + t\boldsymbol{\hat{B}} = (0,0,t)$, so we can write the emission point simply as its z-coordinate, $z = t$.

Now that we have these expressions, the partial derivatives of z with respect to the independent variables $(x_1, ..., x_6, E_0, E_1)$ can be calculated using the chain rule:

$$\frac{\partial z(y_1, ..., y_N)}{\partial x_j} = \sum_{n=1}^{N} \left(\frac{\partial z}{\partial y_n}\right)\left(\frac{\partial y_n}{\partial x_j}\right) \tag{A.67}$$

Here, z is a function of the variables $a(x_1, ..., x_6, E_0, E_1)$, $b(x_1, ..., x_6, E_0, E_1)$, and $c(x_1, ..., x_6, E_0, E_1)$ from our earlier quadratic equation. So, for example:

$$\frac{\partial z}{\partial x_1} = \frac{\partial z}{\partial a}\frac{\partial a}{\partial x_1} + \frac{\partial z}{\partial b}\frac{\partial b}{\partial x_1} + \frac{\partial z}{\partial c}\frac{\partial c}{\partial x_1} \tag{A.68}$$

Calculating the partial derivatives was a lengthy ordeal, and so I'll just provide the results below. Note that the partial derivatives of z contain a ± or ∓ sign, which reflect the root chosen in Equation A.58. (This only works when Compton imaging yields a unique emission point for the photon.)

Partial Derivatives of z

$$\frac{\partial z}{\partial a} = \frac{b}{2a^2} \pm \frac{c - b^2/2a}{a\sqrt{b^2 - 4ac}} \tag{A.69}$$

$$\frac{\partial z}{\partial b} = \frac{-1 \pm b/\sqrt{b^2 - 4ac}}{2a} \tag{A.70}$$

$$\frac{\partial z}{\partial c} = \frac{\mp 1}{\sqrt{b^2 - 4ac}} \tag{A.71}$$

Partial Derivatives of a

$$\frac{\partial a}{\partial x_1} = -\frac{2v_1 v_3^2}{L} \qquad \frac{\partial a}{\partial x_4} = -\frac{\partial a}{\partial x_1} \tag{A.72}$$

$$\frac{\partial a}{\partial x_2} = -\frac{2v_2 v_3^2}{L} \qquad \frac{\partial a}{\partial x_5} = -\frac{\partial a}{\partial x_2} \tag{A.73}$$

$$\frac{\partial a}{\partial x_3} = \frac{2v_3(1 - v_3^2)}{L} \qquad \frac{\partial a}{\partial x_6} = -\frac{\partial a}{\partial x_3} \tag{A.74}$$

$$\frac{\partial a}{\partial E_0} = \frac{2\mu m_e}{E_0^2} \qquad \frac{\partial a}{\partial E_0} = -\frac{2\mu m_e}{E_1^2} \tag{A.75}$$

Partial Derivatives of b

$$\frac{\partial b}{\partial x_1} = \frac{2v_3(2v_1^2 x_1 - 2x_1 + x_4) + 4v_1v_2v_3x_2}{L} - 2x_3\frac{\partial a}{\partial x_1} \tag{A.76}$$

$$\frac{\partial b}{\partial x_2} = \frac{2v_3(2v_2^2 x_2 - 2x_2 + x_5) + 4v_1v_2v_3x_1}{L} - 2x_3\frac{\partial a}{\partial x_2} \tag{A.77}$$

$$\frac{\partial b}{\partial x_3} = \frac{2(2v_3^2 - 1)(v_1x_1 + v_2x_2)}{L} - 2(a + x_3\frac{\partial a}{\partial x_1}) \tag{A.78}$$

$$\frac{\partial b}{\partial x_4} = -\frac{2v_3x_1(2v_1^2 - 1) - 4v_1v_2v_3x_2}{L} - 2x_3\frac{\partial a}{\partial x_4} \tag{A.79}$$

$$\frac{\partial b}{\partial x_5} = -\frac{2v_3x_2(2v_2^2 - 1) - 4v_1v_2v_3x_1}{L} - 2x_3\frac{\partial a}{\partial x_5} \tag{A.80}$$

$$\frac{\partial b}{\partial x_6} = -\frac{2(2v_3^2 - 1)(v_1x_1 + v_2x_2)}{L} - 2x_3\frac{\partial a}{\partial x_6} \tag{A.81}$$

$$\frac{\partial b}{\partial E_0} = -2x_3\frac{\partial a}{\partial E_0} \qquad \frac{\partial b}{\partial E_1} = -2x_3\frac{\partial a}{\partial E_1} \tag{A.82}$$

Partial Derivatives of c

$$\begin{aligned}\frac{\partial c}{\partial x_1} =& 2v_1x_1^2(1-v_1^2)/L + 2v_1v_2x_2(1-v_2x_2)/L - 4v_1v_2v_3x_2x_3/L \\ &+ 2x_1(v_2x_2+v_3x_3)(1-2v_1^2)/L + x_3^2\frac{\partial a}{\partial x_1} + 2x_1(v_1^2-\mu^2) + 2v_1v_3x_3\end{aligned} \tag{A.83}$$

$$\begin{aligned}\frac{\partial c}{\partial x_2} =& 2v_2x_2^2(1-v_2^2)/L + 2v_1v_2x_1(1-v_1x_1)/L - 4v_1v_2v_3x_1x_3/L \\ &+ 2x_2(v_1x_1+v_3x_3)(1-2v_2^2)/L + x_3^2\frac{\partial a}{\partial x_2} + 2x_2(v_2^2-\mu^2) + 2v_2v_3x_3\end{aligned} \tag{A.84}$$

$$\begin{aligned}\frac{\partial c}{\partial x_3} =& 2x_3(v_1x_1+v_2x_2)(1-2v_3^2)/L - 2v_3(v_1^2x_1^2+v_2^2x_2^2)/L - 4v_1v_2v_3x_1x_2/L \\ &+ 2v_3(v_1x_1+v_2x_2) + x_3^2\frac{\partial a}{\partial x_3} + 2x_3a\end{aligned} \tag{A.85}$$

$$\begin{aligned}\frac{\partial c}{\partial x_4} =& -2v_1x_1^2(1-v_1^2)/L + 2v_1v_2^2x_2^2/L + 4v_1v_2v_3x_2x_3/L \\ &- 2x_1(v_2x_2+v_3x_3)(1-2v_1^2)/L + x_3^2\frac{\partial a}{\partial x_4}\end{aligned} \tag{A.86}$$

$$\begin{aligned}\frac{\partial c}{\partial x_5} =& -2v_2x_2^2(1-v_2^2)/L + 2v_2v_1^2x_1^2/L + 4v_1v_2v_3x_1x_3/L \\ &- 2x_2(v_1x_1+v_3x_3)(1-2v_2^2)/L + x_3^2\frac{\partial a}{\partial x_5}\end{aligned} \tag{A.87}$$

$$\begin{aligned}\frac{\partial c}{\partial x_6} =& -2x_3(v_1x_1+v_2x_2)(1-2v_3^2)/L + 2v_3(v_1^2x_1^2+v_2^2x_2^2)/L \\ &+ 4v_1v_2v_3x_1x_2/L + x_3^2\frac{\partial a}{\partial x_6}\end{aligned} \tag{A.88}$$

$$\frac{\partial c}{\partial E_0} = \frac{2\mu m_e}{E_0^2}(x_1^2+x_2^2) + x_3^2\frac{\partial a}{\partial E_0} \tag{A.89}$$

$$\frac{\partial c}{\partial E_1} = -\frac{2\mu m_e}{E_1^2}(x_1^2+x_2^2) + x_3^2\frac{\partial a}{\partial E_1} \tag{A.90}$$

For my work, I have assumed that $(x_1, ..., x_6)$ are all equally-affected by position resolution, σ_{xyz}, and E_0 and E_1 are equally-affected by energy resolution, σ_E. To avoid confusion, we will refer to the estimated imaging resolution as σ_{img} instead of σ_z. Summing everything together with the Chain Rule, we find:

$$\begin{aligned}\sigma_{img}^2 &= \left[\left(\frac{\partial z}{\partial x_1}\right)^2 + \left(\frac{\partial z}{\partial x_2}\right)^2 + \left(\frac{\partial z}{\partial x_3}\right)^2 + \left(\frac{\partial z}{\partial x_4}\right)^2 + \left(\frac{\partial z}{\partial x_5}\right)^2 + \left(\frac{\partial z}{\partial x_6}\right)^2\right]\sigma_{xyz}^2 \\ &\quad + \left[\left(\frac{\partial z}{\partial E_0}\right)^2 + \left(\frac{\partial z}{\partial E_1}\right)^2\right]\sigma_E^2 \qquad \text{(A.91)} \\ &= \sigma_{img,pos}^2 + \sigma_{img,energy}^2 \qquad \text{(A.92)}\end{aligned}$$

I've separated the resolution estimate into two components – one depending entirely on position resolution ($\sigma_{img,pos}$) and one only on energy resolution ($\sigma_{img,energy}$). For typical resolutions in GRETINA, $\sigma_{img,pos} >> \sigma_{img,energy}$. (See Figure 4.3)

As mentioned, the derivation of the above partial derivatives was a lengthy process, and certainly open to error. I checked each expression numerically using Mathematica's procedural derivative-calculator (which unfortunately did *not* produce tractable formulae). In addition, I performed an independent numerical check by tweaking each independent variable for a sample Compton reconstruction. By introducing small changes in x_1 or another of the variables, I obtained numerical derivatives to compare with the results of the analytical expressions above.

Table A.2 shows the comparison for the following photon track. To determine numerical derivatives, I shifted positions in 0.01 mm increments and energies in 0.025 keV increments.

Hit	**x (mm)**	**y (mm)**	**z (mm)**	**ΔE (keV)**
#1	-81.4542	172.469	-30.0678	288.424
#2	-100.3864	193.4548	-49.6538	210.0868
#3	-101.4564	193.9505	-52.1735	474.4475
#4	-96.0459	197.7831	-44.1857	0.6924
#5	-95.9333	197.857	-43.978	199.5873

Table A.1: Sample photon track used in error estimates
Hits: 5, Track Energy: 1173.238keV

As we can see, the differences between the analytical and numerical results are generally within 0.5%. This confirms the formulas above. A final note – both the analytic and numeric estimated errors for this sample track are 29.253 mm, assuming (3.000 mm, 2.000 keV) detector resolution. The track has a Compton lever arm of 34.387 mm, which is why the error is relatively small. Other tracks I tested have errors in the hundreds or even thousands of mm. It's also clear that the position resolution error component dominates ($\sigma_{img,pos}$). Energy resolution only affects the Compton cone angle, and in this case we see $\sigma_\theta = 0.00292$ radians (0.168°).

Partial Derivative	**Analytic Estimate**	**Numeric Estimate**	**Partial Derivative**	**Analytic Estimate**	**Numeric Estimate**
$\partial z/\partial a$	-0.08191	–	$\partial \theta/\partial E_0$	0.000723	0.000720
$\partial z/\partial b$	0.02344	–	$\partial \theta/\partial E_1$	-0.001271	-0.001266
$\partial z/\partial c$	-0.00671	–	–	–	–
$\partial a/\partial x_1$	-0.01039	-0.01040	$\partial b/\partial x_1$	-4.0290	-4.0284
$\partial a/\partial x_2$	0.01152	0.01150	$\partial b/\partial x_2$	1.7436	1.7467
$\partial a/\partial x_3$	0.02238	0.02237	$\partial b/\partial x_3$	5.2351	5.2424
$\partial a/\partial x_4$	0.01039	0.01040	$\partial b/\partial x_4$	3.4018	3.4033
$\partial a/\partial x_5$	-0.01152	-0.01153	$\partial b/\partial x_5$	-1.0484	-1.0458
$\partial a/\partial x_6$	-0.02244	-0.02237	$\partial b/\partial x_6$	-4.4115	-4.4043
$\partial a/\partial E_0$	0.000637	0.000640	$\partial b/\partial E_0$	0.0383	0.0383
$\partial a/\partial E_1$	-0.001120	-0.001120	$\partial b/\partial E_1$	-0.0674	-0.0673
$\partial c/\partial x_1$	-167.46	-166.95	$\partial z/\partial x_1$	1.0295	1.0253
$\partial c/\partial x_2$	-734.68	-733.81	$\partial z/\partial x_2$	4.9671	4.9613
$\partial c/\partial x_3$	-780.21	-780.22	$\partial z/\partial x_3$	5.3535	5.3571
$\partial c/\partial x_4$	103.26	103.73	$\partial z/\partial x_4$	-0.6136	-0.6170
$\partial c/\partial x_5$	684.85	685.43	$\partial z/\partial x_5$	-4.6166	-4.6217
$\partial c/\partial x_6$	633.98	633.96	$\partial z/\partial x_6$	-4.3535	-4.3510
$\partial c/\partial E_0$	23.752	23.746	$\partial z/\partial E_0$	-0.1585	-0.1584
$\partial c/\partial E_1$	-41.761	-41.755	$\partial z/\partial E_1$	0.2786	0.2785

Table A.2: Numerical check of Compton imaging error estimates

Partial Derivative	**Units**	**Partial Derivative**	**Units**	**Partial Derivative**	**Units**
$\partial a/\partial x_j$	mm^{-1}	$\partial b/\partial x_j$	–	$\partial c/\partial x_j$	mm
$\partial a/\partial E_k$	keV^{-1}	$\partial b/\partial E_k$	mm keV^{-1}	$\partial c/\partial E_k$	mm^2 keV^{-1}
$\partial z/\partial a$	mm	$\partial z/\partial x_j$	–	$\partial \theta/\partial E_k$	rad keV^{-1}
$\partial z/\partial b$	–	$\partial z/\partial E_k$	mm keV^{-1}	–	–
$\partial z/\partial c$	mm^{-1}	–	–	–	–

Table A.3: Units for partial derivatives

A.8 Error Propagation in Doppler-Shift Imaging

This section is very similar to the previous one, Section A.7. However, the math behind analytic imaging errors in Doppler-shift imaging is much simpler.

In Section A.5 we solved for a photon emission point based on the measured lab-frame energy, assumed CM-frame energy, and track vertex. As with Compton imaging, we are interested in estimating the imaging error per each track. Here, though, the math is much simpler. There are only 5 independent variables: $\boldsymbol{X_1} = (x_1, x_2, x_3)$, E_{Lab}, and E_{CM}. Again, we're ignoring the variations in the beam for simplicity. Of these properties, the beam speed would be expected to have the most effect, as it directly affects the calculation of emission angle from Doppler-shift. (However, that effect should be small, as recoil speed typically varies only by 1% or less at $\beta = 0.3$c.)

Equation A.93 gives this emission angle in terms of the measured lab-frame energy and assumed CM-frame energy:

$$\mu = \frac{1}{\beta}\left(1 - \frac{E_{CM}}{\gamma E_{Lab}}\right) \tag{A.93}$$

Let the emission point be denoted $\boldsymbol{X_0} = \boldsymbol{B_0} + t\hat{\boldsymbol{B}}$. If we assume an ideal beam as before, then $\boldsymbol{B_0} = (0,0,0)$ and $\hat{\boldsymbol{B}} = (0,0,1)$. This lets us characterize the emission point simply by its $\hat{\boldsymbol{z}}$-coordinate, $z = t$, thereby simplifying the expressions we used in Section A.5. Recall that $\boldsymbol{Z_0} = \boldsymbol{B_0} + t_0\hat{\boldsymbol{B}}$ is the point of closest approach between the track vertex $\boldsymbol{X_1}$ and the beamline.

$$\begin{aligned} t_0 &= \|\boldsymbol{B_0} - \boldsymbol{Z_0}\| = \|\boldsymbol{X_1} - \boldsymbol{B_0}\|\cos\theta = (\boldsymbol{X_1} - \boldsymbol{B_0})\cdot\hat{\boldsymbol{B}} = \boldsymbol{X_1}\cdot\hat{\boldsymbol{B}} \\ &= x_3 \end{aligned} \tag{A.94}$$

$$\begin{aligned} h &= \|\boldsymbol{X_1} - \boldsymbol{Z_0}\| = \|\boldsymbol{X_1} - t_0\hat{\boldsymbol{B}}\| = \|\boldsymbol{X_1} - x_3\hat{\boldsymbol{B}}\| \\ &= \sqrt{x_1^2 + x_2^2} \end{aligned} \tag{A.95}$$

$$\begin{aligned} s &= \|\boldsymbol{X_0} - \boldsymbol{Z_0}\| = h\mu/\sqrt{1-\mu^2} \\ &= \frac{\mu\sqrt{x_1^2 + x_2^2}}{\sqrt{1-\mu^2}} \end{aligned} \tag{A.96}$$

$$\begin{aligned} z &= \|\boldsymbol{Z_0} - s\boldsymbol{B}\| = t_0 - s \\ &= x_3 - \frac{\mu\sqrt{x_1^2 + x_2^2}}{\sqrt{1-\mu^2}} \end{aligned} \tag{A.97}$$

Now we're left to calculate all partial derivatives of z with respect to the independent variables, $(x1, x2, x3, E_{Lab}, E_{CM})$. The math is straightforward and I will simply quote the results here:

Partial Derivatives for Position Measurements

$$\frac{\partial z}{\partial x_1} = -\frac{x_1\mu}{\sqrt{(x_1^2+x_2^2)(1-\mu^2)}} \tag{A.98}$$

$$\frac{\partial z}{\partial x_2} = -\frac{x_2\mu}{\sqrt{(x_1^2+x_2^2)(1-\mu^2)}} \tag{A.99}$$

$$\frac{\partial z}{\partial x_3} = 1 \tag{A.100}$$

$$\tag{A.101}$$

Partial Derivatives for Energy Measurements

$$\frac{\partial z}{\partial \mu} = -\frac{\sqrt{x_1^2+x_2^2}}{(\sqrt{1-\mu^2})^3} \qquad \frac{\partial \theta}{\partial \mu} = -\frac{1}{\sqrt{1-\mu^2}} \tag{A.102}$$

$$\frac{\partial \mu}{\partial E_{Lab}} = \frac{E_{CM}}{\gamma\beta E_{Lab}^2} \qquad \frac{\partial \mu}{\partial E_{CM}} = -\frac{1}{\gamma\beta E_{Lab}} \tag{A.103}$$

$$\frac{\partial z}{\partial E_{Lab}} = \frac{\partial z}{\partial \mu}\frac{\partial \mu}{\partial E_{Lab}} \qquad \frac{\partial z}{\partial E_{CM}} = \frac{\partial z}{\partial \mu}\frac{\partial \mu}{\partial E_{CM}} \tag{A.104}$$

$$\frac{\partial \theta}{\partial E_{Lab}} = \frac{\partial \theta}{\partial \mu}\frac{\partial \mu}{\partial E_{Lab}} \qquad \frac{\partial \theta}{\partial E_{CM}} = \frac{\partial \theta}{\partial \mu}\frac{\partial \mu}{\partial E_{CM}} \tag{A.105}$$

I again assumed (x_1, x_2, x_3) are all equally-affected by position resolution, σ_{xyz}, while E_{Lab} and E_{CM} are equally-affected by energy resolution, σ_E. To avoid confusion, we will refer to the estimated imaging resolution as σ_{img} instead of σ_z. Summing everything together with Equation A.55, we get:

$$\begin{aligned}\sigma_{img}^2 &= \left[\left(\frac{\partial z}{\partial x_1}\right)^2 + \left(\frac{\partial z}{\partial x_2}\right)^2 + \left(\frac{\partial z}{\partial x_3}\right)^2\right]\sigma_{xyz}^2 \\ &\quad + \left[\left(\frac{\partial z}{\partial E_{Lab}}\right)^2 + \left(\frac{\partial z}{\partial E_{CM}}\right)^2\right]\sigma_E^2 \qquad \text{(A.106)} \\ &= \sigma_{img,pos}^2 + \sigma_{img,energy}^2 \qquad \text{(A.107)}\end{aligned}$$

As before, I've separated the resolution estimate into two components – one depending entirely on position resolution ($\sigma_{img,pos}$) and one only on energy resolution ($\sigma_{img,energy}$). However, in this case we see that $\sigma_{img,pos} \approx \sigma_{img,energy}$ for typical resolutions – very different than in Compton imaging. (Compare Figures 4.3 and 5.2.) For these tests, I assumed E_{CM} was precisely known, so that it did not affect the overall error estimates. Similarly, I assumed the beam velocity was precisely controlled – though as we can see from Appendix A.5, uncertainty in β will certainly have an effect on the imaging error. The beam-cone intersections explicitly depend on β.

I ran the same numerical checks of these error propagation formulas as I did for Compton imaging. Table A.5 shows the comparison for a sample photon track. To determine numerical derivatives, I shifted positions in 0.01 mm increments and energies in 0.025 keV increments.

Hit	**x (mm)**	**y (mm)**	**z (mm)**	**ΔE (keV)**
#1	-81.4542	172.469	-30.0678	288.424
#2	-100.3864	193.4548	-49.6538	210.0868
#3	-101.4564	193.9505	-52.1735	474.4475
#4	-96.0459	197.7831	-44.1857	0.6924
#5	-95.9333	197.857	-43.978	199.5873

Table A.4: Sample photon track used in error estimates
Hits: 5, Lab Energy: 1173.238keV, CM Energy: 1000.000keV

The differences between the analytical and numerical results are generally within 0.5%. This confirms the formulas above. A final note – both the analytic and numeric estimated errors for this sample track are 4.255 mm, assuming (3.000 mm, 2.000 keV) detector resolution. Both the position and energy resolution error components are on similar scales. The emission angle is only affected by energy resolution, and in this case we find $\sigma_\theta = 0.00591$ radians (0.338°).

Partial Derivative	**Analytic Estimate**	**Numeric Estimate**	**Partial Derivative**	**Analytic Estimate**	**Numeric Estimate**
$\partial z/\partial x_1$	0.34018	0.34081	–	–	–
$\partial z/\partial x_2$	-0.72028	-0.71972	–	–	–
$\partial z/\partial x_3$	1.00000	0.99997	$\partial \theta/\partial \mu$	-1.2785	-1.2759
$\partial z/\partial \mu$	-398.59	-396.82	$\partial \theta/\partial \beta$	–	–
$\partial z/\partial E_{Lab}$	-0.92076	-0.92122	$\partial z/\partial E_{CM}$	–	–
$\partial \mu/\partial E_{Lab}$	0.00231	0.00232	$\partial \mu/\partial E_{CM}$	–	–
$\partial \theta/\partial E_{Lab}$	-0.00295	-0.00296	$\partial \theta/\partial E_{CM}$	–	–

Table A.5: Numerical check of Doppler-Shift imaging error estimates

Partial Derivative	**Units**	**Partial Derivative**	**Units**
$\partial z/\partial x_j$	–	$\partial \mu/\partial E_k$	keV^{-1}
$\partial z/\partial E_k$	mm keV^{-1}	$\partial \theta/\partial \mu$	radians
$\partial z/\partial \mu$	mm	$\partial \theta/\partial E_k$	radians keV^{-1}

Table A.6: Units for partial derivatives

A.9 Gaussian Curve Fitting

I used Gaussian fits extensively in Chapters 4 and 5. This section goes into the details of the curve-fitting algorithm I employed.

A Gaussian has the form:

$$y(x) = Ae^{-(x-x_0)^2/2\sigma^2} \tag{A.108}$$

where A is the Gaussian's amplitude, x_0 is its centroid, and σ is its standard deviation. For a normalized Gaussian, $A = 1/\sigma\sqrt{2\pi}$. The Full-Width-Half-Max (FWHM) is related to the standard deviation by FWHM $= 2\sqrt{2ln2}\sigma$.

Suppose we're given a set of data points $\{(x', y')\}$ and want to fit a Gaussian shape to them. One way is to linearize Equation A.108:

$$y/A = e^{-\frac{(x-x_0)^2}{2\sigma^2}} \tag{A.109}$$

$$\ln y - \ln A = -\frac{(x-x_0)^2}{2\sigma^2} \tag{A.110}$$

$$= -\frac{x^2 - 2xx_0 + x_0^2}{2\sigma^2} \tag{A.111}$$

$$\ln y = -\frac{1}{2\sigma^2}x^2 + \frac{x_0}{\sigma^2}x + \left(\ln A - \frac{x_0^2}{2\sigma^2}\right) \tag{A.112}$$

$$= ax^2 + bx + c \tag{A.113}$$

where $a = -1/(2\sigma^2)$, $b = x_0/\sigma^2$, and $c = \ln A - x_0^2/2\sigma^2$. This equation is now in a form that is readily solved by Matlab's polyfit() function. [10]

Matlab's polyval() function returns value for the coefficients a, b, and c above. We can then solve for the Gaussian's standard deviation, centroid, and amplitude using:

$$\sigma = \sqrt{-1/2a} \qquad x_0 = b\sigma^2 \qquad A = e^{c+x0^2/(2*\sigma^2)} \tag{A.114}$$

Furthermore, we can use error propagation on these expressions to estimate the error on each parameter:

$$\sigma_\sigma = \frac{1}{2\sqrt{-2a^3}}\sigma_a \tag{A.115}$$

$$\sigma_{x_0} = \sqrt{(b/2a^2)^2\sigma_a^2 + (1/2a)^2\sigma_b^2} \tag{A.116}$$

$$\sigma_A = A\sqrt{(b^2/2a^3)^2\sigma_a^2 + (b/2a^2)^2\sigma_b^2 + \sigma_c^2} \tag{A.117}$$

(I'll leave the partial derivative calculations to the reader.) In addition to the coefficients a, b, and c, the polyval() function also returns a covariance matrix from which the values of σ_a, σ_b, and σ_c can be calculated. The formula below gives a vector $\boldsymbol{V}$ whose elements are the standard deviations of the fit parameters:

$$\boldsymbol{V} = \sqrt{\frac{diag(\boldsymbol{C})}{\nu}}\|\boldsymbol{R}\| \tag{A.118}$$

$$= \langle \sigma_a, \sigma_b, \sigma_c \rangle \tag{A.119}$$

$$\|\boldsymbol{R}\|^2 = \sum_{k=1}^{K} (y_{k,meas} - y_{k,fit})^2 \tag{A.120}$$

where C is the covariance matrix, ν is the degrees of freedom of the fit, and $\|\boldsymbol{R}\|$ is the norm of the residuals vector. These residuals are calculated for the kth x-bin as the difference between the measured number of counts $y_{k,meas}$ and the fitted number of counts $y_{k,fit}$.

Deciding the range over which to perform the fit is an important question. In this work, the gamma-ray images extend from -180mm $< z <$ 180mm, and are generally not Gaussian over this entire range. In my approach, I assume the x-bin with the most counts is the centroid of the distribution. From there, I set the left- and right-bounds as the first and last bins with at least half the maximum counts, respectively. I then extend the range by two bins to either side. In special cases where the peak is very wide or very far off-center, the FWHM may not be entirely contained in the imaging range. If we have at least half of the peak, though, we can reflect it about its center to get a full peak to fit to. Otherwise, the fit just uses the entire imaging range. Note that negative-count bins are set to 0 counts.

Lastly, choice of binning can also significantly affect the fit. For example, using overly-wide bins may produce overly-wide FWHM's. Overly-narrow bins will result in a sparse counts vector that obscures the shape of the source distribution. I chose to use David Scott's 1979 "rule of thumb" [19], wherein the number of bins used to histogram data is approximated as:

$$N_{bins} = 2(2N_{pts})^{1/3} \tag{A.121}$$

where N_{pts} is the number of samples to be histogrammed and N_{bins} is rounded up to the nearest integer.

A.10 Source Code

I developed a C++ program called AnalysisTool specially for this project, from which I drew most of my calculations. My work also relies on a series of Octave and Python scripts for data interpretation and plotting.

AnalysisTool is a stand-alone executable written in C++. It depends on both the C++ standard library as well as well-known Boost library [2]. The executable provides a command-line interface for many common tasks, including gamma-ray imaging with both main imaging methods, and using either measured or simulated GRETINA track data. There is also simple macro functionality by which a series of commands can be automated. However, the tool is far from complete. Given more time, I would like to redesign AnalysisTool with a GUI, multi-core support, and a more-unified set of features. As is, the software has been built over many years and would benefit from greater standardization. Many features simply spit out text files for use with an Octave or Python script. I also have yet to write up comprehensive documentation.

The full source code used in this project is well over 1 MB, and would require a few hundred pages to print. Instead, for those for are interested, please download the source archives here: `https://drive.google.com/file/d/0B9vcljsiWJjvamlFcVZwNlVZTXc/view?usp=sharing`

If you would like to use AnalysisTool, the best way would be to contact me directly for instructions. (I can be reached at rdcrabbs@gmail.com.) I am happy to help you get started.

Bibliography

[1] Wolfram Alpha. *Fitting Data to Linear Models by Least-Squares Techniques*. Experimental Data Analyst Documentation. URL: `http://reference.wolfram.com/applications/eda/FittingDataToLinearModelsByLeast-SquaresTechniques.html` (visited on 05/11/2016).

[2] Boost.org. *Boost C++ Libraries*. URL: `http://www.boost.org/` (visited on 07/16/2016).

[3] M. Borsato et al. "Compton Imaging with the Highly Segmented Germanium Detectors of AGATA". In: *LNL Annual Report* Applied, General, and Interdisciplinary Physics Instrumentation (2010), pp. 181–182.

[4] H. Cheung. *Position Determination of Fragile Objects in Nuclear Physics Experiments*. Poster. Chinese University of Hong Kong. URL: `https://people.nscl.msu.edu/\~tsang/Kit_LBAS_poster_accuratenumbers.pdf`.

[5] GRETINA Users Executive Committee. *The Gamma-Ray Energy Tracking Array Whitepaper*. Nuclear Astrophysics and Low Energy Nuclear Physics Town Meeting, Texas A&M. 2014.

[6] M. Cromaz. Personal communication. Apr. 6, 2016.

[7] M. Cromaz. *The GRETINA Spectrometer*. Presentation. CGS 14. Aug. 28, 2011.

[8] D. Eberly. *Distance Between Point and Line, Ray, or Line Segment*. 1999. URL: `http://www.geometrictools.com/Documentation/DistancePointLine.pdf` (visited on 01/03/2008).

[9] D. Eberly. *Intersection of a Line and a Cone*. 2000. URL: `http://www.geometrictools.com/Documentation/IntersectionLineCone.pdf` (visited on 12/29/2014).

[10] Octave Forge. *Function Reference: polyfit()*. URL: `http://octave.sourceforge.net/octave/function/polyfit.html` (visited on 07/16/2016).

[11] GRETINA. *GRETINA GEB Headers*. Internal document. URL: `http://gretina.lbl.gov/tools-etc/gebheaders` (visited on 05/10/2016).

[12] GRETINA. *GRETINA Project Development*. URL: `http://gretina.lbl.gov/project-development` (visited on 05/10/2016).

[13] Claus Grupen and Irène Buvat. *Handbook of Particle Detection and Imaging.* Springer, 2012.

[14] A. Haefner et al. "A Filtered Back-Projection Algorithm for 4-Pi Compton Camera Data". In: *IEEE Transactions on Nuclear Science* 62.4 (2015), pp. 1911–1917.

[15] A. Haefner et al. "Gamma-Ray Momentum Reconstruction from Compton Electron Trajectories by Filtered Back-Projection". In: *Applied Physics Letters* 105.184101 (2014).

[16] K. Heyde. *Basic Ideas and Concepts in Nuclear Physics, 3rd Edition.* Institute of Physics Publishing, 1999.

[17] Isotope Science Facility at Michigan State University. "Upgrade of the NSCL Rare Isotope Research Capabilities". In: *MSUCL* 1345 (2006).

[18] H. Iwasaki et al. "Evolution of Collectivity in ^{72}Kr: Evidence for Rapid Shape Transition". In: *Physical Review Letters* 112.142502 (2014).

[19] A.J. Izenman. "Recent Developments in Nonparametric Density Estimation". In: *Journal of the American Statistical Association* 86.413 (1991), pp. 205–224.

[20] G.F. Knoll. *Radiation Detection and Measurement, 3rd Edition.* Wiley, 2000, pp. 789–794.

[21] K.S. Krane. *Introductory Nuclear Physics, 3rd Edition.* Wiley, 1987, pp. 40–41, 134–149, 170–173, 333–335.

[22] Brookhaven National Laboratory. *Chart of Nuclides.* URL: `http://www.nndc.bnl.gov/chart/` (visited on 06/20/2016).

[23] T. Lauritsen. *Shootout Experiment GSFMA315 at a Glance.* Presentation. Argonne National Laboratory. Apr. 30, 2014.

[24] A. Macchiavelli. *Weighting Fields in GRETINA.* Personal communication. June 17, 2016.

[25] L. Mihailescu et al. *The Compact Compton Imager: a Spectroscopic, Large Field-of-View Gamma-Ray Camera.* Presentation. UCRL-PRES-226138. URL: `https://casis.llnl.gov/casis_06/pdf/pres/mihailescu.pdf` (visited on 08/02/2016).

[26] S. Noji. *GRETINA + S800 Photos.* Internal document. URL: `http://www.rcnp.osaka-u.ac.jp/~noji/gretina_s800` (visited on 04/03/2013).

[27] C. Ordonez, A. Bolozdynya, and W. Chang. "Doppler Broadening of Energy Spectra in Compton Cameras". In: *Nuclear Science Symposium, 1997. IEEE* 2 (1997), pp. 1361–1365.

[28] D. Radford. *GRETA Decomposition Algorithm.* Internal document. Sept. 9, 2004.

[29] L. Riley, C. Campbell, and H. Crawford. *UCGretina v3.0 Geant4 model.* Personal communication. 2015.

[30] M. Schwartz. *Introduction to Quantum Field Theory.* Harvard University, 2008, pp. 131–132.

[31] Y. Shim and Z. Cho. "SVD Pseudoinversion Image Reconstruction". In: *IEEE Transactions on Acoustics, Speech, and Signal Processing* 29.4 (2003), pp. 904–909.

[32] P.A. Soderstrom et al. "Interaction Position Resolution Simulations and In-Beam Measurements of the AGATA HPGe Detectors". In: *Nuclear Instruments and Methods in Physics Research Section A: Accelerators, Spectrometers, Detectors and Associated Equipment* 638.1 (2011), pp. 96–109.

[33] K. Vetter et al. "High-Sensitivity Compton Imaging with Position-Sensitive Si and Ge Detectors". In: *Nuclear Instruments and Methods in Physics Research Sec. A* 579 (2007), 363–366.

[34] E. Weisstein. *Singular Value Decomposition.* Wolfram Mathworld. URL: `http://mathworld.wolfram.com/SingularValueDecomposition.html` (visited on 07/21/2016).

[35] K. Whitmore et al. "Magnetic Response of the Halo Nucleus ^{19}C Studied Via Lifetime Measurement". In: *Physical Review C* 91.041303 (2014).

[36] Wikipedia. *Halo Nucleus.* URL: `https://en.wikipedia.org/wiki/Halo_nucleus` (visited on 07/14/2016).

[37] Wikipedia. *Receiver Operating Characteristic.* URL: `https://en.wikipedia.org/wiki/Receiver\_operating\_characteristic` (visited on 05/12/2016).

[38] Wikipedia. *Sensitivity and Specificity.* URL: `https://en.wikipedia.org/wiki/Sensitivity_and_specificity` (visited on 05/12/2016).

[39] Wikipedia. *Youden's J Statistic.* URL: `https://en.wikipedia.org/wiki/Youden\%27s_J_statistic` (visited on 05/24/2016).

[40] T. Yamazaki et al. "Generation of Quasi-Monochromatic Photon Beams From Compton Backscattered Laser Light at ETL Electron Storage Ring". In: *IEEE Transactions on Nuclear Science* NS-32 (5 1985).